CARBON NANOSTRUCTURED BASED DONOR-ACCEPTOR CONJUGATES FOR LIGHT-INDUCED ENERGY AND ELECTRON TRANSFER

A Dissertation by

Eranda Champika Maligaspe

Bachelor of Science, University of Peradeniya, Sri Lanka 2003

Submitted to the Department of Chemistry

and the faculty of the Graduate School of

Wichita State University

in partial fulfillment of

the requirements for the degree of

Doctor of Philosophy

December 2010

CARBON NANOSTRUCTURED BASED DONOR-ACCEPTOR CONJUGATES FOR LIGHT-INDUCED ENERGY AND ELECTRON TRANSFER

The following faculty members have examined the final copy of this dissertation for form and content, and recommend that it be accepted in partial fulfillment of the requirement for the Doctor of Philosophy with a major in Chemistry.

_____

Francis D'Souza, Committee Chair

_____

Erach Talaty, Committee Member

_____

D. Paul Rillema, Committee Member

_____

Melvin E. Zandler, Committee Member

_____

T. S. Ravigururajan, Committee Member

Accepted for the College of Liberal Arts and Sciences

_____

William D. Bischoff, Dean

Accepted for the Graduate School

_____

J. David McDonald, Dean

DEDICATION

This thesis is dedicated to my parents, Sriyani and Chandrasena Maligaspe for giving love and support.

ACKNOWLEDGEMENTS

First of all, it is a privilege to acknowledge many people who supported, encouraged and inspired me during my five years of graduate program in Wichita State University.

I would like to extend my sincere gratitude to my research advisor Prof. Francis D'Souza for giving this opportunity and his excellent support, guidance and encouragement.

I would like to thank our collaborators Prof. Melvin E. Zandler and Prof. Paul A. Karr and also their students for their effort in performing computational studies which contributed valuable information for the systems studied in this thesis. I would like to thank Prof. Osamu Ito and his co-worker Dr. Atula Sandanayaka for their efforts in providing time-resolved photochemical data and transmission electron microscopy (TEM) data for the nanotube samples mentioned in this thesis. I would like to thank Prof. Shunichi Fukuzumi, Dr. Kei Ohkubo and co-workers for their great effort in performing time-resolved and transient absorption studies to reach our research goals. My sincere gratitude also goes to Drs. Nikolai V. Tkachenko, Helge Lemmetyinen and Tatu Kumpulainen for their efforts in performing photochemical data by using pump-probe and up-conversion methods. I am also thankful to Drs. Claude P. Gros, Jean-Michel Barbe and their co-workers for providing initial precursor for certain

projects. I would like to thank our collaborator Prof. Wlodzimierz Kutner for developing molecular imprinted polymers (MIPs) using some of our compounds.

I would like to thank my thesis committee members Prof. Melvin E Zandler, Prof. Paul Rillema, Prof. Micheal VanStipdonk, and Prof. T. S. Ravigururajan for their valuable time, constant encouragement and support.

I would like to thank my seminar coordinators, Prof. David M. Eichhron and Prof. Kandatege Wimalasena. I would like to thank the entire faculty, Chemistry librarian, Elaine Harvey, Betty Sherwood in Ablah library, and staff of the Chemistry Department at Wichita State University for the excellent support during the time. I am thankful to Dr. Kevin Langenwalter for his support for CHEM 524 lab. I would like to thank my lab mates, Navaneetha Krishanan and Amy Moore for helping to record cyclic voltammetry and providing electrochemical data. I would like to thank all the graduate students here at Wichita State University; especially, my past lab mates Dr. Phillip Smith, Dr. Suresh Gadde, Dr. Raghu Chitta, Dr. Amy Moore and James Blakemore. I would like to mention my special thanks to Dr. Raghu Chitta and Dr. Suresh Gadde for their help, guidance, encouragement and friendship throughout my PhD program. Also present lab mates Aravinda Wijesinghe, Navaneetha Krishnan, Sushnata Das, Anu Amin and K. C. Chandra, Rachel Jacobs, Friduaze Mohtar for their good company, support and valuable discussions regarding research projects. I would like to mention my special thanks to Aravinda Wijesingha for his advice, suggestions, encouragement and being a great friend.

I would also like to thank Dr. J. M. S. Bandara at Institute of Fundamental Studies, Sri Lanka for his support and guidance. Also my warm sincere gratitude goes to faculty members of University of Peradeniya, Sri Lanka, especially Dr. Namal Priyantha, Dr. Ayanthi Navaratne, Dr. R. M. G. Rajapakse and Dr. Anura Wickaramasinghe for giving guidance and support to reach my goals. Also my sincere gratitude goes to all faculty members at the Institute of Chemistry, Sri Lanka. I would like to express my sincere appreciation to all my teachers in undergraduate college and high school for their teaching and guidance.

I would like to thank my sister, brother and my in-laws for all their excellent help, guidance and encouragement. Finally, I would like to thank my parents, Mr Chandrasena Maligaspe and Mrs. Sriyani Maligaspe for their support, encouragement and love which is the greatest gift on earth, without them I could not have made it this far.

ABSTRACT

The research presented in this dissertation deals with the syntheses, characterization, electrochemical, computational and photophysical studies of carbon nanostructures such fullerenes, single-wall carbon nanotubes (SWCNT) and highly colored pigment containing donor-acceptor supramolecular assembles. Using these fascinating chromophores, we have designed and synthesized donor-acceptor systems to mimic natural photosynthesis. Photosynthesis involves two major steps, absorption and transportation of light energy to the reaction center, and photoinduced electron transfer (PET) to generate charge separated entities by using the electronic excitation energy.

We have designed elegant photosynthetic architectures using fullerene as carbon nanostructure based material for mimicry of antenna, mimicry of reaction center and mimicry of ‗combined antenna-reaction center' functionalities in the natural photosynthetic system. Semiconducting single-wall carbon nanotube (SWNT)-based supramolecular nanoarchitectures are constructed using photosensitizing donor and acceptor molecules which reveal efficient photoinduced charge separation. The kinetic and thermodynamic data suggests feasibility of these nanohybrids for the construction of photovoltaic cell and other devices. Interestingly, the photoelectrochemical behavior of the nanohybrids indicates that by choosing nanotubes of appropriate diameter, it is possible to improve the light-harvesting conversion efficiency.

TABLE OF CONTENTS

TABLE OF CONTENTS (continued)

TABLE OF CONTENTS (continued)

TABLE OF CONTENTS (continued)

TABLE OF CONTENTS (continued)

TABLE OF CONTENTS (continued)

TABLE OF CONTENTS (continued)

LIST OF TABLES

LIST OF FIGURES

LIST OF FIGURES (continued)

Figure Page

LIST OF FIGURES (continued)

Figure Page

LIST OF FIGURES (continued)

LIST OF FIGURES (continued)

LIST OF FIGURES (continued)

Figure Page

LIST OF FIGURES (continued)

Figure Page

Figure Page

LIST OF FIGURES (continued)

Figure Page

LIST OF FIGURES (continued)

Figure Page

LIST OF FIGURES (continued)

LIST OF FIGURES (continued)

Figure Page

LIST OF FIGURES (continued)

LIST OF FIGURES (continued)

Figure Page

LIST OF SCHEMES

LIST OF ABBREVATIONS

1 Ag / AgCl Silver / Silver Chloride reference electrode

2 BN Benzonitrile

3 BNAH 1-benzyl-1,4-dihydronicotinamide

4 C_{60}Py N-Methyl-2-(4'-pyridyl)-3,4-fulleropyrrolidine

5 C_{60}Im N-methyl-2-(4'-N-imidazolylphenyl)- 3,4-fulleropyrrolidine

6 DFT Density functional methods

7 DMA *N,N*-methylaminophenyl

8 DMF N,N-Dimethylformamide

9 DPA *N*,*N*-diphenylaminophenyl

10 *o*-DCB *ortho* Dichloro benzene

11 EET Excitation energy transfer

12 EI-mass Electron ionization mass spectrometry

13 ESI-mass spectroscopy Electrospray ionization mass spectrometry

14 $E_{1/2}$ Half wave potential

15 E_{pa} Anodic peak potential

16 E_{pc} Cathodic peak potential

17 $E_{0\text{-}0}$ Singlet excitation energy

18 FAB-mass spectroscopy Fast atom bombardment mass spectrometry

19 Fc Ferrocene

20 Fc / Fc^+ Ferrocene / Ferrocenium internal reference

21 FT-IR spectroscopy Fourier transform infrared spectroscopy

LIST OF ABBREVATIONS (continued)

22 FRET Fluorescence resonance energy transfer

23 HV^{2+} hexyl viologen dication

24 IPCE Incident photon-to-current conversion efficiency

25 k_{et} Rate of electron transfer

26 k_p Decay constant of donor in the absence of acceptor

27 $k_{Forster}$ Rate Forster energy transfer

28 MeOH Methanol

29 NMR Nuclear Magnetic Resonance spectroscopy

30 PET Photoinduced electron transfer

31 $Q_{1/2}$ Concentration needed to achieve 50% quenching

32 $(TBA)ClO_4$ Tetrabutylammoniumperchlorate

33 $TBAPF_6$ Tetrabutylammoniumhexafluorophosphate

34 TPP Tetraphenyl porphyrin

35 SCE Saturated calomel electrode

36 ZnTPP Zinc tetraphenylporphyrin

37 ZnPc Zinc 2,9,16,23-tetra-*tert*-butyl-29H,31H-phthalocaynine

38 ZnNc Zinc tetra-*tert*-butyl-2,3-naphthalocyanine

39 ϕ_f Fluorescence quantum yield

40 λ_{ex} Excitation wavelength

41 λ_{em} Wavelength at which emission is maximum

CHAPTER 1

INTRODUCTION

The economic growth in many parts of the world during the past decade has been sustained by the affordable energy prices.[1] The dependence on oil and electricity has made energy a vital component of our everyday needs. However, the increasing oil and gas price has motivated everyone to take a careful look at the issues dealing with our energy supply and demand. The exponential energy demand is exhausting our fossil fuel supply at an alarming rate. Therefore, scientists have been investigating various alternative energy resources to overcome the energy demand.

Developing environmentally sustainable solutions to the increasing energy demand of the world is one of the most important goals of research. Among different kinds of renewable energy sources, solar energy is most abundant renewable source, which emits more than (120 000 TW) energy onto earth to satisfy the current energy need (13 TW) completely. Sadly, the energy produced from solar source remains less than 0.01% of the total energy demand. Although renewable energy such as solar radiation is an ideal candidate to meet the projected demand, it requires new initiatives to harvest incident photons with greater efficiency and lower cost.

The green plants and bacteria have a better understanding on how to exploit the solar energy than we do. Photosynthesis, the process of converting light energy into chemical energy, involves two major steps, absorption and transportation of light energy of appropriate wavelength by the antenna light harvesting molecules to the reaction center, and photoinduced electron transfer (PET) to generate charge separated entities by using the electronic excitation energy.[2] A deep understanding of phenomenon from nature is an intriguing approach to the problem of solar energy conversion. With that thought in mind and based on the principles of photosynthesis, a variety of donor acceptor hybrids have been synthesized, and sequential energy transfer followed by efficient electron transfer has been demonstrated. However, efficient back electron transfer of majority of the studies resulted in a short-lived charged separated state which is a major drawback for building solar cells.

Photosynthetic reaction centers of green plants and bacteria consist of complex arrays of chromophores noncovalently attached to a protein scaffold, which fixes the cofactors in defined distance and orientation for efficient vectorial electron transfer. The protein also plays vital role to modulate the chemical properties of the cofactors and directs the electron-transfer pathways.[3] In the artificial systems, macrocyclic complexes designed to mimic the structural features of intermolecular interactions and thermodynamic parameters in bacterial photosynthetic system have given insight into the mechanism of self-assembly process. Several covalently and noncovalently linked donor-acceptor

entities with defined distance and orientation have been designed and studied in this regard. To achieve efficient energy transfer and intramolecular electron-transfer processes, both covalent chemistry and biomimetic self-assembly methodologies, such as the formation of π stacks, hydrogen bonds, and van der Waals contacts, have been successfully utilized to connect the donor–acceptor entities. In majority of these studies, porphyrins, phthalocyanines or naphthalocyanines have been used as photosensitizers/electron donors and fullerenes have been employed as acceptors to understand the importance of excitation energy transfer (EET) and photoinduced electron transfer (PET)s reactions.[4-8]

1.1 Excitation energy tarsnfer (EET) and photoinduced electron transfer (PET) for photosynthetic model systems

An understanding of basic principles of photoinduced electron and energy transfer is very important to the design of elegant artificial photosynthetic model systems that mimick the analogous natural system and harvest solar energy with maximum efficiency. The basic components needed to design and build efficient artificial photosynthetic model systems include;

(i) Antenna chromophore that absorbs light and forms an ~~-e~~xcited state species."

(ii) The excited state species must transfer electrons to acceptor chromophore.

(iii) The electron transfer must be directional, and

(iv) The lifetimes of excited states must be long enough for the electron transfer and, thereby, provide long lived charge-separated cation and anion radical ion pairs.

A molecule in the excited state can relax to the ground state by fluorescence, internal conversion, intersystem crossing, non radiative decay, or by two main physical mechanisms: electron transfer or energy transfer to another molecule. Basically, energy and electron transfer are classified as quenching pathways. Quenching is defined as the deactivation of an excited sensitizer by an external component. The external component, quencher usually is a ground-state molecule. During the quenching process, the sensitized chromophore induces permanent or temporary chemical changes in surrounding ground-state molecules. Quenching process may take place between a sensitizer and quencher completely separated or attached to one another via a flexible or rigid spacer molecule. Quenching generates reactive intermediates that rapidly undergo transformation to stable products.

1.2 The Excitation Energy Transfer (EET)

EET can occur either via Dexter's exchange mechanism or Förster's dipole-dipole mechanism. The former mechanism requires the presence of electronic communication (electron exchange) between the donor and acceptor species (via orbital overlap).[9] The Forster energy transfer can take place via a long-range dipole-dipole interaction that occurs through an oscillating electric field in space. A critical difference between electron exchange and dipole-dipole interactions is that a dipole-dipole interaction of two fields does not involve orbital overlap: Since it involves the interactions of fields, dipole-dipole interactions can occur through molecularly occupied space. Thus these mechanisms represent completely two different electronic interactions. Each mechanism will show very different rate constants due to various factors such as the distance separation and optical properties of excited molecule and ground state molecule. (e.g. oscillator strengths and transition dipoles)

The bimolecular rate constant (k) of the primary photochemical process of energy transfer R + M $\rightarrow$ R + *M (by either the exchange or the dipole-dipole interactions) will depend significantly on whether the overall energy-transfer process is energetically downhill (exothermic) or uphill (endothermic) in terms of thermodynamics.[10]

1.3 Visualization of energy transfer by dipole-dipole interactions

The dipole-dipole coupling mechanism for energy transfer is plausible only in multiplicity-conserving (spin allowed) transitions that have large dipoles (μ). Here, the singlet-singlet transitions have large oscillator strengths and are associated with large transition dipoles. Therefore, only singlet-singlet energy transfer is generally plausible by the dipole-dipole mechanism. Transition dipoles of donor and acceptor are very important parameters to observe energy transfer by long range dipole-dipole mechanism. Here, electronic transitions take place exclusively within D (Donor) and A (Acceptor). Excited state donor (D*) acts like an oscillating dipole which is analogous to a transmitting antenna – by inducing the formation of A*. The term resonance energy transfer (RET) is preferred because the process does not involve the appearance of a photon.

Förster has reported that the electrostatic interaction energy (E*)* between two electric dipoles is directly related to the magnitude of the two interacting dipoles of donor (μ_D) and acceptor (μ_A) and inversely related to the cube of the distance between the donor and acceptor (R_{DA}), as shown in Equation (1.1)

$$\text{Electrostatic interaction energy, E (dipole-dipole)} \propto \frac{\mu_D \,.\, \mu_A}{R_{DA}^{\,3}} \qquad \textbf{(1.1)}$$

$$\text{Rate of energy transfer } (k_{ET}) \text{ (dipole-dipole)} \propto E^2 \approx \frac{\mu_D^2 . \mu_A^2}{R_{DA}^6} \quad \textbf{(1.2)}$$

According to Eq: 1.2, the rate of dipole-dipole energy transfer falls off as the inverse sixth power of the separation of the dipoles (R_{DA})

In summary, from Eq: 1.2, Forster theory predicts that k_{ET} for an energy transfer via dipole-dipole interactions will be proportional to the following quantities.

1. The square of the transition dipole moment μ_D, corresponding to the $^*D \rightarrow D$ transition
2. The square of the transition dipole moment μ_A, corresponding to the $A \rightarrow A^*$ transition
3. The inverse sixth power of the separation between $^*D$ and A. (i.e., $1/R^6_{DA}$)

The theoretical quantity of transistion dipole (μ) is related to experimental quantities, such as extinction coefficient (ε) or radiative lifetimes (k^0).

From this relationship, a direct proportionality is deduced as follows.

$$\mu_D^2 (D^* \longleftrightarrow D) \longrightarrow \int \varepsilon_D \quad \text{or} \quad \int k_D^0 \qquad \textbf{(1.3)}$$

$$\mu_A^2 (A^* \leftrightarrow A) \longrightarrow \int \varepsilon_A \quad \text{or} \quad \int k_A^0 \tag{1.4}$$

where $\int\varepsilon$ represents an integration of the experimental excitation coefficient for an absorption band over energy and $\int k^0$ represents an integration of the pure radiative rate constants over an emission band.

The square of the theoretical transition dipole moments (μ) can be replaced by experimentally measurable quantities. (k_D^0 and $\int\varepsilon_A$), as a function of the separation of R_{DA})

$$k_{ET\ (\text{dipole-dipole})} = \frac{\alpha\ k_D^0 \int \varepsilon_D}{R_{DA}^6} \tag{1.5}$$

The value of k_{ET} also depends on the spectral overlap integral. By considering the overlap of *D emission with A absorption,

We can rewrite the Eq. 1.5 as below.

$$k_{ET\ (\text{dipole-dipole})} = \alpha \frac{\kappa^2\ k_D^0 \int \varepsilon_D}{R_{DA}^6} J\ (\varepsilon_A) \tag{1.6}$$

The term α in Eq. 1.6 is a proportionality constant determined by experimental conditions, such as concentration and solvent index of refraction. The term κ^2 (orientation factor) takes into account the fact that the dipoles μ_D and μ_A are vector quantities, and that the interaction between two oscillating dipole vectors of donor and acceptor will depend on the mutual orientation of the dipoles in space. Depending upon the relative orientation of donor and acceptor, this factor can range from 0 to 4. For head-to-tail parallel transition dipoles $\kappa^2 = 4$, and for parallel dipoles $\kappa^2 = 1$. If the dipoles are oriented perpendicular to one another, $\kappa^2 = 0$. For a random distribution of orientations for dipoles in space, $\kappa^2 = 2/3$.

The term J, spectral density integral (overlap integral) expresses the degree of spectral overlap between the donor emission and the acceptor absorption.

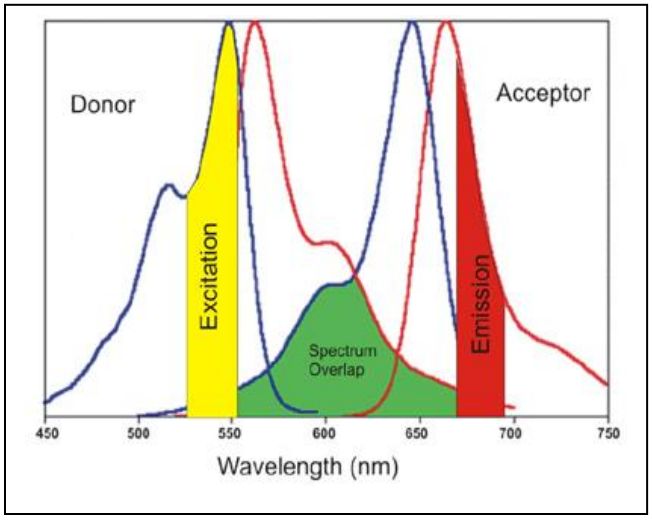

Figure 1.1: Spectral overlap (green color highlighted area) for donor emission and acceptor absorption.

Previous equation 1.6,

$$k_{ET\ (dipole\text{-}dipole)} = \alpha \frac{\kappa^2 k_D{}^0 \int \varepsilon_D \; J\ (\varepsilon_A)}{R_{DA}{}^6} \qquad \textbf{(1.6)}$$

We can rewrite eq. 1.6 by including quantum yield of donor, the refractive index of the medium and τ_D ($\tau_D = 1/k_D$)

$$k_{Forster} = \frac{(\text{proportionality const.})\ \kappa^2\ \phi_D\ J_{Forster}}{n^4\ \ \tau_D\ \ R_{DA}{}^6} \qquad \textbf{(1.7)}$$

$$\text{Proportionality constant} = \frac{9000\ (\ln 10)}{128\ \pi^5\ N} = 8.8 \times 10^{-25} \qquad \textbf{(1.8)}$$

$$k_{Forster} = \frac{8.8 \times 10^{-25}\ \kappa^2\ \ \phi_D\ \ J_{Forster}}{n^4\ \ \tau_D\ \ R_{DA}{}^6} \qquad \textbf{(1.9)}$$

$$J_{Foster} = \int F_D(\lambda)\ \ \varepsilon(\lambda)\ \ \lambda^4 . d\lambda \qquad \textbf{(1.10)}$$

where

Φ_D = the quantum yield of the donor in the absence of acceptor

n = the refractive index of the medium

N = Avogadro's number

R_{DA} = the distance between the donor and the acceptor

τ_D = the lifetime of the donor in the absence of the acceptor

$F_D(\lambda)$ = the corrected fluorescence intensity of the donor in the wavelength range λ to $\lambda + \Delta\lambda$ with the total intensity (area under the curve) normalized to unity.

$\varepsilon(\lambda)$ = the extinction coefficient of the acceptor at λ

κ^2 = the relative orientation factor

1.4 Photoinduced electron transfer (PET)

The study of PET has attracted the attention of numerous research groups because of its major role in governing natural photosynthetic pathways.

In Figure 1.2, the horizontal lines represent orbital populated by electrons (shown by dots and arrows). In electron transfer process, the electron donor (D, sensitizer) transfer an electron to a lowest unoccupied molecular orbital (LUMO) of an acceptor (A, quencher), creating a charge-separated donor-acceptor pair, involving a cation radical ($\mathbf{D}^{\bullet+}$) and an anion radical ($\mathbf{A}^{\bullet-}$)[4-8]

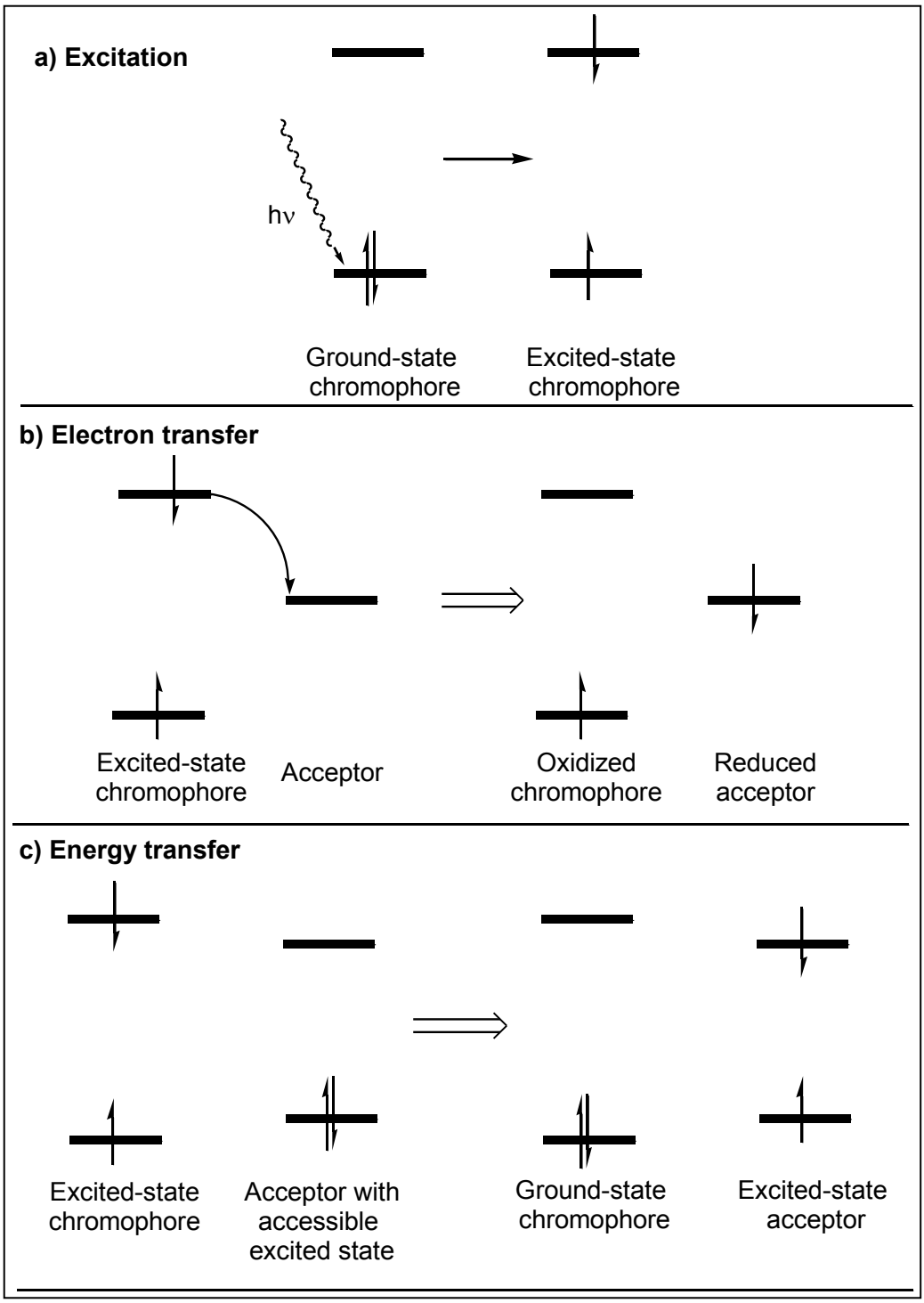

Figure 1.2: Schematic representation (a) excitation of chromophore (b) electron transfer and (c) energy transfer quenching of a chromophore excited state.

In the case of energy transfer, there are two pathways for generating an excited state of acceptor (A*). First, there may be a mutual exchange of electrons, a mechanism known as energy transfer by electron transfer. Here, donor molecule (D) gives up an electron to acceptor (A), while latter in turn returns an electron to D, implies mutual or close proximity of D* and A. Due to back and forth travel of electrons, there must be some overlap of the electron clouds on D* and A.

Photoinduced electron transfer can be regarded as a process where absorbed light energy is transformed into chemical energy. This process can be interpreted by the classical electron transfer theory developed by R. A. Marcus. The theory describes the transition state from an initial state (reactant) to a final state (product). Also the Marcus theory explains the BET (back electron transfer) from D^{+}- A^{-} charge-separated state to the ground state, D-A. Moreover, this theory provides key aspects on the role of certain intermediate states in the ET or BET reactions.

1.5 The classical Marcus theory of electron transfer.

In Marcus theory, the complex, multidimensional potential energy surfaces of the reactant (R) state and the product (P) state are simplified to parabolas of Gibbs free energy vs. the reaction coordinate. Introducing the reaction coordinate reduces the potential energy surfaces to one dimension, i.e change in the

reaction coordinate describes the changes in the nuclear coordinates of the molecule itself and those of the surrounding solvent. Considering all internal (nuclear) and external (solvent) motions of the energy profile along with the reaction coordinate is nonparabolic, but near the energy minima the parabolic approximation of the free energy works well.[11]

The curvature of the reactant and the product parabolas is assumed to be the same, so the product surface obtained from the reactant by shifting the parabola in reaction coordinate and in energy. The shift in reaction coordinate determines the reorganization energy, λ, and the shift in energy gives the Gibbs free energy of the reaction, $-\Delta G$. The electron transfer (ET) reaction takes place at the transition (T) state, where the reactant and product parabolas intersect, *i.e* at the point where the reactant and product have the same configuration of nuclear coordinates. Thus, for ET to take place, the reactant must distort from its equilibrium by the activation energy, E_A.

(A)

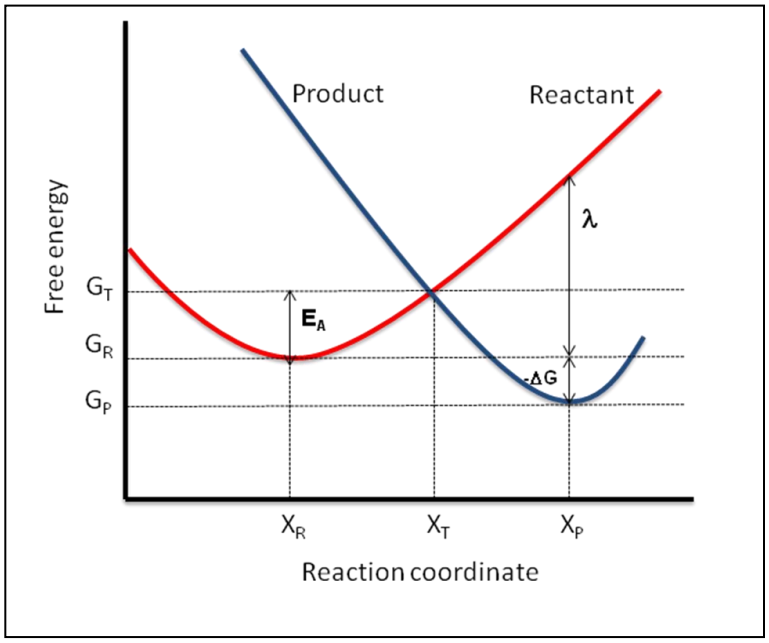

(B)

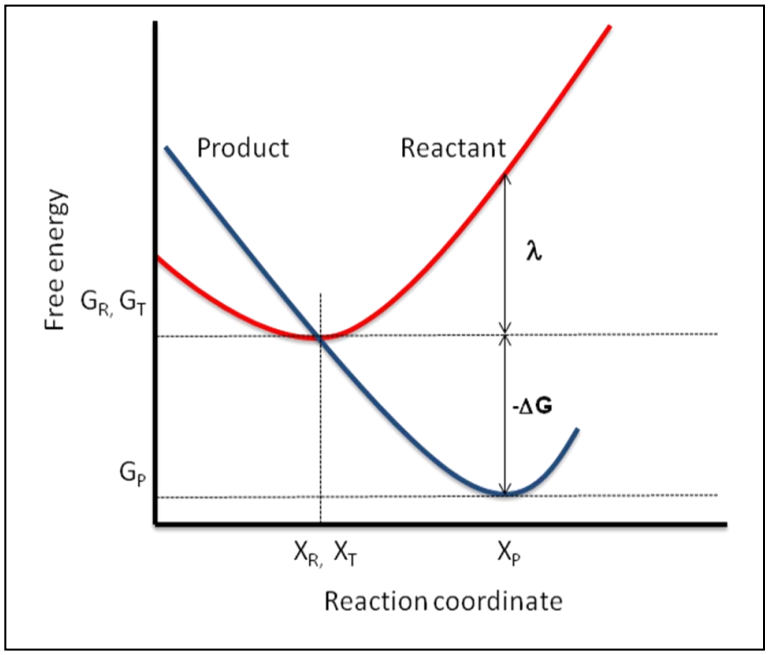

Figure 1.3: Gibbs energy surface of the reactant and products states with (A) $-\Delta G < \lambda$ (normal region) and (B) $-\Delta G = \lambda$ (maximum k_{ET})

Using the notation of Figure: 1.3 the reactant and the product parabolas are

$$E_R(\mathcal{X}) = c(\mathcal{X} - \mathcal{X}_R)^2 + G_R$$

$$E_P(\mathcal{X}) = c(\mathcal{X} - \mathcal{X}_P)^2 + G_P \qquad \textbf{(1.11)}$$

Where,

c = coefficient which describes the parabola curvature and is the same for the reactant and product states as it was assumed above.

The shift in x axis (reaction coordinate) and the shift in y axis (free energy) in figure 1.3 can represented as

$$\Delta\mathcal{X} = \mathcal{X}_R - \mathcal{X}_P$$

$$\Delta G = G_R - G_P$$

The reaction coordinate of the transient state gives the intersection of the two parabolas

$$\mathcal{X} = \frac{\Delta G}{2c\,\Delta\mathcal{X}} + \frac{\mathcal{X}_R - \mathcal{X}_P}{2} \qquad \textbf{(1.12)}$$

The reorganization energy, λ, is given as

$$\lambda = E_R(\chi_P) \quad G_R = c\Delta\chi^2 \tag{1.13}$$

and the activation energy, E_A, of the ET reaction becomes

$$E_A = G_T - G_R = \frac{(\Delta G + \lambda)^2}{4\lambda} \tag{1.14}$$

According to classical transition state theory the population at the transient state follows the Boltzmann distribution and the rate constant for ET is

$$k_{ET} = K_{el}\, \nu_n \exp\left[\frac{E_A}{k_b T}\right] \tag{1.15}$$

where

K_{el} = the electronic transmission coefficient

ν_n = the frequency of passage through the transition state

k_B = the Boltzmann constatnt

T = temperature

In the classical Marcus theory K_{el} is usually estimated to be unity the same order of magnitude as molecular vibrational motion (10^{13} s^{-1})

The classical Marcus equation gives by using eq. **(1.14)** and eq. **(1.15)**

$$k_{ET} = \kappa_{el}\ \nu_n\ \exp\left[-\frac{(\Delta G^o_{ET} + \lambda)^2}{4k_B T} \right] \qquad \textbf{(1.16)}$$

$$\kappa_{el}\ \nu_n = \left(\frac{4\pi^3}{h^2 \lambda k_B T} \right) V^2 \qquad \textbf{(1.17)}$$

$$k_{ET} = \left(\frac{4\pi^3}{h^2 \lambda k_B T} \right) V^2 \exp\left[-\frac{(\Delta G^o_{ET} + \lambda)^2}{4k_B T} \right] \qquad \textbf{(1.18)}$$

The reorganization energy can be separated into two terms.

Thus, $\lambda = \lambda_{in} + \lambda_s$

λ_{in} is the inner-sphere reorganization energy (solvent independent inner term)

λ_s is the outer-sphere reorganization energy (solvent reorganization energy)

Inner-sphere reorganization energy arises due to energy changes accompanying changes in bond lengths and bond angles during the electron-transfer step. It can be expected to be fairly small especially for the big, rigid, and highly symmetrical molecules as ones used in this study. Outer-sphere reorganization energy is the

energy changes due to the orientation and polarization of the solvent molecules around the studied molecule in the reactant state and the product state. Treating the solvent as a dielectric continuum and approximating the electron donor and acceptor as spherical the solvent reorganization energy is

$$\lambda_s = \frac{e}{4\pi\varepsilon_o}\left[\frac{1}{2r_D} + \frac{1}{2r_A} - \frac{1}{r_{DA}}\right]\left[\frac{1}{\varepsilon_{opt}} - \frac{1}{\varepsilon_s}\right] \qquad \textbf{(1.19)}$$

where e is the charge transferred in the reaction, i.e. one electron charge, ε_o is the vacuum permittivity, ε_{opt} (= n^2, where n is the refractive index of the solvent) and ε_s are the optical and static dielectric constants for the solvent, r_D and r_A are the radii of the donor and the acceptor respectively, and r_{DA} is the center-to-center distance between the donor and the acceptor.

As mentioned above, the electronic transmission coefficient, K_{el}, or the probability that transition from the reactant to the product parabola occurs at the transition state, is assumed as unity in the classical theory. For ET reactions with $K_{el} << 1$ a quantum mechanical treatment of the Marcus theory must be used. The quantum mechanical treatment takes into account the probabilities of electron and nuclear tunneling between the reactant and the product states.

1.6 Photoinduced Electron Transfer (PET) and Excitation Energy Transfer (EET) in biological and non-biological systems.

Photosynthesis is the process by which plants, some bacteria, and some proteins use the energy from sunlight to produce sugar, which cellular uses to convert adenosine diphosphate (ADP) into adenosine triphosphate (ATP), which serves as energy source for all living organisms. It is a transmembrane process, and the major components are housed in and span the lipid bilayer of the bacterial cell membrane.[12, 2f]

Sunlight is collected by an antenna system that contains chromophores such as bacteriochlorophyll and carotenoid polyenes. A variety of chromophores and protein environments is used so that light can be efficiently absorbed throughout the solar spectrum. Singlet electronic excitation energy is rapidly transferred among the antenna chromophores and ultimately to the reaction center.

Investigations using X-ray crystallography have revealed detailed structural information for several photosynthetic bacterial reaction centers. These reaction centers have two branches, L and M. All of these moieties are well arranged with C_2 symmetry as shown in Figure 1.4.

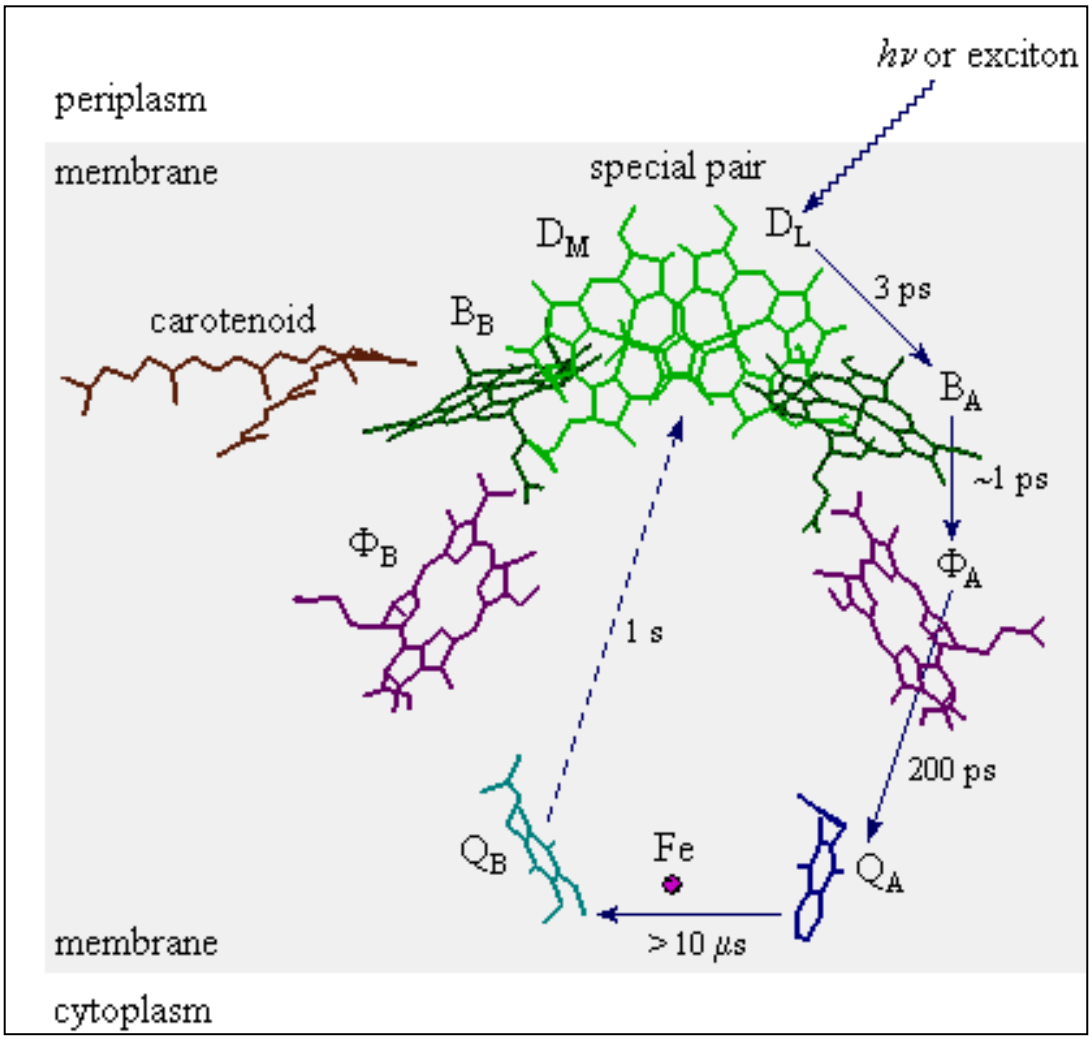

Figure 1.4: X-ray crystal structure and scheme of electron transfer in the photosynthetic reaction center of purple bacterium *Rhodopseudomonas viridis*

In the reaction center, the first step is photoinduced electron transfer from a special pair of bacteriochlorophylls (D_M & D_L), generating its singlet excited state [$^1(D_M$ & $D_L)^*$], which lies 1.4 eV above the ground state, via an accessory bacteriochlorophyll to a bacteriopheophytin molecule (Φ_A), located at a R_{ee} ~ 9 Å

(edge-to-edge distance). The energy of $(D_M \& D_L)^{\bullet+}$ $\Phi_A^{\bullet-}$ (~1.2 eV) is lowered by ~0.2 eV. This matches well with the reorganization energy (λ) of the electron transfer to optimize the forward electron transfer process in Marcus normal region while shifting the charge recombination process deeply into the inverted region. In a subsequent charge-shift step, an electron migrates from the bacteriopheophytin to a quinone Q_A, and then on to a second quinone Q_B. In this final isoenergetic step, an electron transfer takes place with a time constant of ~100 μs[12]. The resulting final charge separated state with life time of ~ 1 s across the membrane eventually leads to the production of chemical energy. After reduction of the oxidized special pair by a *c*-type cytochrome, the energy of a second photon is used to transfer a second electron to Q_B. The resulting hydroquinone diffuses to the cytochrome *bc,* complex, which is a transmembrane proton pump. It reoxidizes the hydroquinone back to a quinone and uses the resulting reduction potential, via the *c*-type cytochrome, to reduce the special pair, thus regenerating the reaction center. The energy released is used to transfer protons across the membrane, establishing a proton motive force across the bilayer. Finally, protons flow back across the membrane in the direction of the proton gradient and the energy produced drives the synthesis of adenosine triphosphate (ATP) from adenosine diphosphate (ADP) and inorganic phosphate (P_i) with catalysis by ATP synthase. Thus, the overall photosynthetic process uses light energy to produce ATP at high chemical potential, and the resulting high-energy phosphate is used to fill the various energy needs of the organism.

A detailed understanding of these natural reactions has been greatly aided by studies of electron and energy transfer reactions in artificial model systems.

1.7 General artificial donor-acceptor systems

The arrangement of the donor–acceptor hybrids in the photosynthetic reaction center (PRC) is accomplished *via* non-covalent incorporation into a well-defined protein matrix. To mimic primary events of natural photosynthesis, the study thereof necessitates simple donor-acceptor model systems. The ultimate goal is to design and synthesis different conjugates which can efficiently convert solar energy into useful chemical energy. A main feature in photosynthetic reaction center modeling is incorporation of a photo excitable chromorphore with a donor or an acceptor using a covalent or non covalent linkage.

Several covalently and non-covalently linked light harvesting model systems, involving different donors such as porphyrins, phthalocyanines, naphthalocyanines, and ferrocene and acceptors such as quinines, fullerenes, perylenecarboxiimides and boron dipyrrines, have been synthesized and investigated to discover basic aspects of light induced electron/energy transfer and to obtain long lived charge separated states. The covalently-linked model systems are substantially different from natural systems, especially with regard to the composition of the medium intervening between donor and acceptor. Therefore, discovery of non-covalently linked donor-acceptor models to mimic

natural systems appears to be more promising in the field of artificial photosynthesis.

Careful design of such molecules must take into account the following factors arising from the electron transfer theory described in the previous section.

1. Proper redox potentials of the donor and acceptor to enable electron transfer;
2. Suitable size and symmetry of the donor and acceptor to optimize λ and thus k_{ET} and k_{BET};
3. Light harvesting ability of at least one of the chromphores, i.e high molar absorption coefficient at a wavelength where excitation can be carried out;
4. Suitable excited state energy of the light harvesting chromophore. i.e. negative free energy of ET from the excited state.
5. Mutual orientation and distance of the chromophores, i.e. control of λ and thus k_{ET} and k_{BET}. These strategies have been incorporated to increase the rates of the forward ET and to slow down the BET such as modification of energies of donor-acceptor dyads, tuning electronic coupling between donor and acceptor moieties, and incorporation of secondary donor or acceptor into multicomponent array. These factors systematically altered to overcome the difficulties encountered in donor-acceptor systems.

In PET process of artificial photosynthetic model systems, charged species, the radical cation of donor ($D^{\bullet+}$) and the radical anion of the acceptor ($A^{\bullet-}$) are utilized as electrons and holes to drive electrical current or promote chemical reactions before back electron transfer leading to the initial state of reactants. (Figure 1.5)[13]

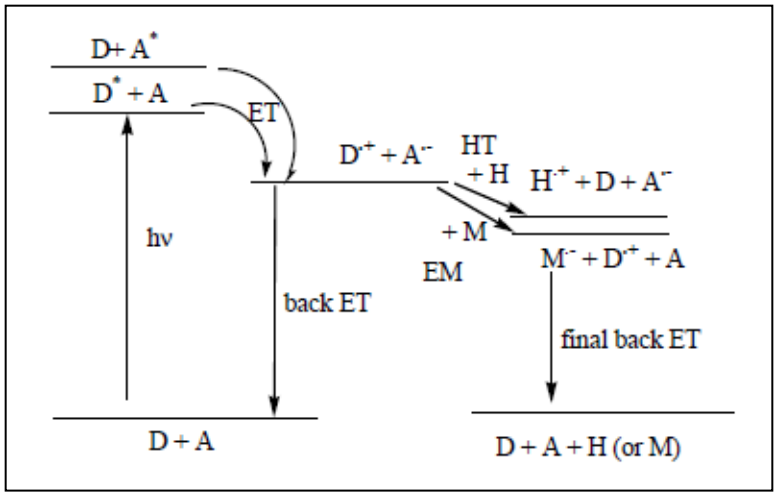

Figure 1.5: Schematic energy diagrams for photoinduced ET processes in bimolecular donor–acceptor systems: HT refers to hole transfer step in the presence of hole acceptor (H) and EM refers to an electron mediation step in the presence of an electron mediator (M).

PART A

Porphyrin as electron donors

Porphyrins, the main chromophores of natural photosynthesis, are obvious candidates for the design of artificial antenna systems. Among different types of donor-acceptor systems, porphyrin and fullerene have attracted to create an efficient donor and an elegant acceptor in recent years. The choice of porphyrins is due their structural similarities to the naturally occurring chlorophyll and pheophytin. Porphyrins and their metal derivatives exhibit strong absorption bands around 400 nm, the soret band and several weak absorption bands (Q bands) at higher wavelengths which can be changed by the peripheral subsitutents on the porphyrin ring or by insertion of metal atoms into the center of the porphyrin ring cavity. The extensively π conjugated systems such as pophyrins enhance their electron donating ability and make them suitable candidates for designing artificial photosynthetic devices. Their redox properties are rich, and easily tunable by proper functionalization on the periphery of the porphyrin or incoperation of different metal ions in the cavity. Moreover, they have high quantum yields and the excited singlet and triplet states of these donors are long enough to allow interactions with other molecules in excited states and/or ground states. The high electronic excitation of porphyrins, typically exceeding 2.0 eV, governs a strongly exergonic electron transfer, which

subsequently intercedes the conversion of the light and the chemical/electrical energy. Synthesis of porphyrins has been widely investigated. The two positions that are easily accessible to modify porphyrins are β pyrrole and meso positions.[13, 14]

Phthalocyanines (Pcs)[16] are synthetic porphyrin analogues that exhibit intense absorption in the region of red/near-infrared, where porphyrins fail to exhibit appreciable absorptions. Therefore, Pcs are attractive candidates for designing donor-acceptor conjugates, where they function as antenna chromophores with both broader absorbing range of solar spectrum and higher fluorescence quantum yields compared with those porphyrins. The absorption spectra of these planar aromatic macrocycles exhibit intense Q-bands in the visible region, usually centered at 620-700 nm.

The architectural flexibility of phthalocyanines[16] is well established by the large number of metallic complexes, as well as by different substituents that can be attached to the phthalocyanine core. All these chemical variations can alter the electronic structure of the macrocyclic core, and therefore, these are promising candidates for the field of nonlinear optics (NLO) which has important applications in the photoelectronics and photonics. These macrocycles can interact with each other by attractive $\pi-\pi$ stacking interactions, leading to aggregation in solution.[17] This kind of cofacial stacking is useful to achieve some

supramolecular properties, for example conductivity along the main axis of the stacked system by electron-delocalization through coplanar macrocycles.

Boradiazaindacenes (borondipyrromethanes, BODIPYs, BDPs) are very bright fluorophores with high quantum yields and large extinction coefficients. the overall architectural modifications of these compounds are known to generate pigments with emission peaks spanning part of the visible spectrum from green to the red end.[18]

These chromophores have a number of favorable physicochemical properties such as sharp (fwhm 25 nm) and moderately strong (ε = 40 000 - 100 000 $M^{-1}cm^{-1}$) absorption near 500 nm, long excited-state lifetimes and good solubility in organic solvents[19]. Boron dipyyrin, as an accessory pigment in porphyrin-containing array systems enhances the absorption properties of associated donor-acceptor conjugates for light harvesting applications and promotes relatively selective excitation in the presence of porphyrin (free base or metallated).

Quinones were used initially as acceptors in artificial photosynthetic systems due to their structural similarities with the natural photosynthetic terminal electron acceptors. But these two dimensional acceptors show high reorganization energies during electron transfer reactions. Lately, however fullerene have attracted much attention for the field of artificial photosynthesis.

One of the most fascinating phenomena in three dimensional fullerene acceptors is the small reorganization energy associated with almost all their reactions, especially in photoinduced electron transfer (PET). The stabilization of charged entities is a unique characteristic feature for fullerene due to rigid and confined structure of π sphere. Fullerenes have very rich electrochemical properties with eight reversible redox states and the first reduction potential being comparable to that of benzoquinone, in which the six electron reductions are equally spaced.

The electronic transitions and photoexcited state processes of fullerenes are directly related to their other properties. Fullerene, especially C_{60} are found to be excellent optical limiters in room temperature solution. They exhibit strong absorption in the UV region and weak, but significant absorption in the visible region. Chemically functionalized fullerenes retain most of their basic properties. However, in the excited state, their absorption is extended to the near IR region, which facilitates the promotion of electrons with low energy light. The excited singlet states then decay rapidly to the energetically low lying triplet state via intersystem crossing with lifetimes longer than 40 μs. The optical absorption spectra of π radical anion of C_{60} show narrow bands in the near IR region, around 1080 nm, serving as diagnostic probes for their identification.

One of the aspects in photoinduced electron transfer is to have fast charge separation and slow charge recombination, which improves the life time of the radical ion pair. Electron acceptors with low reorganization energy can

slow down charge recombination. Due to the high degree of delocalization and structural rigidity, fullerenes have low solvent independent reorganization energy, which means fullerenes need little energy to adjust the excited state to the new solvent environment. This corresponds directly to the symmetrical structure and large size of the fullerene framework.

In recent years, splendid arrays of covalently and non-covalently donor-acceptor supramolecular hybrid systems employing porphyrins, phthalocyanines, naphthalocyanines and fullerenes have been designed, synthesized and studied to understand the intriguing electron and/or energy transfer or energy transfer followed by electron transfer reactions and, thereby mimic antenna-reaction center functionality in photosynthetic reaction center. A few relevant donor-acceptor systems for energy transfer and electron transfer will be presented in this chapter.

1.8 Covalently linked donor-acceptor systems for mimicking antenna functionality

A large number of covalently linked donor-acceptor systems have been elegantly designed, synthesized and studied to understand photoinduced energy transfer reaction to mimic antenna functionality in natural photosynthesis. The development of efficient donor-acceptor molecular array systems that utilize energy transfer presents interwoven design and synthesis challenges.[19] The

design challenges include selection of proper pigment molecule as well as formation of overall three-dimensional architecture. The synthetic challenge is to realize the design objective. The spectral overlap, the energy transfer rates, efficiencies, and mechanisms of energy transfer (through-bond and/or through-space) were properly deduced.

The design of synthetic light-harvesting model systems by incorporating covalently linked porphyrins (metallo and free base) has been developed to mimic natural photosynthetic pigments. Scientists have reported[20, 21] a variety of such array systems, which undergo intramolecular porphyrin-porphyrin energy transfer. The majority of these arrays is bichromophoric and can yield efficient electronic communication channels among the chromphores.

Hsiao, Lindsey and co-workers[20] developed array system (dimeric and trimeric) that are constructed with an ethyne linkage between aryl groups on adjacent tetraarylporphyrin macrocycles, which provides a semirigid architecture that limits direct chromophore interactions. This structural behavior is promoting modest bending and allowing rotation of the porphyrin planes about the ethyne in fluid solution which attributes to activation of efficient energy transfer. Interestingly, the substitution pattern at the periphery of porphyrin is able to change the relative energies of filled orbitals. The resulting orbital ordering difference promotes to disparate the energy transfer rates in the dyad systems.

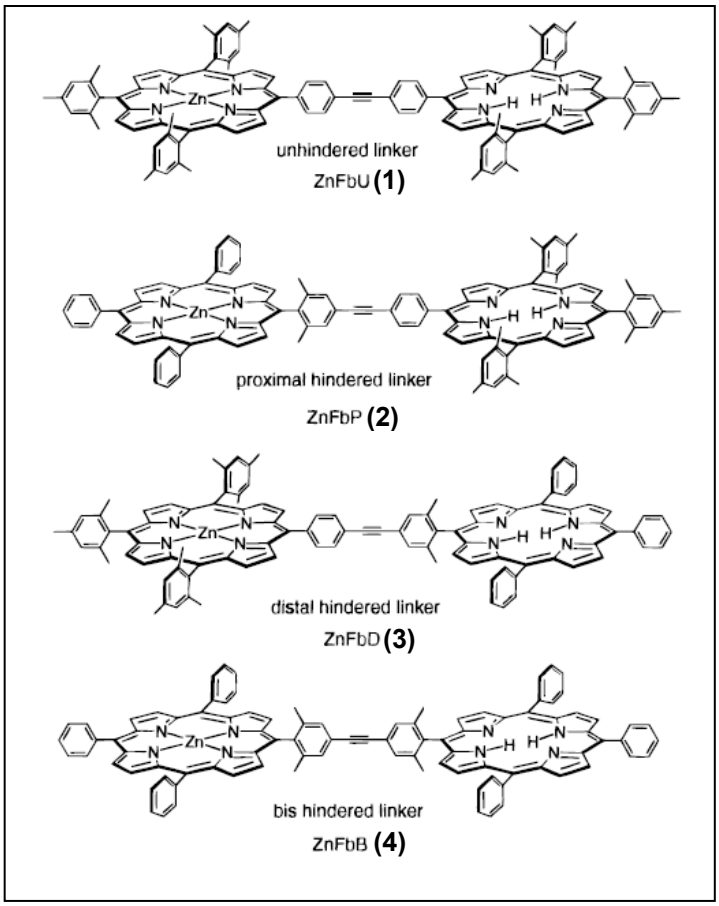

Figure 1.6: The dimers incorporate a Zn porphyrin and a Fb porphyrin connected by the diarylethyne linker.

The dimers consist of Zn porphyrin and a free base porphyrin which is linked by the diarylethyne spacer, as shown in Figure: 1.6. The methyl groups attached on the spacer aryl group adjacent to the porphyrin chromophores revealed torsional constrain. This promoted dyad to make proximally-hindered dimer, **(2)** (ZnFbP), as the Zn porphyrin transfers energy to the Fb porphyrin. The absorption spectrum of ZnFbU, **(1)** (unhindered) showed greater Soret band broadening than that of hindered ZnFbB, **(4)** array. This broad Soret band

reveals significant electronic communication between the B-states of the porphyrins in the dimer. Upon excitation of ZnFbU **(1)** at 648 nm in toulene, where only the free-base (Fb) porphyrin absorbs, results in typical Fb porphyrin emission with quantum yield (0.13) resembling that of monomeric Fb porphyrins. The Zn porphyrin fluorescence is quenched by at least 20-fold compared with control compound that has only Zn porphyrin. Moreover, the occurrence of energy transfer from Zn porphyrin to Fb porphyrin was confirmed by recording the excitation spectrum of ZnFbU **(1)**, while holding the emission monochromator at 720 nm corresponding to Fb porphyrin emission. The lifetime of ZnFbP **(2)** dimers gave a slight increase time scale (~2.3 - 2.4 ns) compared with ZnTPP (2.04 ns). The fluorescence yield, fluorescence excitation, transient absorption, and fluorescence life time studies all reveal that the yield of energy transfer is well over 90% for all the ZnFb dimers. Such studies revealed excitation energy transfer for studied array systems with time constants on the order of 24-88 ps depending upon the type of the array system. Fast energy transfer rates (~720 ps^{-1}) of all the dimers are consistent with a through bond mechanism, rather than through space (Förster) energy transfer. Moreover, torsional constraints due to methyl substituents in the diarylethyne linker would not be expected to strongly influence a through space energy transfer process.

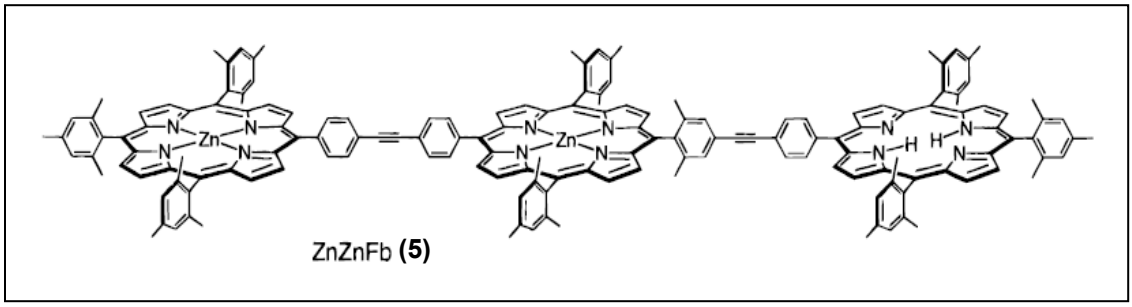

Figure 1.7: ZnZnFb trimer **(5)** consists of two Zn porphyrins and free-base porphyrin

Interestingly, the diarylethyne-linked arrays also promote efficient energy transfer process among isoenergetic pigments. To reveal that, a ZnZnFb trimer **(5)**[20,21] is reported. This trimer consists of two Zn porphyrins and one free-base (Fb) porphyrin in a linear array system. Two isoenergetic Zn porphyrin pigments makes isoenergetic energy transfer which is an essential mechanism is natural photosynthetic system.

Lindsey and coworkers[19] reported another light harvesting arrays containing one, two, or eight boron-dipyrrin (BDPY) pigments and one porphyrin (free base or Zn chelate), linked via *p,p'*-diarylethyne spacers. In this array system, boron-dipyrrin acts as energy donor and porphyrin acts as energy acceptor. Efficient energy transfer from the BDPY pigment(s) to the porphyrin (free base or Zn chelate) is observed in arrays containing one **(6)** or two **(7,8)** (>90%) or eight **(9)** (>85%) accessory pigments per porphyrin. Here also,

energy transfer via a linker-mediated through-bond (TB) process is predominant rather than a through-space (TS) mechanism.

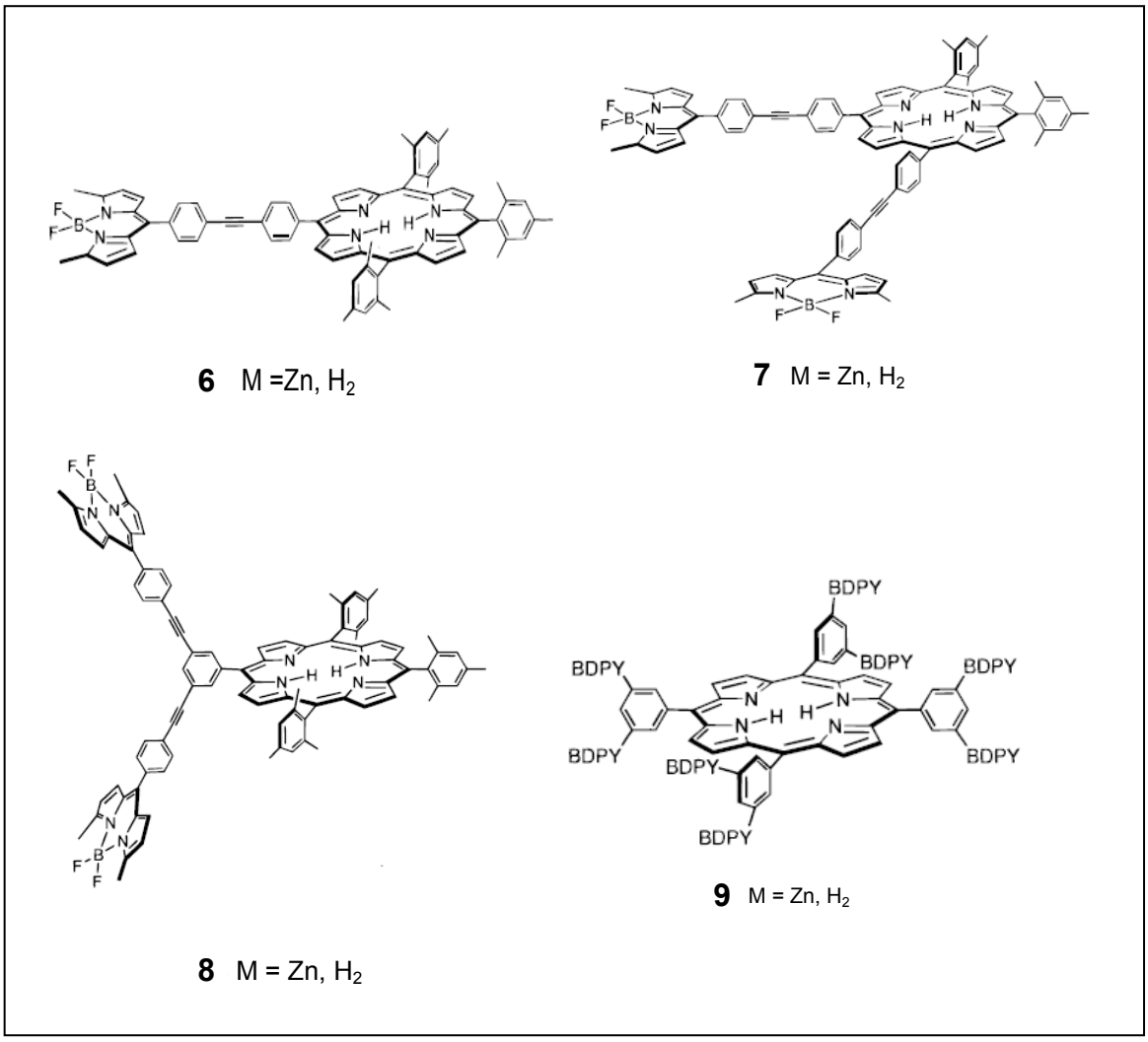

Figure 1.8: Different BDP-porphyrin dyads by increasing number of BDP units

In absorption spectroscopy, the Soret band (421-423 nm) of dyads consist of one **(6)** or two BDP **(7,8)** moieties show slight bathochromic shift (1-4 nm) compared to those of parent tetraphenyl- and tetramesitylporphyrins. Eight BDP

(8) units contained porphyrin (H_2 and Zn) array system reveals relatively large red shift (10-14 nm). Moreover, upon excitation of BDP unit at 485 nm (where the BDP absorb 70 - 95 % of light), the emission of BDP reveals significant quenching. Static fluorescence spectra used to quantify the yield of energy transfer in three different ways: (1) determine the extent of fluorescence quenching, (2) compare the yield of porphyrin emission upon excitation of matched samples of porphyrin (λ_{ex} = 420 nm) and the BDP-porphyrin dyad (λ_{ex} = 516 nm), and (3) compare the absorption and fluorescence excitation spectra of BDP-porphyrin (normalized to Soret band). The emission of BDP showed 7-30 fold of quenching in various array systems, with extent of energy transfer of 90-96% for all one and two contained BDP porphyrin dyads. Eight BDP free base porphyrin dyad displayed 86%. Moreover, the experimental evidence greatly attributes that through bond (TB) Forster energy transfer is most dominant contributor. These array systems reveal biexponential decay with the energy transfer time constants of ~2 and 20 ps. The arrays with equal number of BDP units at *p*- or *m*- aryl positions exhibit similar photochemical properties.

Furthermore, in the overall photodynamics of the compounds, the 5-aryl ring in the BDP moiety plays vital role. Specially, this structural feature promotes a short lifetime of the dominant excited state decay pathway and a high contribution of a fast excited-state deactivation route, which in turn modulates the energy transfer channels in the BDP-porphyrin arrays.

Construction of molecular wires using BDP, Zn porphyrin and free-base porphyrin is inspired by natural photosynthesis which consists of hundreds of pigments in a solid protein matrix. Wagner and Lindsey[21, 22, 23] have constructed a molecular wire composed of BDP **(10)**, a linear array of three Zn porphyrins and free-base porphyrin.

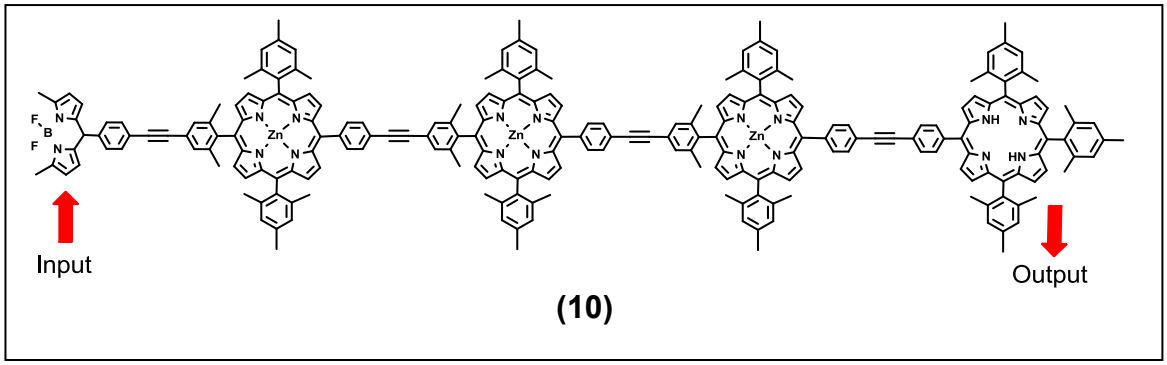

(10)

Figure 1.9: A molecular wire composed of BDP, three Zn porphyrins and free-base porphyrin.

Here, BDP acts as an optical input at one end; a linear array of three zinc porphyrins is involved as a signal transmission element, and a free base porphyrin act as an optical output at the other end. Upon excitation at 485 nm BDP (input dye) absorbs 62% of the light, 12% is absorbed by the free-base porphyrin (output dye), and 26% is absorbed by the three Zn porphyrins (signal transmission element). The stepwise energy transfer efficiencies from input to output are 95%, 93%, 93%, and 93%.

This strategy is extended with readily available tetraarylporphyrin as modular building blocks. This rigid molecular architecture is tailored with four peripheral facially-encumbered Zn porphyrins to the middle free-base porphyrin moiety (Figure 1.10).[24] The absorption spectrum of **$H_2P(ZnP)_4$, (11)**, pentmer showed slight bathochromic shift and broad Soret band compared to that of reference compounds. The fluorescence emission spectrum is identical, when the pentmer excites at 428 nm (Soret band) or 547 nm (Q-band). Moreover, fluorescence excitation spectrum consistence with the absorption spectrum of the pentmer.

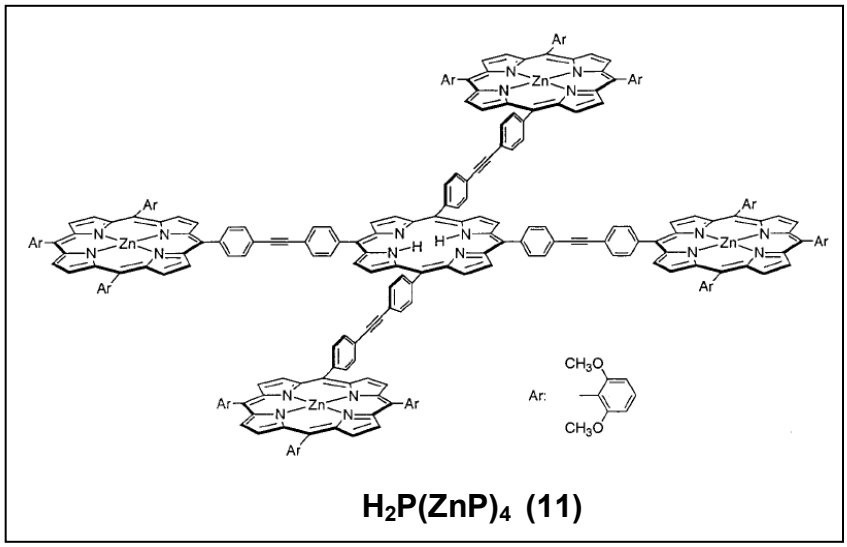

$H_2P(ZnP)_4$ (11)

Figure 1.10: The structure of **$H_2P(ZnP)_4$** pentamer

Based on fluorescence quenching studies, nearly 90% of the extent of energy transfer was estimated from Zn to free-base porphyrin. Since this pentamer array system shows less spectral coverage in absorption spectrum,

scientists have reported phthalocyanine contained arrays which absorb strongly both in the blue and in the red, thereby a large part of the solar spectrum. Compared to multiporphyrin arrays, relatively few arrays consists of multiple phthalocyanines[25] and even fewer porphyrin-phthalocyanine dyads[26,27] and tetraporphyrin-phthalocyanine pentads[28] have been prepared. Lindsey, Li and coworkers have constructed a light-harvesting array containing four porphyrins covalently linked to a phthalocyanine in a star-shaped architecture[29].

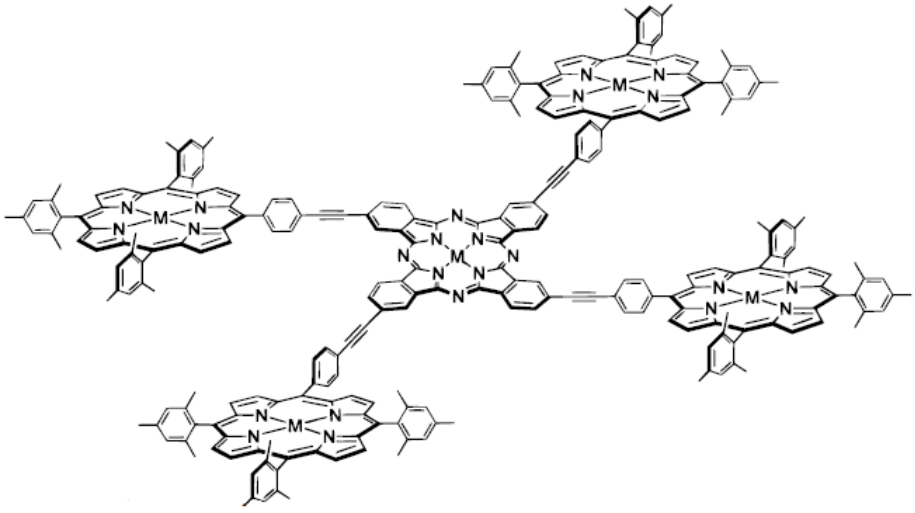

M = H_2; $(H_2P)_4H_2Pc$ (12)

M = Mg; $(MgP)_4MgPc$ (13) **M = Zn; $(ZnP)_4ZnPc$ (14)**

Figure 1.11: Porphyrin-phthalocaynine pentads

The absorption spectrum of each pentad displayed an intense Soret band located near 420nm for multiple porphyrin units, a weaker porphyrin Q-bands

between 500 and 650 nm, a Soret band of the phthalocyanine core located near 350 nm and a strong Q-band absorption of phthalocyanine near 720 and 690 nm. Upon excitation of $(H_2P)_4H_2Pc$ **(12)** at 515 nm corresponding to porphyrin absorption, fluorescence emission of free base porphyrin in the pentad is quenched with simultaneous appearance of Zn porphyrin emission bands. Similar results were observed for other pentads listed in the Figure 1.11.

Array	porphyrin lifetime (ps)	phthalocyanine lifetime (ns)	phthalocyanine Φ_f	$(k_{trans}^{-1})_{avg}$ (ps)	Φ_{trans} (%)
$(H_2P)_4H_2Pc$ **(12)**	1.2 ± 0.2 (62%) 13 ± 3 (38%)	4.6 ± 0.7	0.76	5.6	>99
$(MgP)_4MgPc$ **(13)**	0.8 ± 0.3 (68%) 15 ± 3 (32%)	4.3 ± 0.7	~0.4	5.3	~60
$(ZnP)_4ZnPc$ **(14)**	0.9 ± 0.3 (55%) 7 ± 2 (45%)	2.4 ± 0.4	0.38	3.6	>99

Table 1.1: Excited-state properties of porphyrin-phthalocyanine arrays[29]

Fluorescence lifetimes of pentads were established by fluorescence modulation spectroscopy. The zinc phthalocyanine has lifetime of about 2.5 ns, whereas the free-base and magnesium phthalocyanine have lifetimes of about 4.5 ns (Table 1.1). These lifetimes are similar to those of phthalocyanines monomeric reference compounds. Interestingly, aggregation of phthalocyanine promotes higher lifetime as concentration increased. The effect obeys the

following trend, pentads < dyads < monomers. The photoexcited porphyrins are weakly emissive and short-lived to record via fluorescence spectroscopy, since the occurrence of rapid energy transfer from porphyrin to phthalocyanine in those dyads. Therefore, time-resolved absorption spectroscopy was used to determine decay properties of the excited porphyrin. Table 1.1 shows the energy transfer rate constants of picoseconds time scale, attributing to extreme rapid and efficient energy.

All above molecular architectures are incorporated with different covalent linkers such as diarylethynes to employ covalently linked donor-acceptor hybrids for mimicking photoinduced energy transfer in antenna chromophore of natural photosystem. To get more insight into the influence of spacer/linker on energy transfer, non-covalently fashioned donor-acceptor hybrids will be discussed in next section.

1.9 Non-covalently linked donor-acceptor systems for mimicking antenna functionality

The covalent supramolecular approach substantially differs from natural systems since the bacterial photosynthetic reaction centers where different photo- and redox-active components are arranged via noncovalent interactions into a protein matrix. In such donor-acceptor assemblies, chromophores are linked together through noncovalent bonds, such as hydrogen bonding, metal

coordination and $\pi-\pi$ stacking interactions which considered as biomimetic methodologies. Strength and directionality are important required properties for those noncovalent intermolecular interactions joining chromophores. Another important issue to concern that whether the intermolecular interaction facilitates the excitation energy transfer process from one chromophore to another.[30]

1.9.1 Energy transfer via hydrogen bonding

In recent years, designing of donor-acceptor systems to mimic antenna functionality in photosynthetic reaction center via hydrogen bonding and electrostatic interaction has attracted a lot of attention.

(1) Unidirectional energy transfer

Ito and coworkers reported amidinium-carboxylate ion pairs or salt bridges, which used to assemble an energy donor-acceptor dyad and pentad.[31] The salt bridge consists of complementary double hydrogen bonds and electrostatic interaction to promote the properties of directionality and strength. In this study, the Zn-porphyrin complex with an amidine group **(ZnPA)** acts as the energy donor and the free-base porphyrin with a carboxylate froup acts as the energy acceptor.

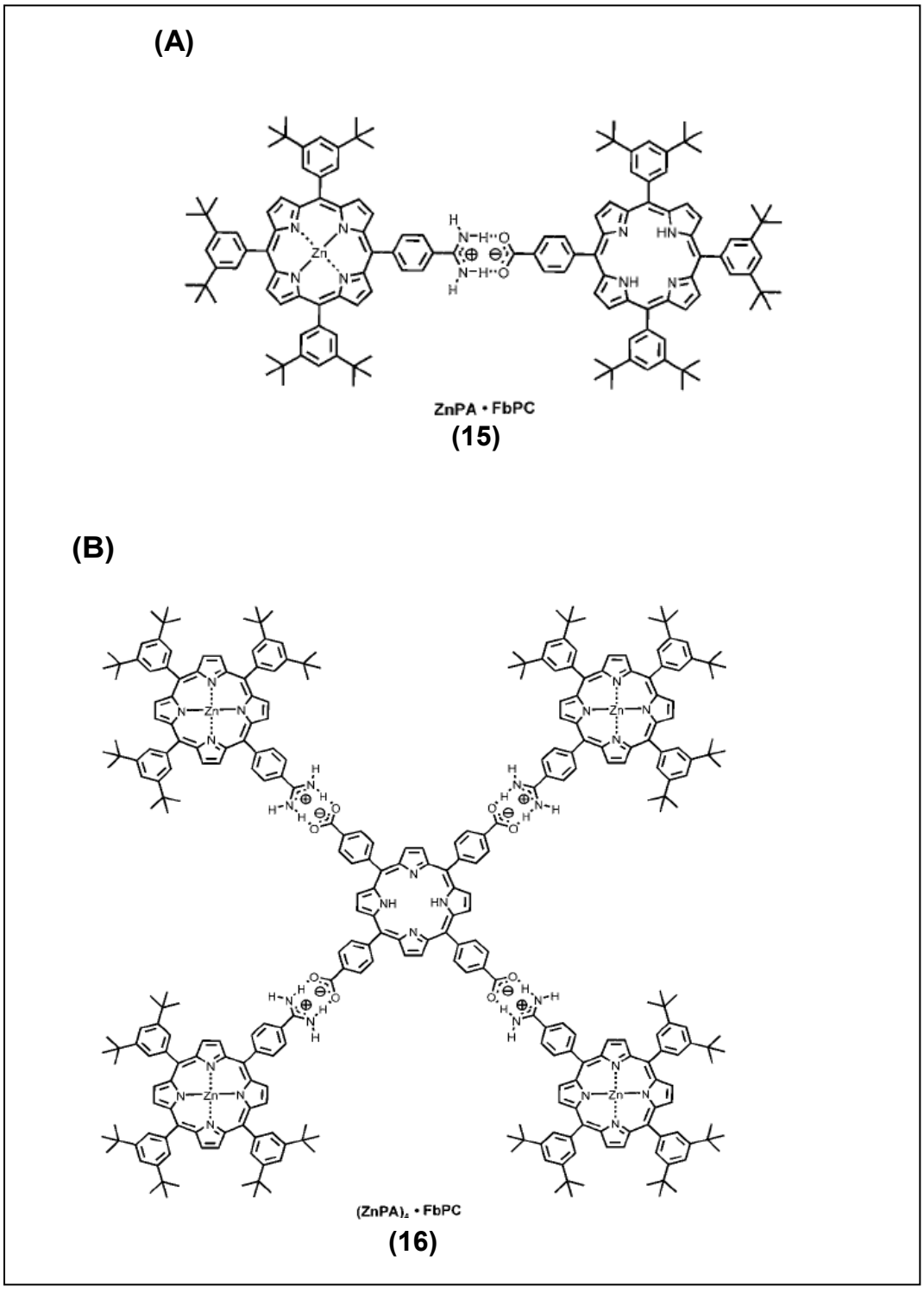

Figure 1.12 : The supramolecular self-assembly formation of (A) 1:1 ratio (dyad, **15**) and (B) 1:4 ratio (pentad, **16**) of free-base porphyrin:Zn-porphyrin.

The Zn-porphyrin was combined with the free-base porphyrins bearing either one **(FbPC),** and four **($FbPC_4$)** carboxy groups to prepare the 1:1 donor-acceptor pair, **ZnPA-FbPC (15)**, and the antenna-type 4:1 assembly, **$(ZnPA)_4$.FbPC (16)**, respectively. Increasing addition of **ZnPA** to a solution of **FbPC** lead to diminish fluorescence from **FbPC** and increase that from **ZnPA**. This reveals occurrence of unidirectional excitation energy transfer from **ZnPA** to free base porphyrin (**FbPC** and **$FbPC_4$**) via amidimium-corboxylate salt bridge. Assuming that, this sensitization is due to the formation of dyad and pentad with formation constants of 2.9(±0.1) x 10^6 M^{-1} and 2.2(±0.2) x 10^6 M^{-1}, respectively. The through space Förster energy-transfer rates ($k_{Förster}$ / theoretical rates) for the dyad and pentad are estimated to be 5.1 x 10^8 and 6.8 x 10^8 s^{-1}, respectively, from Förster equation. The value of the orientation factor, K^2, of 1.01 is for parallel Zn-porphyrin/free-base porphyrin arrays. It is based on assumption that the transition dipoles of **FbPC** is oriented along the imidazole NH-NH and N-N axes. Time-resolved fluorescence measurements were monitored to determine the experimental rates of energy transfer. For the 1:1 mixture, **ZnPA.FbPC (15),** the fast life time component of 0.22 ns was attributed to the energy transfer within the complex. The energy transfer life time of 1:4 complex, **$(ZnPA)_4$.FbPC (16)** was 0.08 ns. Moreover, the observed rates of energy transfer are much faster than expected from the Förster mechanism.

These considerations infer that a through-bond mechanism is in operation in the excited energy transfer in these Zn/Fb porphyrin assemblies through the

amidinium-carboxylate salt bridges. Thus, it is suggested that hydrogen bonds, augmented by electrostatic attraction in this particular case, can mediate through-bond energy transfer.

(2) Vectorial energy tarnsfer

Sessler and co-workers[32] reported the molecular recognition and vectorial energy transfer in a system which is based on salt bridge formation between a carboxyl-bearing porphyrin and an anion-binding protonated sapphyrin. In ensembles **I** and **II**, carboxyl-substituted porphyrin (**17** or **18**) could serve as both a simple-to-bind anionic substrate and a high-energy donor and the protonated sapphyrin moiety **19** would function both as the geometry-inducing, carboxylate-binding receptor and the critical (low) energy acceptor.

These complexes were formed with a K_a of ca. 10^3 M^{-1} upon mixing the receptor and substrate in their respective free-acid and free-base forms in CD_2Cl_2 during the ^1H NMR titration. The occurrence of singlet-singlet energy transfer from the porphyrin to the sapphyrin was revealed by using fluorescence emission studies.

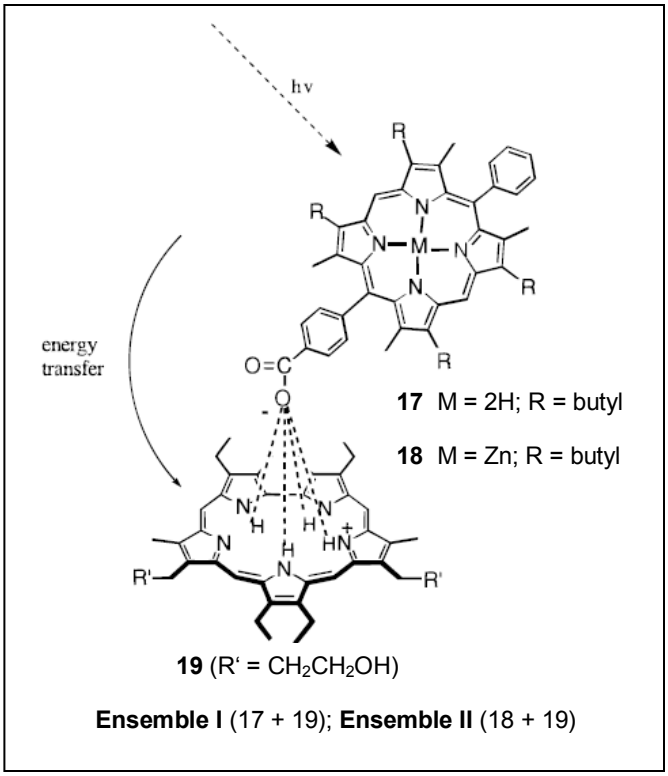

Figure 1.13: The suparmolecular donor acceptor dyad formation using porphyrin and sapphyrin

Upon photo excitation of phorphyrin, the sapphyrin fluorescence is significantly quenched and a new emission band appears at 722 nm that is characteristic of the fluorescence spectrum of the mono-*p*-toluic acid salt of sapphyrin.

Transient absorbance measurements were carried out to characterize intraensemble energy-transfer processes. When a mixture of **17** and **19** (Ensemble **I**) is excited at 417, the Q-band of porphyrin bleaches which ascribed to the porphyrin excited singlet state. Additional bleaching is observed in the

region corresponding to photoexcited sapphyrin. The net result is that at 80 ps, which corresponds to time constant for excitation transfer from the excited state of the porphyrin to sapphyrin.

The rate constants for energy transfer from (**17*** to **19**) and (**18*** to **19**) were determined according to following equation and found to be 4.3 x 10^{10} s^{-1} and 1.1 x 10^{11} s^{-1} for Ensembles **I** and **II**, respectively.

$$k_{ET} = 1/\tau - 1/\tau_o$$

Where, τ_o is the fluorescence lifetime of the donor subunit and, τ is the average of the energy transfer rise and decay times as recorded at six different wavelengths following photoexcitation of mixtures of (**17** and **19**) or (**18** and **19**). The magnitude of the rate constants is rationalized the intraensemble energy transfer by using Förster theory alone, without contribution from a Dexter mechanism.

ensemble	J_F (mmol/cm^{-6})	R_c (Å)	K^2	calc k_{ET} (s^{-1})	obs k_{ET} (s^{-1})
I	**1.43 x 10^{-13}**	**12.5**	**0.69**	**5.0 x 10^{10}**	**4.3 x 10^{10}**
II	**2.43 x 10^{-13}**	**12.5**	**0.69**	**1.1 x 10^{11}**	**1.6 x 10^{11}**

Table 1.2: Overlap integrals and calculated rate constants for Förster energy transfer within porphyrin-sapphyrin ensembles **I** and **II**[32]

The fast excitation energy transfer with high efficiency in Ensembles **I** and **II** is ascribable in part to the large overlap integrals between porphyrin and sapphyrin.

1.9.2 Energy transfer via axial coordination

Over the year, a number of studies have been reported regarding macrocycles such as porphyrins, phthalocyanines and naphthalocyanines with covalently attached axial ligands as model compounds to understand the various biological reactions, viz., hemoxygenation, cytochrome oxidase and peroxidase etc. Various studies have revealed the occurrence of stable five- or six-coordinate metalloporphyrins, thus mimicking active sites of various heme proteins in which axial ligands are provided to the heme by side chains of the protein entity. This penta or hexa coordination strategy for porphyrins has been extended in designing donor-acceptor hybrids that can mimic natural photosynthesis. Several photosynthetic model systems composed of metalloporphyrins display interchromophore energy transfer rates comparable to those observed in natural light harvesting proteins. In particular, self-assembled aggregates of metalloporphyrin arrays have been used as building blocks for artificial light harvesting systems.

Several studies have been focused on porphyrin tetramers as models for plant pigments, such as chlorophyll organized in various protein complexes. Those tetramers have a fixed, defined structure and show fast energy transfer

from a particular excited porphyrin to one or more of its neighbors and loss of excitation energy by relaxation to the ground state. Schaafsma and co-workers[33] reported formation of cyclic tetramers via zinc pyridyl ligation in zinc pyridyl porphyrins (Figure 1.14)

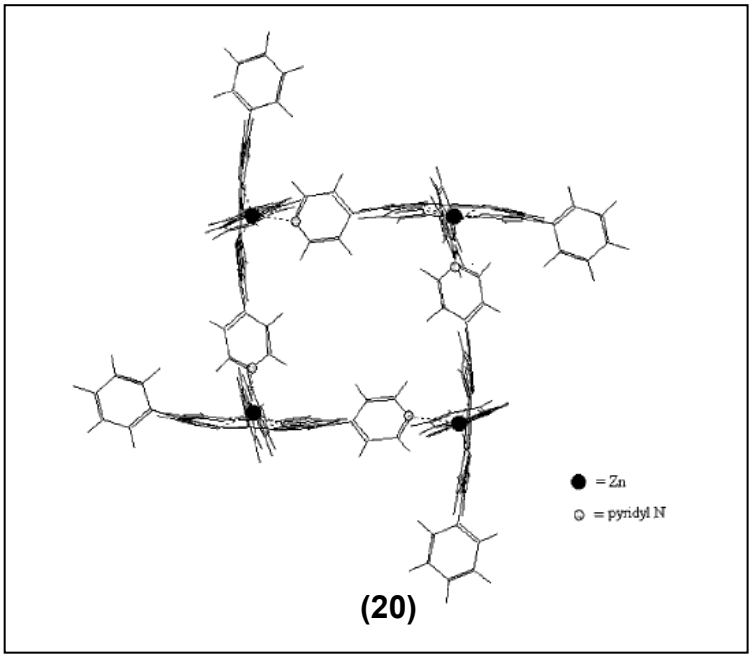

(20)

Figure 1.14: The formation of cyclic tetramer via Zn pyridyl porphyrins (*J.Phys.Chem. A*. **2001**, *105*, 11425-11431)

The absorption spectrum of the tetramer porphyrin exhibits split Soret band which attributes to exciton coupling between porphyrins. The shift of the Soret and Q-bands reveal axial coordination of N atom in the pyridine group to the Zn atom in the porphyrin. The equilibrium constant for the monomer-tetramer equilibrium is $(6.2 \pm 0.8) \times 10^{13}\ M^{-1}$.

The fluorescence lifetime of the cyclic tetramer **(20)** was close to that of pyridine ligated ZnTPP. Furthermore, the energy transfer between the porphyrin units of the tetramer did not affect the lifetime because all monomer units of the tetramer were identical. These self-assembled porphyrin based tetramer showed slower energy transfer rate (100 times less) than those of analogous covalent molecular architectures.

Wasielewski and coworkers[34] reported a zinc chlorophyll (ZC) derivative, **(21)**, that self-assembles into a cyclic tetramer. This self-assembled structure exhibited higher intramolecular energy transfer rates which are comparable to those observed for covalent ring structures.

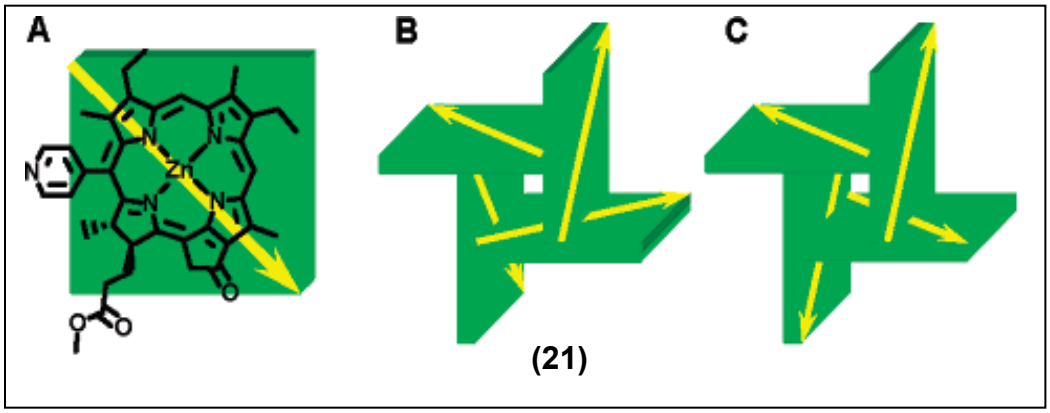

(21)

Figure 1.15: (A) Structure of **(21)**; (B) tetramer $(21)_4$ with a transition dipole orientation which minimizes the steric repulsion of the propionic esters; (C) Tetramer $(21)_4$ with a transition dipole orientation that minimizes the ground-state dipole moment of the aggregate. (*J. Am. Chem. Soc*. **2007**, 1*29*, 6384-6385)

The larger transition dipole moment for the lowest energy electronic transition of the ZCs, **(21)** compared to that of the porphyrins increases the rate of Forster (through-space) energy transfer between the chlorophylls. The bathochromic shift of the Soret and Q-bands in UV-vis studies reveals exciton coupling between two or more ZC molecules **(21)** as a consequence of aggregate formation in the non-coordinating solvent. Figure 1.15 shows the direction of the ZC transition dipole moment which lies approximately along N-N line. Depending on orientation of the chromophore within the tetramer, the orientation of dipole varies.

The rate of energy transfer within ^{1}**(21)*$_4$** is ~20 times faster than that observed for the self-assembled porphyrin tetramer. However, the rate for ZC tetramer is still ~10 times slower than the fastest rates observed in photosynthetic proteins due to less optimal alignment of the transition dipole moments in **(21)$_4$**.

1.10 Donor-acceptor systems for mimicking reaction center functionality

Study of photoinduced electron transfer in donor–acceptor dyads is a topic of interest in artificial photosynthesis. This concept of mimicking reaction center functionality in bacterial photosynthesis addresses the mechanistic details of electron transfer in chemistry and biology, to develop artificial photosynthetic

systems for light energy harvesting, and also, to develop molecular optoelectronic devices.

The core of photosynthesis is photoinitiated multistep electron transfer between donors and acceptors in the reaction center. Sunlight is absorbed by the antenna complexes, and collected energy is funneled into bacteriochlorophyll dimer (special pair) in the reaction center. These reaction centers undergo sequential multistep electron transfer generating long-lived charge-separated states, a key feature needed for efficient harvesting of light energy. A long-lived charge-separated state in donor-acceptor conjugates is generated by tuning the electronic coupling between the donor and acceptor which corresponds to the length and the nature of spacers.

In general, the electronic coupling increases in strength as the number of bonds connecting the donor and acceptor decreases. Thus, the forward electron transfer rate increases as the length of spacer decreases, resulting in the increased efficiency in the production of charged separated state. In contrast, forward and backward electron transfer rates increase with a decrease of the spacer lengths so that the life time of the charge-separated state decreases. But natural photosynthesis overcome this dilemma by employing a multistep electron transfer processes in donor-acceptor conjugates in protein matrix. Therefore, photosynthetic multiple electron transfer strategy is useful to construct

photosynthetic model systems with a large charge separation long with prolong lifetime of a final charge separated state.

1.10.1 Photoinduced single-step electron transfer versus multi-step electron transfer

Photoinduced single step electron transfer (PISET)[35] has single, short-range ET process, it can minimize losing the input photon energy, whereas multi-step electron transfer loses some of input photo energy. The electronic coupling between the resulting donor radical and acceptor radical anion is intense under the PISET conditions. Hence, the charge recombination takes place so rapidly.

Phtoinduced multi-step electron transfer is considered as a key strategy in natural photosynthesis, even though this leads to substantial loss of the input photon energy by each electron transfer process, the resulting distinctly separated radical ion pair attenuates the electronic coupling drastically, thereby increasing the lifetime of final charge separated states.

To modulate the electron transfer efficiency and the lifetime of the charge-separated state, the composition, interchromophore distance and orientation, and electronic coupling are important factors. Both covalent chemistry and biomimetic self-assembly methodologies, such as the formation of π stacks, hydrogen bonds, and van der Waals contacts, have been successfully utilized to connect

the donor–acceptor entities to achieve efficient intramolecular electron transfer processes. First covalently linked donor-acceptors conjugates which mimic reaction center functionality will be elaborated.

1.11 Covalently linked donor-acceptor systems for mimicking reaction center functionality

1.11.1 Donor-acceptor conjugates for photoinduced single-step electron transfer

Donor-acceptor dyad systems.

Several comprehensive reviews in the literature of donor–fullerene dyads, which includes larger hybrids (triads, tetrads, pentads, etc.), that incorporate a wide variety of electron donors and linkers have been published. To get more insight into the influence of molecular topology on electron transfer, donor-acceptor dyads with different molecular arrangements such as face-to-face and linear arrangements have been elegantly designed and studied.

The face-to-face conformation in these dyad systems exhibit π–π interaction between the two chromophores. This phenomenon is also attributed to strong van der Waals attraction between donor and acceptor such as porphyrin and C_{60} moieties, in the solid state as well as in solution. Such

conformations facilitate through-space communication between the donor and the acceptor.

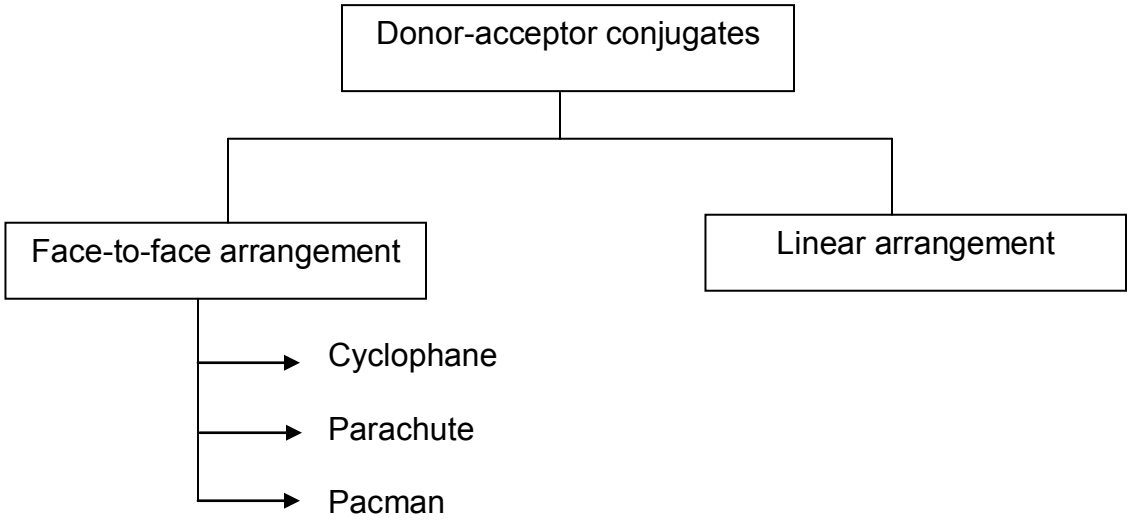

Scheme 1.1: A classification of donor-acceptor conjugates

1. Face-to-face arrangement of donor-acceptor dyads

Porphyrin-fullerene dyads

The simplest way to alter the defined distance and mutual orientation of a two-dimensional planar electron donor (ZnP) with respect to a three-dimensional spherical electron acceptor (C_{60}) is through synthetic strategies. Those synthetic modifications always assist to make different topological arrangements of porphyrin-fullerene dyad systems. Three types of dyads, namely, cyclophane (a), parachute (b) and pacman (c) type porphyrin-fullerene dyads (Figure 1.16),

have been designed and synthesized to investigate photoinduced electron transfer to mimic reaction functionality in natural photosyntehsis[36]

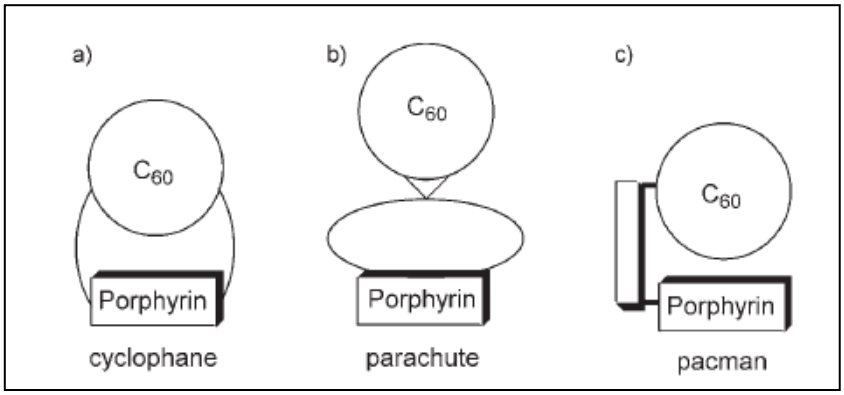

Figure 1.16: Examples of closely held porphyrin-fullerene dyads

(a) Cyclophane type systems

Hirsch, Guldi, Prato and co-workers[37] reported regioselective cyclopropanation of C_{60} with a porphyrin bismalonate which leads to a fullerene–porphyrin dyad.

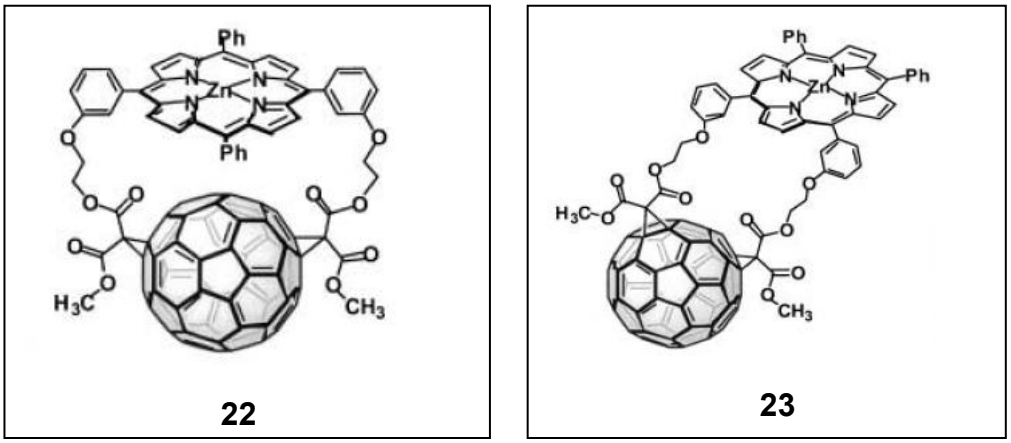

Figure 1.17: Cyclophane type porphyrin-fullerene dyads (*Chem. Eur. J*. **2003**, *9*, 4968-4979)

The variability of relative orientation of the two chromophores within each dyad is very limited due to the double linkage. These two different dyads can access to very little conformational space. In **22**, the face-to-face alignment is completely locked, while in **23** only two types of face-to-edge orientations (vertical and horizontal) were found in molecular dynamics calculations. The face-to-face alignment in **22** with the shortest interplanar distance (Zn-C: 3 Å) promotes appreciable $\pi-\pi$ stacking, whereas the face-to-edge alignment in **23** prohibits effective $\pi-\pi$ interaction. These strong $\pi-\pi$ interactions modulate the spectral and electrochemical properties of the dyads. In UV-Vis spectroscopy, the Soret- and Q-bands of **22** show a bathochromic shift and decrease of the molar absorption coefficients with compared to parent ZnP. Moreover, these two dyads reveal a new broad band in the 700-800 nm region which corresponds to charge transfer (CT) band. This additional band confirms CT transition or electronic interaction between the two chromophores in the dyads. The fluorescence quantum yield of dyad **22** did not change appreciably with the solvent. This spectral behavior corresponds to the intramolecular charge-transfer reaction, which is mediated through the overlapping π orbitals and does not use bridging solvent molecules.

Electrochemical studies of **22** reveal slight shifts, for example of 16 mV, to a more negative potential for the first porphyrin oxidation. All these spectral behaviors attribute a considerable photoinduced interaction between the two

chromophores. Also photophysical analyses of **22** reflect the close proximity and stacking interaction between the corresponding π-systems.

The electronic coupling in **22** and **23** is 436, and 76 cm^{-1} respectively. A strong red shift of the CT absorption in **22** was revealed by increasing the solvent polarity from toluene to benzonitrile. This effect is caused by the better solvation that radical cation and/or radical anions in a more polar environment. Therefore, the strength of electronic interaction of **22** between ZnP and C_{60} in the ground state is higher than that of **23**.

A weak band at around wavelength of 825 nm, charge transfer emission band, was observed when the dyads were excited at 680 nm, which corresponds to the charge-transfer absorption band. The life times of the singlet excited state of ZnP decreased with the solvent polarity. Moreover, when the solvent polarity increased, the free energy associated with CR would be less negative, while CS would be opposite trend. Therefore combination of ZnP and C60 consistently produces charge recombination in the inverted Marcus region with remarkably low reorganization energies.

(b) Parachute type systems

To investigate more topological control of intramolecular electron transfer in Zn porphyrin – C_{60} systems, Schuster and co-workers[38] reported a symmetrical parachute-shaped octaethylporphyrin-fullerene dyad. Here, the fullerene was anchored to malonate moiety inserted in a strapped porphyrin derivative.

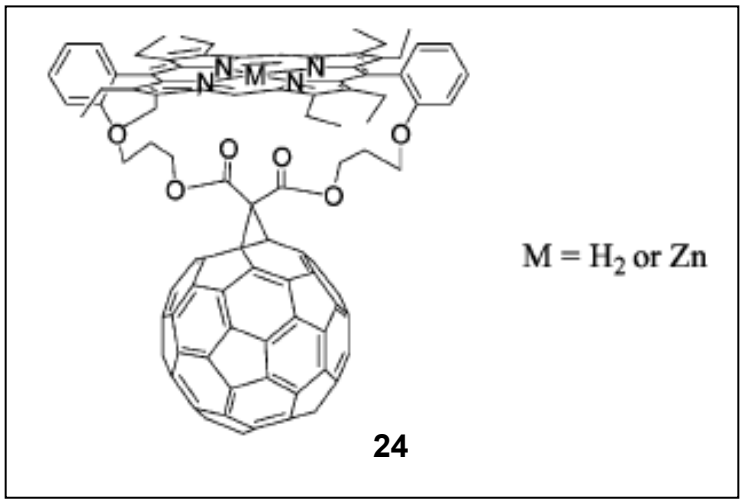

24

Figure 1.18: Parachute shaped porphyrin-fullerene dyad

The distance between the electron donor, ZnP and the electron acceptor, C_{60} in **24** dyad system is regulated by the conformational properties of the system. The molecular modeling studies on the parachute-shaped **24** dyad reveals two conformations, ie bent and symmetric.

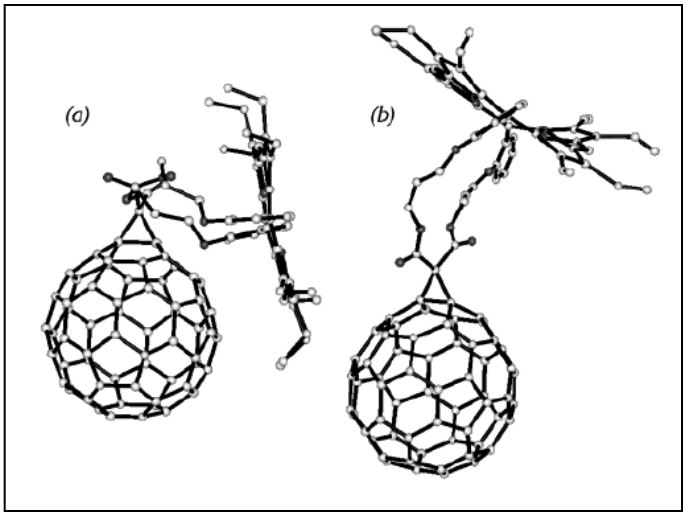

Figure 1.19: Bent (a) and symmetric (b) conformations of dyad **24**. The more stable structure is (a) on the left. (*J. Am. Chem. Soc.* **2004**, *126*, 7257-7270)

Therefore, the fullerene and the porphyrin chromophores in **24** are flexibly held in a face-to-face parachute topology. This flexible linker permits the porphyrin ring to move back and forth between conformations in which van der Waals interactions are maximized, but are not permanently maintained. Thus, UV-Vis studies reveal the absence of spectral shifts and CT absorption in **24** which are importantly different from **22**. This indicates that there is no significant ground state electronic interaction between the porphyrin and the fullerene in **24**. Both the free base and Zn dyads exhibit extensive fluorescence quenching along with an extremely rapid photoinduced electron transfer process ($k \approx 10^{11}$ s^{-1}), generating porphyrin radical cations and fullerene radical anions. Photophysical properties of the **24** are similar to those of structurally related rigid π stacked **22**, with the exception that there is no detectable charge transfer absorption in the

parachute systems. The charge separation in parachute type donor-acceptor systems occurs through space in bent conformation, where the center-to-center distance between the chromophores is 7.8 Å.

Phthalocyanine-fullerene dyads

Porphyrin donors in previous dyad systems absorbs efficiently only in a rather narrow spectral region around 430 nm, which is a major drawback considering applications in light harvesting devices.[39] Replcacing porphyrin with a phthalocyanine chromophore extends the absorption range of the dyad which is more useful flor photonic devices.

Isosomppi and co-workers[40] reported double bridge phthalocyanine-fullerene dyad systems **(25)** (Figure 1.20) to study exciplex mediated photoinduced electron transfer. Depending on the excitation wavelength the phthalocyanine (**Pc**) chromophore of the dyad is promoted to the second, ^{2S}**Pc*** **-** **C$_{60}$**, or the first excited singlet state, ^{1S}**Pc*** **-** **C$_{60}$**, which is in equilibrium with the exciplex, **(Pc-C$_{60}$)***. Formation of the CS state, **Pc**$^{\cdot+}$ **-** **C$_{60}$**$^{\cdot-}$, follows from **(Pc-C$_{60}$)*** [exciplex] and BET occurs directly to ground state.

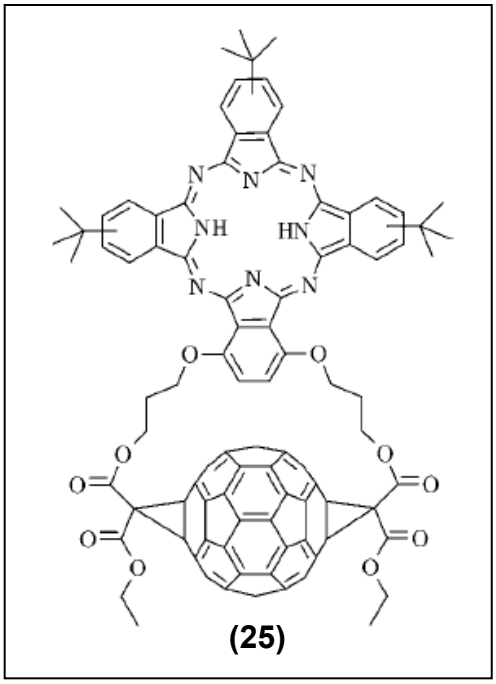

(25)

Figure 1.20: Double bridge phthalocyanine-fullerene dyad (*Chem. Phys. Lett*. **2006**, *430*, 36-40)

2. Linear arrangement of donor acceptor dyads

To achieve long-lived charge separated state, linear arrangement of donor-spacer-acceptor does a good job of mimicking the gross features of the electron transfer step in the photosynthetic reaction center. The most extensively studied fullerene-based systems are porphyrin-linked fullerenes to study primary events of bacterial photosynthesis.

Imahori and co-workers[41] reported Zn porphyrin-fullerene dyad system **(26)** in different organic solvents to investigate photoinduced processes (Figure 1.21). The occurrence of photoinduced electron transfer is investigated by using

fluorescence life time measurements and pico- and nanosecond time-resolved transient absorption spectroscopies.

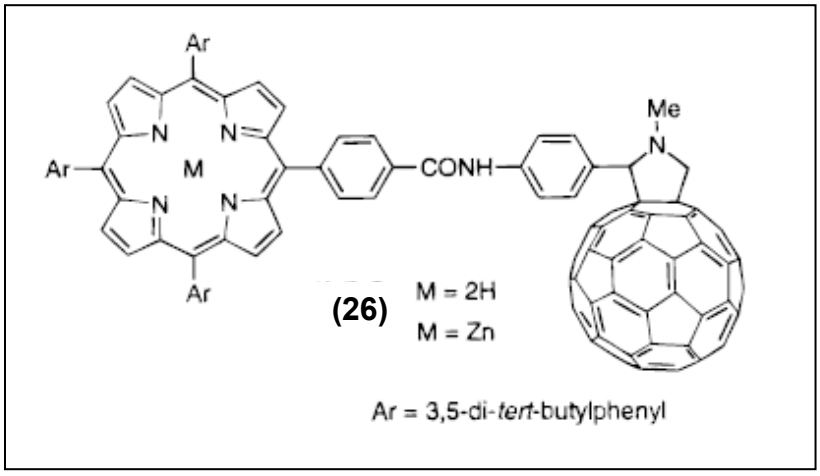

Figure 1.21: Linear arrangement of porphyrin-fullerene dyad (*J. Am. Chem. Soc*. **2000**, *122*, 6535).

The charge-separated state ($ZnP^{\cdot+}$- $C_{60}^{\cdot-}$) is formed via photoinduced electron transfer from all the excited states, that is , $^1ZnP^*$ and $^3ZnP^*$ to C_{60} and from ZnP to $^1C_{60}^*$ and $^3C_{60}^*$. (Figure: 1.22). The resulting chare separated state recombines to regenerate the ground state with a rate constant (k_{CR}) of 1.3 x 10^6 s^{-1} (0.77 μs) in PhCN. The λ and *V* values were 0.66 eV and 3.9 cm^{-1} respectively, in polar solvents. There were three different kinds of region in the Marcus curve for above photochemical events. Those are;

1) Marcus normal region- the charge separation process from the porphyrin to the $^1C_{60}^*$ and $^3C_{60}^*$
2) Marcus top region – the charge separation process from $^1ZnP^*$ to C_{60}.

3) Marcus inverted region – the charge recombination process from the charge-separated state to the ground state.

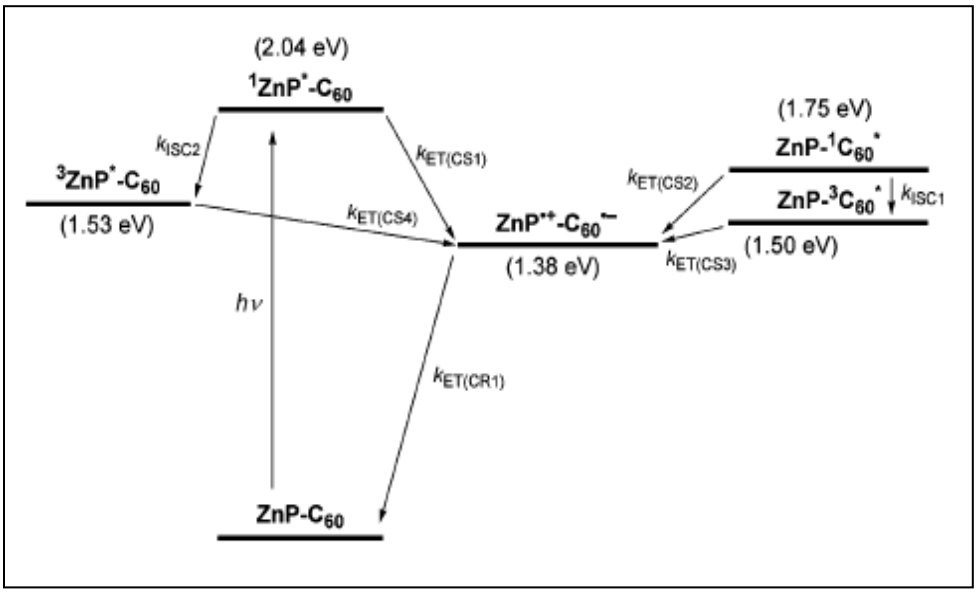

Figure 1.22: Energy diagram for **ZnP-C_{60}** in PhCN (*Org. Biomol. Chem*. **2004**, *2*, 1425-1433).

In nonpolar solvents such as benzene, the charge-separated state undergoes charge recombination to yield the C_{60} singlet excited state, followed by intersystem crossing to the C_{60} triplet excited state, since the energy level of the charge separated state is higher than that of the C_{60} singlet excited state (1.75 eV).

Similarly, the free-base porphyrin-C_{60} dyad in PhCN showed photoinduced charge separation from free-base porphyrin singlet excited state to C_{60} in PhCN, yielding $H_2P^{\bullet+}$ - $C_{60}^{\bullet-}$ with rate constant of 6.7 x 10^8 s^{-1}. Here, the charge-

separated state decays to the porphyrin ($^3H_2P^*$) and fullerene ($^3C_{60}^*$) triplet states rather than ground states.

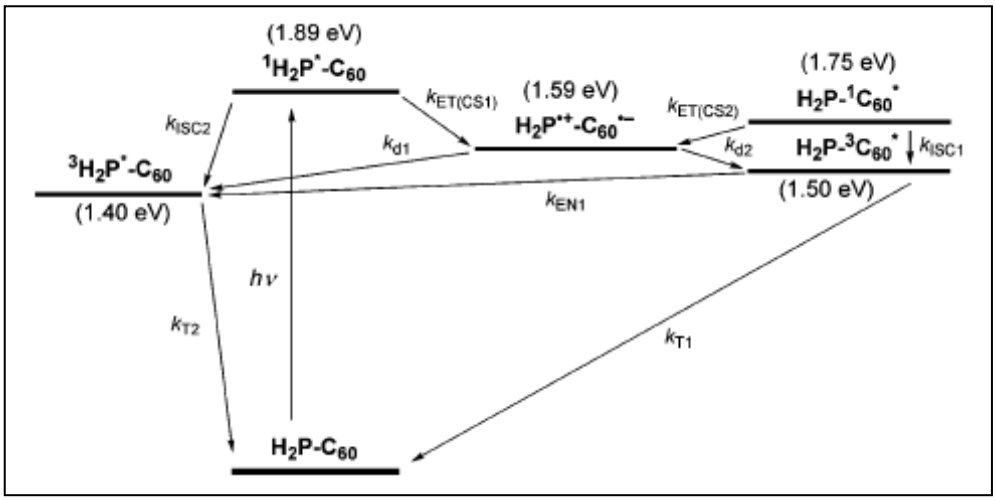

Figure 1.23: Energy diagram for **H_2P-C_{60}** in PhCN (*Org. Biomol. Chem*. **2004**, *2*, 1425-1433).

Fukuzumi, Imahori, Kadish[42] and coworkers have reported photophysical and electrochemical properties of chlorine-C_{60} dyads (**ZnCh-C_{60}**,Figure: 1.24) to compare with porphyrin-C_{60} dyads. Interestingly, photoexcitation of zinc chlorine-C_{60} with –CH_2- short spacer **(27 and 28)** results in formation of long-lived radical ion pair. The formation of zinc chlorin cation radical and C_{60} anion radical shows characteristic absorption peaks at 790 and 1000 nm respectively. The radical ion pair decays with the rate constants of 9.1 x 10^3 s^{-1} (110 μs) and 2.0 x 10^4 s^{-1} (50 μs) for **27** and **28** respectively. The zinc chlorin-fullerene dyad with extremely short spacer (**29**) revealed the formation the ultra-long lived charge-separated state with the lifetime of 120 s (8.3 x 10^{-3} s^{-1}) in frozen PhCN at 123 K. This

lifetime is the longest value of charge separation ever reported for donor-acceptor conjugate systems containing a porphyrin or chlorine as the donor and C_{60} as the acceptor.

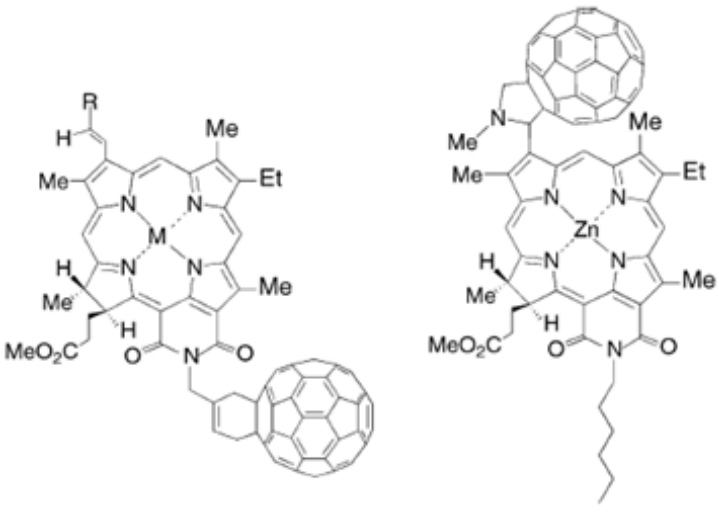

Figure 1.24: Structures of zinc chlorine-fullerene (ZnCh-C_{60}) dyads (*J. Am. Chem. Soc.* **2001**, 123, 10676).

According to energy diagram in Figure 1.25, the energy of radical ion pair state ($ZnCh^{\bullet+}$ - $C_{60}^{\bullet-}$, 1.33 eV) is lower than that of both the triplet excited state of C_{60} (1.45 eV) and ZnCh (1.36-1.45 eV). Therefore, photoinduced electron transfer from the singlet excited state of ZnCh to the C_{60} competes with two photochemical pathways i.e the intersystem crossing to ^{3}ZnCh* and energy transfer to produce ZnCh-$^1C_{60}^*$ and ZnCh-$^3C_{60}^*$.

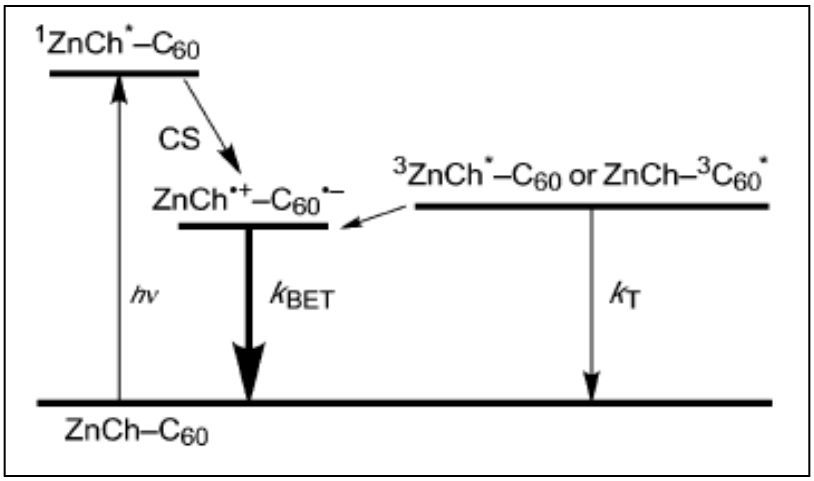

Figure 1.25: Energy level diagram of Zn chlorine-fullerene dyad (*Org. Biomol. Chem*. **2004**, *2*, 1425-1433).

Incorporation of chromophores, such as phthalocyanines which harvest red part of the solar spectrum is another fascinating strategy for developing donor-acceptor multicomponent systems. Torres, Guldi, and Hieringer and co-workers[43] have developed a series of Zn phthalocyanine–C_{60} conjugates (Figure: 1.26) bearing different spacers, namely, direct linkage **(31)**, single **(30c)**, double **(30b)**, and triple bond **(30a)** between two chromophores. An intramolecular electron transfer from the photoexcited ZnPc to the electron-accepting C_{60} governs photoreactivity of **30a-30c** and **31**. In absorption spectroscopy, the Q-bands of phthalocyanine reveal higher wavelength shifts due extended π–conjugation, especially ethynyl spacer. The femtosecond transient absorption spectroscopy reveals three distinct maxima at 520, 840, and 1000 nm. The bands located at 520, and 840 nm attribute to the one-electron-oxidized ZnPc

radical and the band at 1000 nm matches the absorption of the one-electron-reduced fullerene radical anion. Moreover, complementary density functional calculations confirm this assignment by virtue of the excitation spectra of $ZnPc^{\cdot+}$ and $C_{60}^{\cdot-}$

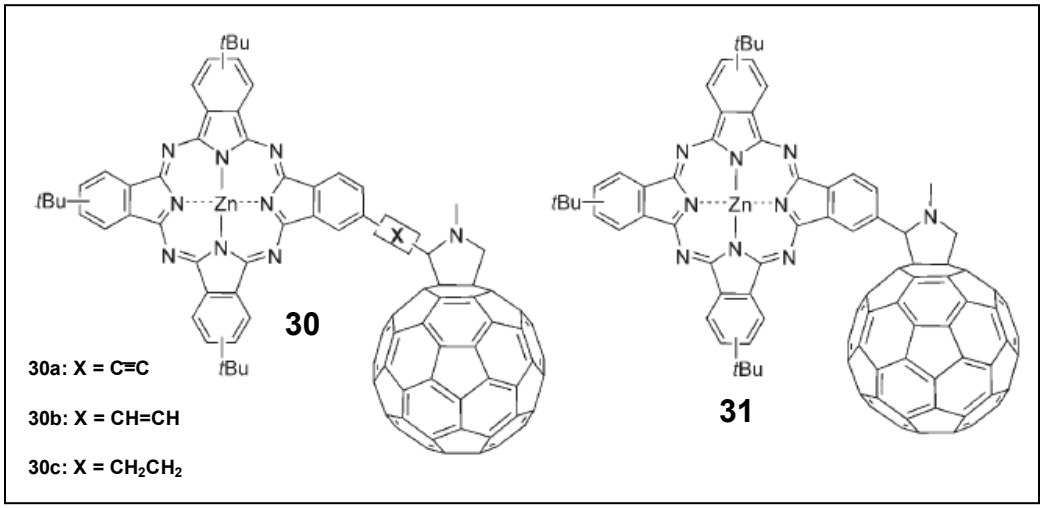

Figure 1.26: A series of Zn phthalocyanine-fullerene conjugates bearing different spacers.

The impact of the linker (single, double, or triple bond) on the charge separation and charge recombination features is rather marginal, the triple-bonded system **(30a)** is, showing the longest lifetime radical ion-pair state. Furthermore, the difference between the double-bonded **(30b)** and triple-bonded **(30a)** system resembles the trend seen in *p*-phenylenevinylene and *p*-phenyleneethynylene.

Compound **(31)** shows additional band at 740 nm which corresponds to a charge-transfer transition. With the features of the charge-transfer absorption, the

electronic coupling elements (*V*) were estimated in chloroform as 525 cm^{-1} and in *o*-dichlorobenzene as 298 $cm^{-1.}$ The charge transfer emission band relates to $(4\pi\lambda_s k_B T)^{1/2}$, lowering the temperature to 77 K helped to convolute the emission bands, which are broad at room temperature.

1.11.2 Donor-acceptor conjugates for photoinduced multi-step electron transfer

Donor-acceptor triad systems

The combination of more than two entities in the donor-acceptor architectures show multi-step electron transfer which promotes to yield a long-lived charge separated state with a high quantum yield. One of the representative examples for carotenoid polyenen-diarylporphyrin-fullerene triad[44] which is shown in Figure: 1.27.

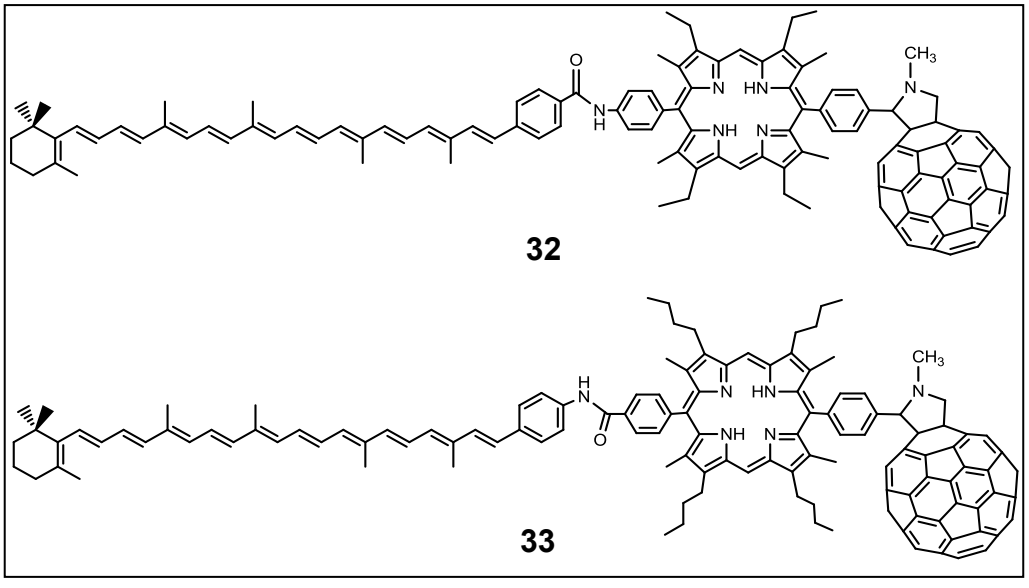

Figure 1.27: Carotenoid polyenen-diarylporphyrin-fullerene triad (*J. Am. Chem. Soc*. **1997**, *119*, 1400-1405)

In this system, porphyrin (P) act as primary electron donor, fullerene (C_{60}) as an acceptor while carotene (C) act as a secondary electron donor. In 2-methyltetrahydrofuran solution, the triad reveals photoinduced electron transfer to yield C-$P^{\bullet+}$-$C_{60}^{\bullet}$. This charge separated state evolves by electron donation from the caroteniod to give the final charge separated state $C^{\bullet+}$-P-$C_{60}^{\bullet}$ with involving an overall quantum yield of 0.14 and creating lifetime of 170 ns. Even in a glass at 77 K, the lifetime of the charge separated state, $C^{\bullet+}$-P-$C_{60}^{\bullet-}$ is 1.5 μs with the quantum yield of ~0.10. This charge separated state further decays mainly by charge recombination to give the carotenoid triplet ^{3*}C-P-C_{60} rather than ground state.

In order to understand the excited state of species time resolved EPR studies were employed.[45,46] In the presence of a small (20 mT) static magnetic field, the lifetime of the charge separated state is increased by 50%. This is because of the effect of the magnetic field on interconversion of the singlet and triplet biradicals. In the absence of a magnetic field, the initially formed singlet biradical state is in equilibrium with the three triplet biradical sublevels, and all four states have comparable populations. The interconversion among all four states via hyperfine coupling interactions (HFI)-induced intersystem crossing is rapid on the time scale of charge recombination which leads to decay to the carotenoid triplet state solely from the three triplet sublevels. In the presence of magnetic field, the S and T_o states are still rapidly interconverting, but the T+ and T- states are isolated from the other two due to the electronic Zeeman interaction, and are not significantly populated. Under these conditions,

recombination to the triplet occurs only from T_o, and the lifetime of the charge-separated state increases. Although this triad was considered as a good candidate for mimicry of several aspects of photosynthetic electron transfer, the quantum yield of long-lived charge separation was significantly lower than the yield of essentially unity measured for the natural photosynthetic reaction center.

In order to get more insight of the structural features giving rise to this phenomenon, **32** is modified porphyrin core and carotene-porphyrin linkage. The photoinduced electron transfer behavior was studied at varying temperatures in different solvents. The apparently small structural differences between **32** and **33** lead to significant changes in thermodynamic driving force, electronic coupling, and other factors that affect the rates of electron-transfer reactions and yields of charge-separated states. The energy of the $C^{\bullet+}$-P-$C_{60}^{\bullet-}$ state for **33** was lowered compared to that in **32** by 0.18 eV leading to the increase in the thermodynamic driving force for the conversion of C-$P^{\bullet+}$-$C_{60}^{\bullet-}$ to $C^{\bullet+}$-P-$C_{60}^{\bullet-}$ and thus the rate constant of charge separation, as the charge separation reaction occurs in the Marcus normal region. The energy of the C-$P^{\bullet+}$-$C_{60}^{\bullet-}$ state for **33** is 0.05 eV higher than that for **32**, attributing slow charge recombination in **33**, as the CR occurs in the Marcus inverted region.

Instead of carotenoid in triad system, Imahori and coworkers[47] have reported ferrocene as a secondary electron donor in triads, Fc-H_2P-C_{60} and Fc-ZnP-C_{60}.

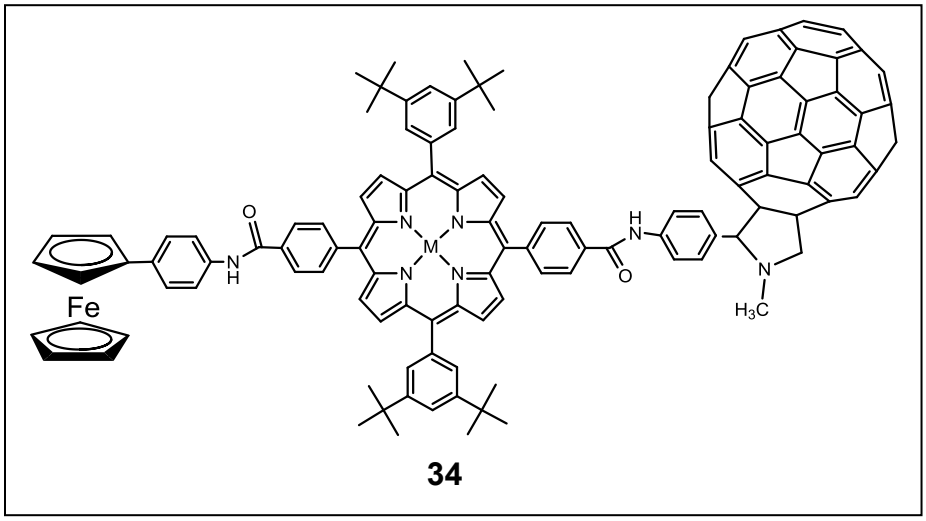

34

Figure 1.28: Covalently linked ferrocene-porphyrin-fullerene triad (*J. Am. Chem. Soc*. **2001**, *123*, 2607-2617)

In benzonitrile at room temperature, photoinduced charge separation via electron transfer pathway occurs from all of the excited states, i.e., porphyrin singlet excited state ^{1}ZnP* and porphyrin triplet excited state ^{3}ZnP* to the C_{60} moiety, and from the porphyrin moiety to the C_{60} singlet excited state $^{1}C_{60}$* and the C_{60} triplet excited state $^{3}C_{60}$*, to initially produce Fc-ZnP$^{\bullet+}$-$C_{60}^{\bullet-}$ with high quantum yield.

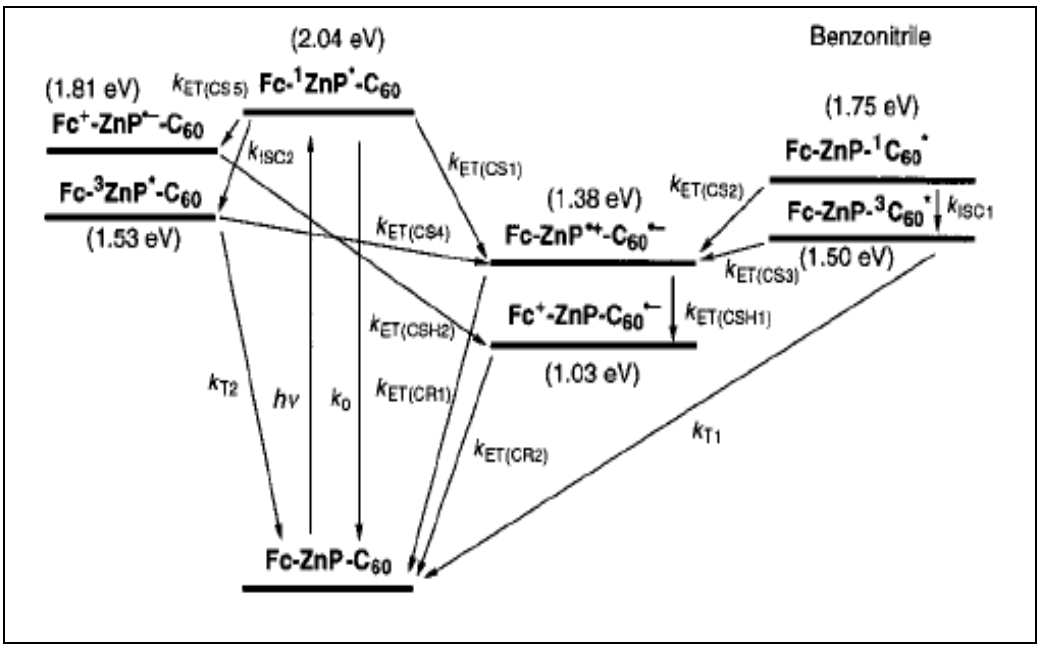

Figure 1.29: Energy Diagram for **Fc-ZnP-C_{60}** in benzonitrile (*Org. Biomol. Chem*. **2004**, *2*, 1425-1433).

The resulting transient state of Fc-ZnP$^{\bullet+}$-$C_{60}^{\bullet-}$ undergoes to form a long lived charge separated state of Fc$^{\bullet+}$-ZnP-$C_{60}^{\bullet-}$ (16 μs in DMF) via secondary electron transfer (exothermic charge shift or hole shift) from ferrocene moiety to ZnP$^{\bullet+}$ with quantum yields close to unity. This can be rationalized by the small reorganization energy of C_{60} in multistep ET processes, where forward ET is accelerated and back ET is decelerated. The charge shift rate constant in benzonitrile was determined as 2.8 x 10^9 s^{-1}. The Fc$^{\bullet+}$-ZnP-$C_{60}^{\bullet--}$ decays mainly by charge recombination to ground state, rather than to the secondary donor triplet state excited state, as seen in the case of triads **32** and **33**.

The electron transfer rate constants for the charge recombination in Fc^{+}-ZnP-$C_{60}^{\bullet-}$ were determined in solvents of increasing polarity by analyzing the decay kinetics of the $C_{60}^{\bullet-}$ fingerprint at 1000 nm in transient absorption spectra. These charge recombination rates decrease with increasing solvent polarity, implying that these are in the Marcus normal region.

The efficiencies of light harvesting and charge separation by covalently synthesized donor-acceptor array systems are much less than that of the natural systems. Therefore, it is meaningful to exploit noncovalent donor-acceptor molecular architectures for mimicking reaction center functionality.

1.12 Noncovalently linked donor-acceptor systems for mimicking reaction center functionality

Although covalent donor-acceptor conjugates exhibited excellent ground state and excited state properties in electron transfer reactions in reaction center functionality, they substantially differ from natural systems, especially in the mode of binding between donor and acceptor. Meaningful incentives can be borrowed from methodologies and strategies of the bacterial photosynthesis reaction center wherein the natural chromphores are self-assembled in a protein matrix and which convert the excited-state energy to a potential gradient. The light harvesting efficiencies arise from the precise nanoarchitecture components of the photosynthetic reaction center (PRC) mediated by intermolecular

interactions between the chromophores and between the protein scaffolds. Moreover, electron pump in the PRC is operating in a lubricating solvent, water and lipids, which also tunes the dynamics. Thus, the dynamics of specific solute-solvent interactions are also key components of the function. Biomimetic methodologies such as hydrogen bonding, metal coordination, electrostatic interactions and π–π stacking, guarantee the control over modulating the composition and thus provide the opportunity to achieve well-defined and rigid architectures with high directionality and selectivity. Therefore, construction of noncovalent donor-acceptor systems for mimicking reaction centre functionality is important to obtain efficient light harvesting performances. Scientists have been developed noncovalently linked porphyrin/phthalocyanine and fullerene[48] based donor-acceptor hybrids with different modes of binding to understand the basic concepts of photoinduced electron transfer in photosynthetic reaction center.

1.12.1 Electron transfer via hydrogen bonding

Different types of donor-acceptor conjugates held together by hydrogen bonding interactions have been assembled in order to mimic natural photosynthesis and for the design of photoactive devices. Recently, the Watson–Crick hydrogen bonding paradigm (specifically the three-point guanosine–cytidine couple) as a scaffold to assemble dyads has been used to mimic reaction center functionality.

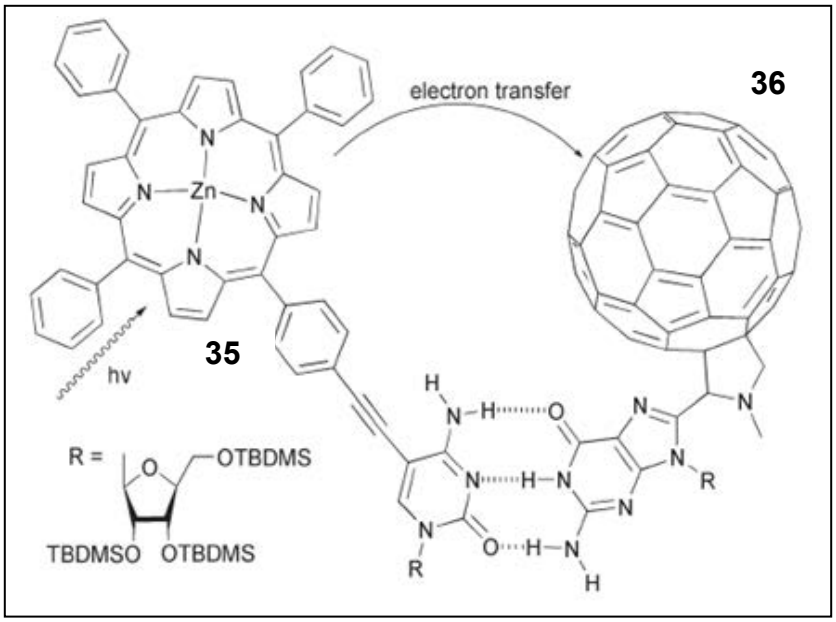

Figure 1.30: Self-assembly of porphyrin–fullerene dyad through Watson–Crick hydrogen bonding interactions (*Chem. Commun*. **2005**, 1892-1894)

Sessler and coworkers utilized Watson-Crick hydrogen bonding to study the photoinduced electron transfer between porphyrin and fullerene entities[49,50]. Cyclic voltammetric studies revealed the energetic of photoinduced electron transfer in this porphyrin-fuulerene dyad system. The first one electron oxidation potential for **35** ($E_{1/2}$ ZnP/$ZnP^{\bullet+}$) and the first one electron reduction potential for **36** ($E_{1/2}$ $C_{60}/C_{60}^{\bullet-}$) determined versus an Fc/Fc^{+} reference were found to be 0.32 V and -1.08 V, respectively. From these values, the driving force for the initial PET (ΔG_{CS}^{o} = -0.81 eV) and the subsequent charge recombination (ΔG_{CR}^{o} = -1.4 eV) processes were estimated. In steady state fluorescence studies, the emission of cytidine-porphyrin **35** is quenched upon addition of guanosine-

fullerene **36** with forming a donor-nucleoside-nucleoside-acceptor complex with a binding constant of 5.1 ± 0.5 x 10^4 M^{-1}. From the derived lifetimes, a rate constant (*ca*. k_{cs} = 1.2 x 10^9 s^{-1}) for forward electron transfer was estimated. Furthermore, transient absorption studies were performed to support for PET in this self-assembled system. The transient spectra revealed a weak band in the 600–800 nm region and a peak at around 1000 nm, corresponding to zinc–porphyrin radical cation ($ZnP^{\bullet+}$) and the fullerene radical anion ($C_{60}^{\bullet-}$), respectively. Kinetic analysis of the transient absorption data resulted in a long lived charge separated state with lifetime of 2.02 μs which was substantially higher lifetime than those reported for related covalently tethered porphyrin–fullerene dyads.

Inspired by this finding, the concept of Watson-Crick base paring strategy for building noncovalent supramolecular system was extended with phthalocyanines[51], in order to take advantage of the good optical properties of this class of macrocyclic compounds. However, initial UV-vis studies indicated band broadening, suggesting electronic interactions between ZnPc and C_{60}. Increasing addition of G–$C_{60,}$ **38** subunit to a dichloromethane solution of cytidine functionalized phthalocyanine, **37** (ZnPc–C) leads to a non-linear decrease in the fluorescence intensity of this latter chromophore with a binding constant of 2.6 ± 0.2 x10^6 M^{-1}. The magnitude of formation constant is several orders of magnitude larger than that of the analogous ZnP-C:G-C_{60} dyad. This high strength of the interaction is rationalized π–π interactions and/or charge-transfer interactions.

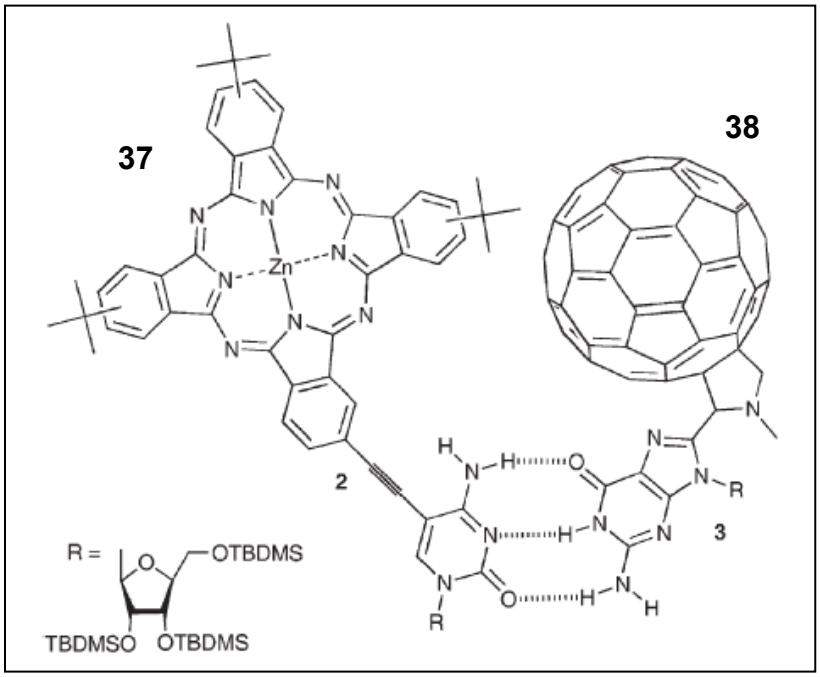

Figure 1.31: Structure of ZnPc–C:G–C_{60} dyad (*Chem.commun.* **2007**, 292-294)

In cyclic voltammetry, redox potentials for dyad, **37-38** reveals that the C_{60}-based reduction potentials are negatively shifted with respect to those of **38** by about -20, -60 and -70 mV for the first, second and third processes, respectively. Likewise, the first and second anodic ZnPc-based potentials are less positive than those of **37** by about 20 and 10 mV, respectively. These electrochemical shifts attribute to significant ground-state interactions between the phthalocyanine donor and the fullerene acceptor under ambient conditions. The transient absorption measurements revealed characteristics of the radical ions. The transient maxima at 525, 850 nm corresponds to cation radical of ZnPc-C while the 1000 nm peak resembles anaion radical of C_{60} which is an

evidence for PET. The lifetime for the charge separated state was estimated to be 3 ns which is three orders of magnitude shorter thanZnP-C:G-C_{60} dyad (2 μs). This behavior suggests the significant coupling between the ZnPc and C_{60} in the supramolecular self-assemble.

The through space interaction in these donor-acceptor conjugates with the complementary base pairs must be assumed to control the charge separation and charge recombination dynamics. To satisfy this argument, donor-acceptor hybrid should be in a linear arrangement.

1.12.2 Electron transfer via Ion-paring interactions

Incorporation of strong and highly directional hydrogen bonding to bio-inspired supramolecular assemblies is more efficient than those found in comparable ζ or π bonding networks for electron transfer events. Among these noncovalent architectures, placing the amidinium and carboxylate functionalities with the porphyrins (**39**) and C_{60} (**40**), respectively (Figure 1.32), rationalize an optimal pathway for the motion of charges and the electronic coupling between both electroactive units for mimicking reaction center functionality[52].

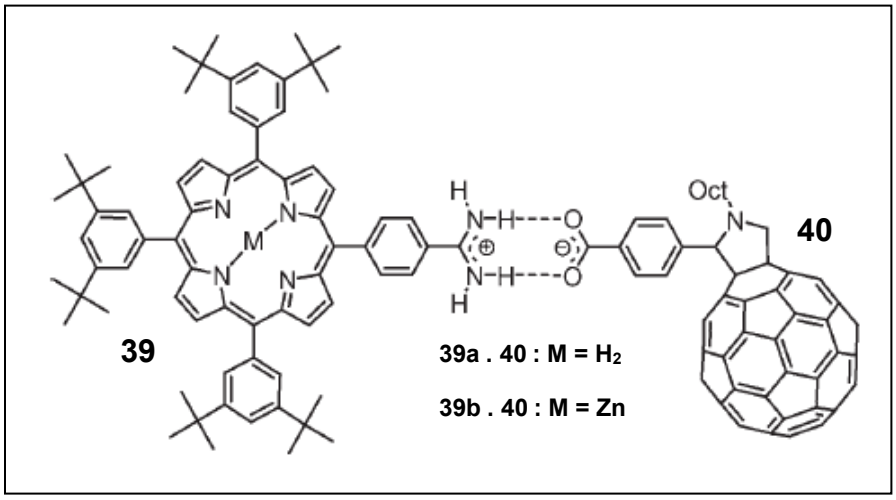

Figure 1.32: Amidinium–carboxylate interfaced porphyrin–C_{60} assemblies (**39-40**) (*Angew. Chem. Int. Ed*. **2006**, *45*, 4637-4641)

Complex formation between **39a** and **40** was monitored by ^{1}H NMR spectroscopy. Upon titration of one equivalent of **40** into a solution of **39a**, a most significant shift ($\Delta\delta$ = 0.35 ppm) which involves with the aryl protons ortho to the amidine functionality confirms 1:1 supramolecular complex formation. The UV-vis absorption and fluorescence studies reveal further information about 1: 1 supramolecular assembly formation. Upon addition of fullerene, dramatic red shift of the Soret and Q-band and the presence of isobestic points attribute to stable complex formation in the solution phase. Moreover, exceptional fluorescence quenching with binding constant of ~10^5- 10^7 M^{-1} supports the formation of noncovalent hydrogen bonded porphyrin-fullerene ion pair.

In cyclic voltammetry, the observed slight shifts in the redox potentials of the porphyrin-fullerene assemblies could be accounted for by a pronounced electronic coupling between both electroactive components. The formation of transient species as a result of PET, were determined by transient absorption studies. The transient maxima at 600-800 nm, corresponding to $ZnP^{\bullet+}$, and the fingerprint of $C_{60}^{\bullet-}$ around 1000 nm, suggesting the formation of long lived charge separated species with the lifetime of 10 μs.

1.12.3 Electron transfer via complementary electrostatics

Another important noncovalent interaction is coulomb interaction or complementary electrostatic which are employed in several facets in biological systems (Figure 1.33). The Coulomb complex formation of a dendritic fullerene oligocarboxylate (**1**$^{8-}$) and an octapyridinium zinc porphyrin salt (**ZnP**$^{8+}$) was reported [53, 54]. The combination of the two entities, **41**$^{8-}$ and **ZnP**$^{8+}$, promotes to the stable supramolecular assembly **ZnP**$^{8+}$/**41**$^{8-}$, which gives rise to a photoinduced intracomplex electron transfer.

In absorption spectroscopy, the Soret band of **ZnP**$^{8+}$ revealed a 4 nm bathochromic shift, upon addition of the **41**$^{8-}$. The Jobs plot obtained from UV absorbance shows a stable 1:1 complex in aqueous buffered solution (pH = 7.2, ionic strength = 0.012), with a binding constant of 3.5 ± 1.0 x 10^8 M^{-1}. Parallel fluorescence titration experiments revealed that the **ZnP**$^{8+}$ emission is strongly

quenched in the 1:1 donor-acceptor complex with a binding constant of 1.1 ± 0.1 x 10^8 M^{-1}. In particular, the significant decrease of fluorescence intensity in **ZnP**$^{8+}$ with variation of **41**$^{8-}$ and evidence for a new short-lived emissive component suggest a static quenching event inside a **ZnP**$^{8+}$/**41**$^{8-}$ complex. When the ionic strength of the solution was increased, the binding constant of the complex is decreased. Photoinduced electron-transfer was confirmed by transient absorption spectroscopy, which revealed the fingerprint absorptions of the **ZnP**$^{8+}$ radical cation and the **41**$^{8-}$ radical anion and a lifetime of 1.1 μs for the charge-separated state.

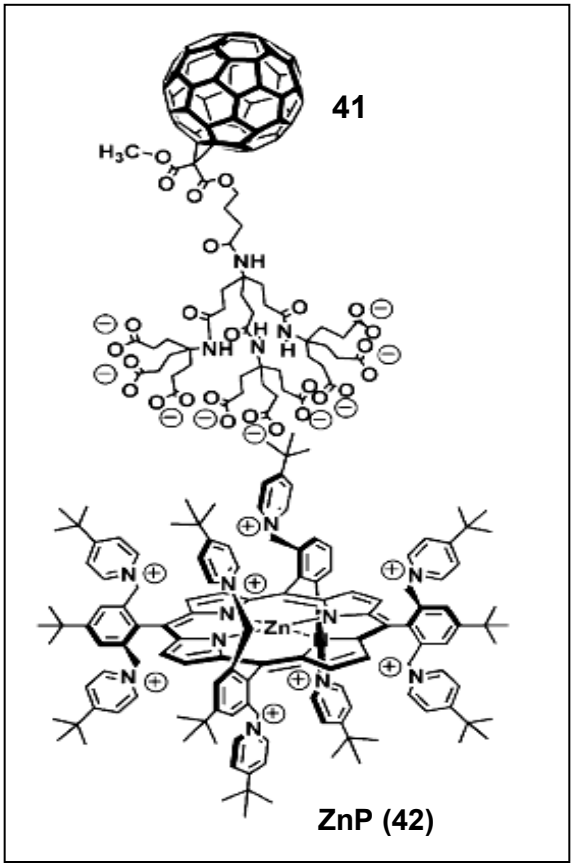

Figure 1.33: Electrostatically assembled porphyrin-fullerene dendritic dyad (*Chem. Commun.* **2004**, 96-97)

1.12.4 Electron transfer via π–π interactions

Another interesting noncovalent interaction for mimicry of reaction center functionality is π–π interaction. Inclusion of host molecule as fullerene to guest molecule, porphyrin has a great importance for investigation of electron transfer event. This strategy is highly interesting in view of possible supramolecular modulation of electronic properties of fullerenes. A face-to-face cyclic dimer of zinc porphyrin (**43**) is formed a highly stable 1:1 inclusion complex with C_{60} via donor-acceptor interactions (Figure 1.34)[55].

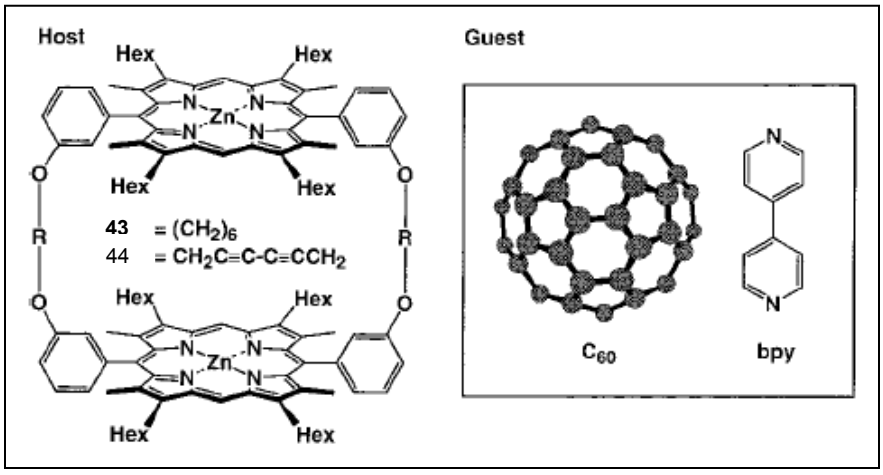

Figure 1.34: Host-guest complexation through π–π interactions (*J. Am. Chem. Soc.* **1999**, *121*, 9477-9478)

In absorption studies, upon addition of C_{60} to the benzene solution of porphyrin dimer was revealed 7 nm bathochromic shift of the Soret band of **43** with clear isobestic point around 418 nm. These spectral behaviors are attributed

to an electronic interaction between **43** and C_{60}. The stable 1:1 complex formation is revealed by Job's plot at 25 ^{o}C with the change in absorbance at 410.5 nm. Moreover, the binding constant of 6.7 x 10^5 M^{-1} suggests the 1:1 complexation. ^{13}C NMR spectrum of the inclusion complex of **43** and C_{60} in C_6D_6 at 30°C showed a single signal due to the included C_{60} at δ 140.10 ppm, which is upfield-shifted from that of free C_{60}. This upfield shift is reflected the shielding effect and/or the electronic effect of the zinc porphyrin π-cloud. Finally, the change in redox potentials of the included C_{60} also suggests a complexation of the supramolecular donor-acceptor approach.

1.12.5 Electron transfer via axial coordination

In hemoglobin, for example, the protein provides a single axial histidine ligand and protects the vacant sixth coordination site for oxygen binding.[56] On the other hand, the cytochromes ***c*** are six-coordinate with histidine and methionine ligation, a situation apparently desirable for electron transport. Inspired by these natural behaviors, scientists have been reported a number of studies porphyrin with covalently attached axial ligands as compounds to understand the mechanism of various biological events and reactions. Specially, this concept of penta- and hexa- coordination of porphyrin has extended for construction of artificial photosynthetic donor-acceptor model systems to understand the mechanistic details of electron transfer processes in natural photosynthesis. Among the several donor-acceptor entities via axial ligation, the central metal ion

of the metalloporphyrin and fullerene conjugates are commonly used to mimic reaction center functionality.

The formation of porphyrin-fullerene supramolecular dyads has reported by axial coordination of fulleropyrrolidine bearing either pyridine or imidazole ligands with zinc tetraphenyl porphyrin (ZnTPP)[57]. UV-vis, ^{1}H NMR, and ESI-mass spectral studies revealed 1:1 molecular stoichiometry between the donor, ZnTPP and the acceptor, fulleropyrrolidine entities.

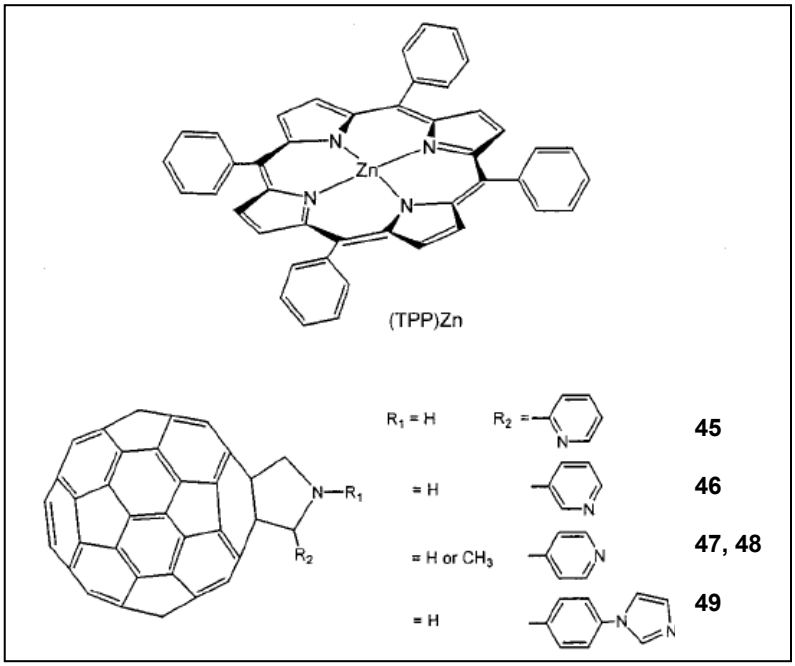

Figure 1.35: Axial coordination of fulleropyrrolidine bearing pyridine/imidazole ligands with Zn porphyrin (*J. Phys. Chem A.* **2002**, *106*, 3243-3252)

Among all fulleropyrrolidine compounds, the imidazole bearing fulleropyrrolidine revealed more stable self-assembled dyads due to its higher

basicity. The molecular stoichiometry, association constants, and thermodynamic parameters have been evaluated by using optical absorption methods. The determined formation constants *K* follow the trend *o*-pyridyl << *m*-pyridyl ≈ *p*-pyridyl, << *N*-phenyl imidazole entities of the fulleropyrrolidine: that is, they are controlled by the nature of the axial ligand and the associated steric factors. Ab initio B3LYP/3-21G(*) methods visualize the geometric and electronic structure of the dyads. Cyclic voltammetric studies revealed a total of seven one-electron redox processes within the accessible potential window of *o*-dichlorobenzene, 0.1 (TBA)ClO_4.These redox processes correspond to the oxidation and reduction of zinc porphyrin ring, and the reduction of fullerene entities. The experimentally calculated HOMO-LUMO gap for the studied dyads compared fairly well with the computed one. The steady-state fluorescence studies show about 30% quenching of ZnTPP bands, increasing addition of either of compounds **2**-**5** to a argon saturated *o*-dichlorobenzene solution of ZnTPP.

In *o*-dichlorobenzene, upon coordination of either the pyridine or imidazole entities of fulleropyrrolidine to ZnTPP, charge separation occurs from the singlet excited ZnTPP to the C_{60} moiety. Depending upon the axial ligand (pyridine or imidazole) of the fulleropyrrolidine, the calculated rate of charge separation was found to range between 10^7 and 10^{10} s^{-1}. However, in a coordinating solvent like benzonitrile, intermolecular electron transfer predominantly takes place mainly from the triplet excited ZnTPP to the C_{60} moiety.

1.12.6 Electron transfer via crown ether-ammonium cation interactions

Crown ethers are particularly widely used class of receptor in host-guest complexation which is a subject of the fields of supramolecular and fullerene chemistry[58]. Recently, scientists have developed various donor-acceptor supramolecualar systems which consist of benzo-18-crown-6 and quaternary alkyl ammonium cations to form hydrogen bond or ion-dipole interaction.

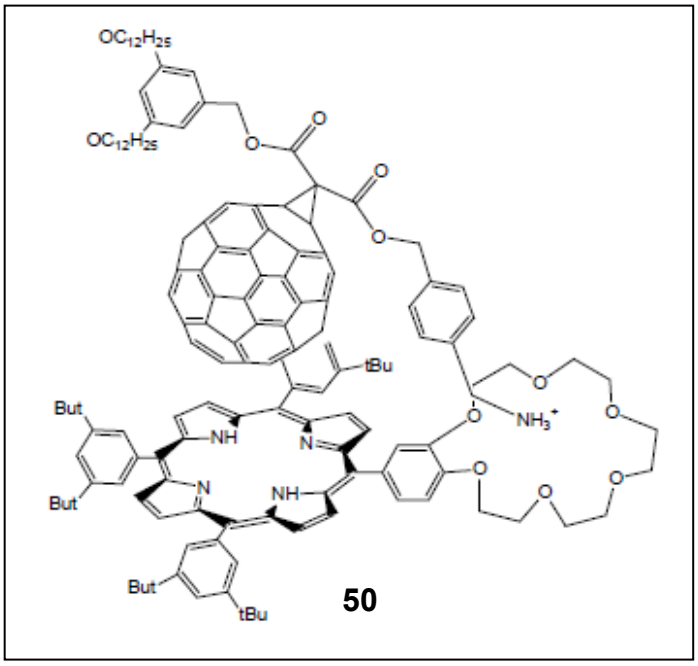

50

Figure 1.36: Structure of porphyrin crown ether complexed to fullerene bearing alkyl ammonium cation conjugate (*Chem. Commun.* **2003**, 2412-2413)

Nierengarten and coworkers[59] have reported a system consists of a C_{60} bearing a quaternary ammonium unit and a free base porphyrin (H_2TPP)

functioalized to bear a benzo-18-crown-6 unit, **50** (Figure 1.36). In addition to the ammonium–crown ether interaction, intramolecular stacking of the fullerene moiety and the porphyrin subunit exists in this supramolecular assembly. The formation of supramolecular complex using porphyrin and ammonium compound was evidenced by ^{1}H-NMR binding studies performed at 298 K in $CDCl_3$. Upon addition of the C_{60} derivative to crown ether appended porphyrin, the β–pyrrole positions of the porphyrin ring experienced an upfield shift due to π–π stacking between two chromophores. Further evidence for C_{60}–porphyrin interactions came from UV–vis measurements. Increasing addition of C_{60} to a CH_2Cl_2 solution of crown porphyrin causes a red shift of the Soret band which attributes the existence of the C_{60}–porphyrin interactions in supramolecular assembly. The binding constant of about 3.75 x 10^5 M^{-1} from the Benesi-Hildebrand plot suggests the stable complex formation. Steady-state fluorescence experiments indicate that the presence of the C_{60} quaternary ammonium derivative quenches the singlet excited state of the porphyrin crown ether moiety efficiently. Finally, the formation of supramolecular complex was also evidenced in the gas phase by electrospray mass spectrometry (ESI-MS).

Guldi and coworkers[60] reported self-assembled supramolecular dyad and triad systems consist of one or two phthalocyanine units (ZnPc or ZnPc-ZnPc) appended with a benzo-24-crown-8 unit capable of hydrogen bonding with a C_{60} moiety appended with a tertiary ammonium group (C_{60}amm) (Figure 1.37)

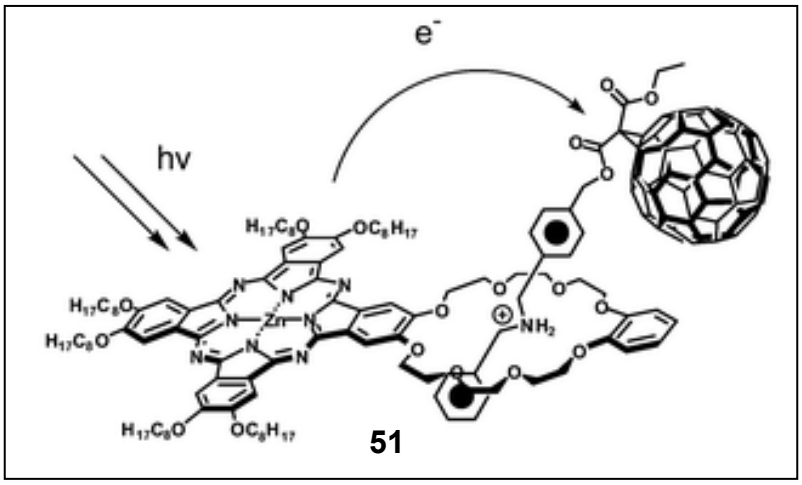

Figure 1.37: Structure of crown ether phthalocyanine self-assembled with fullerene appended alkyl ammonium cation (*Chem. Commun.***2002**, 2774-2775)

Steady state fluorescence data revealed the quenching of ZnPc, upon addition of a o-DCB solution of C_{60}. The binding constant values of 1.4 x 10^4 M^{-1} for the dyad system (**51**,ZnPc-C_{60}amm) and 1.9 x 10^4 M^{-1} for the triad system (ZnPc-C_{60}amm-ZnPc) were determined by using fluorescence spectral data. The nature of the excited state photochemical reactions for the dyad and the triad systems were determined by time-resolved fluorescence experiments. Increasing addition of C_{60}amm, a short-lived component with a lifetime of 0.28 ns developed progressively, and a mono-exponential decay of long-lived component (a lifetime of 3.1 ns) simultaneously decreased. The fast decay of the excited state of ^{1}ZnPc* upon complexation with C_{60}amm reveals that intramolecular ET from ^{1}ZnPc* is the predominant quenching mechanism.

The nature of the transient species during the course of the excited state photochemical reaction was determined by transient absorption spectral studies. Upon excitation of crown ether porphyrin, bands at 1040 nm corresponding to $C_{60}amm^{\bullet -}$ and bands at 500 and 860 nm corresponding to $ZnPc^{\bullet +}$. These data suggest that the formation of solvent-separated ion pair (SSIP) occurs with a high quantum yield of charge separation value about 0.90 and a lifetime of 1.5 μs.

1.12.7 Electron transfer via axial coordination and crown ether-ammonium cation interaction

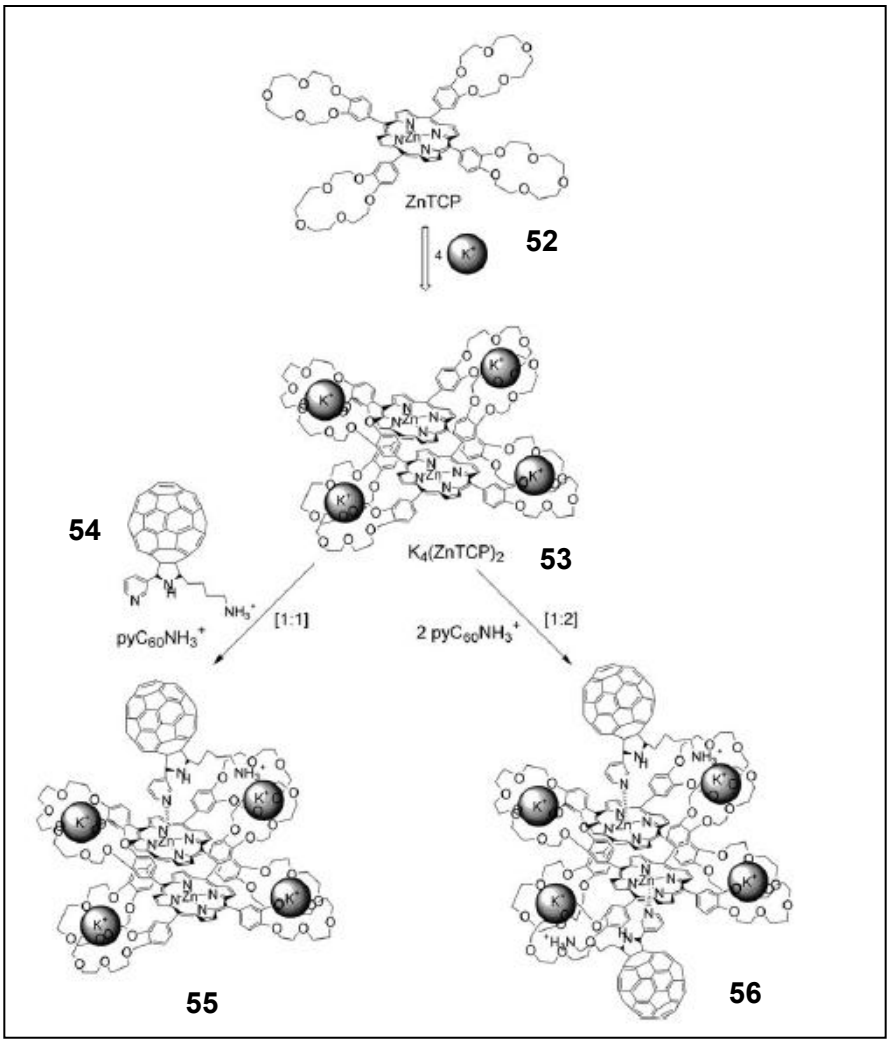

Figure 1.38: Construction of the supramolecular ―special pair" porphyrin dimer–fullerene triad and tetrad (*Chem. Euro. J.* **2007**, *13*, 916-922)

Incorporation of both axial coordination and ion-dipole interaction (crown ether-ammonium cation) to biomimetic bacterial photosynthetic reaction center

complex yields higher stability with defined geometry and orientation. The ~~-s~~special pair" donor, a cofacial porphyrin dimer (**52**), was formed via potassium ion induced dimerization of meso-(benzo-[15]crown-5)porphyrinatozinc[61]. The dimer was subsequently self-assembled with functionalized fullerenes (**54**) via ~~-tw~~o-point" binding, axial coordination and crown ether–alkyl ammonium cation complexation to form the donor–acceptor triads (**55**) and tetrads (**56**), mimicking the noncovalently bound entities of the photosynthetic reaction center. The structure of these novel supramolecules is deduced from spectroscopic and electrochemical methods.

The cofacail porphyrin dimer formation is revealed by the blue-shift Soret band and the red-shift visible bands in UV-visible absorption. Such spectral behavior was attributed to the cofacial porphyrin dimer formation with strong exciton coupling between the two macrocycles. Upon addition of pyridine and alkyl ammonium cation functionalized fullerene (**54**,$pyC_{60}NH_3^+$) to the cofacial porphyrin dimer (**53**) results in a decreased Soret intensity with a small red shift and two isobestic points. These spectral features and the binding constant of 1.03×10^4 M^{-2} suggests the tetrad formation, in which two $pyC_{60}NH_3^+$ are bound to the two the zinc centers of $K_4[ZnTCP]_2$ in addition of two of eight crown ethers. Moreover, the existence of the supramolecular tetrad confirms anodic shift of oxidation and cathodic shift of reduction in the porphyrin moiety.

The calculated DFT B3LYP/3-21G(*) suggests the photoinduced charge separated state in the triad and tetrad supramolecular donor-acceptor pairs. Steady state fluorescence studies show efficient quenching of the singlet excited state of zinc porphyrin in the $K_4[ZnTCP]_2$ to form the supramolecular triad and tetrad by addition of one equivalent and two equivalents of $pyC_{60}NH_3^+$ respectively. The calculated rate and quantum yield, k_{CS} and Φ_{CS}, were found to be 5.3 x 10^9 s^{-1} and 0.91 for tetrad, respectively. The k_{CS} and Φ_{CS} for simple dyad formed by self-assembling ZnTCP and $pyC_{60}NH_3^+$ were found to be 2.9 x 10^9 s^{-1} and 0.85 respectively.

The transient absorption studies revealed the characteristic band at 1000 nm of fulleropyrrolidine anion radical, serving as a direct proof of charge separation within the supramolecular triad. The absorption of the radical cation of $[K_4(ZnTCP)_2]$ dimer would be expected to appear in the 600–700 nm region.

1.13 Donor-acceptor systems (covalent and noncovalent) for mimicking antenna-reaction center functionality

To mimic the antenna-reaction functionality, covalently linked or self-assembled donor-acceptor conjugates have been extensively studied. Developing such an artificial light harvesting system with a reaction center mimic to produce a complex capable of absorbing light, transferring the resulting

excitation to an energy sink, and using the captured energy to initiate PET is one of the major advancements in the area of artificial photosynthesis research.

Among variety of donor-acceptor systems for mimicking antenna reaction center functionality, porphyrin-fullerene linked triads have synthesized by various research groups. One of the representative examples is zinc porphyrin-free base porphyrin-fullerene triad (ZnP-H_2P-C_{60}) which exhibits sequential energy transfer and charge separation processes (Figure 1.39)[62,47].

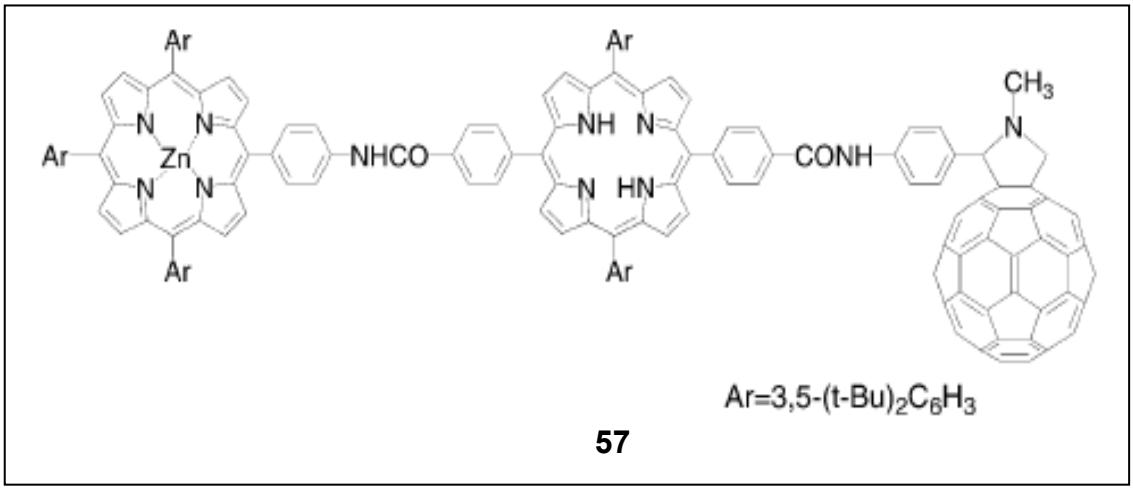

57

Figure 1.39: ZnP-H_2P-C_{60} triad for antenna-reaction center functionality (*J. Am. Chem. Soc*. **2000**, *122*, 6535-6551)

In this study, the ZnP chromophore acts as an antenna molecule, which transfers its singlet excited-state energy to the adjacent H_2P chromophore. Then, the photoinduced charge separation from the free-base porphyrin to the C_{60} excited state (1.75 eV) also occurs to produce yield ZnP-$H_2P^{\bullet+}$-$C_{60}^{\bullet-}$ (1.59 eV),

whereas unquenched ZnP-H_2P-$^1C_{60}^*$ undergoes an intersystem crossing to yield ZnP-H_2P-$^3C_{60}^*$ (1.50 eV). Then this triplet state of C_{60} decays either to the ground state or to the ZnP-$^3H_2P^*$-C_{60} state (1.40 eV). In lifetime of 21 μs was obtained for the final charge separated state with a quantum yield of ~0.4 in deoxygenated benzonitrile.

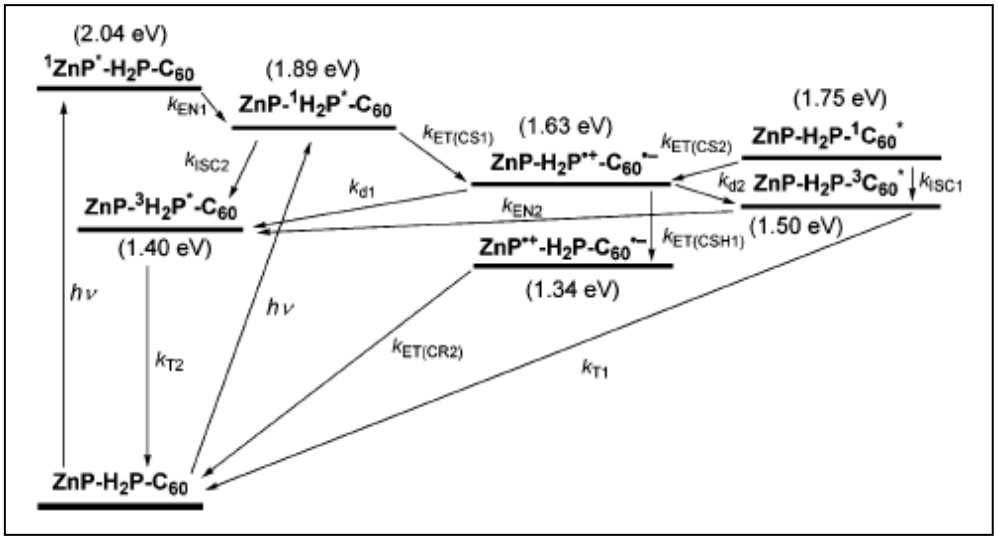

Figure 1.40: Energy diagram for ZnP-H_2P-C_{60} in PhCN (*Org. Biomol. Chem*. **2004**, *2*, 1425-1433).

This system (ZnP-H_2P-C_{60} triad) is tethered at the end of the triad by using ferrocene moiety to achieve photoinduced energy transfer followed by multiple step electron transfer with a long lived charge separated state in frozen media and also in solutions[63].

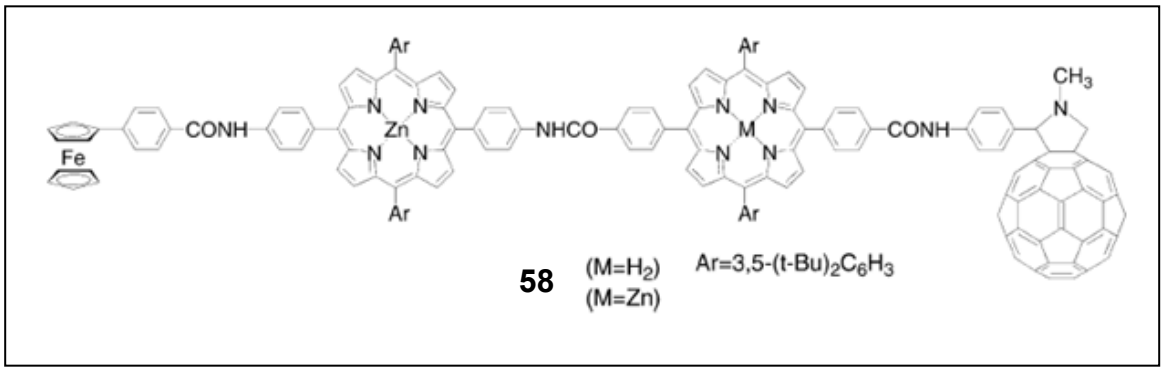

Figure 1.41: Ferrocene-(porphyrin)$_2$-fullerene tetrad (*J. Am. Chem. Soc*. **2001**, *123*, 6617-6628)

Upon excitation, singlet excited energy transfer takes place from zinc porphyrin, $^1ZnP^*$, to free base porphyrin followed by electron transfer from singlet excited free base porphyrin ($^1H_2P^*$) to fullerene involving an initial charge separated state, Fc-ZnP-$H_2P^{\bullet+}$-$C_{60}^{\bullet-}$. The resulting Fc-ZnP-$H_2P^{\bullet+}$-$C_{60}^{\bullet-}$ undergoes a cascade of short range-charge shift reactions by forming Fc-$ZnP^{\bullet+}$-H_2P-$C_{60}^{\bullet-}$ followed by final charge separated state of $Fc^{\bullet+}$-ZnP-H_2P-$C_{60}^{\bullet-}$. The lifetime of final charge separated state was found to be 0.38 s in frozen benzonitrile, which is more than one order of magnitude longer than any other intramolecular charge recombination processes of artificial photosynthetic models, and is comparable to that observed for the bacterial photosynthetic reaction center.

To increase light harvesting efficiency, *meso,meso*-porphyrin arrays are good candidates in artificial model systems. The length of *meso,meso*-porphyrin

arrays can be increased by facile oligomerization of the porphyrin monomer. By improving this methodology, these model systems can absorb more visible light than a linear corresponding porphyrin monomer. This is mainly due to the exciton coupling of porphyrin, which can be seen in molecular assemblies of chlorophylls in antenna complex. Inspired by this natural phenomenon, a zinc atom is incorporated into the free base porphyrin moiety of Fc-ZnP-H_2P-C_{60} system to construct ferrocene-*meso,meso*-linked porphyrin dimer-fullerene tetrad [ferrocene-zinc porphyrin-zinc porphyrin-fullerne (Fc-ZnP-ZnP-C_{60})][64]. Photoirradiation of Fc-ZnP-ZnP-C_{60} tetrad in PhCN results in photoinduced electron transfer from the singlet excited state of the zinc porphyrin dimer [$^1(ZnP)_2^*$] to the C_{60} moiety to produce cation radical of porphyrin dimer and anion radical of C_{60} [Fc-$(ZnP)_2^{\bullet+}$-$C_{60}^{\bullet-}$]. Then subsequent electron transfer from Fc to $(ZnP)_2^{\bullet+}$ occurs to give final the final charge separated state of $Fc^{\bullet+}$-$(ZnP)_2$-$C_{60}^{\bullet-}$. The total quantum yield of the final charge separated state was found to be 0.88 with a lifetime of 19 μs in PhCN in 298 K.

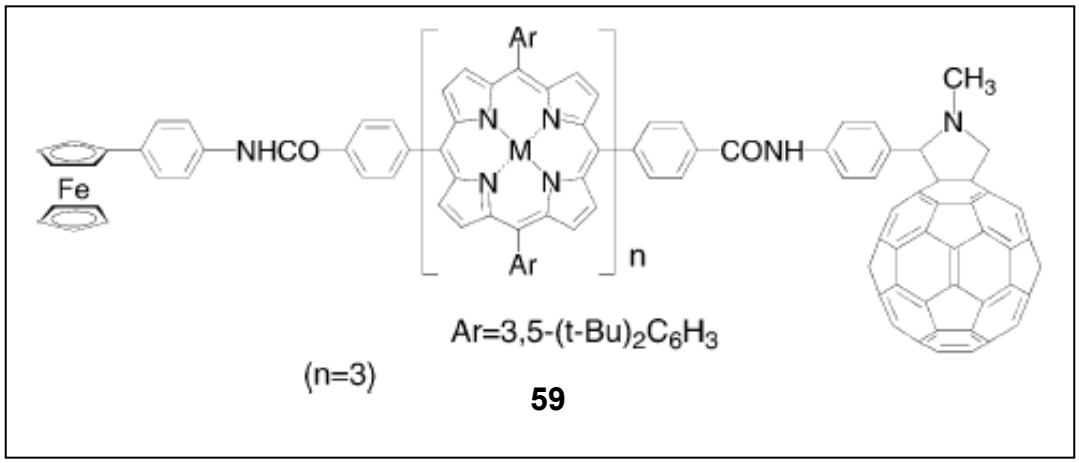

Figure 1.42: *Meso-meso* linked porphyrin trimer donor-acceptor system (*Chem. Eur. J.* **2004**, *10*, 3184-3196).

A *meso-meso*-linked trimer $[(ZnP)_3]$[65] which linked to ferrocene and fullerene (**59**) improved more light harvesting efficiency in the visible region due to the exciton coupling in porphyrin trimer as well as an increase number of the porphyrins. This pentad ($Fc\text{-}(ZnP)_3\text{-}C_{60}$) results in photoinduced electron transfer eventsyielding a final charge separated state of $Fc^{\bullet+}\text{-}(ZnP)_3\text{ -}C_{60}^{\bullet-}$. Upon excitation of $Fc(ZnP)_3\text{-}C_{60}$ in PhCN results photoinduced electron transfer from both the singlet excited state and triplet excited state of the porphyrin trimer to C_{60} moiety to produce the charge separated state of $Fc\text{-}(ZnP)_3^{\bullet+}\text{-}C_{60}^{\bullet-}$. In competition of with charge recombination from $C_{60}^{\bullet-}$ to $(ZnP)_3^{\bullet+}$ to ground state, an electron transfer from Fc to $(ZnP)_3^{\bullet+}$ occurs to give the final charge-separated state, $Fc^{\bullet+}\text{-}(ZnP)_3\text{ -}C_{60}^{\bullet-}$. The final long range charge-separated state decays obeying first order kinetics with a lifetime of 0.53 s ($1.9\ s^{-1}$) in frozen DMF at 163 K. The total quantum yield of this state was determined to be 0.83 in benzonitrile.

This remarkably high quantum yield attributes the efficient charge separation through the trimer and slow charge recombination which is associated with the localized porphyrin radical cation in the porphyrin trimer.

To increase energy transfer efficiency, scientists have been inserted different antenna chromophores such as boron dipyrromethane (BDP) and antracene etc. D'Souza and coworkers[66] reported a supramolecular triad which is assembled by axially coordinating imidazole-appended fulleropyrrolidine to the zinc center of a covalently linked zinc porphyrin-boron dipyrrin dyad.

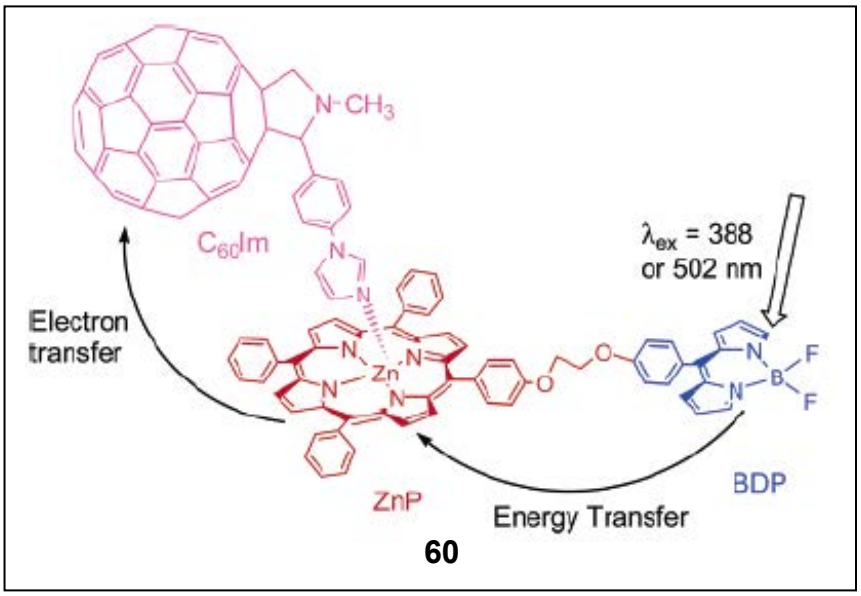

Figure 1.43: Borondipyrrin-porphyrin-fullerene (**60**) based energy and electron transfer donor-acceptor traid (*J. Am. Chem. Soc*. **2004**, *126*, 7898).

In Figure 1.43, boron dipyrrin (BDP) acts as an energy absorbing and transferring antenna, and zinc porphyrin (ZnP) acts as an energy acceptor from

the antenna and promotes electron transfer to the fullerene moiety by using the excitation energy, with the fullerene (C_{60}-Im) being the electron acceptor. Selective excitation of the BDP moiety resulted in efficient intramolecular energy transfer ($k_{ENT}^{singlet}$ = 9.2 x 10^9 s^{-1}) creating singlet excited ZnP with quantum yield of ~ 0.83. Electron transfer from the excited zinc porphyrin to fullerene subsequently follows, resulting in the formation of the charge-separated state with a lifetime of 5 ns ($\Phi_{CS}^{singlet}$ = 0.9). The important feature of this model system is its relative ―simplicity" because of the utilized supramolecular approach to mimic rather complex ―combined antenna-reaction center" events of photosynthesis.

In order to increase light harvesting efficiency, incorporation of multiple antenna chromophores to the photosynthetic model systems is important strategy for mimicking antenna-reaction center functionality in artificial photosynthesis. In this regard, Gust and coworkers reported[67] a synthetic molecular heptad (**63**) that features two bis(phenylethynyl)anthracene (BPEA) and two borondipyyromethane (BDP) antennas linked to a hexaphenyl benzene core that also bears two zinc porphyrins. Two pyridine moieties appended fullerene electron acceptor (**61**) self-assembles to both zinc porphyrins via axial coordination. Two BPEA absorb in the 400-500 nm region and two BDP absorb in the 450-550 and 30-430 nm ranges. Upon excitation of both kinds of antennas results occurrence of singlet excitation energy transfer to zinc poprhyrin and electron transfer to the fullerene to generate a charge-separated state.

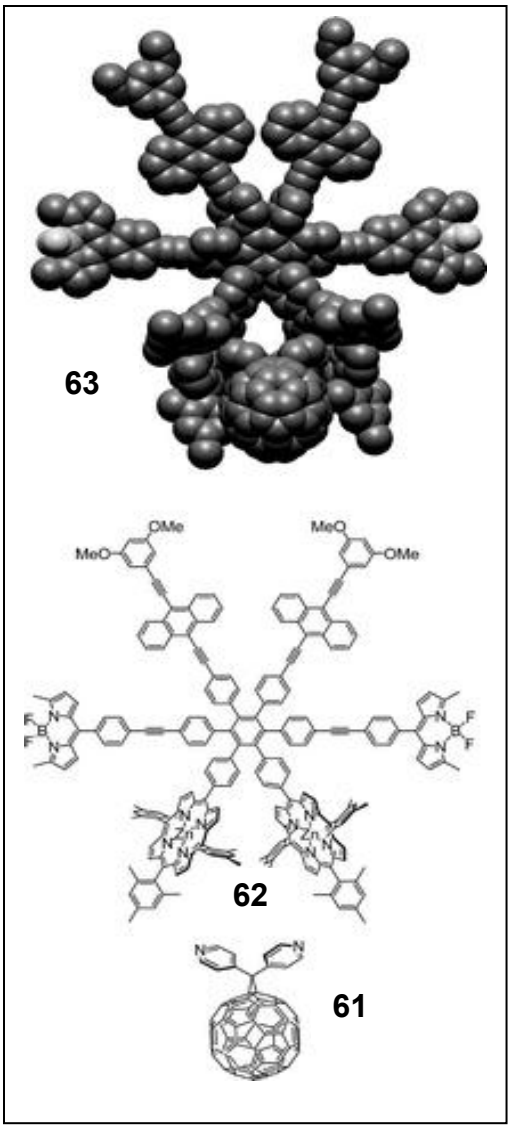

Figure 1.44: Molecular model of self-assembled heptad **63** and components hexad **62** and fullerene derivative **61** (*J. Phys. Chem. B.* **2009**, *113,* 7147-7155)

Energy transfer from BPEA to BDP and directly to the porphyrin is very fast relative to decay of ^{1}BPEA by unichromophoric photophysical processes. This results the unity quantum yield of energy transfer. And energy transfer from ^{1}BDP to the porphyrin is also multiexponential, and the fastest process (4 – 5 ps) is

essentially quantitative. (Φ ≥ 0.98). Transfer by the slower process ijiks slightly less effective, but the quantum yield is still ~0.96. Calculations based on molecular models and using Förster treatment of singlet – singlet energy transfer yield rate constants consistent with those observed. Therefore, overall, the two kinds of chromophore are highly effective antenna for the zinc porphyrins in complex 1. The energy transfer occurs both directly and stepwise mechanism whereby migration around the hexaphenylbenzene ~~-~~wheel" from BPEA to BDP and on to the porphyrin.

Upon addition of two pyridine moieties appended fullerene to hexad forms a supramolecular heptad which undergoes photoinduced electron transfer from Zn porphyrin to fullerene with a time constant of 3 ps. This results the final charge separated state with a lifetime of 230 ps. Incorporation of multiple antennas to the supramolecular system makes an efficient light harvesting capability throughout the visible from ultraviolet wavelengths out to ~650 nm with the overall quantum yield of one.

Part B

Carbon Nanotubes

1.14 General introduction of carbon nanotubes

The unidirectional growth of materials to form nanowires or nanotubes has attracted enormous interest in recent years. Within the different classes of tubes made of organic or inorganic materials and exhibiting interesting electronic, mechanical, and structural properties, carbon nanotubes (CNT) are extremely promising for applications in materials science and medicinal chemistry[68]. CNT consist of graphitic sheets, which have been rolled up into a cylindrical shape. They are basically divided into two types with high structural perfection, i.e, single wall carbon nanotubes (SWNT) and multi wall carbon nanotubes (MWNT)[69].

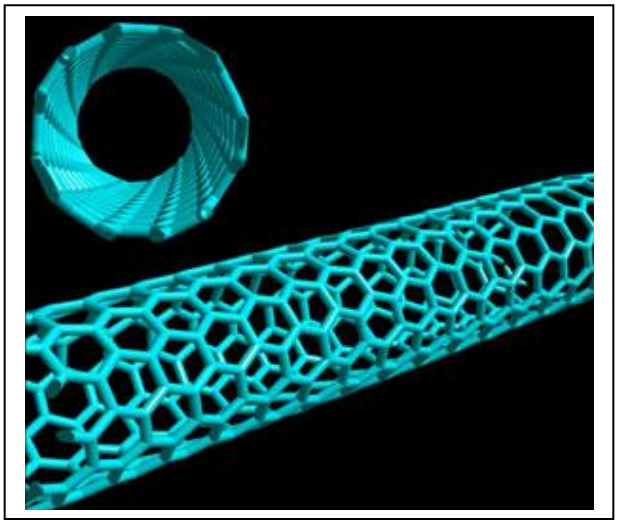

Figure 1.45: Schematic representation of single wall carbon nanotube. (*www.biomedme.com*)

SWNT are 1-dimensional nanostructures. They are hexagon networks of carbon atoms, rolled up to create seamless cylinders, along an (*m*,*n*) lattice vector in the graphene plane. The (*m*,*n*) indices determine the diameter and chirality, which are key parameters of a nanotube. Depending on the chirality (the chiral angle between hexagons and the tube axis), SWNTs can be either metallic or semiconducting, with band gaps that are relatively large (~0.5 eV for typical diameter of 1.5 nm) or small (~10 meV), even if they have nearly identical diameters. For same-chirality semiconducting nanotubes, the band gap is inversely proportional to the diameter. They readily accept electrons, which can then be transported under nearly ideal conditions along the axis[70].

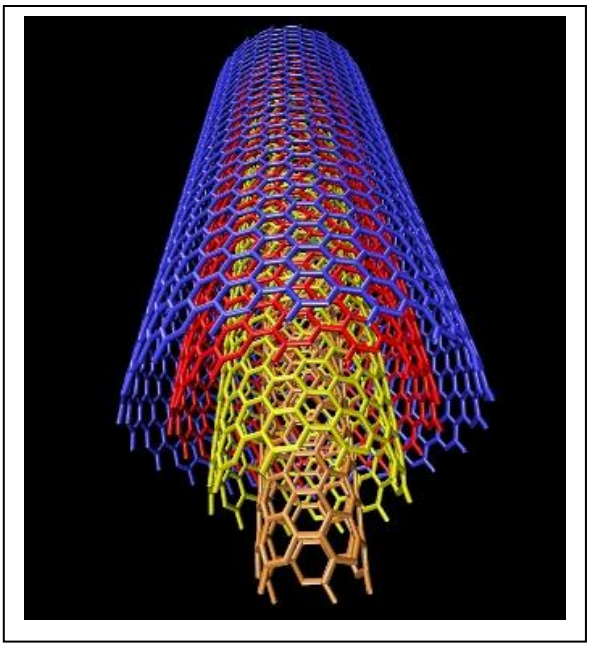

Figure 1.46: Schematic representation of multi-wall carbon nanotube. *(www.biomedme.com)*

Multiwall carbon nanotubes (MWNT) or multiple concentric graphene cylinders exhibit metallic or semiconducting properties, which depend solely on their outermost shell. These MWNT are more suitable in electron-donor–acceptor ensembles than SWNT, since large number of concentric cylindrical graphitic tubes present in MWNT.

1.14.1 Properties, applications and syntheses of carbon nanotubes

The past two decades, metallic SWNTs have been used as model systems for investigating the rich quantum phenomena in quasi-1d solids, including single-electron charging, Luttinger liquid, weak localization, ballistic transport, and quantum interference. On the other hand, semiconducting nanotubes have been exploited as novel building blocks for nanoelectronics, including transistors and logic, memory, and sensory devices[70, 71, 72]

The extreme sensitivity of nanotube structure-property relations promotes a wide range of applications; it poses a significant challenge to chemical synthesis in controlling the nanotube diameter and chirality. The chemical synthesis of nanotubes with predictable properties essentially requires exquisite control of atomic arrangement along the tubes. Arc-discharge, laser ablation, and

chemical vapor deposition have been the three main methods used for carbon nanotube synthesis[73].

Carbon nanotubes are natural electron acceptors. Evidence for electron accepting capability is obtained mathematically even by qualitative molecular orbital theory. The argument starts from isolated C2 fragments that are brought together starting from infinite distance. Each fragment has a π and a π^* orbital. As they are brought together to form, for example, a CNT, the two degenerate sets of π and π^* orbitals mix prevalently between themselves and spread in energy. The low-lying end of the π^* orbitals is very stable and readily accept electrons[74, 75].

Carbon nanotubes have an additional advantage of their sheer size. Upon receiving the charge, the charge transport along the axis of the nanometers-long carbon structure can contribute to a reduced probability of back electron transfer to the oxidized donor. This phenomenon is largest in metallic nanotubes.

Due to multiple electron conducting concentric cylindrical graphitic tubes, MWNT act as better electron donors than SWNTs. But scientists more concern on SWNT, because of the well-understood and characteristic fingerprints in several analytical and spectroscopic techniques.

1.14.2 Chemical functionalization approaches of CNT

The lack of solubility and the difficult manipulation in any solvents have imposed great limitations to the use of CNT. Indeed, as-produced CNT are insoluble in all organic solvents and aqueous solutions. Sonication promotes to disperse CNT in some solvents, but precipitation immediately occurs when this process is interrupted. These CNTs can interact with different types of compounds for various applications. The formation of supramolecular complexes allows a better processing of CNT toward the fabrication of innovative nanodevices. In addition, CNT can undergo chemical reactions that make them more soluble for their integration into inorganic, organic, and biological systems[76].

Basically, the modification/functionalization of these CNTs can be classified into three categories:

(a) the covalent attachment of chemical groups through reactions.

(b) the noncovalent adsorption or wrapping of various functional molecules; and

(c) the endohedral filling of their inner empty cavity.

Eventually, these approaches make almost similar results, but they differ in the degree of involvement of the carbon skeleton in the formation of chemical bonds.

1.14.3 CNT as electron acceptor in donor–acceptor systems

Among different photoactive components bound to CNTs, porphyrins are the most widely studied photoactive substance which is known to be good light harvesting chromophores and/or excited state energy/electron donors. A quick literature survey shows that in majority of the studies SWNTs acted as good electron acceptors, and only in a very few examples they have been shown to be electron donors. First we would like to elaborate covalently functionalized SWNT as electron acceptors in donor-acceptor nanoconjugates.

1. **Covalent functionlaiztion of carbon nanotubes**

Covalent functionaliztion of CNT results in a change of hybridization from sp^2 to sp^3 leading to a partial loss of conjugation with effects on electron-acceptor and/or electron transport properties. Two general approaches for the functionalization of CNTs have been reported: the covalent attachment of molecules to the open edges or sidewalls of CNTs. Among various types of covalent approaches, esterification or amidation of oxidized nanotubes and covalent side-wall functionalization are most general.

Covalent decoration of porphyrin/phthalocyanine-carbon nanotube donor – acceptor nanohybrids

As mentioned earlier, SWNT exhibit either metallic or semiconducting properties. They readily accept charges, which can then be transported efficiently along the tubular SWNT axis. And poprhyrins act as efficient electron donors in various photoinduced electron transfer processes. Incorporation of porphyrin or phthalocyanine like light absorbing antenna chromophores through extended π electrons of CNT would make artificial photosynthetic model systems which promote harvesting solar energy with high quantum yield and convert it to chemical energy with maximum efficiency.

(a) Functionaliztion of oxidized nanotubes via ester linakge.

One of the purification methods of raw carbon nanotubes involves oxidation of the corresponding materials in the acidic media[77]. In the presence of these reaction conditions, the end caps of the CNT are opened, and acidic functionalities are obtained at these defect sites and also side walls, which can be utilized for the further derivatization. Direct condensation of oxidized CNTs with amines (or alcohols) or activation of the carboxylic groups using reagents like thionyl chloride followed by the condensation with amines (or alcohols) yielded various soluble functionalized CNT materials[78]. After modification of CNT, their electronic properties are slightly changed.

Esterification of hydroxyl groups appended porphyrins with CNT containing carboxylic acid is an efficient covalent tethering of SWNTs. In

particular, Sun and coworkers[79] reported the derivatized porphyrins containing a terminal hydroxyl groups connected to covalently appended acid groups of SWNT with varying linkages (Figure 1.47). The structural arrangement between the tethered porphyrin and nanotube may have an important role in the intramolecular energy transfer. In the long linkage bearing donor-acceptor nanoconjugates (**64**), a photinduced energy transfer was envisioned from the singlet excited state porphyrin to the carbon nanotube framework. This long linkage porphyrin-SWNT configuration allows porphyrin to take a position facing the nanotube surface.

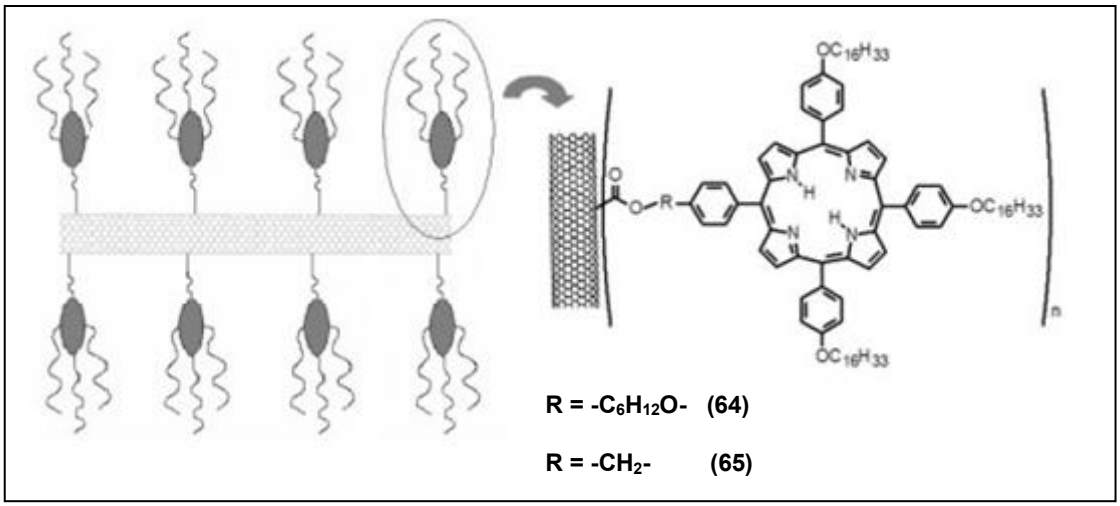

Figure 1.47: Structure of porphyrin-decorated SWNTs **64** and **65** (*Adv. Mater*. **2004**, *16*, 896)

The same porphyrin-SWNT configuration is not possible in **65** because of the reduced flexibility associated with the shorter tether which promotes to attach

a large number of porphyrin molecules to nanotube surface. This system showed relatively long and amenable fluorescence lifetime which attributes to intramolecular electron quenching.

Subsequently, the synthesis of meso-substituted porphyrin-grafted carbon nanotubes, **66** (por-CNTs), including multiwalled nanotubes ((por-MWNTs) and SWNT (por-SWNTs), and the study of their photoinduced electron-transfer properties were reported by Baskaran and coworkers[80].

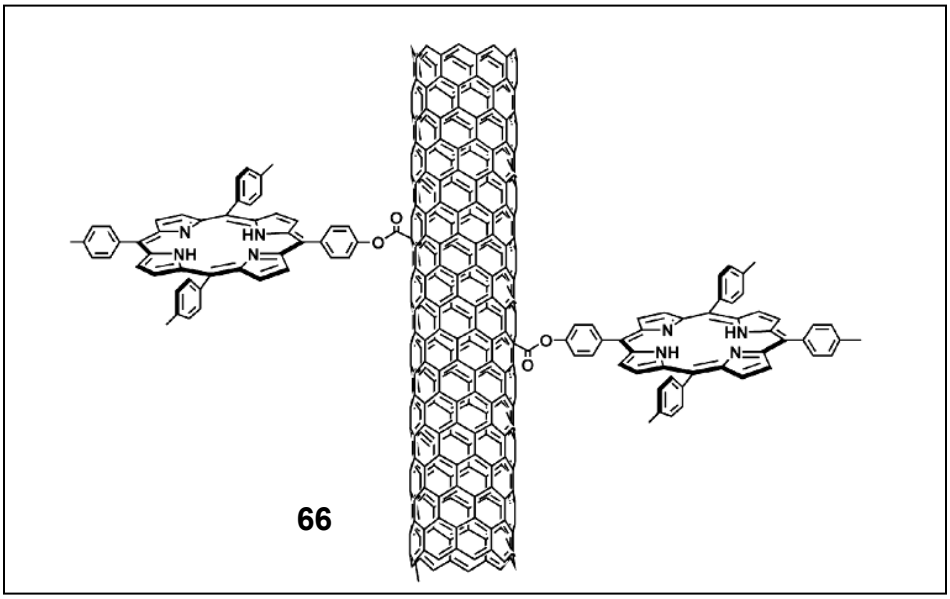

66

Figure 1.48: Covalently linked H_2P-SWNT nanoconjugate (*J. Am. Chem. Soc*. **2005**, *127*, 6916)

The absorption and fluorescence of these complexes show that the carbon nanotubes serve as an efficient electron acceptor. Upon photoexcitation

at 550 nm, efficient quenching (>95%) of the porphyrin emission bands at 650 and 725 nm was observed. This spectral behavior was mainly attributed to the intraconjugate electron transfer from singlet excited porphyrin to carbon nanotube via ester linkage.

(b) Functioanlization via 1,3-dipolar cycloaddition

A Prato protocol, 1,3-dipolar cycloaddition of azomethine ylides is widely used in fullerene field to construct donor-acceptor conjugates[81] to mimic antenna-reaction center functionality. Similarly, the side-walls of the CNT are covalently attached to pyrrolidine rings with various functional groups containing porphyrin and phthalocynanine in various artificial photosynthethic model systems.

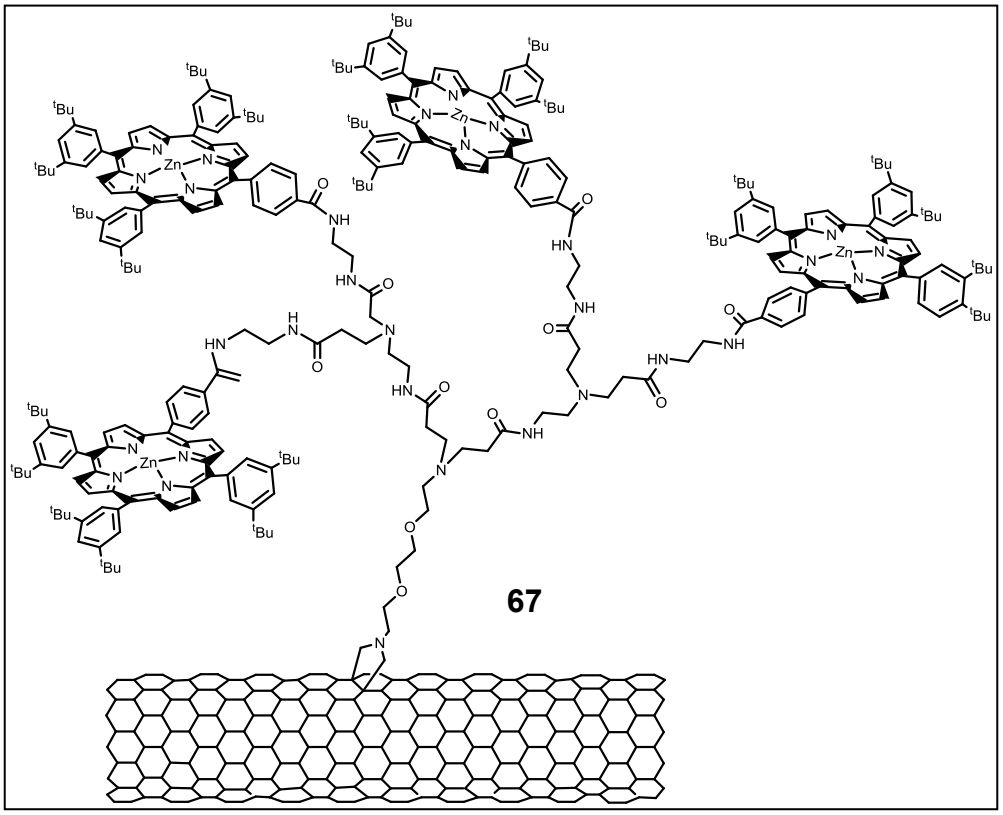

Figure 1.49: Dendrimer functionalized single wall carbon nanotubes via 1,3-dipolar cyclo addition (*J. Am. Chem. Soc*. **2006**, *128*, 12544)

A porphyrin-SWNT based donor-acceptor systems (**67**), consists of SWNT functionalized with polyamidoamine dendrimers was synthesized via 1,3-dipolar cycloaddition for harvesting light to give more efficient electron transfer[82].

The adopted divergent synthetic methodology guarantees an increase of the functional groups on the nanotubes without causing significant damage to the electronic properties of the nanotubes. Photophysical properties of the resulting

nanoconjugates were investigated with a series of steady state and time-resolved spectroscopy. The fluorescence kinetics suggest evidence for two transient decays, one very short-lived (*i.e*., 0.04 ± 0.01 ns) and one long-lived (*i.e*., 8.6 ± 1.2 ns). The possible rationale implies that some of the porphyrins, due to dendritic structure, do not interact with the SWNTs and thus exhibit fluorescence lifetime similar to the free porphyrin. Finally, complementary transient absorption measurements not only corroborate the fast decay of the photoexcited tetraphenylporphyrin but also confirm that intraconjugate charge separation is mainly due to electron transfer from the excited porphyrin to the SWNTs.

Guldi, Torres and coworkers reported SWNT - phthalocyanine ensembles[83] which were prepared with above Prato protocol, via 1,3-dipolar cycloaddition.

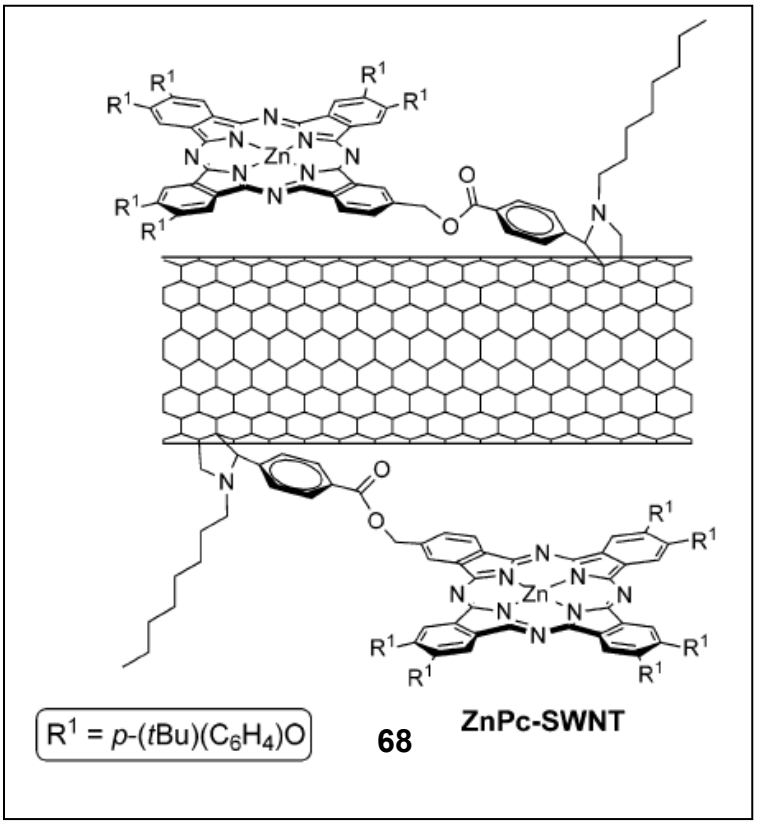

Figure 1.50: Functionalize the sidewalls of SWNTs with Pc molecules (*J. Am. Chem. Soc.* **2007**, *129*, 5061-5068)

These ensembles (**68**) are characterized by using Raman, TGA, and photophysical studies. The occurrence of electron transfer from photoexcited phthalocyanines to the nanotube framework in these ZnPc-SWNT ensembles is observed in transient absorption experiments. Charge-separation (i.e., 2.0 x 10^{10} s^{-1}) and charge-recombination (i.e., 1.5 x 10^{6} s^{-1}) dynamics reveal a notable stabilization of the radical ion pair product in dimethylformamide.

In order to preserve the electronic structure of SWNTs, non-covalent functionalization without irreversible damaging of their electronic structure is important on construction of artificial photosynthestic architectures.

2. Non-covalent functionlaiztion of carbon nanotubes

Since the covalent approach causes a partial loss of the electronic properties of the functionalized CNT, the decoration of CNT noncovalently appears particularly promising in the field of artificial photosynthesis. This noncovalent strategy was achieved by adsorbing carbon nanotubes with pyrene moieties, conjugate polymers, cyclodextrins and biomolecules such as polysaccharides. Here, we will discuss about SWNTs as electron acceptors in non-covalently decorated in donor-acceptor nanohybrids.

Non-covalent decoration of porphyrin/phthalocyanine-carbon nanotube donor –acceptor nanohybrids

Several nanotube based non-covalent supramolecular donor-acceptor systems have been reported in the literature for mimicking antenna-reaction center functionality. Those ensembles consist of porphyrin, phthalocyanine as donors and SWNTs as acceptors which are mainly employed non covalent interactions such as $\pi-\pi$ stacking, complementary electrostatic interactions.

The surface of CNT is easily functionalized through π–π interactions with compounds that possess π-electron rich structures. Prato, Guldi and co-workers explored the immobilization of porphyrins onto the SWNT surface towards electron donor–acceptor nanohybrid structures[84]. Here, SWNTs are suspended in DMF solutions of either tetraphenylporphyrins, (H_2TPP) or the corresponding zinc complex (ZnTPP) (Figure 1.51). TEM studies revealed that ZnTPP is not able to fully exfoliate and/or stabilize individual SWNT in DMF solutions, compared to H_2TPP. This behavior could be attributed to that the zinc metal located at the center of the porphyrin chromophore has weaker interactions between nanotube and porphyrin π system.

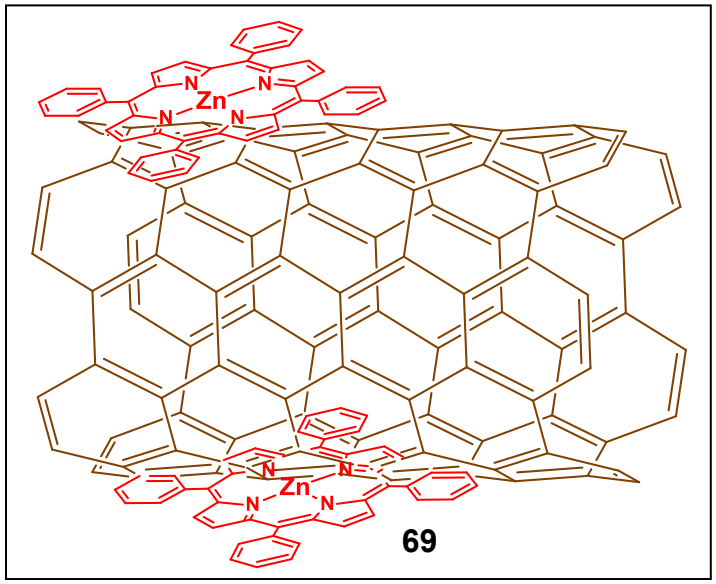

69

Figure 1.51: SWNT-porphyrin donor-acceptor systems formed due to π–π interactions (*J. Mater. Chem.* **2006**, *10*, 62)

The broadening of the Soret band and an apparent red-shift in UV-vis absorption indicate notable electronic communication between the two π-systems of SWNT and porphyrin. Furthermore, these nanohybrids are characterized by fluorescence and transient absorption studies. The lifetime of the radical ion pair for SWNT/H_2TPP nanohybrid, formed due to charge transfer interactions, was calculated to be 110 ns.

Fukuzumi an coworkers[85] reported a noncovalent complexation of the nondestructive nanotubes with a flexible porphyrinic hexa decamer peptide bearing 16 porphyrin units [$P(H_2P)_{16}$] in DMF at 298 K. This supramolecular formation occurs through wrapping of peptidic backbone in $P(H_2P)_{16}$ and π–π interaction between porphyrins and nanotubes to extract the large-diameter nanotubes. UV-vis-near IR, Raman spectroscopy, as well as high-resolution transmission electron microscopy are revealed successful debundling of SWNTs which facilitated to extract the large-diameter nanotubes of 1.3 nm. This behavior indicates the supramolecular formation of $P(H_2P)_{16}$ with SWNT. Photoexcitation of [$P(H_2P)_{16}$]/SWNT in DMF resulted in the photoinduced electron transfer from the singlet to triplet excited states of $P(H_2P)_{16}$ to SWNTs. The lifetime of the charge separated state was determined to be 0.37 ± 0.03 ms.

Unlimited solubility of CNTs aqueous media is essential for incorporation of the CNTs in biological systems. In this regard, various pyrene derivatives [1-(trimethylammonium acetyl) pyrene (pyrene$^+$), 1-pyrenecarboxylic acid, 1-

pyrenebutyric acid, 8-hydroxy-1,3,6-pyrenetrisulfonic acid (pyrene^{-})] are useful to make aqueous solution of pyrene/nanotube via $\pi-\pi$ interactions[86,87]. The coexistence of individual and bundles of CNT in solutions is characterized by using TEM and AFM images.

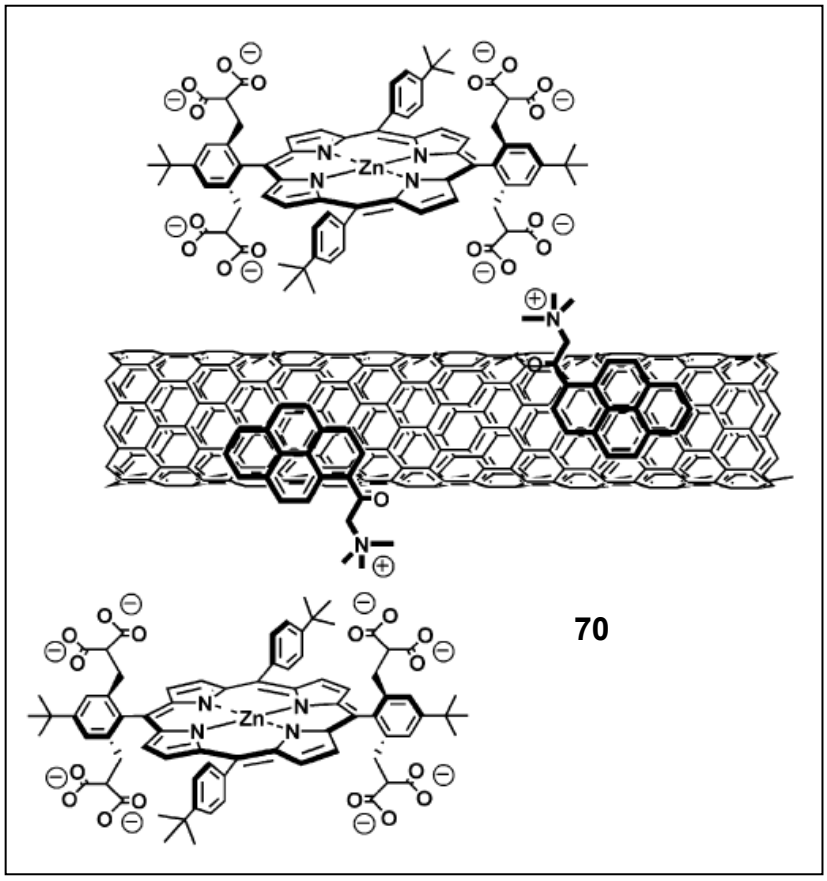

Figure 1.52: SWNT-($\pi-\pi$-interaction)-pyrene^{+}-electrostatic-ZnP nanohybrid (**70**) (*J. Am. Chem. Soc.* **2006**, *128*, 11222-11231)

Carbon nanotubes, SWNTs are functionalized with ionic head groups such as positively charged pyrene and negatively charged porphyrins via $\pi-\pi$, van der Waals and electrostatic interactions. Water soluble porphyrins (*i.e.*,

octapyridinium ZnP/H_2P salts or octacarboxylate ZnP/H_2P salts) have been used to form SWNT-($\pi-\pi-$interaction)-pyrene^{+}-electrostatic-ZnP/H_2P, or SWNT-($\pi-\pi$-interaction)-pyrene^{-}electrostatic-ZnP/H_2P electron-donor acceptor nanohybrids. These nanohybrids are characterized by absorption, fluorescence, TEM and AFM techniques. In absorption spectroscopy, the spectral behaviors such as red-shifted Soret- and Q-bands and formation of isobestic points are attributed to the interactions among three different chromophores, yielding a successful complex formation. Transient absorption studies revealed the formation of long-lived charge separated radical ion pairs with lifetimes that were in the range of microseconds.

Researchers have been approached another non-covalent functionalization of SWNT using pyrene appended nitrogenous bases through $\pi-\pi$ interactions followed by assembling the electron/energy donor molecules (Zn porphyrins, phthalocyanine and naphthalocyanines) *via* axial coordination. Chitta and coworkers reported noncovalent functionalization of SWNT which involved with functionalized pyrene to form soluble, $\pi-\pi$ interacting SWNT-pyrene conjugates[88]. Through the use of the imidazole ligand of the functionalized pyrene, ZnNc or ZnP was axially coordinated to yield ZnNc-ImPy-SWNT or ZnP-ImPy-SWNT nanohybrids. UV-visible-near IR spectra of dispersed solutions revealed the characteristic peaks of the SWNT from 700-1100 nm, which provided the evidence for the π-conjugated framework of SWNT. Furthermore, these nanohybrids are characterized by various physicochemical techniques

including TEM and electrochemical methods. Steady-state and time-resolved emission studies revealed efficient fluorescence quenching of the donor, ZnP and ZnNc entities in the nanohybrids. Direct evidence for the occurrence of electron transfer was obtained from the nanosecond transient absorption spectral studies, which provided spectral proof for the $ZnNc^{\bullet+}$-ImPy-$SWNT^{\bullet-}$ and $ZnP^{\bullet+}$-ImPy-$SWNT^{\bullet-}$ charge-separated states with lifetimes of 100-120 ns. The charge separation was further confirmed with the aid of an electron mediator, hexyl-viologen dication (HV^{2+}) and an electron shifter, 1-benzyl-1,4-dihydronicotinamide. As a result of the photoinduced processes, accumulation of the radical cation $HV^{\bullet+}$ was observed with nearly 70-90% yield thus demonstrating the importance of the present donor-acceptor nanohybrids in photocatalytic applications.

Another interesting non-covalent methodology is ammonium ion-crown ether self-assembly which is one of the powerful methods due to a high degree of directionality with binding energies up to 50-200 kJ mol^{-1}. Previously, we discussed the efficient selectivity of the four 18-crown-6 moiety appended porphyrin towards alkyl ammonium cation bearing fulleropyrrolidine based donor-acceptor supramolecular system for probing photoinduced electron transfer processes. This binding strategy is extended with porphyrin-carbon nanotube donor-acceptor nanohybrids to demonstrate the occurrence of photo-induced charge separation.

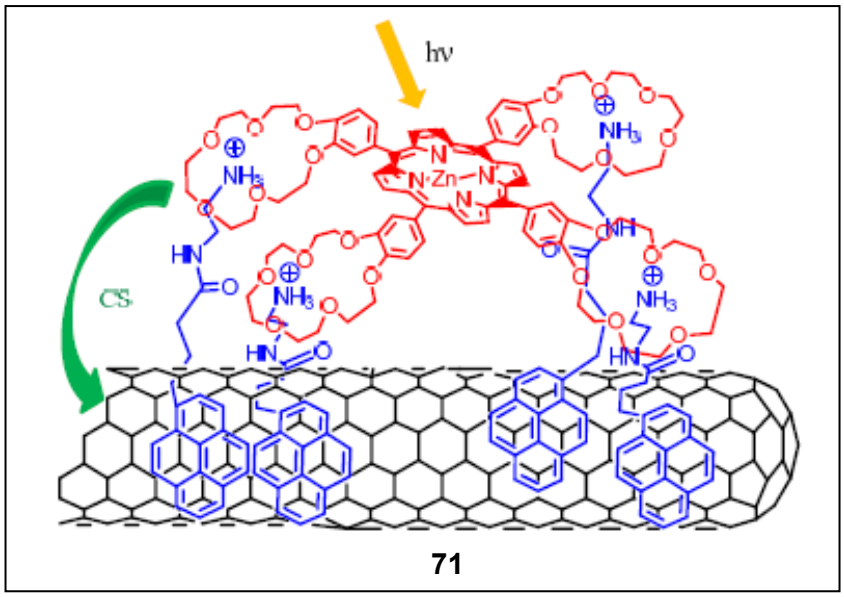

Figure 1.53: The construction of SWNT-Pyrene-ZnTCP hybrids (**71**) (*Chem. Euro. J*. **2007**, *13*, 8277)

The nanohybrids (**71**) were constructed by solubilizing carbon nanotubes by π–π stacking of pyrene functionalized with an alkyl ammonium cation, $PyrNH_3^+$-SWNT[89]. The alkyl ammonium cations of the soluble $PyrNH_3^+$-SWNT are self-assembled with donor porphyrin that contain one or four 18-crown-6 moieties via alkyl ammonium ion-crown ether interactions. The resulting crown porphyrin-pyrene-SWNT nanohybrids were stable and soluble in DMF.

Both steady-state and time-resolved emission studies revealed efficient quenching of the singlet excited state of the porphyrins and free-energy calculations suggested electron-transfer quenching. Furthermore, charge separation quenching process is supported by nanosecond transient absorption

spectral results. Charge-stabilization was also observed for the nanohybrids in which the lifetime of the radical ion pairs was around 100 ns. The present nanohybrids were further utilized to reduce HV^{2+} and to oxidize BNAH in solution in an electron-pooling experiment. Accumulation of the radical cation $HV^{\bullet+}$ was observed in high yields, which offers additional proof for the occurrence of photoinduced charge separation. This demonstrates that the ammonium ion–crown ether binding motif is a successful self-assembly method to build SWNTs bearing donor–acceptor nanohybrids and are useful for light-energy conversion and photovoltaic applications.

1.14.4 CNT as electron donors in donor–acceptor systems

Above supramolecular concept, crown ether-ammonium cation interaction, has also been extended with self-assembled single-wall carbon nanotube (SWNT)-fullerene-(C_{60}) hybrid with SWNT acting as an electron donor and fullerene as an electron acceptor for probing photoinduced electron transfer[90]. These nanohybrids were isolated and characterized by TEM, UV-visible-near IR, and electrochemical methods. The possibility of electron transfer from the carbon nanotube to the singlet excited fullerene in the SWNT/Pyr-NH_3^+/crown-C_{60} nanohybrids (**72** in Figure 1.54) was determined by free-energy calculations. Accordingly, steady-state and time-resolved fluorescence studies revealed efficient quenching of the singlet excited-state of C_{60} in the nanohybrids. Further studies involving nanosecond transient absorption studies confirmed electron

transfer to be the quenching mechanism, in which the electron-transfer product, fullerene anion radical, was possible to spectrally characterize. The rates of charge separation, k_{CS}, and charge recombination, k_{CR}, were found to be 3.46 x 10^9 and 1.04 x 10^7 s^{-1}, respectively. The calculated lifetime of the radical ion-pair was found to be over 100 ns, suggesting charge stabilization in the novel supramolecular nanohybrids.

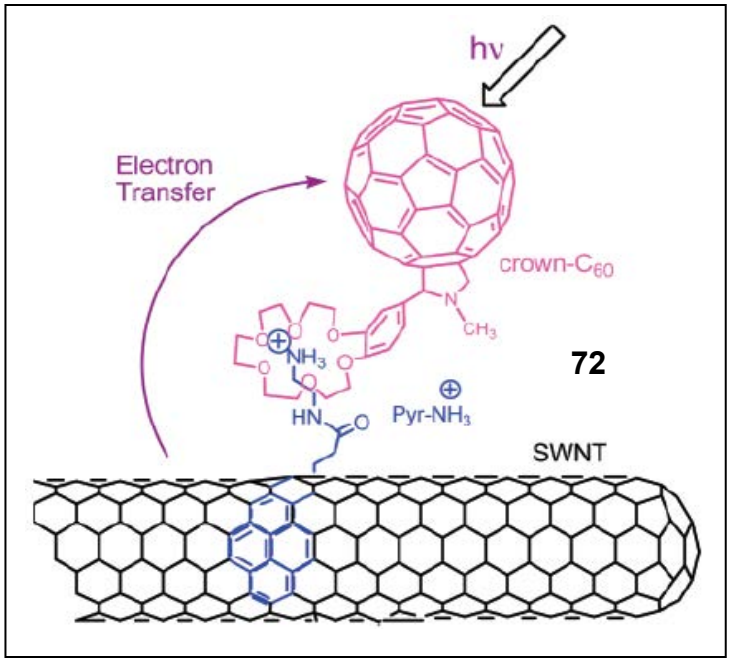

Figure 1.54: The self-assembly formation of SWNT-pyrene-$C_{60}NH_3^+$ (*J. Am. Chem. Soc.* **2007**, *129*, 15865)

1.15 Summary

Primary events of bacterial photosynthetic system, excitation energy transfer and photoinduced electron transfer are demonstrated for our understanding the process of bio-energetics which also holds promise for technological advances in solar energy conversion. Mimicking the –antenna - reaction center" functionality in photosynthesis by using bio-inspired synthetic model compounds is important to construct artificial model systems for harvesting solar energy. These photosynthetic model systems should have basic components to meet efficient energy/electron transfer processes. To get more insight about the photoinduced events, we have demonstrated the principles of photoindued energy and electron transfer processes and optimizing parameters for efficient transfer. Different synthetic methods are used to modulate the photoinduced events in donor–acceptor systems by connecting the donors and the acceptors covalently or noncovalently.

Recently developed self-assembled supramolecular donor–acceptor conjugates using porphyrins/phthalocyanines/naphthalocyanines as donors and fullerenes/carbon nanotubes as electron acceptors are illustrated for the mimicry of antenna, mimicry of reaction center and mimicry of "combined antenna-reaction center' functionalities in the natural photosynthetic system. Self-assemblies through $\pi-\pi$ interactions, ion-pairing, cation–dipole, and hydrogen bonding are demonstrated to accomplish energy and electron transfer events. These model examples illustrate that defined distance and orientation play vital

role to generate long-lived charge separated species, a key feature for light energy harvesting applications. Moreover, we explained strategies of engineering artificial photosynthetic charge separating systems by choosing suitable redox pairs and adjusting electronic coupling, free energy change and reorganization energy.

Extension of the self-assembly approaches to single wall carbon nanotubes (SWNT) results in SWNT–porphyrin/phthalocyanine nanohybrids capable of undergoing photoinduced electron transfer. SWNTs in these nanohybrids can act as both an electron acceptor and electron donor according to the positioning of the HOMO and LUMO levels of the photosensitizing partners. Finally, the results of donor-acceptor nanohybrids reveals that these hybrids could be used in photocatalysis to generate redox active products in addition of demonstrating fundamental photoinduced electron transfer events.

CHAPTER 2

MATERIALS AND PHYSICAL METHODS

This chapter presents a listing of all chemicals and solvents employed at various stages of research work. General procedures used for the purification of solvents and chemicals, general synthetic procedures employed for the syntheweses of porphyrin, fullerene derivatives and also control compounds are discussed here. Further, a brief discussion of the physicochemical techniques employed during the course of studies is presented here.

2.1 Materials:

Buckminsterfullerene, C_{60} (+99.95%) was from SES Research, (Houston, TX), The (6,5)- and (7,6)-enriched SWNTs were produced by CoMoCAT, SouthWest Nano Technologies, Inc. (Norman, OK), marketed by Aldrich Chemicals (Milwaukee, WI).

Aldehyde derivatives such as methyl-4-formylbenzoate, *p*-tolualdehyde, pyridine derivatives such as pyridine, 4-dimethylamino pyridine, 4-pyridine carboxaldehyde and imidazole derivatives, 2-(3-bromophenyl)-1,3-dioxolane, 2-[3-(1*H*-Imidazol-1-yl)phenyl-1,3-dioxolane, imidazole, crown ethers such as

benzo-15-crown-5 and benzo-18-crown, reagents such as pyrrole, 4-nitroaniline, boron tribromide (1M in CH_2Cl_2), boron trifluoride diethyletherate 1, 3-dicyclohexyl-carbodiimide, *p*-chloranil, zinc acetate hexahydrate, palladium carbon (5%), Cu powder, Fe powder, I_2, Br_2, CuCN, sodium methoxide, 2-(dimethylamino)ethanol, 4-hydroxy benzaldehyde, amino acids such as sarcosine and amino acid precursors such as ethylene diamine, benzyl 2-bromo acetate were purchased from Aldrich Chemicals (Milwaukee, WI).

Crown ether derivative, 4‘-aminobenzo-18-crown-6, N-terminal protected aminoacid, H-Lys(Boc)-OH, reagents such as (2-bromoethyl) amine, di-tert-butyl bicarbonate, thionyl chloride and Tetra-*n*-butylammonium perchlorate, (TBA)ClO_4, used for the electrochemical studies were purchased from Fluka chemicals and 1-pyrene butyric acid was purchased from Acros organics.

All the chromatographic materials silica gel, basic alumina and solvents *o*-dichlorobenzene, benzonitrile dichloromethane, chloroform, toluene, 1,4-dioxane, N,N-dimethylformamide, methanol were procured from Fisher Scientific and were used as received.

Propionic acid, acetic acid, acetic anhydride, trifluoroacetic acid hydrochloric acid, and sulfuric acid were from Fisher chemicals.

2.2 Synthesis of control compounds:

5,10,15,20-tetraphenylporphyrin (2a):

Compound **2a** was synthesized by a previously reported procedure.[96] In 200 ml of propionic acid, 18.9 mmol (2.0 g) of benzaldehyde and 18.9 mmol (1.26 g) of pyrrole were added. The solution was refluxed for 45 minutes and the solvent was removed under reduced pressure. The crude product was then washed several times with methanol and dissolved in minimum amount of $CHCl_3$/hexane 1:1 and loaded on a basic alumina column and eluted with $CHCl_3$/hexane 1:1. Yield: 1.74 g (15 %). ^{1}H NMR ($CHCl_3$-d): δ (in ppm) 8.85 (s, 8H, β-pyrrole), 8.13 (m, 6H ortho-phenyl *H*), 7.65 (m, 9H, meta and para-phenyl *H*) and -2.78 (s, br, 2H, imino *H*). UV-Vis (benzonitrile) (nm, log ε): 415 (5.43), 511.5 (4.15), 544 (3.82), 589 (3.71), 642 (3.59). FAB-mass (CH_3CN): 614.1 (614.7).

5,10,15,20-tetraphenylporphyrinatozinc(II), 2b:

Compound **2b** was synthesized by metallation of **2a** with zinc acetate. To 0.33 mmol (200 mg) of **2a** in $CHCl_3$, excess of zinc acetate in methanol was added.[33] The solution was stirred for 30 minutes and then concentrated and loaded on a basic alumina column and eluted with $CHCl_3$. Yield 0.21 g (93%). ^{1}H NMR ($CHCl_3$-d): δ (in ppm) 8.93 (s, 8H, β-pyrrole), 8.2 (d, 6H, ortho-phenyl *H*) and 7.74 (m, 9H, meta and para-phenyl *H*). UV-Vis

(benzonitrile) (nm, log ε): 418(5.38), 549(3.92), 618(3.42). FAB-mass (CH_3CN): 677.9 (678.1).

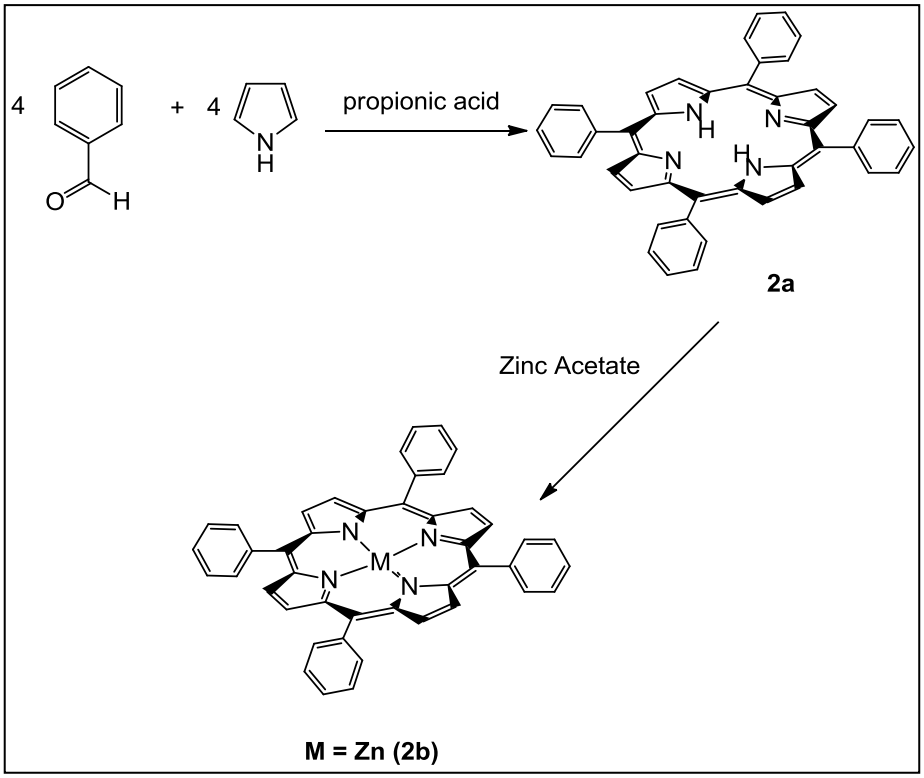

Scheme 2.1: Synthetic scheme adopted for compounds **2a** and **2b**

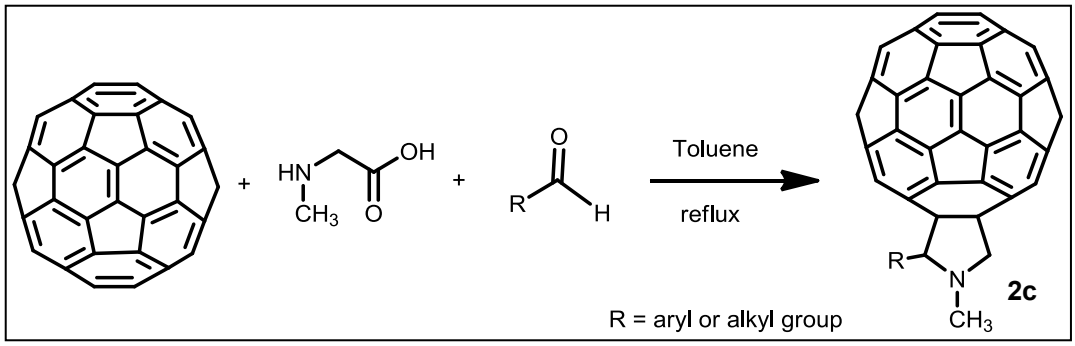

Scheme 2.2: General scheme for synthesis of fulleropyrrolidines

N-methyl-2-phenyl-3,4- fulleropyrrolidine (2c):

To a solution of C_{60} (100 mg, 0.14 mmol) in dry toluene (60 ml), sarcosine (29 mg, 0.26 mmol), and benzaldehyde (74 mg, 0.7 mmol) were added. The combined solution was refluxed for 5 h. At the end, the solvent was evaporated under reduced pressure. The solid was adsorbed on silica gel and purified over a silica gel column by using toluene as eluent. Yield: (25%). ^{1}H NMR (CS_2:$CDCl_3$ 1:1 (v/v)): δ (in ppm) 2.81, (s, 3H, N-methyl *H*), 4.82 (d, 1H, pyrrolidine *H*), 5.18 (d, 1H, pyrrolidine *H*), 5.83 (s, 1H, pyrrolidine *H*), 7.51, 7.35 (m, 3H, phenyl *H*), 7.88, 7.80 (d, 2H, phenyl *H*), UV-Vis (*o*-dichlorobenzene): 327.5 and 432 nm. FAB mass, cald. 853.7, found 854.0.

2.3 Physical methods

Instrumentation:

The UV-visible spectral measurements were carried out with a Shimadzu Model 1600 UV-visible spectrophotometer. The fluorescence emission was monitored by using a Spex Fluorolog-tau or Varian spectrometers. A right angle detection method was used. The ^{1}H NMR studies were carried out on a Varian 400 MHz or 300 MHz spectrometers. Tetramethylsilane (TMS) was used as an internal standard. Cyclic voltammograms were recorded on a EG&G Model 263A potentiostat using a three electrode system. A platinum button or glassy carbon electrode was used as the working electrode. A platinum wire served as the counter electrode and a Ag/AgCl was used as the reference electrode. Ferrocene/ferrocenium redox couple was used as an internal standard. All the solutions were purged prior to electrochemical and spectral measurements using argon gas.

The computational calculations were performed in collaboration with Dr Melvin E. Zandler, Wichita State University and Dr. Paul A. Karr, Wayne State College. These calculations were performed by DFT B3LYP/3-21G(*) methods with GAUSSIAN 98 or 03[99] software packages on various PCs and a SGI ORIGIN 2000 computer. The graphics of HOMO and LUMO coefficients were generated with the help of *GaussView* software. The ESI-Mass spectral analyses of the newly synthesized compounds were performed by using a

Fennigan LCQ-Deca mass spectrometer. For this, the compounds (about 1 mM concentration) were prepared in CH_2Cl_2, freshly distilled over calcium hydride.

Time-resolved Emission and Transient Absorption Measurements:

The time-resolved emission and transient absorption studies were performed in collaboration with Prof. Osamu Ito and Dr. Athula S. D. Sandanayaka, Tohoku University, Sendai, Japan, Dr. K. Ohkubo, Prof. S. Fukuzumi, Osaka University, Japan and Dr. Tatu Kumpulainen, Dr. Helge Lemmetyinen, Dr. Nikolai V. Tkachenko, Tampere University of Technology, Finland.

Femtosecond laser flash photolysis was conducted by using a lark MXR 2010 laser system and an optical detection system provided by Ultrafast Systems (Helios). The source for the pump and probe pulses were derived from the fundamental output of a Clarklaser system (775 nm, 1 mJ per pulse, fwhm= 150 fs) at a repetition rate of 1 kHz. A second harmonic generator introduced in the path of the laser beam provided laser pulses at λ=410 nm for excitation. The second harmonic was generated by using 95% of the fundamental output of the laser, whereas 5% of the deflected output was used for the generation of white light. Prior to generating the probe continuum, the laser pulse was fed to a delay line that provided an experimental time window of 1.6 ns with a maximum step resolution of 7 fs. The pump beam was attenuated at 5 mJ per pulse with a spot

size 2 mm in diameter at the sample cell where it was merged with the white probe pulse in a close angle (<10°). The probe beam, after passing through the 2 mm sample cell, was focused on a 200 mm fiber optic cable that was connected to a CCD spectrograph (Ocean Optics, S2000-UV/Vis for the visible region and Horiba, CP-140 for the NIR region) for recording the time-resolved spectra (λ=420–800 and 800–1200 nm). Typically, 5000 excitation pulses were averaged to obtain the transient spectrum at a set delay time. The kinetic traces at appropriate wavelengths were assembled from the time-resolved spectral data. Measurements of nanosecond transient absorption spectra were performed according to the following procedure: A deaerated solution that contained the dyad was excited by a Panther OPO pumped by an Nd:YAG laser (Continuum, SLII-10, 4–6 ns fwhm) at l=430 nm. The photodynamics were monitored by continuous exposure to a xenon lamp (150 W) as a probe light and a photomultiplier tube (Hamamatsu 2949) as a detector. Transient spectra were recorded by using fresh solutions in each laser excitation. The solution was deoxygenated by purging with argon for 15 min prior to measurements being recorded.

Up-conversion instrument (FOG-100, CDP Corp.) for time-resolved fluorescence was used to detect the fast processes with a time resolution of ~200 fs. The primary Ti:sapphire generator (TiF-50, CDP Corp.) was pumped by Nd CW laser (Verdi-6, Coherent Inc.), and a second harmonic (~410 nm) was used to excite the sample solution in a rotating cuvette. Emission from the sample was

collected to a nonlinear crystal (NLC), where it was mixed with the so-called gate pulse, which was the laser fundamental. The signal was measured at a sum frequency of the gate pulse and the selected emission maximum of the sample. The gate pulses were passed through a delay line so that it arrived at NLC at a desired time after sample excitation. The emission decay curve of the sample was detected by scanning through the delay line. Pump-probe and up-conversion techniques for time-resolved absorption and fluorescence, respectively, were used to detect the fast processes with a time resolution shorter than 0.2 ps.

Transmission Electron Microscopy (TEM) studies

Transmission electron microscopy studies were performed in collaboration with Dr. Athula S. D. Sandanayaka and Prof. Osamu Ito, Tohoku University, Sendai, Japan. Transmission electron micrograph (TEM) measurements were recorded by applying a drop of the sample to a copper grid. Images were recorded on a Hitachi H-7650 TEM at an accelerating voltage of 120 kV. A TEM equipped with EDX (H-2300, Hitachi) was operated at 120 kV, and the elemental map was obtained by using a scanning spot size of 0.5 nm and a scanning rate of 0.5 nm/ms.

Raman Spectroscopy studies

Raman spectroscopy measurements were performed using a Tokyo Instruments Nanofinder 30) with three different laser excitations, namely, λ = 441.6 (HeCd), 532.0 (Nd:YAG), and 632.8 nm (HeNe), and the laser spot size was about 2 mm in diameter.

Photoelectrochemical Studies

Photoelectrochemical measurements were carried out with the help of Navaneetha Krishnan. These studies were performed in a standard two-compartment cell consisting of a working electrode and a Pt wire gauze counter electrode in the electrolyte. The electrolyte was 0.5 M LiI and 0.01 M I_2 in acetonitrile. In the case of incident photon-to-current conversion efficiency (IPCE) measurement, a monochromator (SM-25, Bunkoh-Keiki Co., Ltd.) was introduced into the path of the excitation beam (300-W xenon lamp, Bunkoh-Keiki Co., Ltd.) for the selected wavelength. The lamp intensity at each wavelength was determined by using a Si photodiode (Hamamatsu Photonics S1337-1010BQ) and corrected.

2.4 Summary

In summary, free-base, zinc tetraphenylporphyrin and fullerene derivatives and naotube were successfully prepared and characterized by proton NMR and ESI-Mass spectroscopy. These compounds are used as control compounds in later chapters. Further characterization is carried out by using optical absorption, emission, photochemical and electrochemical methods. In computational studies, B3LYP/3-21G* basis set is used to visualize the geometry and electronic structure of the donor-acceptor hybrids. TEM and Raman spectroscopic studies are performed for characterization of donor-acceptor nanohybrids. Finally, photoelectrochemical studies are carried out to measure IPCE for fabricated films of zinc tatrapyrene prophyrin appended semiconducting nanotubes.

CHAPTER 3

Photo-induced Energy Transfer in Donor-Accepor Conjugates

(A) Ultrafast Singlet-Singlet Energy Transfer in Self-Assembled via Metal-Ligand Axial Coordination Free-Base Porphyrin-Zinc Phthalocyanine and Free-base Porphyrin-Zinc Naphthalocyanine Dyads

3.1 Introduction

In artificial photosynthesis two photoinduced events are mainly targeted, viz., excitation energy transfer to mimic the antenna functionality, and electron transfer to mimic reaction center functionality.[2,91,92] Several strategies have been employed to mimic the natural energy transfer process, including covalently linked dyads and polyads, polymers, dendrimers and self-assembled systems. In these model compounds, successful excitation energy transfer from donor to the acceptor entities has been demonstrated. In the majority of these studies porphyrins and phthalocyanines have been used as energy/electron donor/acceptor due to their close resemblance to the photosynthetic pigment, chlorophyll, and the established synthetic methodologies.

Self-assembly via metal-ligand axial coordination is one of the successful approaches developed to study photoinduced electron transfer in donor-acceptor

dyads. However, utilization of this strategy to build dyads comprised of different donor and acceptor fluorophores to mimic the natural energy transfer process has not been fully explored. This has been accomplished in the present study by constructing donor-acceptor dyads using free-base porphyrin as energy donor and zinc phthalocyanine (ZnPc) as energy acceptor via axial ligand coordination. Further, zinc naphthalocyanine (ZnNc), a phthalocyanine structural analog, having absorption and emission well into near-IR region has been utilized to verify energy transfer from singlet excited porphyrin to a near-IR emitting fluorophore. To achieve axial coordination, free-base porphyrin has been functionalized with an imidazole entity at the ortho, meta or para positions of one of the *meso*-aryl groups (see Figure 3.1). The different substitution is expected to result in dyads of different orientations. Photochemical studies using both steady-state and time-resolved transient absorption techniques have been performed to probe efficiency and kinetics of excitation energy transfer in the newly formed dyads.

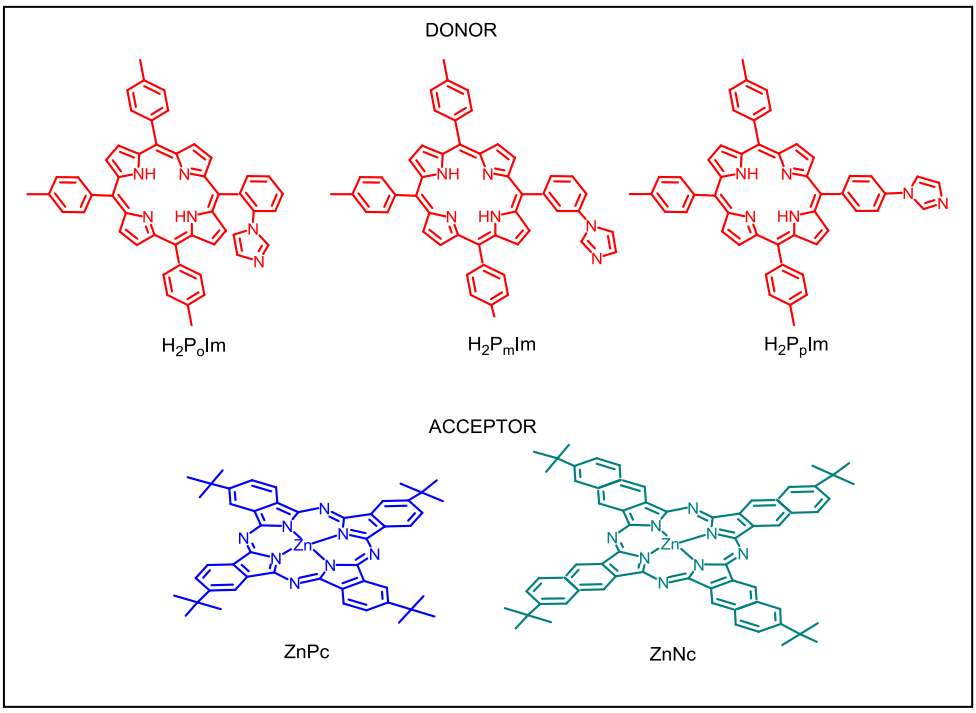

Figure 3.1: Structure of the donors and acceptors employed in the present study to probe excitation energy transfer.

3.2 Experimental Section

Syntheses

2-[3-(1*H*-Imidazol-1-yl)phenyl]-1,3-dioxolane (3m). Imidazole (0.01 mol) was added to a suspension of sodium hydride (0.01 mol) in 10 mL of DMF. The resulting solution was stirred at room temperature for 20 min. Next, 2-(3-bromophenyl)-1,3-dioxolane (0.01 mol) and copper powder (0.001 mol) were added to the reaction mixture which was refluxed for 5 h. The mixture was cooled to room temperature, chloroform and water were added, and the mixture was

stirred for 2 h and filtered. The filtrate was washed with water and dried over sodium sulfate. The solvent was evaporated under reduced pressure. The compound was purified over a flash silica gel column using CH_2Cl_2/MeOH (95:5 v/v) as eluent. ^{1}H NMR (400 MHz, $CDCl_3$): δ 3.80-4.05 (m, 4 H), 5.68 (s, 1H), 7.05-7.38 (m, 6 H), 7.72 (s, 1H). Mass (APCI mode in CH_2Cl_2): calcd, 184.3; found [M + 1] 185.1.

3-(1*H*-Imidazol-1-yl)benzaldehyde (4m). 2-[3-(1*H*-Imidazol-1-yl)phenyl-1,3-dioxolane was stirred at room temperature for 3 h in 20 mL of 1 M HCl. Aqueous $NaHCO_3$ was added to the reaction and extracted with ethyl acetate. The organic layer was washed with aqueous NaCl, dried over Na_2SO_4, and evaporated under reduced pressure to obtain the product as a pale yellow solid. ^{1}H NMR (400 MHz, $CDCl_3$): δ 7.25 (s, 1H), 7.36 (s, 1H), 7.67-7.72 (m, 2H), 7.87-7.97 (m, 3H), 10.08 (s, 1H). Mass (APCI mode in CH_2Cl_2): calcd, 172.18; found 173.0.

5-[3′-(1*H*-Imidazol-1-yl)phenyl]-10,15,20-tritolylporphyrin (5m). Compound **5m** was synthesized by reacting **4m** (450 mg, 2.6 mmol), toylaldehyde (7.8 mmol), and pyrrole (10.5 mmol) in refluxing propionic acid. The crude product was purified on a basic alumina column with chloroform/methanol (95:5 v/v) as eluent. ^{1}H NMR (400 MHz, CDCl3): δ -2.79 (s, 2H), 2.78 (s, 9H), 7.05 (d, 1H), 7.37 (s, 1H), 7.55 (d, 6H), 7.78-7.85 (m, 3H), 8.15 (d, 6H), 8.18 (s, 1H), 8.30 (d, 1H), 8.80-8.91 (m, 8H). Mass (APCI mode in CH_2Cl_2): calcd, 722.88; found [M + 1] 723.6.

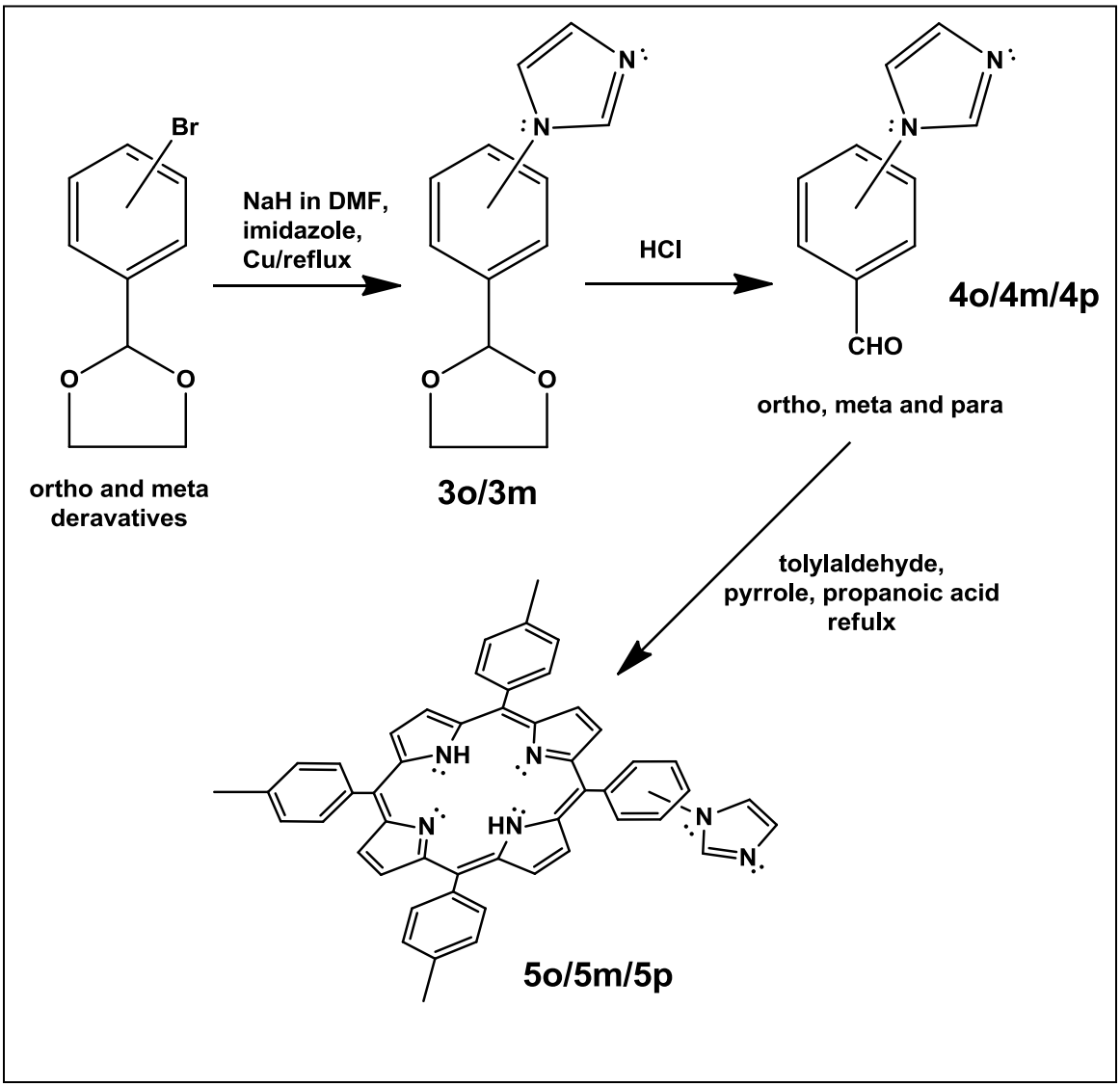

Scheme 3.1: Synthetic scheme for ortho, meta and para substituted imidazole groups to free base porphyrin

2-[2-(1*H*-Imidazol-1-yl)phenyl]-1,3-dioxolane (3o). Imidazole (0.01 mol) was added to a suspension of sodium hydride (0.01 mol) in 10 mL of DMF. The resulting solution was stirred at room temperature for 20 min. Next, 2-(3-bromophenyl)-1,3- dioxolane (0.01 mol) and copper powder (0.001 mol) were added to the reaction mixture which was refluxed for 4 h. The mixture was cooled to room temperature, chloroform and water were added, and the mixture was stirred for 2 h and filtered. The filtrate was washed with water and dried over sodium sulfate. The solvent was evaporated under reduced pressure. The compound was purified over flash silica gel column using CH_2Cl_2/MeOH (96:4 v/v) as eluent. ^{1}H NMR (400 MHz, $CDCl_3$): δ 3.75-4.00 (m, 4 H), 5.35 (s, 1H), 7.01 (s, 1 H), 7.10-7.60 (m, 6H). Mass (APCI mode in CH_2Cl_2): calcd, 184.3; found [M + 1] 185.1.

2-(1*H*-Imidazol-1-yl)benzaldehyde (4o)[96b] 2-[3-(1*H*-Imidazol-1-yl)phenyl-1,3-dioxolane was stirred at room temperature for 3 h in 20 mL of 1 M HCl. Aqueous $NaHCO_3$ was added to the reaction and extracted with ethyl acetate. The organic layer was washed with aqueous NaCl, dried over Na_2SO_4, and evaporated under reduced pressure to obtain the product as a pale yellow solid. ^{1}H NMR (400 MHz, $CDCl_3$): δ 7.00-7.45 (m, 3H), 7.55 (m, 2H), 7.81 (dd, 1H), 9.58 (s, 1H). Mass (APCI mode in CH_2Cl_2): calcd, 172.18; found [M + 1] 173.1.

5-[2′-(1*H*-Imidazol-1-yl)phenyl]-10,15,20-tritolylporphyrin (5o). Compound **5o** was synthesized by reacting **4o** (452 mg, 2.6 mmol), toylaldehyde (7.8 mmol), and pyrrole (10.5 mmol) in refluxing propionic acid. The crude product was purified on a basic alumina column with chloroform/methanol (95:5 v/v) as eluent. ^{1}H NMR (400 MHz, $CDCl_3$): δ -2.79 (s, 2H), 2.72 (s, 9H), 7.01 (d, 1H), 7.55 (d, 6H), 7.70-7.89 (m, 4H), 8.15 (d, 6H), 8.18 (s, 1H), 8.30 (d, 1H), 8.80-8.91 (m, 8H). Mass (APCI mode in CH_2Cl_2): calcd, 722.8; found [M + 1] 723.8.

5-[4′-(1*H*-Imidazol-1-yl)phenyl]-10,15,20-tritolylporphyrin (5p). Compound **3c** was synthesized by reacting 4-(1*H*imidazol-1-yl)benzaldehyde (450 mg, 2.6 mmol), tolualdehyde (7.8 mmol), and pyrrole (10.5 mmol) in refluxing propionic acid. The crude product was purified on a basic alumina column with chloroform/methanol (95:5 v/v) as eluent. ^{1}H NMR (400 MHz, $CDCl_3$): δ -2.79 (s, 2H), 2.75 (s, 9H), 7.01 (d, 1H), 7.38 (d, 2H), 7.55 (d, 6H), 7.78 (d, 2H), 8.15 (d, 6H), 8.18 (s, 1H), 8.30 (d, 1H), 8.80-8.91 (m, 8H). Mass (APCI mode in CH_2Cl_2): calcd, 722.8; found [M + 1] 723.8.

3.3 Results and discussion

Optical Absorbance Studies

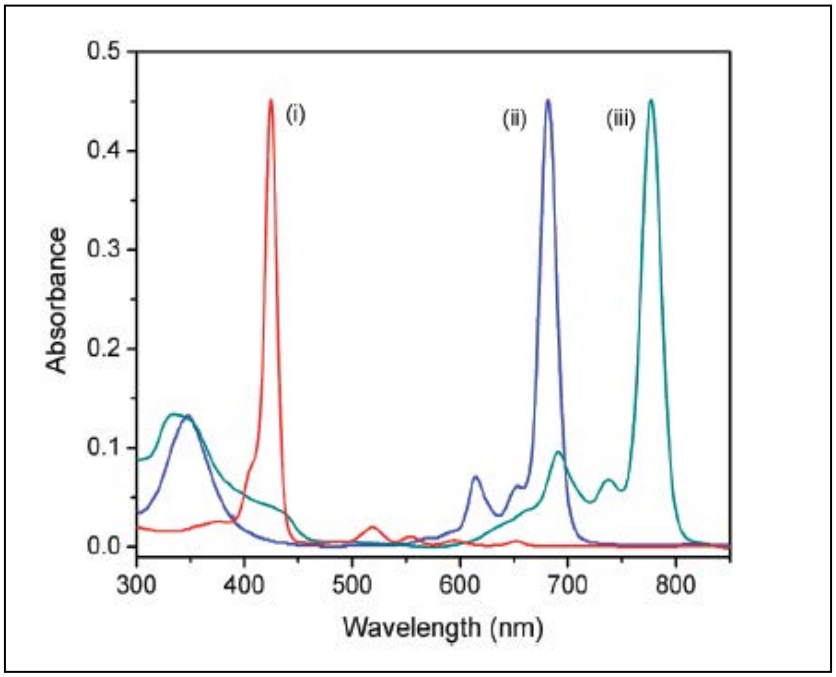

Figure 3.2: Absorption spectra of (i) H_2P_oIm, (ii) ZnPc, and (iii) ZnNc in DCB, normalized to their most intense bands. The concentrations are in the range of 5-10 μM.

Figure 3.2 shows the optical absorption spectra of H_2P_oIm, ZnPc, and ZnNc derivatives in *o*-dichlorobenzene (DCB), normalized to their most intense absorption bands. The absorption spectrum of H_2PmIm and H_2PpIm were found to be similar to that of H_2P_oIm with an intense Soret at 424 and four visible bands at 518, 553, 594, and 652 nm. The spectrum of ZnPc exhibited bands at 348, 614, 653, and 681 nm while the spectrum of ZnNc revealed peaks at 335, 690,

737, and 777 nm, respectively; that is, the spectrum of ZnNc is stretched well into the near-IR region. Importantly, the H_2PIm band at 518 nm had no overlap with the absorption bands of either ZnPc or ZnNc, providing the possibility for selective excitation of the donor, free-base porphyrin.

Figure 3.3 and 3.4 show absorption spectral changes recorded during increasing addition of H_2P_pIm to the solutions of ZnPc and ZnNc, respectively. Similar spectral changes were observed for H_2P_oIm and H_2P_mIm binding to the acceptor zinc macrocycles. The binding of H_2P_pIm to ZnPc was characterized by diminished intensity of 614 and 681 nm bands with isosbestic points at 609, 663, and 672 nm, indicating existence of only one equilibrium process in solution. Similarly the binding of H_2P_pIm to ZnNc was characterized by diminished intensity of 690, 737, and 777 nm bands with 2-4 nm blue shifts (Figure 3.4). Isosbestic points were also observed at 665, 686, 731, and 750 nm, indicating existence of only one equilibrium process in solution. Plots of method of continuous variation confirmed 1:1 complex formation between the donor and acceptor entities. The formation constants, *K*, for H_2PIm binding to ZnPc and ZnNc were obtained from the absorption spectral data using the Benesi-Hildebrand method[93] (Figure 2a and 2b insets) and are listed in Table 3.1.

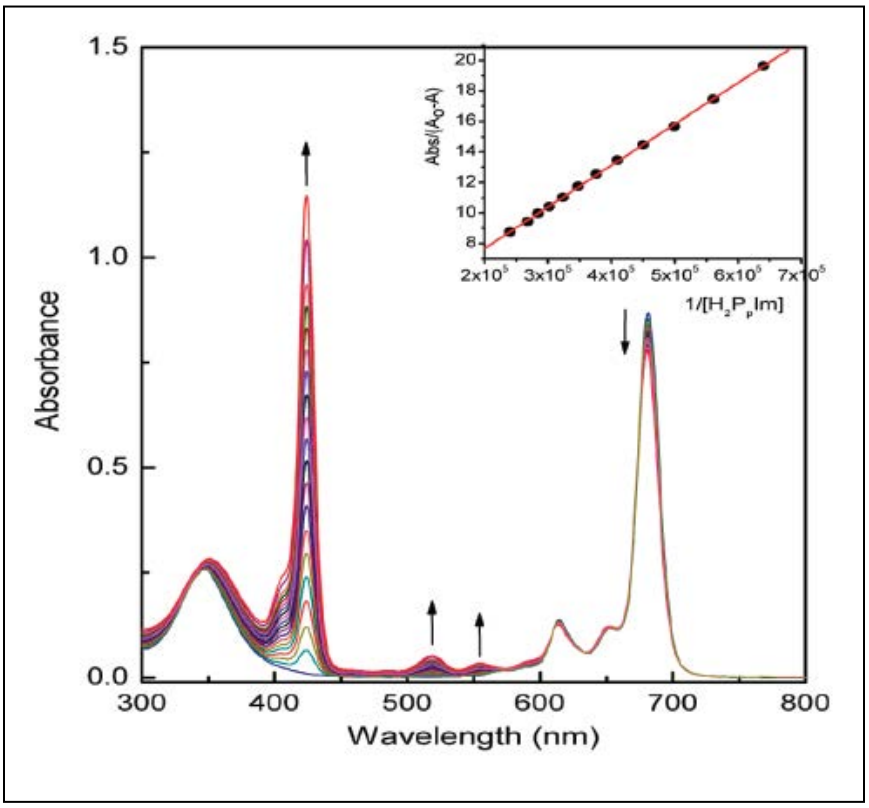

Figure 3.3: UV-visible-near IR spectral changes observed during increasing addition of H_2P_pIm (0.1 equiv) to a solution of ZnPc (0.11 mM) in DCB. The figure insets show Benesi-Hildebrand plots constructed to obtain the binding constants. The absorption changes of the 681 nm band of ZnPc was utilized.

The magnitude of the *K* values suggests stable complex formation. The *K* values follow the trend: para ~ meta > ortho of imidazole substitution on the phenyl ring of porphyrin macrocycle for a given zinc macrocycle binding, a trend that could be easily attributed to the steric constraints of the ortho substituted porphyrin derivative. Additionally, binding constants for ZnNc were found to be 2-

3 times higher than that obtained for the corresponding ZnPc binding. This could be attributed to the electron-rich ZnNc macrocycle compared to ZnPc macrocycle as revealed by their electrochemical oxidation potentials, discussed in the next section.

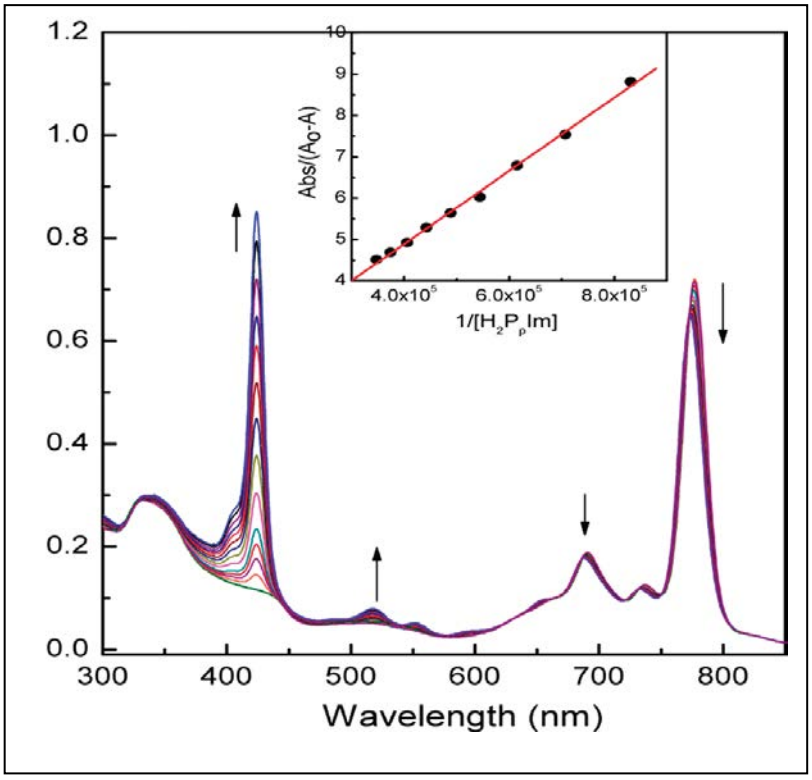

Figure 3.4: UV-visible-near IR spectral changes observed during increasing addition of H_2P_pIm (0.1 equiv) to a solution of ZnNc (0.11 mM) in DCB. The figure insets show Benesi-Hildebrand plots constructed to obtain the binding constants. The absorption changes of the 776 nm band of ZnNc were utilized.

Electrochemical Studies

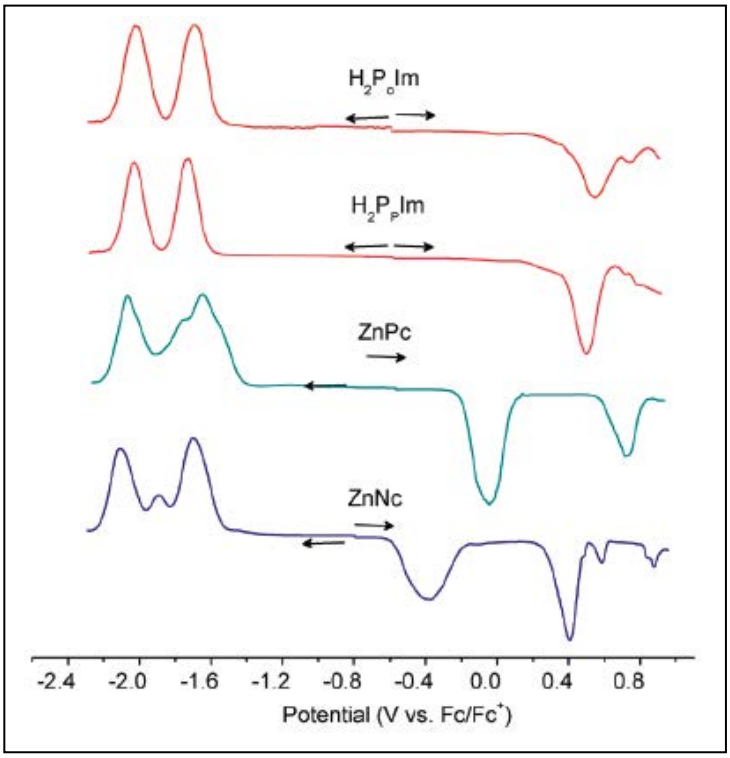

Figure 3.5: Differential pulse voltammograms of the investigated compounds (~0.5 mM) in DCB containing 0.1 M (TBAP)ClO_4. DPV conditions: scan rate) 20 mV/s, pulse width) 50 ms, step time) 100 ms, and pulse height) 0.025 V.

Differential pulse voltammetric studies (DPV) were performed to evaluate the oxidation and reduction potential of the investigated donor-acceptor entities. The first reversible oxidation and first two reversible reductions of H_2P_oIm were located at 0.55 V, and -1.67 and -2.02 V vs Fc/Fc^+ in 0.1M (TBA)ClO_4, respectively. For H_2P_mIm and H_2P_pIm, the first reduction was shifted in the negative direction by 50-60 mV while the first oxidation was anodically shifted by

40 mV (see Figure 3.5). The first oxidation of ZnPc and ZnNc were overlapping two one-electron processes. The peak potential were located at -0.05 V vs -0.38 V vs Fc/Fc^{+}, respectively, for ZnPc and ZnNc. That is, these compounds revealed easier oxidations compared to the free-base porphyrins used in the present study. The first reduction peaks of ZnPc and ZnNc were located at -1.65 and -1.70 V vs Fc/Fc^{+}, indicating these to be poor electron acceptors (vide infra).

DFT B3LYP/3-21(*) Computational Studies.

Since the relative orientation of the donor and acceptor dipoles in the dyads is crucial for energy transfer efficiency, the structures of the supramolecular dyads were visualized by performing computational studies at the B3LYP/3-21G(*) level.[94,95] Figure 3.6 and 3.7 show the structures of the dyad optimized on a Born-Oppenheimer potential energy surface. The two macrocyclic rings of the H_2P_oIm:ZnPc and H2P_oIm:ZnNc dyads were found to be in a skipped coplanar arrangement while for the meta and para imidazole derivatized dyads, H_2PIm:ZnPc and H_2PIm: ZnNc, they were positioned at an angle less than 90°. The edge-to-edge distances, center-to-center distances, and angles between the two macrocycle planes of the donor-acceptor entities are listed in Table 3.1.

Dyad[a]	K mol^{-1}, [b]	Center-to-center distance, Å	Edge-to-edge distance, Å	Angle between rings	HOMO-LUMO gap, eV
H_2P_oIm:ZnPc	4.20 x 10^4	7.4	5.75	46	2.09
H_2P_mIm:ZnPc	3.50 x 10^4	10.7	6.11	35	2.11
H_2P_pIm:ZnPc	8.23 x 10^4	13.0	8.83	56	2.08
H_2P_oIm:ZnNc	6.60 x 10^4	8.06	5.75	35	1.79
H_2P_mIm:ZnNc	1.48 x 10^5	12.1	9.96	55	1.78
H_2P_pIm:ZnNc	1.53 x 10^5	13.0	9.22	55	1.82

[a]-see Chart 1 for the structure of different donor and acceptor entities; in DCB at room temperature. [b]-Error = $\pm$10%

Table 3.1: Binding constants, K and B3LYP/3-21G(*) computed results for dyads formed by binding imidazole appended free-base porphyrin to zinc phthalocyanine or zinc naphthalocyanine.

Generally, the distances varied as follows: ortho < meta < para imidazole-substituted porphyrins. That is, a closer distance and skipped coplanar configuration for the ortho derivatives, and a relatively longer distance and near-orthogonal configuration for the meta and para substituted derivatives, were

observed. The frontier orbitals, HOMO and LUMO, were also evaluated for both types of dyads, and the representative orbitals for selected dyads are shown in Figure 3.6 and 3.7. It is important to note that the HOMO for all of the studied dyads was fully localized on the ZnPc or ZnNc macrocycles while the LUMO was located on the porphyrin macrocycle. In conjunction with the earlier discussed electrochemical results, these results point out that electron transfer from the excited free-base porphyrin to either the coordinated ZnPc or ZnNc is less likely to take place. The gas-phase HOMO-LUMO gap is found to be smaller by ~300 mV for the H_2PIm:ZnNc series of dyads compared to the H_2PIm ZnPc series of dyads, a result that readily agrees with the electrochemical results.

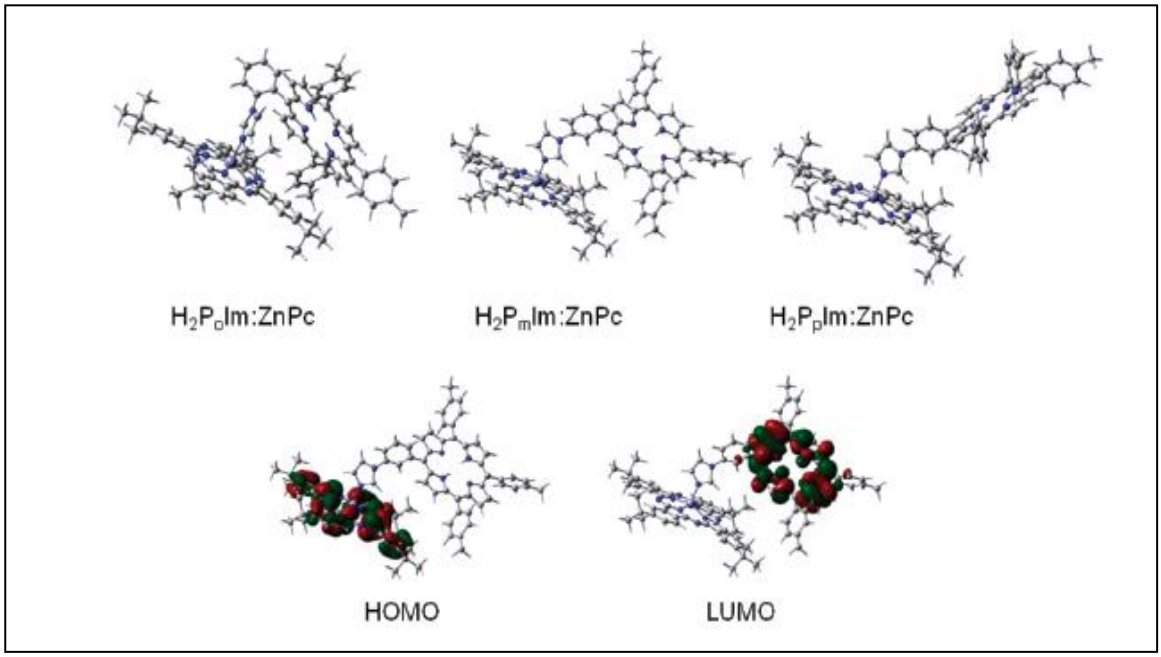

Figure 3.6: B3LYP/3-21G(*) optimized structures of the dyads formed via axial coordination of H_2PIm (ortho, meta, or para) to ZnPc.

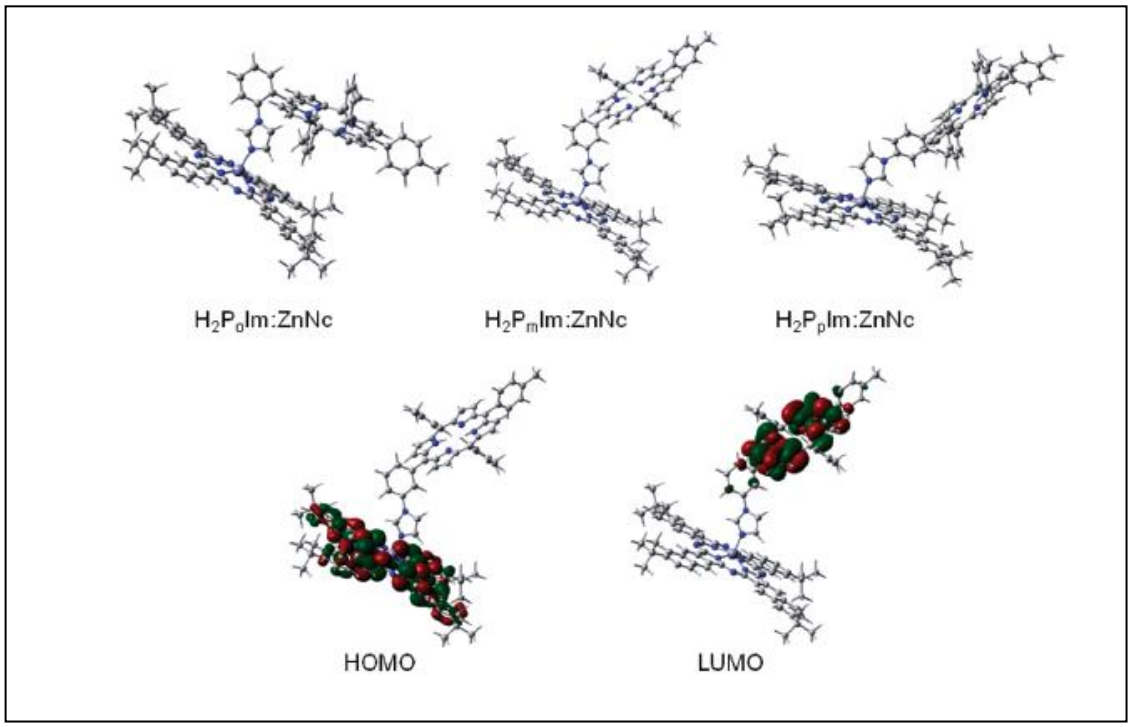

Figure 3.7: B3LYP/3-21G(*) optimized structures of the dyads formed via axial coordination of H_2PIm (ortho, meta, or para) to ZnNc.

Using the electrochemical, computational, and excited energy data, the free energies of charge-separation (ΔG_{CS}) were calculated using eq 1 by Weller's approach.[96]

$$- \Delta G_{CS} = \Delta E_{0\text{-}0} - e(E_{ox} - E_{red}) + \Delta G_S \qquad \textbf{(3.1)}$$

where

$\Delta E_{0\text{-}0}$ is the energy of the lowest excited state of H_2P (1.89 eV),

$\Delta G_S = -e^2/(4\pi\ \varepsilon_0\ \varepsilon_R\ R_{Ct\text{-}Ct})$, and ε_0 and ε_R refer to vacuum permittivity and dielectric constant of DCB.

The calculations revealed ΔG_{CS} values to be endothermic by 0.1-0.2 eV for electron transfer from the singlet excited freebase porphyrin to either ZnPc or ZnNc, suggesting the less likely occurrence of such reactions in the studied dyads.

Fluorescence Emission Studies

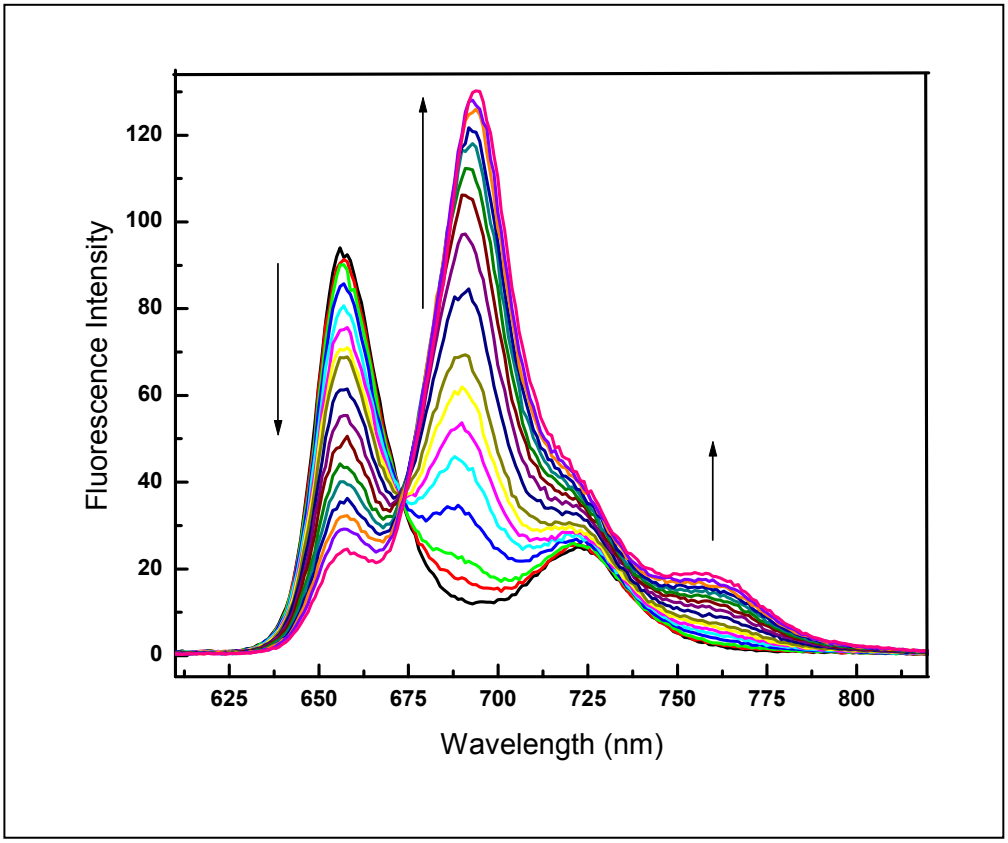

Figure 3.8: Steady-state fluorescence spectra of H_2P_pIm (1.2×10^{-4} M) upon increasing addition of ZnPc in DCB, excited at 518 nm.

As pointed out earlier, excitation of the donor, H_2PIm, at 518 nm to a large extent selectively excites the free base porphyrin, thus allowing us to monitor energy transfer to the acceptor, ZnPc or ZnNc entities, without them being directly getting excited. Figure 3.8 and 3.9 show the spectral changes observed for H_2P_pIm emission during increasing addition of ZnPc and ZnNc in DCB. The emission band of H_2P_pIm located at 655 nm revealed quenching with simultaneous appearance of new emission bands at 694 and 758 nm corresponding to ZnPc (Figure 3.8), and 782 and 820 nm corresponding to ZnNc (Figure 3.9). Similar results were obtained when H_2P_mIm and H_2P_oIm were titrated with either ZnPc or ZnNc.

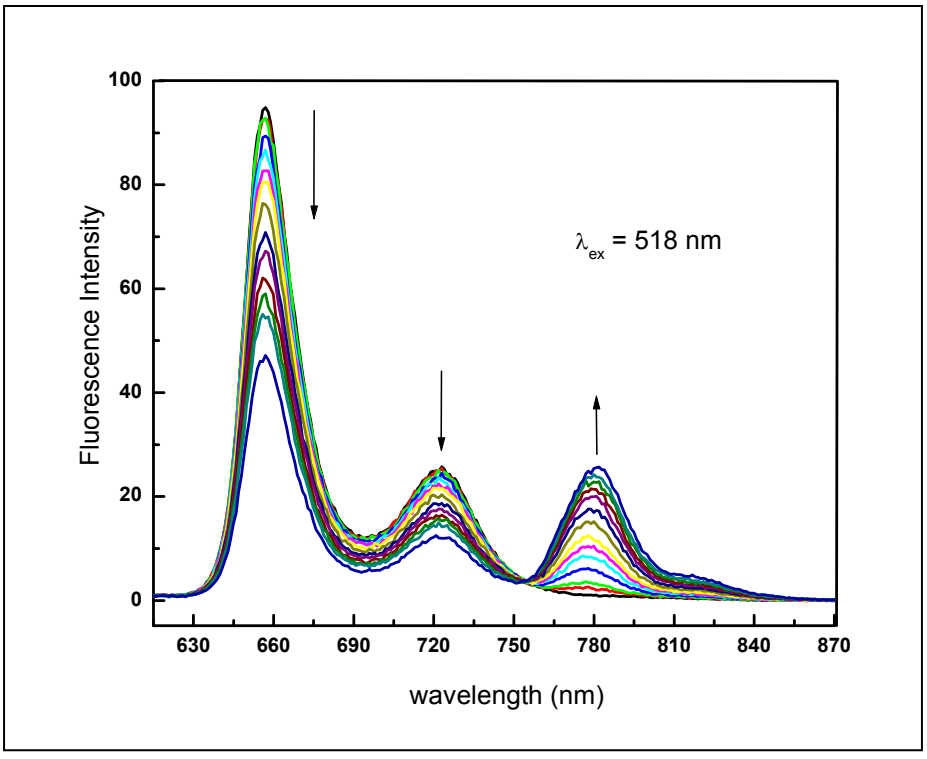

Figure 3.9: Steady-state fluorescence spectra of H_2P_pIm (1.2×10^{-4} M) upon increasing addition of ZnNc in DCB, excited at 518 nm.

Further, the excitation spectra of the dyads were recorded by holding the excitation wavelength at 758 for ZnPc and 782 for ZnNc. Such spectra revealed absorption bands corresponding to both donor and acceptor entities. In a control experiment, free-base *meso* tetraphenylporphyrin, H_2TPP, was also titrated with the acceptor molecules. Under these conditions, only a slight increase of the acceptor emission in the near-IR region was observed. These results confirm occurrence of singlet-singlet energy transfer in the self-assembled dyads.

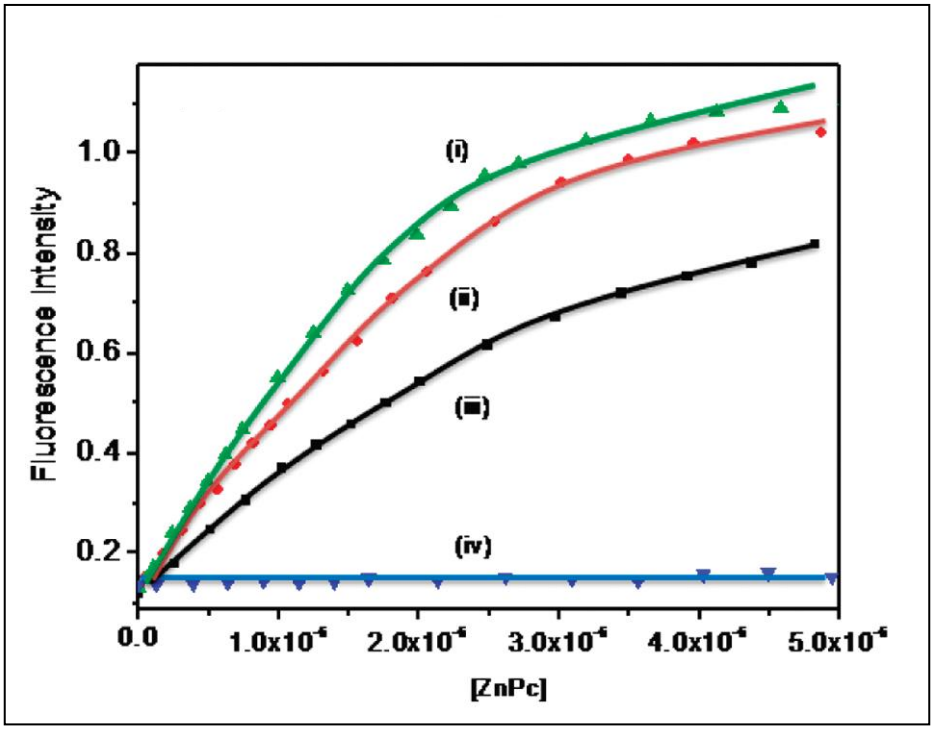

Figure 3.10: Emission intensities of ZnPc monitored at 758 nm for the titration involving (i)H_2P_pIm, (ii) H_2P_mIm, (iii) H_2P_oIm, and (iv) H_2TPP, demonstrating the extent of energy transfer efficiency.

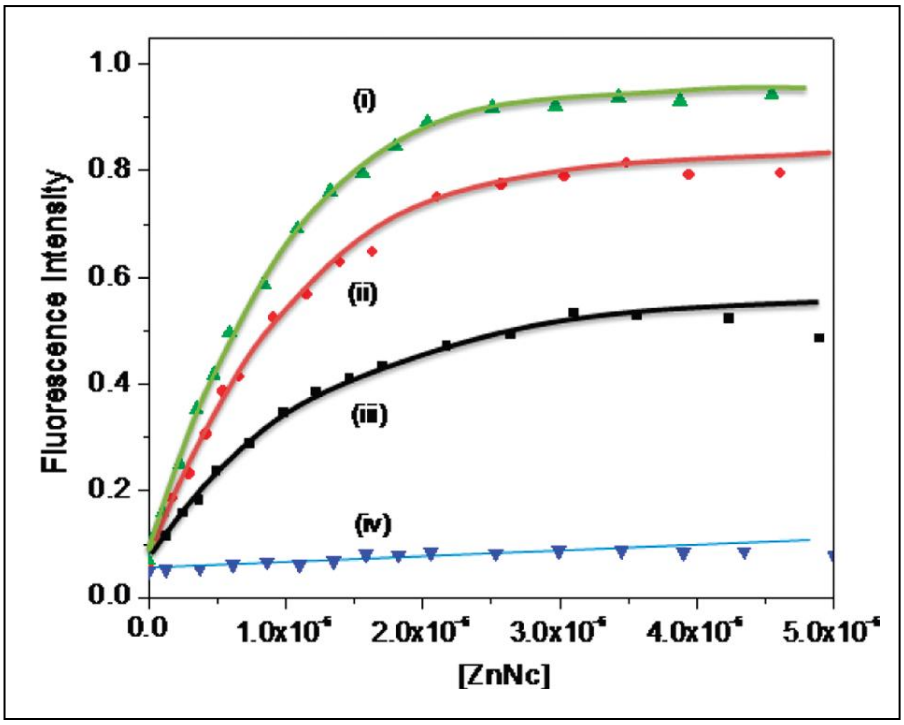

Figure 3.11: Emission intensities of ZnNc monitored at 781 nm for the titration involving (i)H_2P_pIm, (ii) H_2P_mIm, (iii) H_2P_oIm, and (iv) H_2TPP, demonstrating the extent of energy transfer efficiency.

Figure 3.10 and 3.11 shows the extent of energy transfer for each of the porphyrin derivatives upon increasing addition of ZnPc and ZnNc, respectively. It is clear from these plots that after addition of about 3-4 equiv of the acceptor entities, the energy transfer has attained its maximum value. Further, the extent of energy transfer followed the order: H_2P_pIm > H_2P_mIm > H_2P_oIm >> H_2TPP according to their binding constants. The latter plots for H_2TPP interactions being virtually horizontal imply occurrence of little or no energy transfer.

Excited State Energy Transfer: Theoretical Consideration

The observed excitation energy transfer (EET) could occur either via Dexter's exchange mechanism or Forster's dipole-dipole mechanism. The former mechanism requires the presence of electronic communication between the donor and acceptor species (via orbital overlap)[9]. However, the frontier orbitals from the DFT studies (Figure 3.6 and 3.7) in conjunction with the spectroscopic studies reveal that such intramolecular interactions are almost nonexistent. Therefore, the results of the present study have been analyzed according to Forster's mechanism. According to this mechanism, the rate of excitation energy transfer, $k_{Forster}$, is given by equation (3.2).

$$k_{Forster} = \frac{8.8 \times 10^{-25}\ \kappa^2\ \phi_D\ J_{Forster}}{n^4\ \tau_D\ R_{DA}^{\ 6}} \qquad \textbf{(3.2)}$$

where n is the solvent refractive index, Φ_D and τ_D are the fluorescence quantum yield (= 0.12) and the fluorescence lifetime of the isolated donor (free-base porphyrin), $J_{Forster}$ is the Forster overlap integral representing the emission of the donor and absorption of the acceptor ZnPc or ZnNc, and R is the donor-acceptor center-to-center distance (Table 3.1).

The τ values measured using a strobe technique were found to be 11.50, 9.95, and 9.45 ns, respectively, for the ortho, meta, and para imidazole-derivatized free-base porphyrins, values close to those reported for free-base

tetraphenylporphyrins in the literature[13,14]. In eq 3.2, κ^2 is the orientation factor as described in eq 3.3, often playing a key role in determining the directionality of excitation energy transfer.

$$\kappa^2 = [\cos\nu - 3\cos\alpha\cos\beta]^2 \quad \textbf{(3.3)}$$

where, α and β are the angles made by the transition dipoles of the donor and acceptor entities with the line joining the centers of the transitions, and ν is the angle between the two transition dipoles. The transition dipoles of tetrapyrroles are known to lie along a line joining two opposing pyrrole nitrogens.(28) Depending upon the relative orientation of the donor and acceptor, the value of κ^2 could range from 0 to 4. For head-to-tail parallel transition dipoles, $\kappa^2 = 4$, for parallel dipoles, $\kappa^2 = 1$, and for dipoles oriented perpendicular to each other, $\kappa^2 = 0$. An analysis of the results presented in Figure 4 shows different orientations for the ortho, meta, and para substituted derivatives. However, considering the flexible nature of the connecting axial bond, a value of $\kappa^2 = 2/3$, generally used for randomly oriented dipoles, is employed. The $J_{Forster}$ spectral overlap integral representing the emission of the donor and absorption of the acceptor is given by eq 3.4.

$$J_{Foster} = \int F_D(\lambda)\ \varepsilon(\lambda)\ \lambda^4.d\lambda \quad \textbf{(3.4)}$$

where $F_D(\lambda)$ is the fluorescence intensity of the donor with total intensity normalized to unity, and $\varepsilon(\lambda)$ is the molar extinction coefficient of the acceptor

expressed in units of M^{-1} cm^{-1} and λ in nanometers. Figure 3.12 shows the spectral overlap of the donor and acceptor absorption and emission bands for both types of dyads.

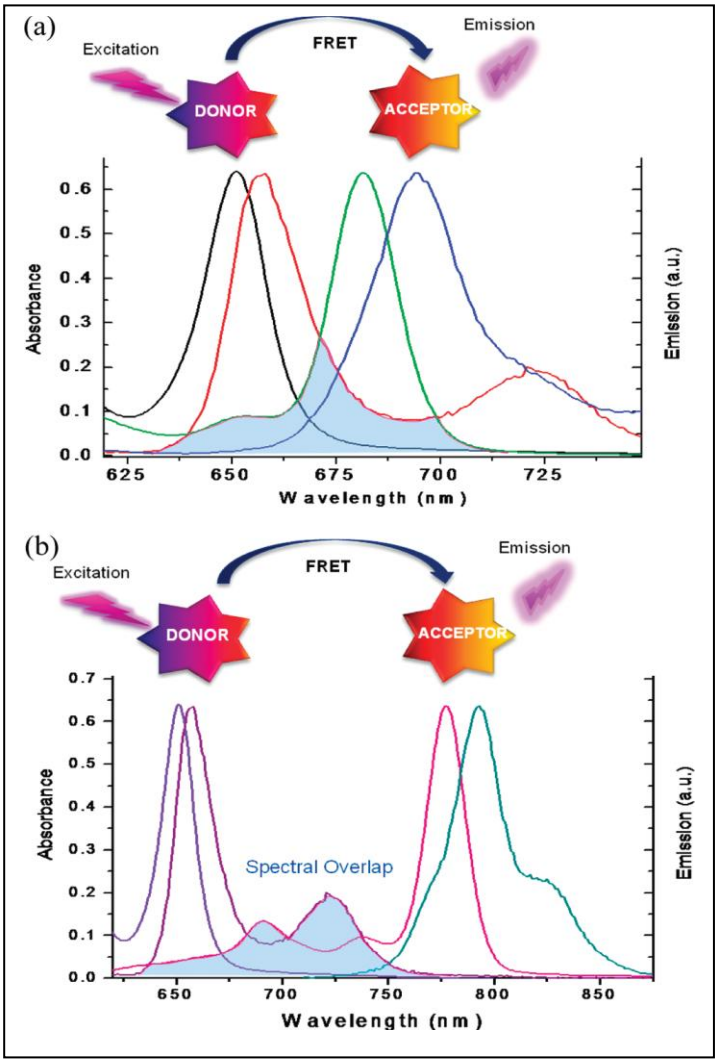

Figure 3.12: Spectral overlap (highlighted area) for (a) H_2PIm:ZnPc and (b) H_2PIm:ZnNc type dyads. The donor absorption and emission, and acceptor absorption and emission (all normalized), on an increasing wavelength scale.

The schematic above each spectrum shows the energy transfer path for each type of dyad.

Analysis of the data according to eq. 3.4 resulted in *J* values of 3.52×10^{-12} M^{-1} cm^3 and 4.21×10^{-12} M^{-1} cm^3, respectively, for the H_2PIm:ZnPc and H_2PIm:ZnNc dyads.

Equation 3.2 can be further simplified in terms of Forster distance, R_0, where half the donor molecules decay by energy transfer and half decay by the usual radiative and nonradiative mechanisms.

$$k_{Forster} = \frac{1}{\tau_D}\left(\frac{R_0}{R_{DA}}\right) \qquad \textbf{(3.5)}$$

Further, the EET efficiency can be measured by using relative fluorescence intensity or lifetime of the donor in the absence and presence of acceptor, according to equation 3.6.

$$\text{Efficiency, E} = 1 - \frac{I_{DA}}{I_D} = 1 - \frac{\tau_{DA}}{\tau_D} \qquad \textbf{(3.6)}$$

From the steady-state data, values of *E* obtained were found to be 0.55, 0.70, and 0.74, for the H_2PIm:ZnPc (o, m, and p) dyads, and 0.40, 0.50, and 0.56 for the H_2PIm:ZnNc (o, m, and p) dyads by monitoring the emission intensity of H_2PIm at 656 nm. The efficiency for ortho derivatives is found to be generally smaller, a trend that readily follows their K values. It is interesting to note that

both of the acceptors have good spectral overlap and transfer efficiency in the studied series of dyads. The $k_{Forster}$ values were estimated by using the parameters described in eqs 3.1- 3.5 and found to be on the order of 10^{10}-10^{11} s^{-1}, revealing ultrafast energy transfer (Table 3.2). As explained in the subsequent paragraphs, the rate of energy transfer measured using pump-probe and up-conversion techniques agree well with the predictions of ultrafast energy transfer in the dyads.

Dyad[a]	$k_{Forster}$, s^{-1}, [b]	k, s^{-1}, [c]
H_2P_oIm:ZnPc	2.72 x10^{12}	1.4 x10^{11}
H_2P_mIm:ZnPc	2.82 x10^{11}	1.7 x10^{10}
H_2P_pIm:ZnPc	7.54 x10^{10}	3.3 x10^{10}
H_2P_oIm:ZnNc	1.63 x10^{12}	2.0 x10^{11}
H_2P_mIm:ZnNc	1.40 x10^{11}	9.0 x10^{10}
H_2P_pIm:ZnNc	7.54 x10^{10}	4.0 x10^{10}

[a]-see Figure 3.1 for the structure of different donor and acceptor entities.

[b]-Estimeated according to equations 3.1 – 3.5; error = ±10%

[c]-determined from pump-probe technique

Table 3.2: Estimated and experimentally determined rates of energy transfer for the dyads formed by coordination of imidazole appended free-base porphyrin to zinc phthalocyanine or zinc naphthalocyanine in DCB.

Pump probe and up-conversion studies

The photodynamics of the energy transfer of the newly formed dyads was studied by transient spectroscopy techniques. Transient absorption spectrum of H_2P_mIm in toluene obtained from the pump-probe technique is shown in Figure 3.13(a).

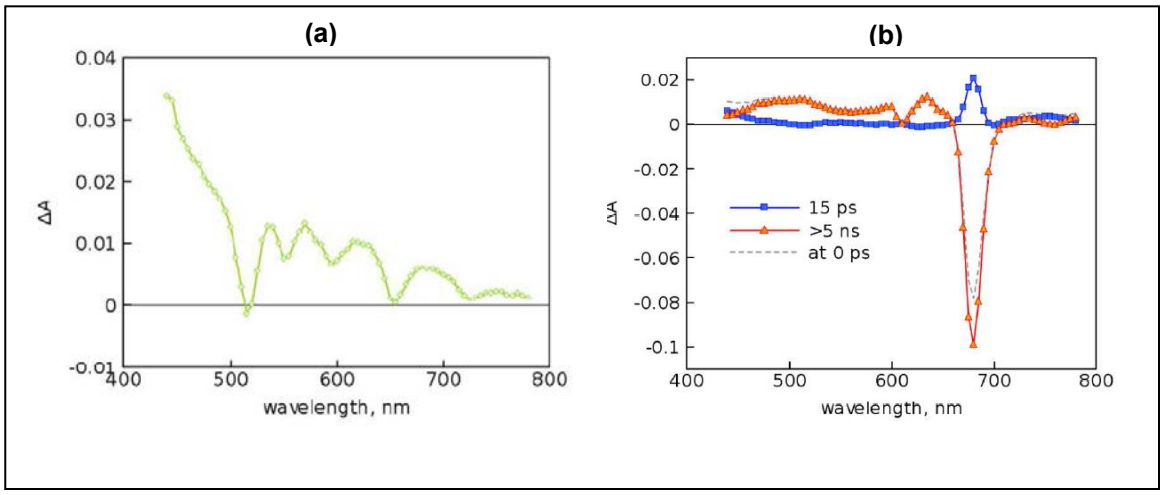

Figure 3.13: (a) Transient absorption spectrum of H_2P_mIm in toluene measured by pump-probe method. The spectrum corresponds to excited singlet state of porphyrin chromophore. (b) Transient absorption decay component spectra of ZnPc in toluene. The dashed line presents the time resolved differential absorption spectrum right after excitation (at 0 ps delay).

At the excitation wavelength of 410 nm, the internal conversion ($S_2 \rightarrow S_1$) was faster than the time resolution of the pump-probe instrument, 200 fs; hence, the signal showed instant formation of the lowest excited state. The transient absorption response of ZnPc was relatively more complex and at least biexponential fit had to be used to achieve a reasonable fit of the results as presented in Figure 3.13(b). Similar results indicating the presence of a minor transient absorption perturbation in 2-20 ps time domain have been already reported,[20d,e] and a few explanations were proposed, but the origin of this signal remains unclear. However, after instant formation of a typical transient absorption spectrum of the singlet excited ZnPc after an excitation pulse at 410 nm, there was a minor (<20%) increase in Q-band bleaching with a relatively slow time constant (15 ps). Apparently this slow component had something to do with photodynamics of the ZnPc, although it had only a minor effect on the transient absorption spectrum of the compound. A similar component was then observed for the porphyrin-phthlocyanine dyads. To distinguish this component from the energy transfer processes taking place in the dyad, one can notice that it has virtually zero intensity in 500-650 nm wavelength range (Figure 3.13(b)), whereas the porphyrin excited-state specific feature are well pronounced in this range (Figure 3.13(a)).

Figure 3.14 shows transient absorption decay component spectra of the H_2P_pIm:ZnPc dyad together with the time-resolved spectrum just after excitation

(at 0 ps delay time), while Figure 3.15 reveals the decay profiles of the 455 and 680 nm bands. The spectrum of the dyad immediately after excitation (at 0 ps) had features typical of the excited singlet state of the porphyrin except for a band around 680 nm which was due to a small portion of directly excited zinc phthalocyanine. This band increased in intensity with a time constant of 30 ps. Additionally, the 30 ps component showed the disappearance of the porphyrin excited-state features and conversion of the spectrum to one corresponding to the excited singlet state of ZnPc. Thus, the 30 ps time constant has been attributed to the energy transfer from H_2P_pIm to ZnPc. The minor component with a 0.5 ps lifetime was similar to the one observed for reference ZnPc and can be attributed to photodynamics of directly excited phthalocyanines.

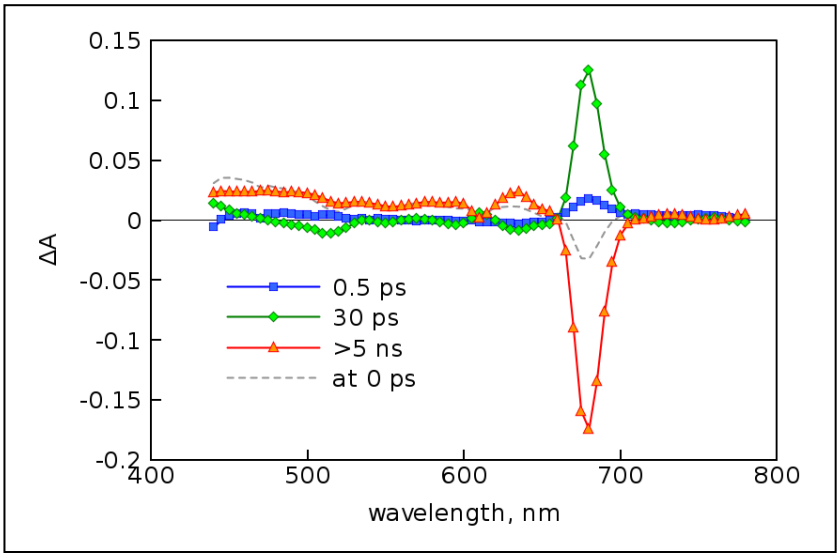

Figure 3.14: Transient absorption decay component spectra of H_2P_pIm:ZnPc dyad in toluene. The dashed line shows the differential absorption spectrum right after excitation (at 0 ps delay time).

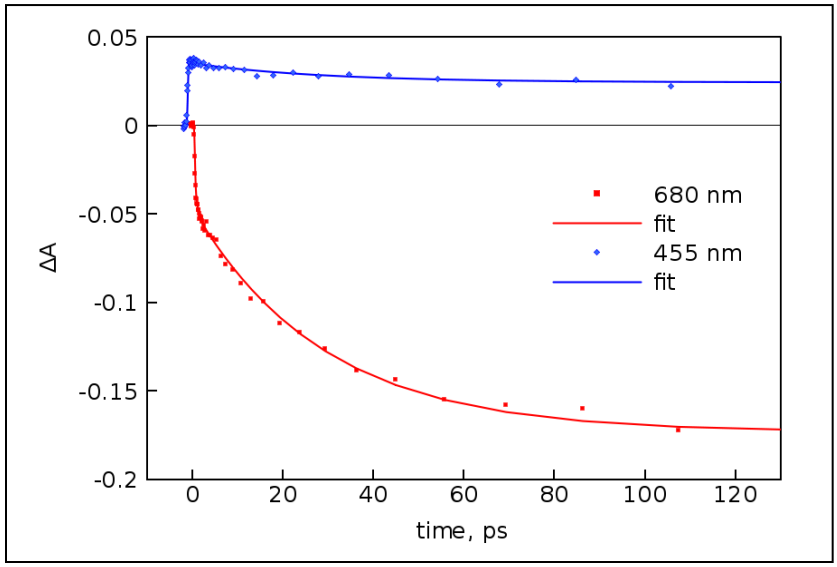

Figure 3.15: Transient absorption decays of the dyad monitored at 680 and 455 nm. The solid lines present the global fits at these wavelengths.

The transient absorption spectra of the H_2P_oIm:ZnPc dyad shown in figure 3.16 revealed similar spectral features. The component corresponding to energy transfer had a 7 ps time constant. The free-base porphyrin features were also observed for the H_2P_mIm:ZnPc dyad (Figure 3.17) even at the longest available delay time of 1 ns. However, the 600 ps component had a shape similar to the energy transfer component of the ortho and para derivatives. From these studies, the energy transfer time constant was found to follows the order: ortho > para > meta substitution of the free-base porphyrin.

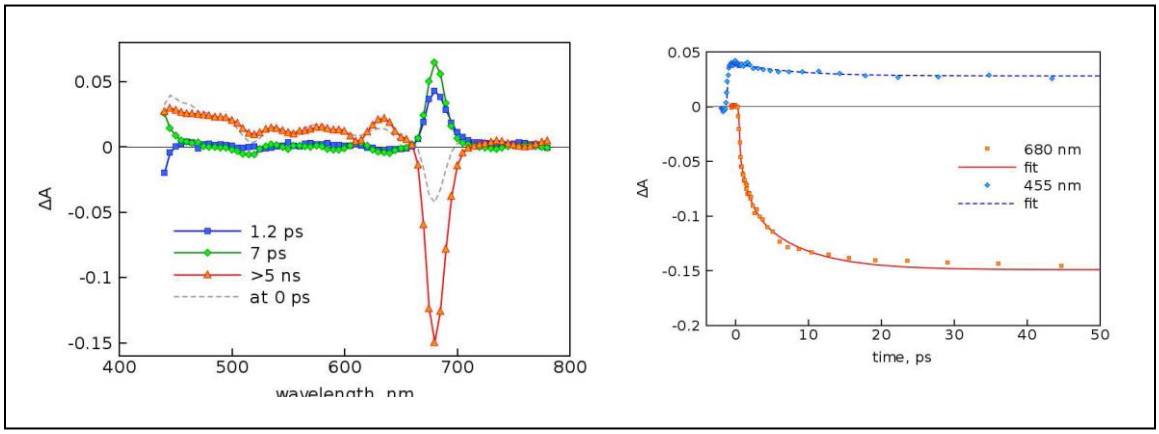

Figure 3.16: (a) Transient absorption decay component spectra of H_2P_oIm:ZnPc complex in toluene. The dashed line shows the differential absorption spectrum right after excitation (at 0 ps delay time). (b) Transient absorption decays of H_2P_pIm:ZnPc in toluene at 680 and 455 nm. The solid lines present the global fits at these wavelengths.

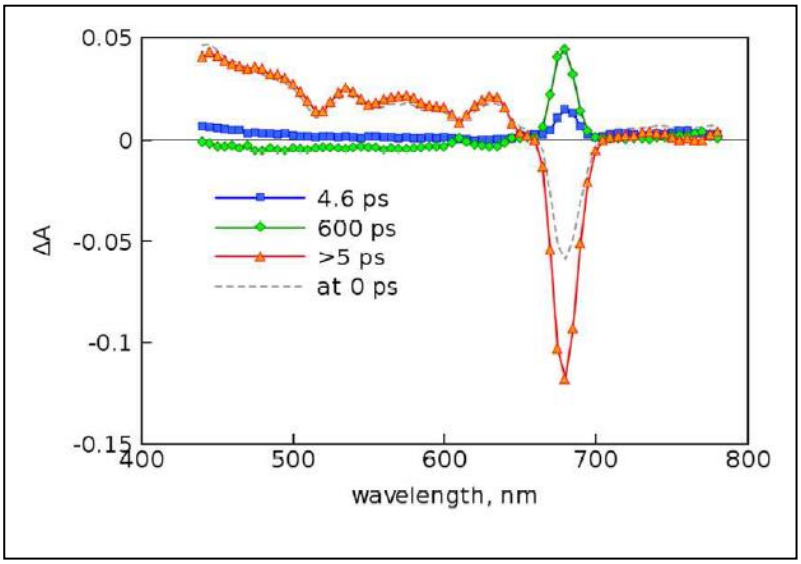

Figure 3.17: Transient absorption decay component spectra of H_2P_mIm:ZnPc dyad in toluene. The dashed line shows the differential absorption spectrum right after excitation (at 0 ps delay time).

The dyads were also investigated using a complementary upconversion technique. Figure 3.18 shows the fluorescence decay of the free-base porphyrin emission at 650 nm and the rise of the zinc phthalocyanine emission at 690 nm for the H_2P_pIm:ZnPc dyad in toluene. The time constant for the fast decay at 650 nm was 80 ± 100 ps while for the rising component at 690 nm it was 18 ± 5 ps. These values are slightly higher than that observed from the pump-probe measurements. Among these three time constants, the one from the pump-probe experiments is the most reliable because of less spectral interference; hence, the energy transfer time constant for this dyad was concluded to be 30 ps.

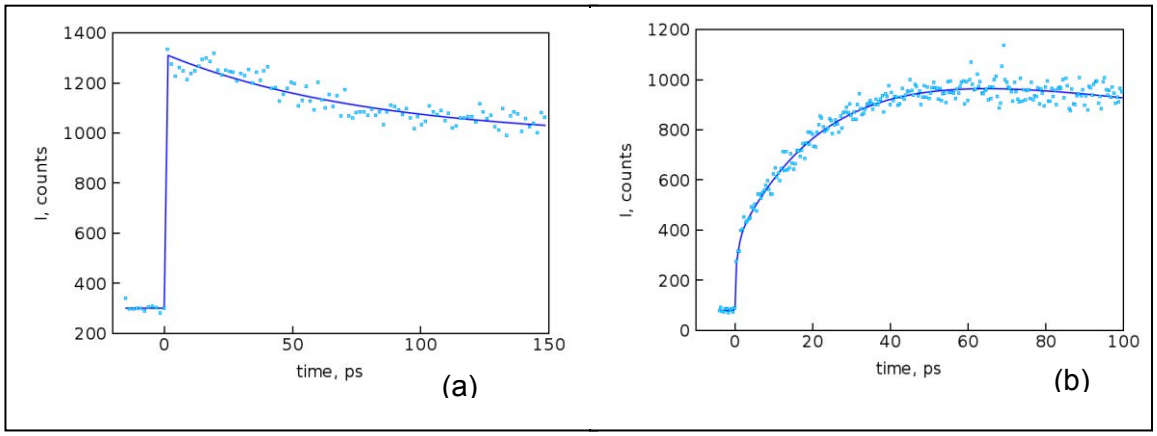

Figure 3.18: Time profiles showing (a) the porphyrin emission decay monitored at 656 nm and (b) rise of fluorescence of the phthalocyanine entity at 690 nm of the H_2P_pIm:ZnPc dyad in toluene.

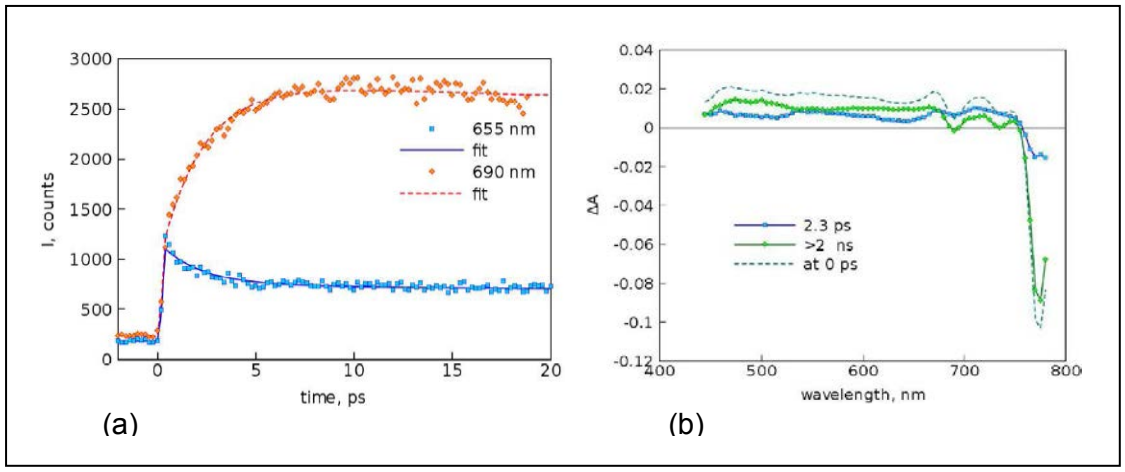

Figure 3.19: (a) Time profiles showing the emission decay monitored at 656 nm and rise of fluorescence of the 690 nm band of the H_2P_oIm:ZnPc dyad in toluene. (b) Transient absorption component spectra of ZnNPc in toluene. The dashed line shows the differential absorption spectrum right after excitation (at 0 ps delay time).

As shown in Figure 3.19(a), the fast decay and rise in fluorescence can also be seen for the H_2P_oIm:ZnPc dyad. For this sample, a common fit of emission at two wavelengths gave a time constant of 2.2 ± 0.5 ps for the energy transfer which agreed well with the corresponding value from the pump-probe measurements of 7 ps. As pointed out earlier, because of the interference of the photodynamics of phthalocyanine to some extent makes the pump-probe results less reliable, an energy transfer time constant of 2 ps from the pump-probe technique was assigned for this dyad. No reliable results were obtained for the H_2P_mIm:ZnPc dyad from the up conversion technique. The transient absorption component spectra for ZnNc from the pump-probe technique are shown in Figure 3.19(b). The results are essentially the same as for the ZnPc reference compound shown in Figure 3.13(b). There is some photodynamics of the excited state with a time constant of 2.3 ps. Otherwise the transient spectrum (longer-lived component) showed bleaching of the ground-state absorption bands at 770 and 685 nm and broadband absorption through the visible part of the spectrum. The transient absorption component spectra of H_2P_pIm:ZnNc dyad in toluene are presented in Figure 3.20.

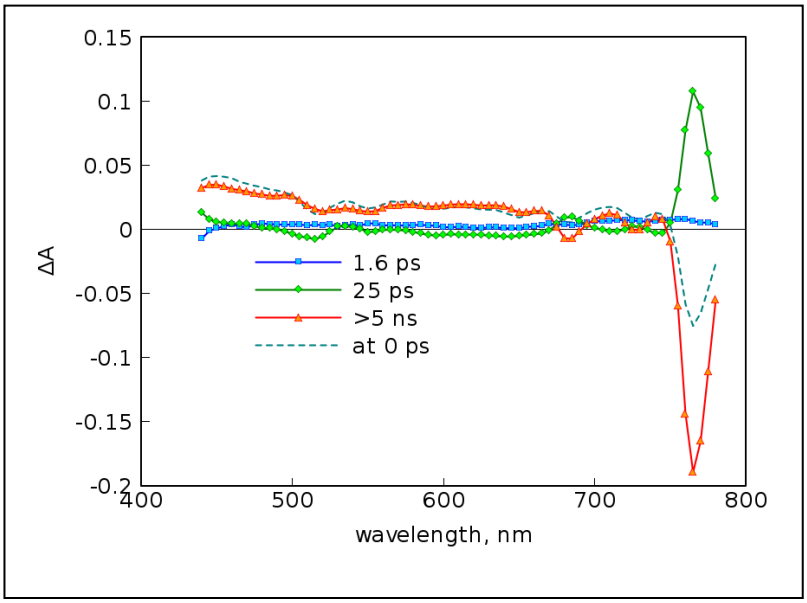

Figure 3.20: Transient absorption component spectra of H_2P_pIm:ZnNc dyad in toluene. The dashed line shows the differential absorption spectrum right after excitation (at 0 ps delay time).

The spectrum of the dyad just after excitation (at 0 ps) had features typical for the excited singlet state of the porphyrin except for a band around 770 nm which was due to a small portion of directly excited ZnNc. This band increased in intensity with a time constant of 25 ps. Additionally, the 25 ps component showed a disappearance of the porphyrin excited-state features and conversion of the spectrum to the one corresponding to excited singlet state of ZnNc.

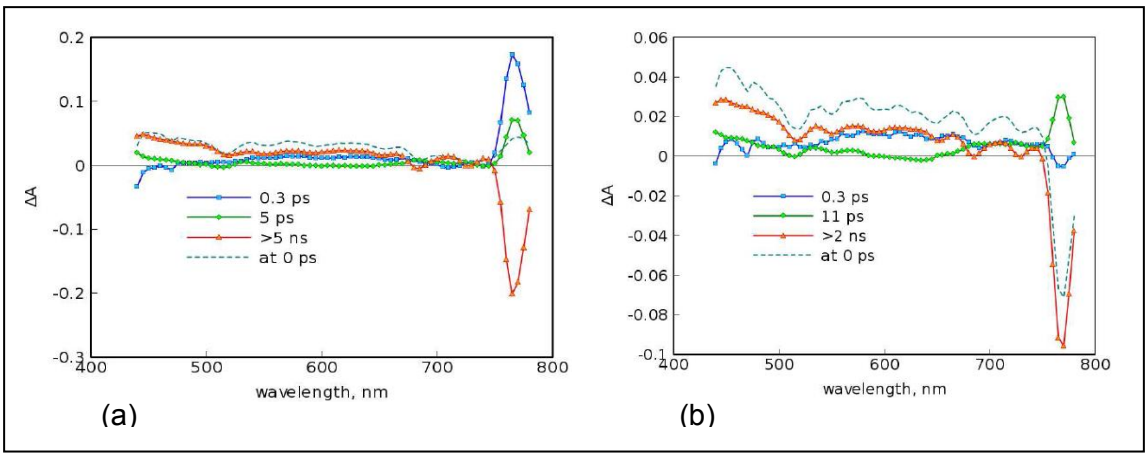

Figure 3.21: (a) Transient absorption component spectra of H_2P_oIm:ZnNc dyad in toluene. The dashed line shows the differential absorption spectrum right after excitation (at 0 ps delay time). (b) Transient absorption component spectra of H_2P_mIm:ZnNc dyad in toluene. The dashed line shows the differential absorption spectrum right after excitation (at 0 ps delay time).

Similar results were also obtained for the H_2P_oIm:ZnNc dyad (Figure 3.21(a)). The energy transfer time constant was 5 ps (±1.6 ps), somewhat faster than that obtained for the H_2P_pIm:ZnPc dyad of 25 ps. As shown in Figure 3.21(b), somewhat uncertain results were obtained for the H_2P_mIm:ZnNc dyad. The component with a lifetime of 11 ps (±4 ps) seems to be one coming from the energy transfer (there are few deeps corresponding to porphyrin Q-bands), which did not agree with the results for the H_2P_mIm: ZnPc dyad. However, for both dyads formed with H_2P_mIm, the interpretation of the pump-probe spectra is rather speculative, as the intensity of the component responsible for the energy transfer was found to be not well-defined. The data from the transient spectroscopic

studies confirm the occurrence of ultrafast excitation energy transfer in the studied dyads. The magnitude of measured rates of energy transfer agrees well with the estimated rate based on Forster‘s mechanism.

Further, the energy transfer rates for dyads originated from ortho imidazole-substituted free-base porphyrin are generally higher compared to meta and para imidazole-substituted porphyrin likely because of closer proximity and favorable orientations.

3.4 Summary

Supramolecular free-base porphyrin-zinc phthalocyanine and free-base porphyrin-zinc naphthalocyanine dyads via metal-ligand axial coordination approach have been formed in non-coordinating solvents and characterized by spectroscopic, computational and electrochemical methods. The formation of 1:1 complex was evident from an analysis of spectral data and the measured binding constants were found to be in the order of 10^4-10^5 mol^{-1} depending upon the nature of the free-base porphyrin and zinc macrocycle suggesting moderate-to-stable complex formation. The structures of the dyads were deduced from computational studies using B3LYP/3-21G(*) method and such studies, although highly flexible, revealed structures depending upon the nature of imidazole appended free-base porphyrins. The redox potential of the donor and acceptor

entities were measured using differential pulse technique and free-energy calculated suggested electron transfer to be an inefficient process when free-base porphyrin is selectively excited in these dyads. Selective excitation of the donor free-base porphyrin entity was possible in both types of dyads formed by either of the ZnPc or ZnNc energy acceptors. Efficient singlet-singlet energy transfer was observed in the studied dyads and the position of imidazole linkage on the free-base porphyrin entity seem to have little control over the overall efficiency, perhaps due to the flexible nature of the single-point axial linkage. Kinetics of energy transfer was monitored by performing transient absorption measurements using both up-conversion and pump-probe techniques. Such studies revealed ultrafast excitation energy transfer in the studied dyads with time constants in the order of 2-25 ps depending upon the type of the dyad.

CHAPTER 4

Photo-induced Electron Transfer in Donor-Accepor Conjugates

(A) Face-to-Face Pacman-Type Porphyrin–Fullerene Dyads

4.1 Introduction

Molecular and supramolecular donor–acceptor dyads capable of undergoing light-induced energy and electron transfer have been widely studied as mimics of natural photosynthetic reaction centers and as photochemical molecular devices[1-8]. The composition, interchromophore distance and orientation, and electronic coupling are important factors in modulating the electron-transfer efficiency and the lifetime of the charge-separated state. To achieve efficient intramolecular electron-transfer processes, both covalent chemistry and biomimetic self-assembly methodologies, such as the formation of π stacks, hydrogen bonds, and van der Waals contacts, have been successfully utilized to connect the donor–acceptor entities.[3b,c,12,14,41,42,61,97,98,100,101,102]. In the majority of these studies, porphyrins or phthalocyanines have been used as photosensitizers and a variety of electron acceptors have been employed. Among the different electron acceptors employed, fullerene C_{60} has become the ultimate electron acceptor owing to favorable reduction potentials and small reorganization energies in electron-transfer reactions[14,41,42,61,97,98,100,101,102]. As a

consequence, C_{60} promotes photoinduced charge separation (CS), but retards the charge-recombination (CR) process, which results in the formation of much desired long-lived charge-separated states[14,41,42,61,97,98,100,101,102]. Several comprehensive reviews of the literature of donor–fullerene dyads, which includes larger hybrids (triads, tetrads, pentads, etc.), that incorporate a wide variety of electron donors and linkers have been published[3b,c,14,41,42,61]. To get more insight into the influence of molecular topology on electron transfer, a few porphyrin–fullerene dyads in which the p systems are structurally forced into a face-to-face arrangement have been elegantly designed and studied.

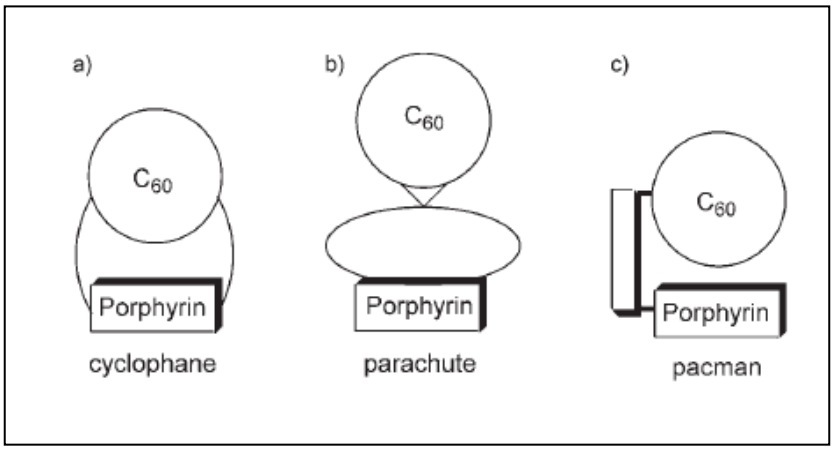

Figure 4.1: Examples of closely held porphyrin–fullerene dyads.

Two types of dyads, namely, porphyrin–fullerene cyclophane dyads (Figure 4.1), which were synthesized independently by the groups of Diederich and Hirsch,[37] and porphyrin–fullerene parachute dyads synthesized by Schuster and coworkers (Figure 4.1),[38] are well known. For the synthesis of these dyads,

tethers with terminal malonate moieties were attached at the meta positions of the 5,15-phenyl rings of a tetraphenylporphyrin precursor. In addition, supramolecular systems that employ multiple modes of binding to attain defined distances and orientations have also been reported[14,100,101,102]. Additionally, a few dyads with porphyrin and fullerene entities positioned face-to-face, but with relatively more structural flexibility are also known[103]. In the present study, we wish to report a series of Pacman-type face-to-face porphyrin–fullerene dyads of the type shown in Figure 1c. In these dyads, the porphyrin and fullerene entities are held closely together by either flexible or rigid spacers (Figure 4.2).

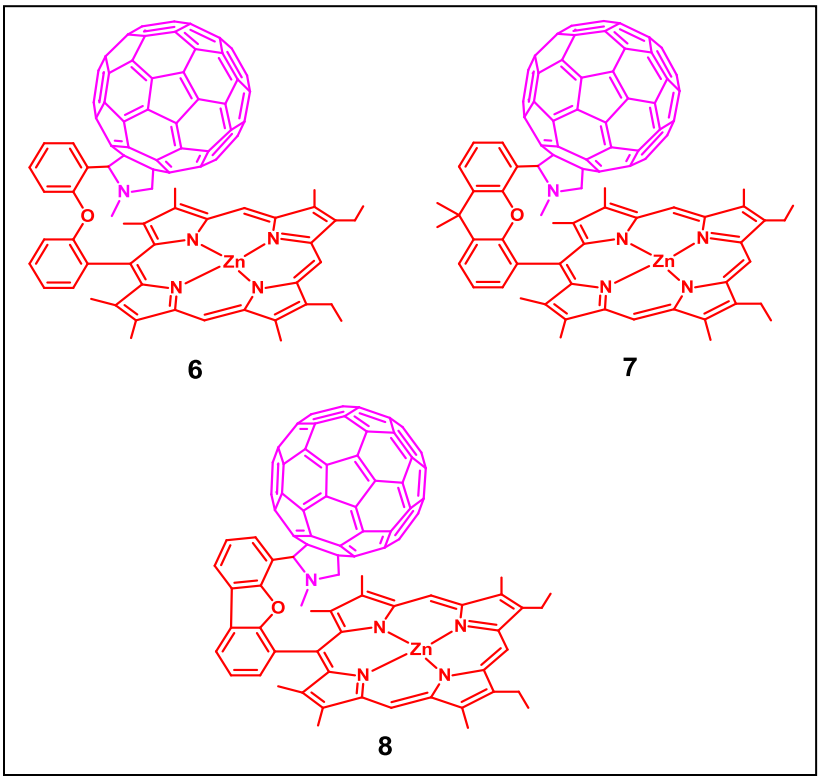

Figure 4.2: Examples of Pacman-type porphyrin–fullerene dyads with rigid or flexible spacers.

It may be mentioned here that the Pacman-type approach employed has been one of the successful approaches used to obtain closely held porphyrin–porphyrin dimers in the literature[104-107]. Owing to the nature of the spacer, the present porphyrin–fullerene dyads are expected to be structurally more rigid compared with the dyads shown in Figure 4.1a and b.

4.2 Experimental Section

Syntheses

13,17-diethyl-2,3,7,8,12,18-hexamethyl-5-[8-(fulleropyrrolidine) diphenylether] (6): A solution of C_{60} (20 mg, 0.027 mmol), N-methylglycine (4.9 mg, 0.055 mmol), and diphenyl ether bridged porphyrin aldehyde (59.2 mg, 0.055 mmol) in toluene (100 mL) was heated at reflux for 6 h before the solvent was evaporated. The crude product was purified by column chromatography (silica gel, hexane/toluene 45:55) to give the product (22 mg, 55%). ^{1}H NMR (300 MHz, $CDCl_3$): δ=9.98 (s, 1 H), 9.90 (s, 1H), 9.81 (s, 1 H), 8.14 (dd, J=7.8 Hz, 1H), 7.77 (t, *J*=7.8 Hz, 2H), 7.52–7.58 (m, 1 H), 7.31–7.33 (m, 2H), 7.20–7.30 (m, 2H), 4.75 (s, 1H), 4.21 (dd, *J*=9.01 Hz, 2 H), 4.00–4.10 (m, 4H), 3.65 (s, 3 H), 3.50 (s, 3H), 3.48 (s, 3H), 3.43 (s, 3 H), 2.82 (s, 3 H), 2.75 (s, 3H), 2.68 (s, 3H), 1.95 (t, *J*=7.5 Hz, 3 H), 1.77 ppm (t, *J*=7.5 Hz, 3H); UV/Vis (PhCN): λ_{max}=330.0, 416.6, 538.8, 571.6 nm; MS (MALDI-TOF): m/z: 1457.8 $[M]^+$.

13,17-diethyl-2,3,7,8,12,18-hexamethyl-5-[8-(fulleropyrrolidine)-9,9-dimethyl-9 H-xanthene] (7): A solution of C_{60} (40 mg, 0.083 mmol), *N*-methylglycine (10 mg, 0.11 mmol), and pyran bridged porphyrin aldehyde (40 mg, 0.055 mmol) in toluene (100 mL) was heated at reflux for 6 h before the solvent was evaporated. The crude product was purified by column chromatography (silica gel, hexane/toluene 55:45) to give the product (11.0 mg, 28.1%). ^{1}H NMR (300 MHz, $CDCl_3$): δ=10.25 (s, 1H), 9.90 (s, 1H), 9.81 (s, 1 H), 8.14 (d, J=7.8 Hz, 1H), 7.88 (d, J=7.8 Hz, 1H), 7.68–7.70 (m, 2 H), 7.50 (d, J=7.8 Hz, 1H), 7.35 (d, J=7.7 Hz, 1H), 5.30 (s, 1 H), 4.20–4.30 (m, 4 H), 4.19 (dd, J= 9.0 Hz, 2H), 3.70 (s, 3H), 3.57 (s, 3H), 3.49 (s, 3H), 3.28 (s, 3H), 2.48 (s, 3H), 2.23 (s, 3 H), 2.07 (s, 3H), 1.80 ppm (t, J=7.5 Hz, 6H); UV/Vis (PhCN): λ_{max}=326.1, 415.5, 538.5, 573.1 nm; MS (MALDI-TOF): m/z: 1497.5 $[M]^+$.

13,17-diethyl-2,3,7,8,12,18-hexamethyl-5-[8-(fulleropyrrolidine) dibenzofuran] (8): A solution of C_{60} (75 mg, 0.105 mmol), N-methylglycine (12.5 mg, 0.140 mmol), and furan bridged porphyrin aldehyde (52.5 mg, 0.072 mmol) in toluene (100 mL) was heated at reflux for 6 h before the solvent was removed in vacuo. The residue was purified by column chromatography (Silica gel, hexane/toluene 40:60) to give the product (27 mg, 25.4%). ^{1}H NMR (300 MHz, $CDCl_3$): δ=10.18 (s, 1H), 9.98 (s, 1 H), 9.92 (s, 1H), 8.35 (d, J=7.4 Hz, 1H), 8.11 (d, J=7.8 Hz, 1H), 8.06 (d, J=7.5 Hz, 1H), 7.93 (d, J=7.4 Hz, 1 H), 7.74 (t, J=7.3 Hz, 1H), 7.51 (t, J=7.4 Hz, 1H), 4.84 (s, 1 H), 4.19 (dd, J=9.4 Hz, 2 H), 4.08–4.15

(m, 4 H), 3.66 (s, 3 H), 3.39 (s, 3H), 2.56 (s, 3 H), 2.50 (s, 3H), 2.40 (s, 3H), 2.29 (s, 3 H), 1.87 (t, J=7.5 Hz, 6H), 1.80 ppm (s, 3H); UV/Vis (PhCN): λ_{max}=329.1, 412.1, 536.9, 572.1 nm; MS (MALDI-TOF): m/z: 1454.7 $[M]^+$.

4.3 Results and Discussion

Synthesis of the Pacman porphyrin–fullerene dyads was accomplished first by synthesizing a porphyrin with an aldehyde-functionalized spacer at the meso position[106]. Subsequently, the aldehyde group was treated with C_{60} and sarcosine by using the standard Prato method for fulleropyrrolidine synthesis[108]. The structural integrity of the newly synthesized dyads was established by UV-visible and NMR spectroscopies, mass spectrometry, and electrochemical methods.

Ground-state charge-transfer interactions

Optical absorption studies

The optical absorption spectrum of dyad **6** and the reference compounds, recorded separately for the Soret and visible regions, are shown in Figure 4.3. The zinc–porphyrin (ZnP) with a meso-substituted spacer group (compounds **6–8** in the absence of a fullerene unit) and a zinc–octaethylporphyrin (ZnOEP) were used as reference compounds. The dyads have a band at around λ=330 nm that

corresponds to the fulleropyrrolidine entity. The Soret band of the dyads was red-shifted by 8 to 15 nm compared with the reference compounds. Such a trend was also observed for the positions of the visible bands. Interestingly, in the near-IR portion of the spectrum, which includes the region from 600 to 800 nm, a broad ab- sorption was observed for these dyads. Based on the results of earlier reports, this band was attributed to the charge ftransfer interactions between the two π entities.[109,110]

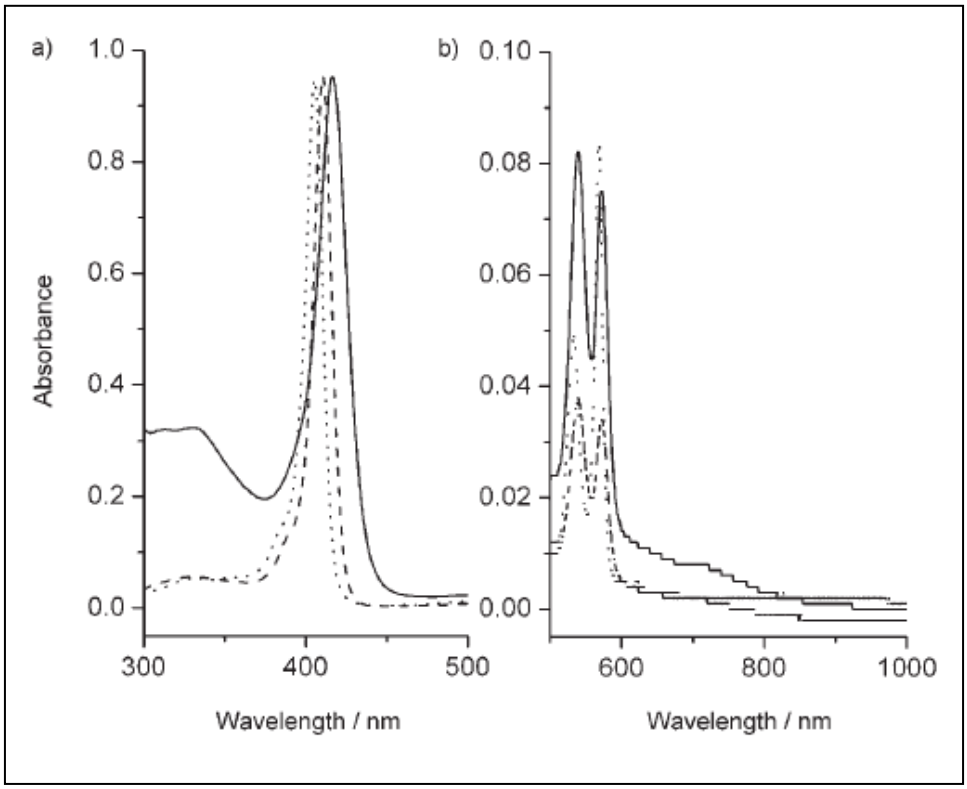

Figure 4.3: UV-visible spectrum of dyad **6** (——), Pacman porphyrin reference (- - - -), and zinc–octaethylporphyrin (…….) in o-dichlorobenzene. The concentration was held at 2.7 mm. The broad absorption of **6** in the 600–800 nm region is attributed to the charge-transfer interactions.

Further computational studies were performed at the B3LYP/3-21G(*) level[94,95] to visualize the geometry and electronic structure of the dyads. For these computational studies the molecules were optimized on a Born–Oppenheimer potential-energy surface and a global minimum was obtained for each of these dyads. The structures of two such dyads, **6** and **7**, are shown in Figure 4.4, in which a face-to-face orientation of the porphyrin and fullerene entities was clearly observed.

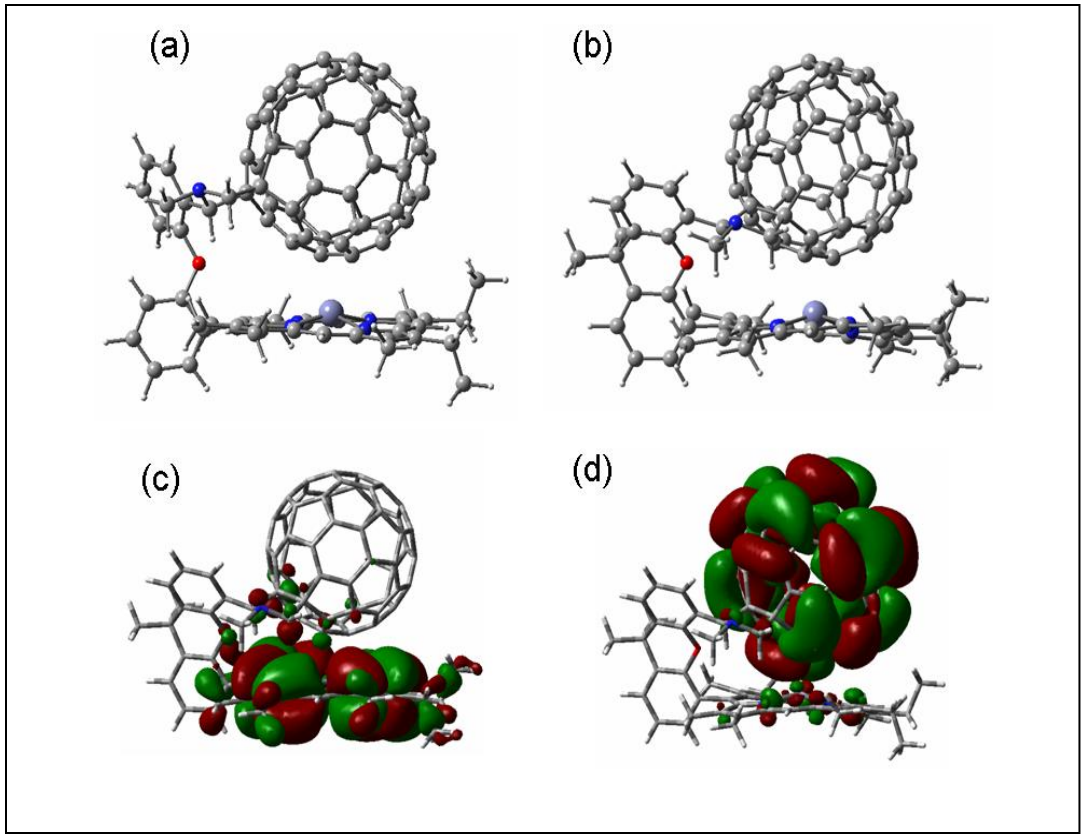

Figure 4.4: B3LYP/3-21G(*) optimized structures of **6** (a) and **7** (b). The frontier HOMO (c) and LUMO of **7** (d) are also shown.

The distance between zinc and the closest carbon of the fullerene spheroid were around 2.2 to 2.3 Å, which indicates that the donor and acceptor entities were within distances suitable for van der Waals interactions. It is important to note that in the case of the flexibly linked dyad (6) this distance was as close as that of dyads with rigid spacers. This could be attributed to the spontaneous attraction between the porphyrin and fullerene entities that was further structurally supported by the small spacer unit[110]. The frontier HOMOs and LUMOs generated at the B3LYP/3-21G(*) level were also suggestive of charge-transfer-type interactions in the ground state of the dyads. As predicted, a large majority of the HOMO was located on the porphyrin π system, whereas the majority of the LUMO was located on the fullerene spheroid for all of the dyads studied. However, a small fraction of the HOMO was located on the fullerene entity and a small fraction of the LUMO was located on the porphyrin entity. Earlier, such partial delocalization of the frontier orbitals was attributed to the ground-state charge-transfer-type interactions between the donor and acceptor entities[103b]. As the majority of the HOMO was on the porphyrin and the majority of the LUMO was on the fullerene, a $ZnP^{\bullet+}$–$C_{60}^{\bullet-}$ charge-separated state could be visualized during photoinduced electron transfer in these dyads. The HOMO–LUMO gap calculated in the gas phase was found to range from 1.68 to 1.79 eV for these dyads, which were comparable to the HOMO–LUMO gaps reported in the literature for related ZnP–fullerene dyads[109].

Electrochemical studies conducted by using cyclic voltammetry techniques were performed to evaluate the redox potentials of the newly synthesized dyads. These measurements were important because the ZnP unit in the present series of dyads had different substituents compared with the zinc– tetraphenylporphyrin (ZnTPP) macrocycle that is traditionally used. Figure 4.5 shows cyclic voltammograms for **6**, whereas the redox potentials for all of the dyads studied, along with the values for reference compounds, are given in Table 4.1.

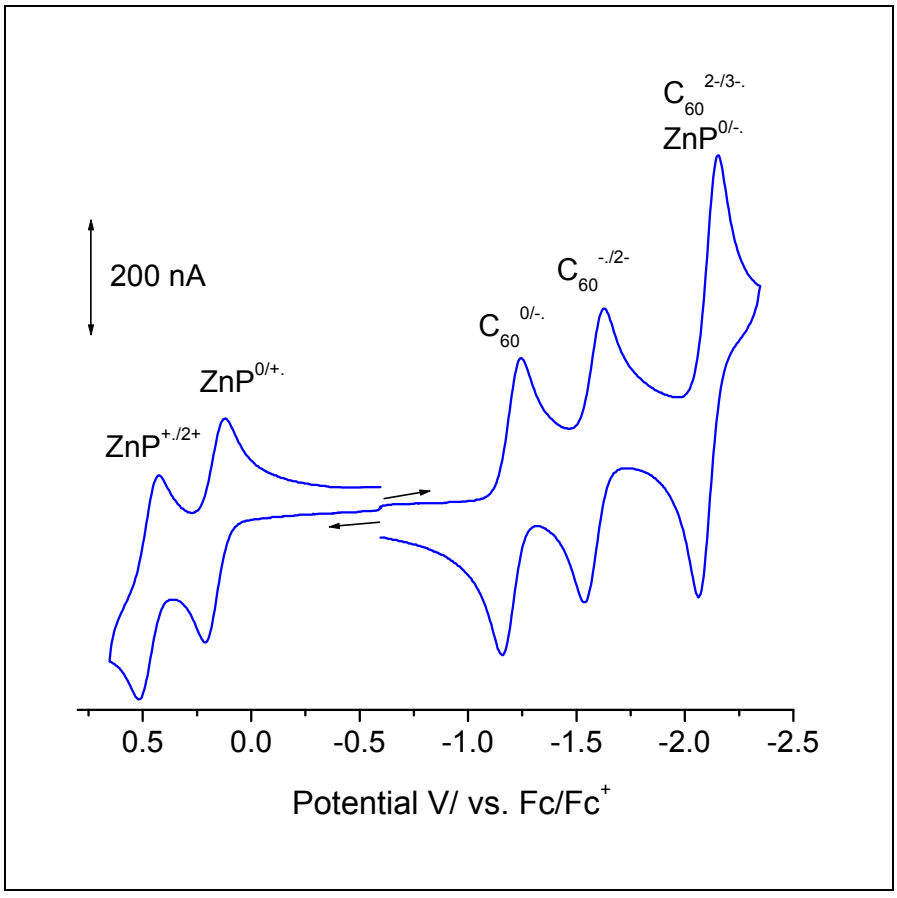

Figure 4.5: Cyclic voltammogram of **8** in PhCN with 0.1M $(nBu)_4NClO_4$. Scan rate=0.1 Vs^{-1}. The concentration of the dyad was ≈0.1 mM.

The ZnP unit exhibited the expected two one-electron oxidations and two one-electron reductions while up to three one-electron reductions that corresponded to the reduction of fulleropyrrolidine were also observed within the potential window of the solvent. The oxidation of the ZnP unit in these dyads was found to be easier by over 100 mV compared with ZnTPP. However, they were 20 to 30 mV more difficult to oxidize compared with the ZnP reference that contained the meso spacer group. The first cathodic process corresponding to the reduction of the fullerene entity was located at approximately -1.20 V versus Fc/Fc^{+}, and was cathodically shifted by 20 to 30 mV compared with pristine fulleropyrrolidine. The small anodic shift of the ZnP oxidation and the small cathodic shift of the fulleropyrrolidine reduction compared with their reference compounds are indicative of charge-transfer-type interactions between them. That is, the charge-transfer interactions make ZnP oxidation and fullerene reduction slightly more difficult.

The experimentally measured HOMO–LUMO gap (the potential difference between the first oxidation of ZnP and the first reduction of fullerene) was found to range from 1.37 to 1.46 V. These values are comparable to ZnP–fullerene dyads in the literature, but slightly lower than that estimated by molecular orbital calculations in the gas phase. The free-energy changes of CS (ΔG_{CS}) were calculated according to the Rehm and Weller method[111] by employing the first oxidation potential of ZnP, the first reduction potential of C_{60}, the singlet

excitation energy of ZnP, and the estimated Coulomb energy. The ΔG_{CS} values for generating $ZnP^{\bullet+}$– $C_{60}^{\bullet}$ radical ion pairs, were found to range from -0.69 to 0.73 eV (Table 4.1), which indicated that the occurrence of photoinduced CS from singlet excited ZnP to the C_{60} entity was an exergonic process.

Compound	Zn-C[b] [Å]	$ZnP^{\cdot +/2+}$ [V]	$ZnP^{0/+}$ [V]	$C_{60}^{0/-}$ [V]	$C_{60}^{\cdot -/2-}$ [V]	$C_{60}^{2-/3-}$ $ZnP^{0/+-}$	$-\Delta G_{RIP}$ [e][eV]	$-\Delta G_{CS}$ [f][eV]
6	2.20	0.46	0.15	-1.23	-1.60	-2.15[c]	1.38	0.72
7	2.24	0.50	0.18	-1.23	-1.68	-2.21[c]	1.41	0.69
8	2.21	0.47	0.17	-1.20	-1.58	-2.11[c]	1.37	0.73
6 ref	-	0.47	0.17	-	-	-2.09[d]	-	-
7 ref	-	0.45	0.16	-	-	-2.11[d]	-	-
8 ref	-	0.48	0.17	-	-	-2.08[d]	-	-
ZnOEP	-	0.51	0.18	-	-	-2.14[d]	-	-

Table 4.1: Electrochemical redox potentials (E, V vs. Fc/Fc^{+}), and free-energy changes for photoinduced electron transfer (ΔG_{RIP}) and charge separation (ΔG_{CS}) for the dyads in benzonitrile.[a]

[a] see Figure 4. 1 for structures; reference compounds are porphyrins with the meso spacer unit. [b] Distance between zinc and closest C_{60} carbon. [c] Overlap of the first reduction of porphyrin and the third reduction of fullerene (two one-electron processes). [d] Corresponds to the first reduction of porphyrin. [e] $\Delta G_{RIP} = e(E_{ox} - E_{red})$, in which the Coulombic interaction in a polar solvent (PhCN)

is neglected. [f] $-\Delta G_{CS} = \Delta E_{0-0} - \Delta G_{RIP}$, in which ΔE_{0-0} is the energy of the lowest ZnP excited state.

The above studies clearly suggest the existence of charge transfer-type interactions between electron-rich ZnP and electron-deficient fullerene in the face-to-face dyads. It is important to note that such interactions resulted in modulating the optical and electrochemical properties. Further studies that involve steady-state and time-resolved emission techniques were performed to probe excited-state electron transfer in these dyads.

Steady-state emission studies

Figure 4.6 shows the fluorescence spectrum of **1** along with the reference compounds. The dyads had two emission bands at around λ = 575 and 626 nm that correspond to the ZnP entity, however, with much diminished intensities compared to the intensities of the reference compounds (over 90% quenching compared with the ZnOEP reference compound). These results indicate the occurrence of excited-state events in the dyads. Attempts were also made to locate the charge-transfer emission bands of the dyads. The inset of Figure 4.6 shows that a weakband at around λ=825 nm was observed when the dyads were excited at 680 nm, which corresponds to the charge-transfer absorption band. The emission band was better defined in polar solvents, such as DMF or benzonitrile, than in less polar solvents, such as o-dichlorobenzene. Excitation of

the charge-transfer band did not result in the formation of new bands that correspond to exciplex formation, perhaps owing to its low ε values.

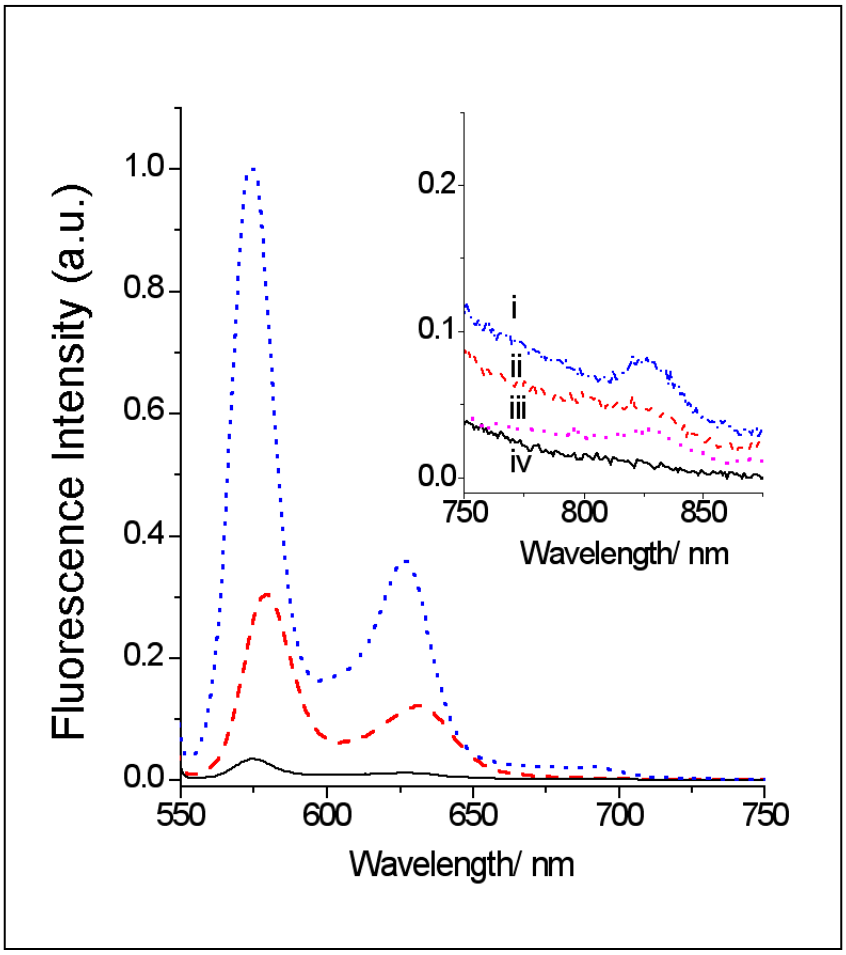

Figure 4.6: Fluorescence spectrum of **6** (___), Pacman porphyrin reference (----), and ZnOEP (.....) in *o*-dichlorobenzene. The porphyrin concentrations were held at 2.7 mM and the samples were excited at the most intense visible band. The inset shows the charge-transfer emission in the near-IR region in DMF (i), benzonitrile (ii), acetonitrile (iii), and *o*-dichlorobenzene (iv). λ_{ex}= 680 nm corresponds to the charge-transfer absorption band.

Transient absorption measurements

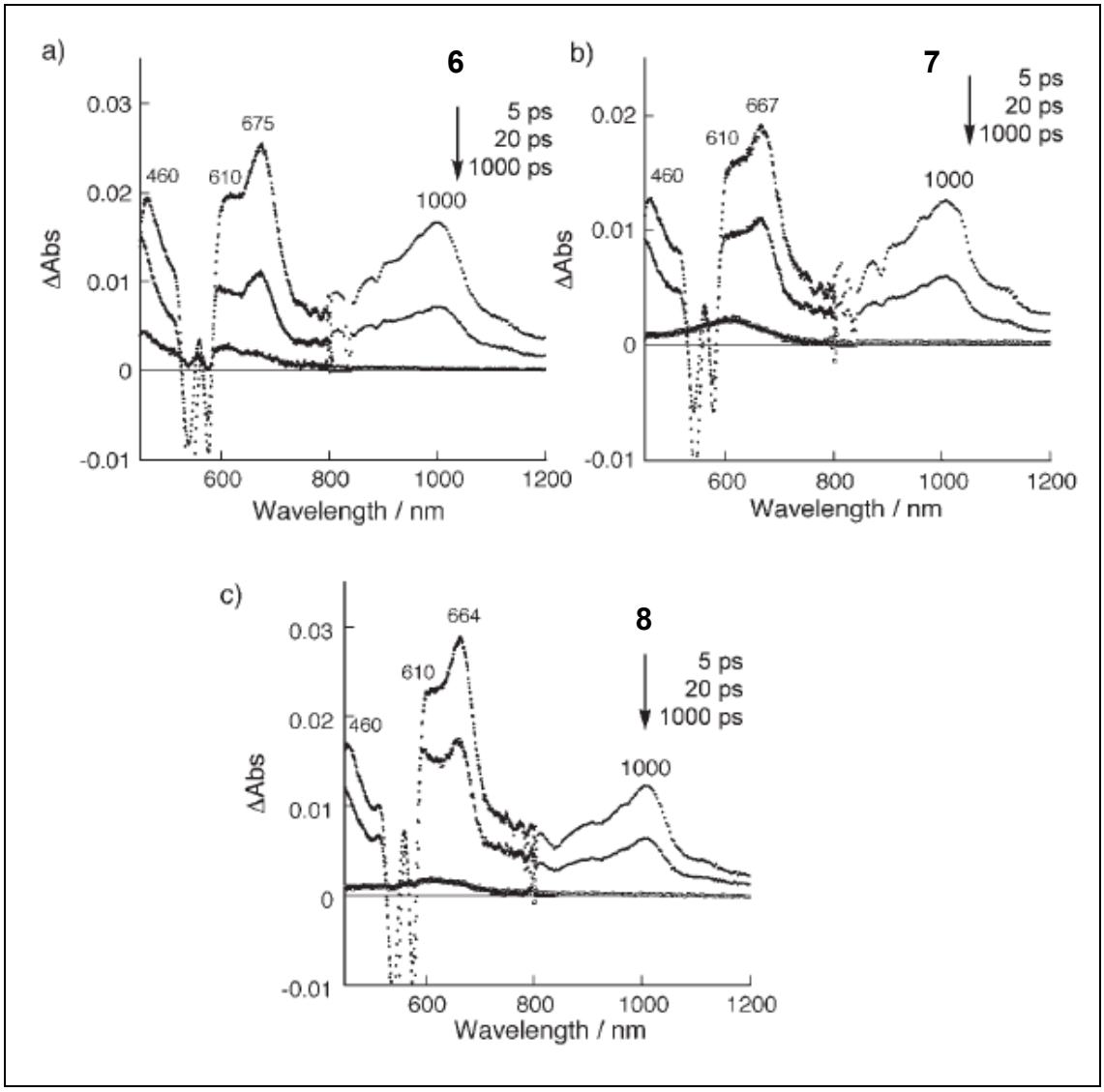

Figure 4.7: Transient absorption spectra of **6** (a), **7** (b), and **8** (c) recorded 5, 20, and 1000 ps after femtosecond laser pulse irradiation at 410 nm in PhCN at 298K.

Time-resolved transient absorption spectra of **6-8** were observed by femtosecond laser flash photolysis in deaerated PhCN, as shown in Figure 4.7. The absorption band observed at λ=1000 nm in each case is a clear attribute of the monofunctionalized fullerene radical anion[42a,47,63,64,65,102].The accompanying absorption band at 675 nm agrees with that of the ZnP π radical cation[42a,47,63,64,65,102]. Thus, the transient absorption spectra shown in Figure 5 indicate the formation of the radical ion pair state ($ZnP^{\bullet+}$– $C_{60}^{\bullet-}$) for **6**, **7**, and **8** in PhCN.

Compound	Solvent	k_{cs} [s^{-1}]	τ_{cs} [ps]	k_{CR} [s^{-1}]
6	PhCN	$2.4 * 10^{12}$	0.42	$6.5 * 10^{10}$
	Toluene	$6.8 * 10^{10}$	14	$1.9 * 10^{10}$
7	PhCN	$9.5 * 10^{11}$	1.1	$5.0 * 10^{10}$
	Toluene	$3.5 * 10^{11}$	29	$2.6 * 10^{9}$
8	PhCN	$1.5 * 10^{12}$	0.67	$5.2 * 10^{10}$
	Toluene	$5.2 * 10^{10}$	19	$2.3 * 10^{9}$

Table 4.2: Values for k_{CS}, the lifetime for CS, k_{CR}, and the lifetime of radical ion pair (τ_{RIP}) of the dyads in benzonitrile and toluene.

The CS rate constants (k_{CS}, Table 4.2) for the formation of the radical ion pairs were determined from the rise in the absorbance at 1000 nm due to $C_{60}^{\bullet -}$ to be 2.4 x 10^{12} s^{-1} for **6** (Figure 4.8a), 9.5 x 10^{11} s^{-1} for **7** (Figure 4.8c), and 1.5 x 10^{12} s^{-1} for **8** (Figure 4.8e). These rates were found to be one or two orders of magnitude higher than those reported for a number of porphyrin–fullerene dyads in the literature.[37,126] From the CS rates, the quantum yields of the charge-separated state are estimated to be almost 100%. The decay rate constants (k_{CR}) of the radical ion pairs are determined from the decay in absorbance at 1000 nm as 6.5 x 10^{10} s^{-1} for **6** (Figure 4.8b), 5.0 x 10^{10} s^{-1} for **7** (Figure 4.8d), and 5.2 x 10^{10} s^{-1} for **8** (Figure 4.8f). Back electron transfer in the radical ion pair occurs to produce the ground state rather than the triplet excited state of C_{60} because the charge-separated state energy is lower than the triplet energy of C_{60} in PhCN. In fact, no C_{60} triplet was observed in the nanosecond laser flash photolysis measurements of the dyads in PhCN.

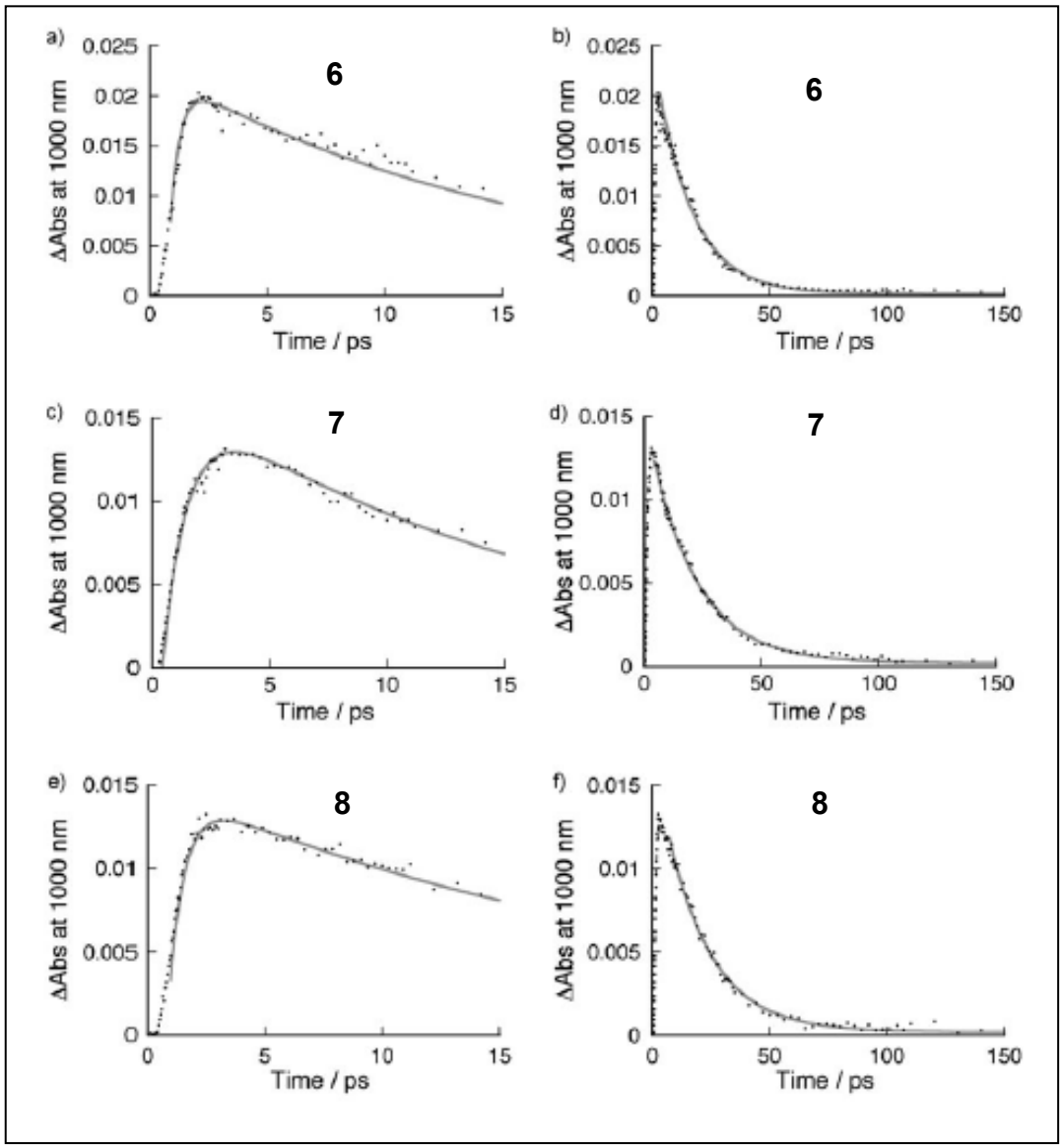

Figure 4.8: Time profiles of absorbance at 1000 nm for **6** at 0–15 (a) and 0–150 ps (b), **7** at 0–15 (c) and 0–150 ps (d), and **8** at 0–15 (e) and 0–150 ps (f) time intervals. The gray curves represent the best fit to the two-exponential rise and decay.

To quantify the driving-force dependence on the electron transfer rate constants (k_{ET}), Equation (4.1) was used, in which V is the electronic coupling

matrix element, k_B is the Boltzmann constant, h is the Planck constant, and T is the absolute temperature[11].

$$k_{ET} = \left(\frac{4\pi^3}{h^2 \lambda k_B T} \right) V^2 \exp\left[- \frac{(\Delta G^o_{ET} + \lambda)^2}{4 k_B T} \right] \quad \textbf{(4.1)}$$

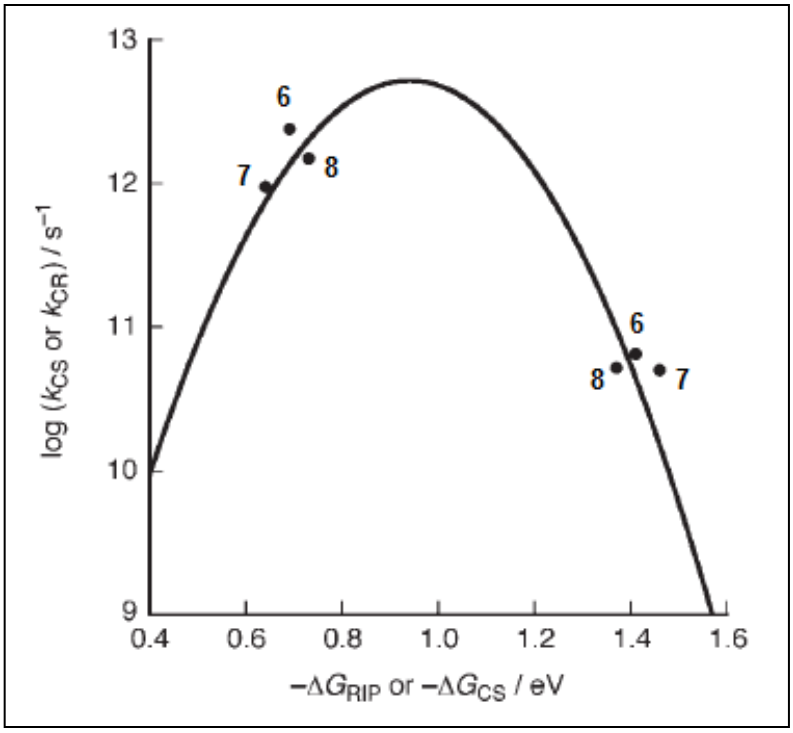

Figure 4.9: Driving force *(-ΔG_{RIP}* or -ΔG_{CS}) dependence on the intramolecular ET rate constants (k_{CS} or k_{CR}) for the dyads investigated in PhCN. The curve represents the best fit to Equation (4.1) to give λ = 0.94 eV and V = 140 cm^{-1}

Figure 4.9 shows the driving-force dependence of log k_{ET} (k_{CS} and k_{CR}) for the CS and CR of **6**, **7**, and **8** in PhCN at 298 K. The solid line is drawn as the best fit line by using the values of λ= 0.94 eV and V= 140 cm^{-1}. The large V value is consistent with adiabatic electron transfer with a close distance between the ZnP and the C_{60} moieties in **6**, **7**, and **8**. As the driving force of CR is larger than the λ value (0.94 eV), the CR process lies in the Marcus inverted region, in which larger driving forces result in smaller electron-transfer rate constants. The overall λ value (0.94 eV) for the present dyads is significantly larger than the value (0.66 eV) reported for the ZnTTP–C_{60} dyad with an edge-to-edge distance (R_{ee}) of 11.9 Å. The R_{ee} values between ZnP and C_{60} in **6**, **7**, and **8** are evaluated to be 2.20, 2.24, and 2.21 Å, respectively, from the optimized structures. In general, the smaller the R_{ee} value the smaller the solvent reorganization energy will be, as expected from the Marcus theory of electron transfer[11]. Thus, the relatively large λ value may result from the significant interaction between closely positioned $ZnP^{\bullet+}$ and $C_{60}^{\bullet-}$ in the charge-separated states. The large λ value is also consistent with the existence of charge-transfer-type interactions between electron-rich ZnP and electron-deficient fullerene in the face-to-face dyads (see above).

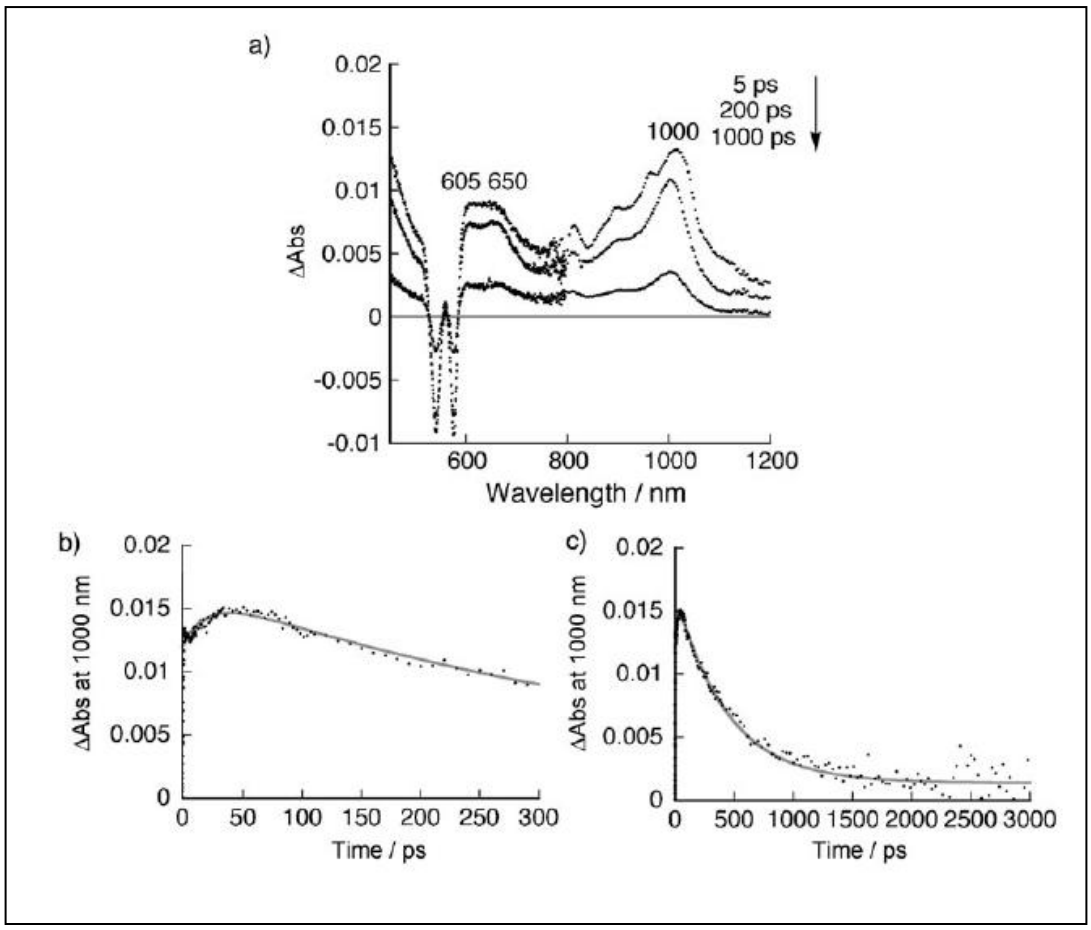

Figure 4.10: a) Transient absorption spectra of **7** taken at 5, 200, and 1000 ps after femtosecond laser pulse irradiation at 410 nm in toluene at 298 K. Time profiles of absorbance at 1000 nm for **7** at 0–300 (b) and 0–3000 ps (c) time intervals. The gray curves represent the best fit to the two-exponential rise and decay.

The charge-separated state of the dyads was also observed in toluene, which is much less polar than PhCN, as shown in Figure 4.10a for **7**. The rate

constant for the formation of the charge-separated state was determined from the rise in the absorbance at 1000 nm due to $C_{60}^{\bullet-}$ (Figure 4.10b), which is much smaller than the corresponding values recorded in PhCN (Table 4.2). The k_{CS} value, which was determined from the decay in the absorbance at 1000 nm (Figure 4.10c), was found to be an order of magnitude smaller than the corresponding values in PhCN. (Table 4.2). The smaller k_{CS} value may result from the smaller driving force of CS in toluene than that in PhCN because the CS process is in the Marcus normal region in Figure 4.9. On the other hand, the larger CR driving force in toluene may result in the smaller CR rate constant in the Marcus inverted region (Figure 4.9). It was confirmed that no C_{60} triplet was observed in the nanosecond laser flash photolysis measurements of **7** in toluene. This observation indicates that back electron transfer to the ground state is faster than that to the triplet excited state of C_{60} in toluene. The formation of relatively long-lived charge-separated states in non polar solvent is an important feature of the present series of Pacman porphyrin–fullerene dyads. Although literature examples of porphyrin–fullerene dyads that do not have strong charge-transfer interactions yielded charge-separated states in polar solvents[1a,3b,12,14,98,100], in a non polar solvent only the population of the triplet state was observed[113]. Owing to the close proximity and the resulting strong charge-transfer-type interactions between the donor and acceptor entities in the Pacman porphyrin–fullerene dyads, it was possible to modulate the energy states that ultimately result in CS in a nonpolar solvent. A similar observation was made for a parachute type porphyrin–fullerene dyad[114], however, the charge separated state is lower than

the triplet excited state in the present series of dyads. Finally, the face-to-face geometry and the comparison of the *V* values of the present dyads with other dyads in the literature indicates that through-space orbital interactions may play a major role in the adiabatic electron-transfer processes, as indicated by the Marcus plot shown in Figure 4.9.

4.4 Summary

A series of closely held porphyrin–fullerene dyads with face-to-face orientation have been reported. Spectral and electrochemical studies indicated the existence of charge-transfer interactions between electron rich ZnP and electron-deficient fullerene in these dyads. The face-to-face geometry of the dyads resulted in the observation of efficient photoinduced electron transfer from the singlet excited state of the ZnP moiety to the C_{60} moiety with a large electron coupling matrix element (V=140 cm^{-1}) to produce the charge-separated state[115]. A relatively long lifetime of the charge-separated state has been achieved in toluene because of the large CR driving force in the Marcus inverted region. This is in sharp contrast to a number of porphyrin–fullerene dyads reported in the literature (with the exception of the parachute-type porphyrin–fullerene dyad mentioned above), in which population of the triplet state, instead of CS, has been the common excited-state deactivation mechanism in nonpolar solvents[41b].

(B) Self-Assembled Co-facial Zinc Phthalocyanine Dimer – Fullerene Conjugates

4.1 Introduction

Structural studies of the photosynthetic reaction center of *R. Viridis* and *R. Sphaeroides* have revealed membrane-bound protein containing four bacteriochlorophylls, two bacteriopheophytins and two quinones[2g,116]. The primary electron donor, a ‗special pair' of two bacteriochlorophylls, is held noncovalently apart by about 3.2 Å with a slipped cofacial orientation. These reaction centers undergo sequential multi-step electron transfer generating long-lived charge separated states, key feature needed for efficient harvesting light energy[2g,116]. A number of studies have reported on model compounds as photosynthetic reaction center mimics with an ultimate aim of harvesting solar energy and constructing photovoltaic devices.[3b,3c,5,12,13,50,63,92c,98,100,117-119]. There have also been a few studies mimicking the reaction centers of photosynthetic systems, by incorporation of a ‗special pair' into these models.[61,120,121]. Although self-assembly approach of building donor-acceptor pairs is more biomimetic, it has been difficult to control the distance and orientation due to weak interactions and the associated multiple equilibrium processes.[122-124]. Majority of these studies utilized porphyrins as a light harvesting unit as well as an electron donor, and fullerenes as an electron acceptor. However, phthalocyanines (Pcs) have more attractive features as compared to porphyrins in view of their strong absorption in the 600-700 nm

region, leading to a blue-coloring ability, which is accompanied by a robust nature and better electron donor ability (when appropriate substituents are present).[98,125]. Despite the excellent light harvesting and electron donor properties of Pcs, supramolecular donor-acceptor ensembles of Pcs and fullerenes still remains challenging because of the synthetic challenges associated in building host-guest assemblies. In addition, the low lying triplet excited state of Pcs, which is generally lower in energy than the charge-separated (CS) state of Pc-fullerene ensembles, has precluded to attain the long-lived CS state.[39,60,126]

We report herein a biomimetic model of the bacterial ‗special pair', that is a supramolecular complex between a cofacial zinc phthalocyanine dimer linked by complexation of four bis crown ether unit with potassium ion, and a fullerene derivative functionalized with a pyridine coordinating entity and an alkyl ammonium cation entity for two point binding. Such potassium ion-induced dimerization of 4,5,4',5',4'',5'',4''',5'''-tetrakis(1,4,7,10,13-pentaoxa-tridecamethylene)phthalocyanine zinc(II), ZnTCPc, was first reported first by Kobayashi and Lever[127,128]. As shown in Scheme 4.1, the potassium ion is sandwiched between two 15-crown-5 entities from two different phthalocyanines due to the size differences[127,128]. Next, the $K_4[ZnTCPc]_2$ dimer was allowed to interact with fullerene functionalized with a pyridine coordinating entity and an alkyl ammonium cation entity as shown in Scheme 4.1.

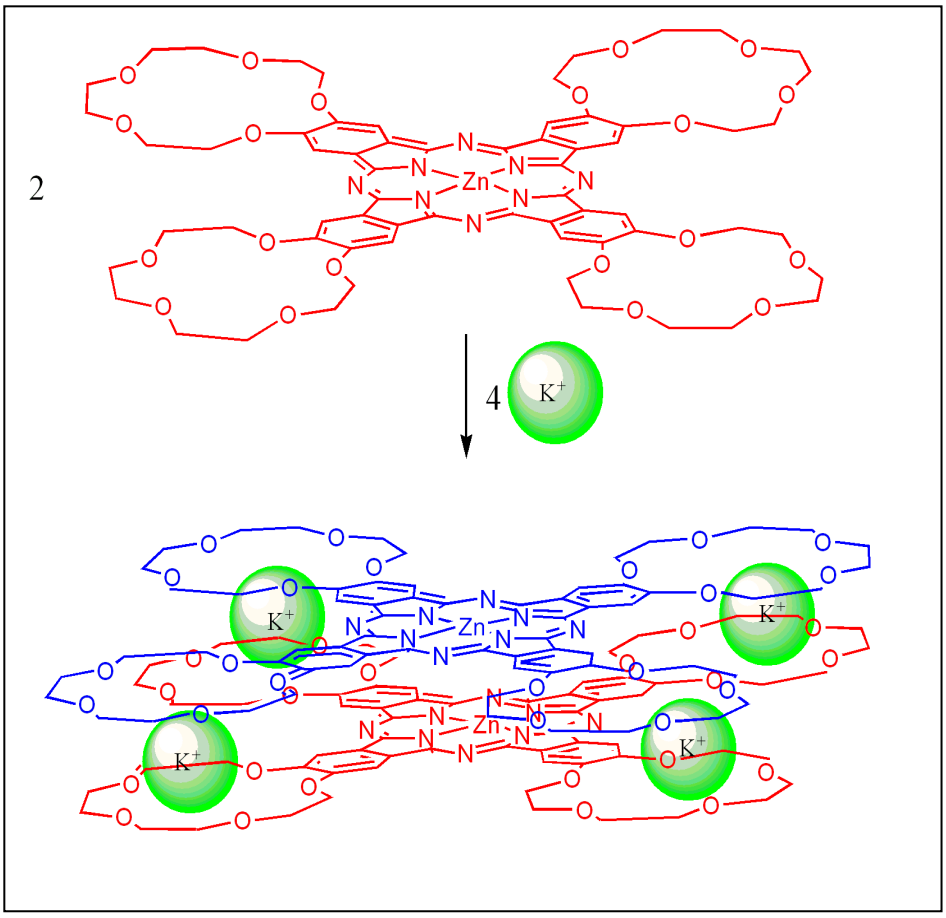

Scheme 4.1: Addition of K^+ to zinc tetrakis(15-crown-5)porphyrin monomer results $K_4[ZnTCP]_2$ dimer formation

The pyridine coordinates to the zinc center while the alkyl ammonium ion forms a complex with one of the crown ether entitis[61,129] (without destroying the K^+-sandwich dimer) *via* a ‗two-point' binding motif[61] (Scheme 4.2). Utilization of such well-defined multiple modes of binding in a controlled fashion results in the formation of biomimetic supramolecular donor-acceptor conjugates. The photoexcitation of the supramolecular $K_4[ZnTCPc]_2$-fullerene complexes affords the charge-separated state with a much longer lifetime as compared with the

corresponding zinc porphyrin supramolecular complex.[61] This is clearly demonstrated by time-resolved spectroscopic measurements performed in this study. Thus, the present donor-acceptor building approach using a zinc phthalocyanine dimer provides valuable insight into the importance of ‗special pair' dimer not only for efficient charge separation but also for stabilizing the charge-separated states.

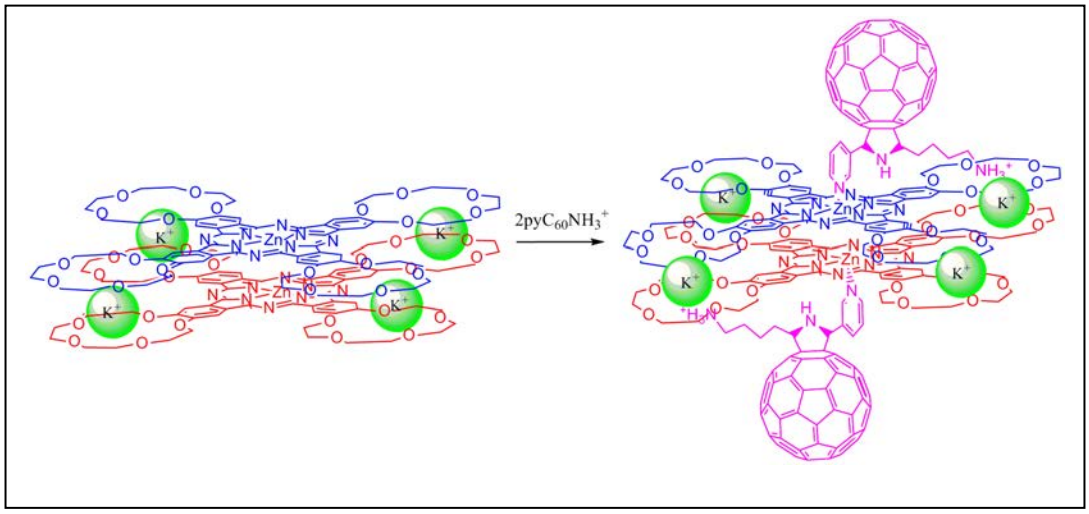

Scheme 4.2: Addition of the functionalized fullerenes, $pyC_{60}NH_3^+$ to $K_4[ZnTCPc]_2$ results $K_4[ZnTCPc]_2$**:**$(pyC_{60}NH_3^+)_2$ complex formation

4.2 Experimental Section

Synthesis of 4,5-Dibromobenzo-15-crown-5 (9). In a two neck 500 mL round-bottomed flask benzo-15-crown-5 (2.2 g, 8.19 mmol), iron powder (64.1 mg, 1.147 mmol) and catalytic amount of I_2 (100 mg) were added to 100 mL of dry

CH_2Cl_2 and 0.90 L (0.0175 mol) of Br_2 was added to above reaction mixture at 0 ^oC over a period of 2 h. The reaction mixture was stirred for 16 h at room temperature, filtered and poured into 100 mL of 10 % aqueous NaOH. The organic layer was separated, washed with water, dried, and removed under vacuum. The crude compound was recrystallized using hexane to obtain dibromo product. The yield was 93.2%. ^1H NMR in $CDCl_3$, δ (ppm) 7.04 (s, 2H, phenyl-H), 3.75-4.20 (m, 16H, crown -CH_2-).

Synthesis of 4,5-Dicyanobenzo-15-crown-5 (10). 4,5-dibromobenzo-15-crown-5, **(9)** (2.97 g, 6.99 mmol), CuCN (1.90 g, 21.33 mmol) and pyridine (332 µL, 4.09 mmol) were dissolved in 100 mL of dry DMF. Then the reaction mixture was refluxed for 20 h under dry nitrogen. The mixture was cooled, poured into 200 mL of 25% ammonium hydroxide, and extracted with $CHCl_3$. The organic layer was washed with water, dried and concentrated. The crude compound was purified on neutral alumina column using hexane:$CHCl_3$ (50:50 v/v) as eluent. Yield: 552 mg (37.2%).^1H NMR in $CDCl_3$, δ (ppm) 7.14 (s, 2H, phenyl-H), 3.75-4.30 (m, 16H, crown -CH_2-).

Synthesis of 4,5-Isoiminoindolen-benzo-15-crown-5 (11). Dicyano product, **(10)** (500 mg, 1.57 mmol) was dissolved in 200 mL of dry methanol. A suspension of dry sodium methoxide (168 mg, 3.10 mmol) was added to the reaction mixture under argon atmosphere. Then, anhydrous ammonia was bubbled through the reaction mixture for 8 h with refluxing. The solvent was

evaporated under reduced pressure, and the crude product (450 mg) was used for next step without purification.

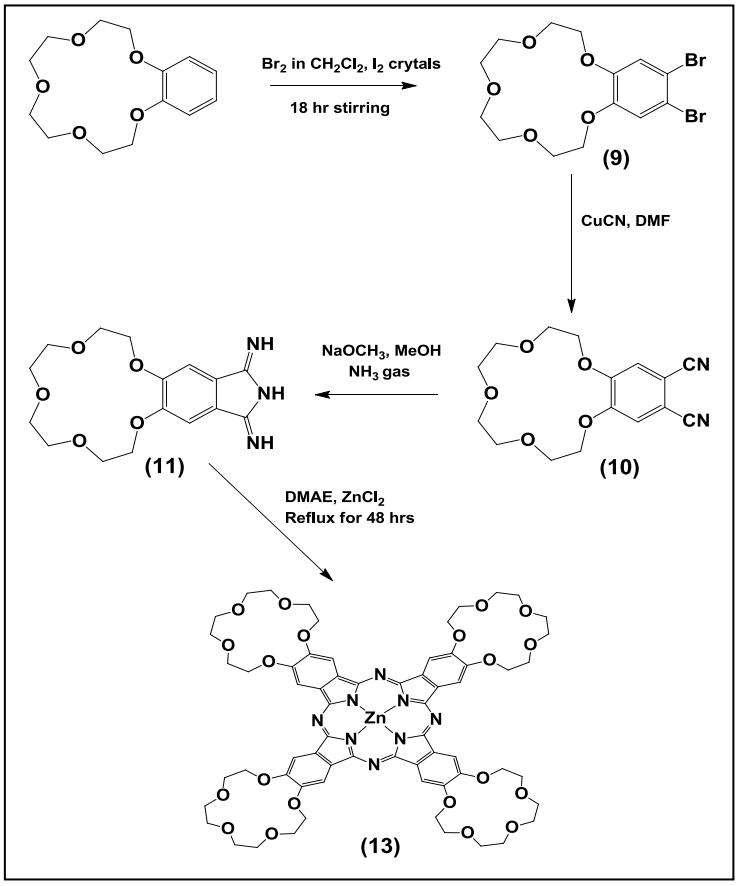

Scheme 4.3: Synthetic scheme adopted for tetrakis(15-crown-5)porphyrin monomer

Synthesis of 4,5,4',5',4'',5'',4''',5'''-Tetrakis(1,4,7,10,13-pentaoxatrideca-methylene)phthalocyanine (H_2TCPc) (12). A precursor of isoiminoindoline compound **(11)** (450 mg) was dissolved in dry 2-(dimethylamino)ethanol (5.0 mL) under argon atmosphere. The reaction mixture was heated and stirred at 150 ºC for 44 h in an oil bath. After solvent evaporation, the resulting dark green reaction mixture was purified on neutral alumina column using $CHCl_3$:MeOH (95:5 v/v) as

eluent. Yield : 55 mg. ^{1}H NMR in $CDCl_3$, δ (ppm) 8.00 (m, 8H, phthalocyanine-H), 3.50-4.75 (m, 64H, crown -CH_2-), -3.40 (s, 2H, inner H of Pc); UV/Vis ($CHCl_3$): λ_{max} = 346, 421, 601, 645, 662, 701 nm.

Synthesis of Zinc 4,5,4',5',4'',5'',4''',5'''-Tetrakis(1,4,7,10,13-pentaoxatrideca-methylene)phthalocyanine, ZnTCPc (13). H_2TCPc **(12)** and a large excess of zinc acetate were dissolved in ethanol and the reaction mixture was refluxed for several hours in the dark, until the 4-band Q spectrum of H_2B15C5Pc had disappeared. Then, the organic layer was washed with water, dried and evaporated under reduced pressure. The crude product was purified on neutral alumina column using chloroform as eluent. Yield : 50 mg (87%). ^{1}H NMR in $CDCl_3$, δ (ppm) 8.00 (m, 8H, phthalocyanine-H), 3.50-4.75 (m, 64H, crown -CH_2-); UV/Vis ($CHCl_3$): λ_{max} = 350, 421, 610, 677 nm.

Synthesis of 2-(3'-Pyridyl)-5-(n-butylammonium)-3,4-fulleropyrrolidine (14). H-Lys-(Boc)-OH (100 mg, 0.406 mmol) and 3-pyridine carboxyaldehyde (76 ml) were added to a solution of C_{60} (100 mg, 0.138 mmol) in toluene, and refluxed for 3 h. The solvent was evaporated by vacuum, purified on silica gel by using toluene/ethyl acetate 8:2 to obtain N-Boc protected compound (85 mg, 62%). Next, to a dichloromethane solution of N-Boc protected compound (75 mg in 5 mL), trifluoroacetic acid (3 mL), and *m*-cresol (50 mL) was added and stirred for

3 h. The solvent and acid were removed under vacuum and the solid product (66 mg, 97%) was washed in toluene several times to desired product. ^{1}H NMR in $CDCl_3$, δ (ppm) 9.13, 8.60, 8.48, 7.64 (s, d, t, t, 4H, 3 pyridine H), 6.15, 5.17, 5. 14 (s, d, d, 3H, pyrrolidine H), 3.01–1.94 (d, m, m, m, 8H, -$(CH_2)_4$-). UV/Vis (MeOH): λ_{max} = 204, 254.5 nm.

4.3 Results and Discussion

Steady-state Absorption Studies.

Figure 4.11 shows the UV-visible spectrum of ZnTCPc in benzonitrile, which revealed a Soret type band at 345 and visible bands at 630 and 676 nm, respectively.[127] Upon addition of K^+ (10 equivalents of potassium tetrakis(4-chlorophenyl)borate), the Soret band revealed slight increase, while the visible band at 676 nm, often assigned to the monomeric species, completely diminished in intensity with concurrent appearance of a peak at 636 nm, corresponding to the existence of the cofacial dimer[127] as shown in Scheme 4.1 due to strong exciton coupling.[130] Further, as shown in Figure 4.11b, a plot of absorbance of the 676 nm band versus the number of equivalents of K+ added revealed a break at 2, a value expected for the 2:1 stoichiometric ratio between K^+ and ZnTCPc of the K_4[ZnTCPc]$_2$ complex. From the procedure adopted by Thanabal and Krishnan for the determination of the binding constant of related zinc tetrakis(15-crown-5)porphyrin dimer, K_4[ZnTCP]$_2$,[128a] the binding constant

for $K_4[ZnTCPc]_2$ formation evaluated to be K_{dimer} ~ 5.05 x 10^{23} M^{-5} in benzonitrile. This value is close to that reported for K^+ induced dimer formation ZnTCP[128a,e] suggesting very stable zinc phthalocyanine dimer formation.

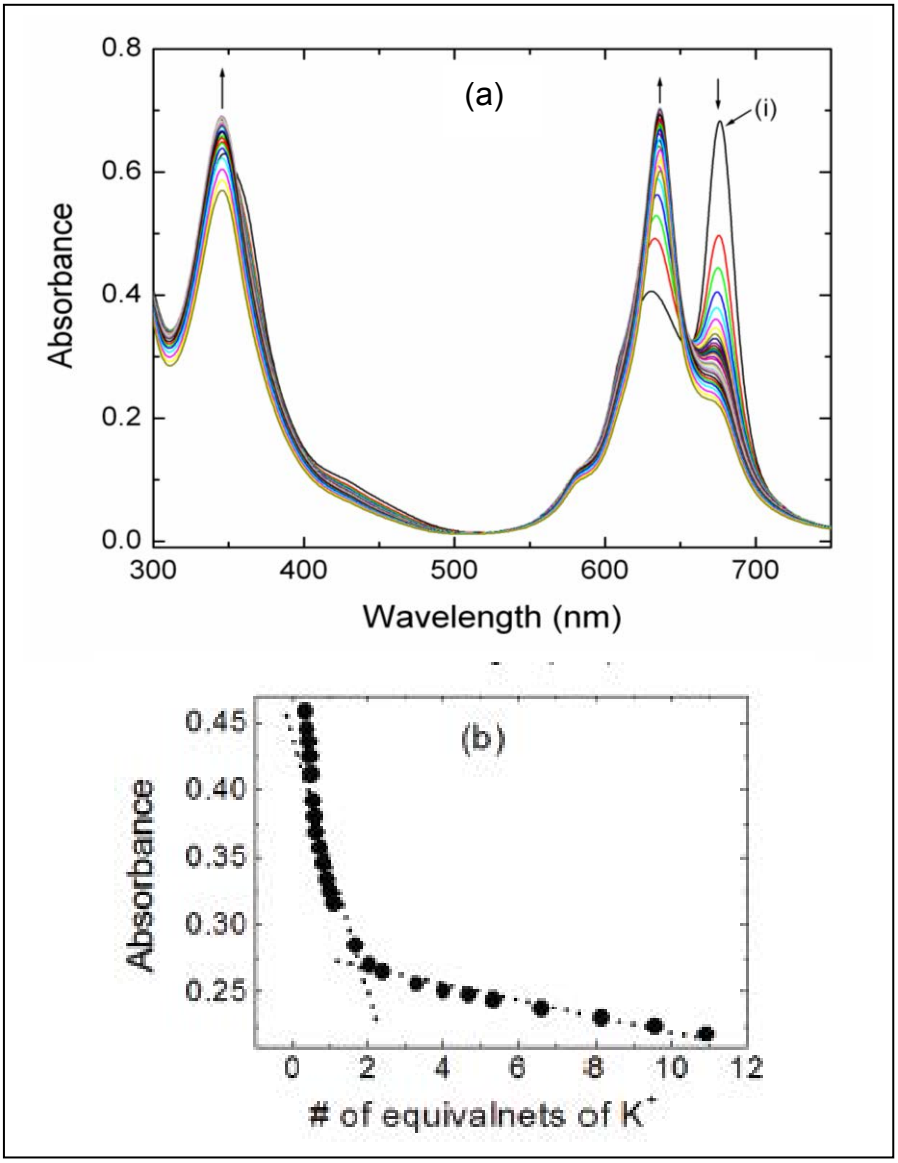

Figure 4.11. (a) UV-vis spectrum revealing the formation of the cofacial dimer of ZnTCPc (5.0 μM) upon increasing addition of K^+ in benzonitrile. Curve i represents the spectrum of monomeric ZnTCPc in the absence of added K^+.

Potassium tetrakis(4-chlorophenyl)borate was used as K^+ source. (b) Plot of absorbance of the 676 nm band versus number of equivalents of K^+ added to arrive at the K^+:ZnTCPc stoichiometry. A break at 2 represents $K_4[ZnTCPc]_2$ formation.

Addition of the functionalized fullerenes, $pyC_{60}NH_3^+$ to $K_4[ZnTCPc]_2$ resulted in a decreased intensity of the 636 nm with the appearance of isosbestic points at 627 and 647 nm, respectively (Figure 4.12a). The Soret band at 345 nm revealed a blue shift of up to 9 nm. A sharp peak at 433 nm corresponding to that of the fulleropyrrolidine was also observed. These spectral shifts are typical of axial coordination of pyridine to zinc phthalocyanine analogs. It should be pointed out here that the addition of fullerene ligands did not cause breaking in the K^+-sandwich dimer since the original zinc phthalocyanine monomer spectrum could not be observed under these conditions. From the data of an independent experiment, a Job's plot was constructed to determine the stoichiometry of the supramolecular complex (Figure 4.12b) by monitoring the absorbance at 636 nm. Such a plot revealed a break at ~0.63 for the number of moles of $pyC_{60}NH_3^+$ to the total number of moles of $pyC_{60}NH_3^+$ and $K_4[ZnTCPc]_2$ indicating a 2:1 supramolecular stoichiometry for the fullerene:ZnPc dimer, which is in agreement with the supramolecular structure of tetrad $K_4[ZnTCPc]_2$:$(pyC_{60}NH_3^+)_2$,shown in Scheme 4.2. Additionally, the monomeric ZnTCPc-$PyC_{60}NH_3^+$ dyad, formed by treating 1:1 equivalents of the donor and acceptor, was treated with K^+ ions to check whether the penta coordinated ZnTCPc would form the K^+ induced phthalocyanine dimer. Such

an experiment indeed revealed the final spectrum of the tetrad similar to that shown in Figure 4.12a indicating formation of K^+ induced phthalocyanine dimer of the penta coordinated species, ultimately resulting into the formation of the tetrad. That is, existence of the ZnTCPc dimer and not higher ZnTCPc oligomers under the present experimental conditions is clear from these studies. The binding constant calculated by constructing the Benesi-Hildebrand plot[93] was found to be $K_{complex}$ = (2.5 ± 0.5) × 10^3 M^{-1}, suggesting moderate stability for the supramolecular donor-acceptor conjugate (Figure 4.12c). The observed isosbestic points for $K_4[ZnTCPc]_2$ dimer binding to $pyC_{60}NH_3^+$ (Figure 4.12a) and the straight line Benesi-Hildebrand plot (Figure 4.12c) suggest occurrence of a one-step binding process for the 1:2 dimer-fullerene complex, that is, simultaneous binding of 2 equiv of $pyC_{60}NH_3^+$ to the metal centers of $K_4[ZnTCPc]_2$[132b]. In the control experiments, monomeric ZnTCPc was titrated with $pyC_{60}NH_3^+$, which also revealed spectral changes characteristic of axial coordination and 1:1 molecular stoichiometry as arrived from Job‘s plot. The binding constant calculated from the Benesi-Hildebrand plot was found to be (1.5 ±0.05) × 10^4 M^{-1}.

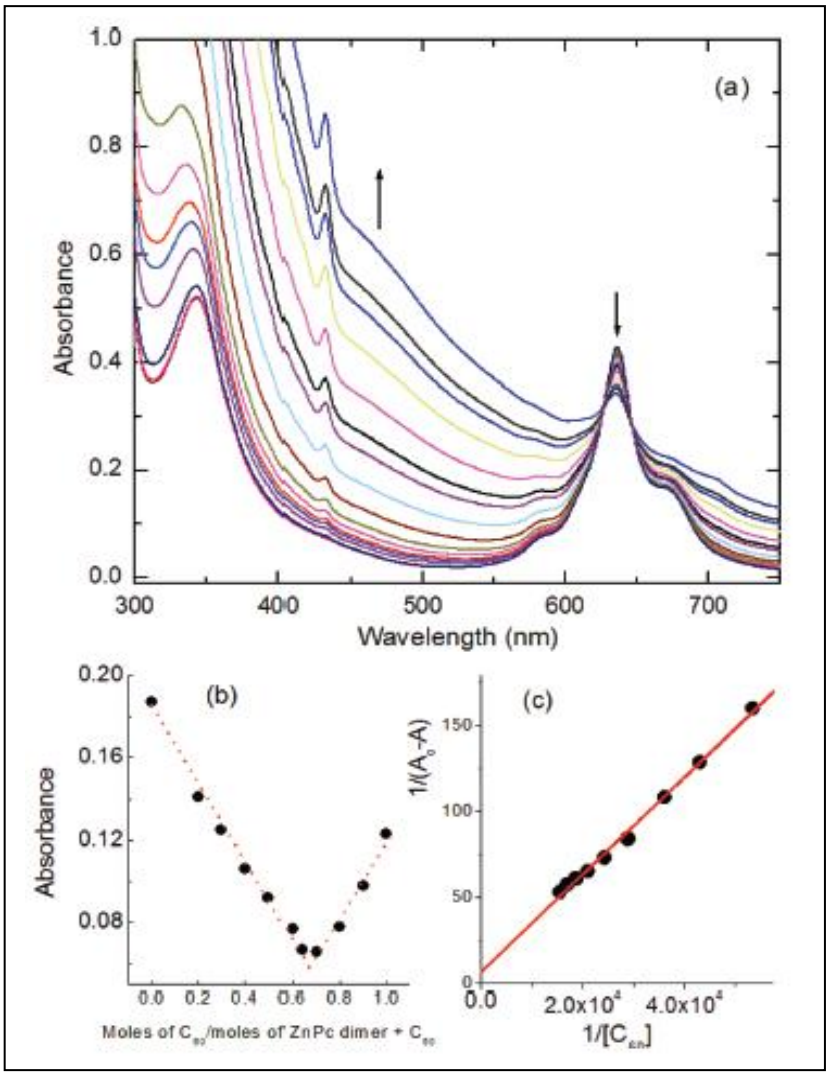

Figure 4.12: (a) Spectral changes observed during the titration of $pyC_{60}NH_3^+$ to the solution of $K_4[ZnTCPc]_2$ in benzonitrile. (b) Job's plot constructed to obtain the stoichiometry of the supramolecular complex (the absorbance was monitored at 636 nm). (c) Benesi-Hildebrand plot constructed to evaluate the binding constant. A_0 and A represent the absorbance of the ZnPc dimer in the absence and presence of added fulleropyrrolidine, respectively.

DFT B3LYP/3-21G(*) computational studies.

Various spectroscopic methods including optical absorption and EPR have reported K^+ induced dimerization of crown ether appended phthalocyanines and porphyrins[127,128]. From the resulting ground state triplet spectrum of the paramagnetic Cu^{2+} containing porphyrin derivatives, it has been possible to spectroscopically estimate the metal-metal distance of ~4.1 Å in the dimer.[127,128]. In the present study, using DFT B3LYP/3-21G$^{(*)}$ method,[133] the geometry and electronic structure of the dimer was probed to arrive at the geometry and electronic structures.[133] Figures 4.13a and b show the optimized structure of the dimer in two orientations. In the dimer structure, the two phthalocyanine rings are cofacially stacked with a Zn-Zn distance of 3.94 Å and inter-ring N-N distance of 3.97 Å. The N-Zn-Zn-N dihedral angle was found to be less than 1^o indicating almost perfect co-facial arrangement, in agreement with spectral shifts shown in Figure 4.11. The calculated HOMO's and LUMO's for the K^+ induced dimer were all π-orbitals and were nearly degenerate. As predicted for the closely interacting π-systems, the orbital coefficients were localized over both of the phthalocyanine rings (Figure 4.13c and d).

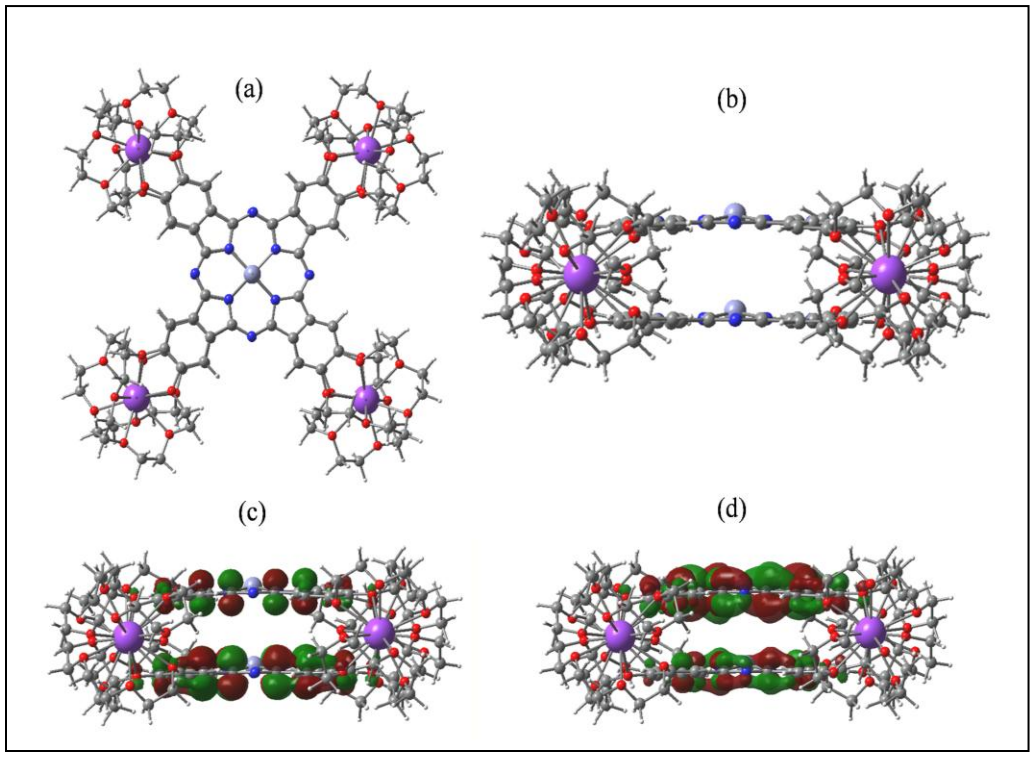

Figure 4.13: B3LYP/3-21G$^{(*)}$ optimized structure of $K_4[ZnTCPc]_2$ dimer (a and b). The HOMO and LUMO of the dimer are shown in c and d, respectively.

No orbital coefficient was present on the K^+ bound crown ether entities, suggesting absence of their involvement either an electron donor or an electron acceptor in electron transfer reaction.

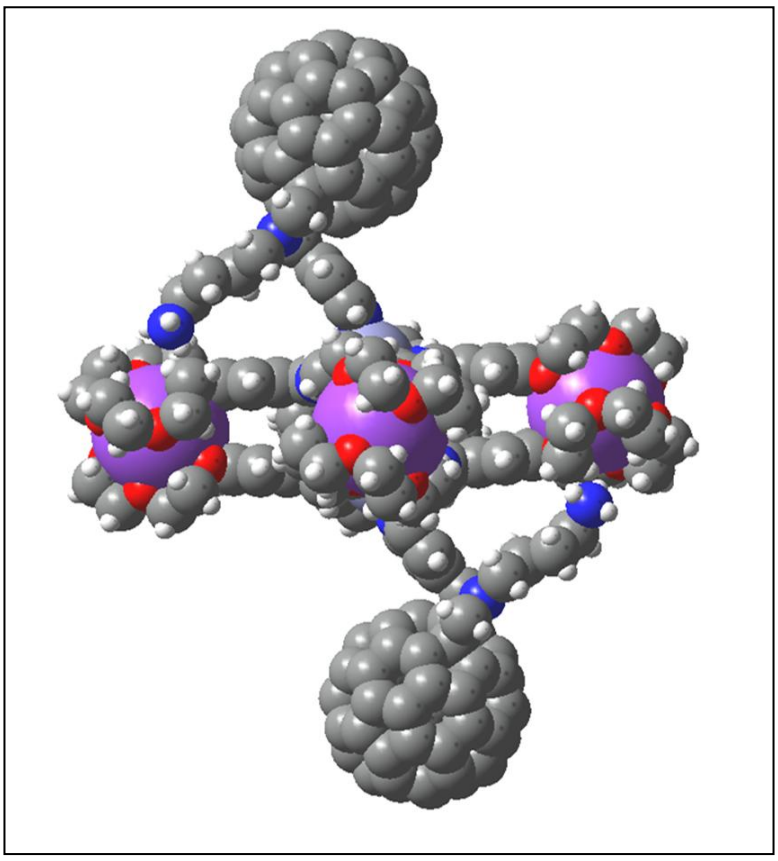

Figure 4.14: B3LYP/3-21G$^{(*)}$ optimized structure of the supramolecular $K_4[ZnTCPc]_2$:$(pyC_{60}NH_3^+)_2$ conjugate The counter cations and anions are omitted for keeping the structures simple.

Upon axial coordination of two equivalents of $pyC_{60}NH_3^+$ to the zinc phthalocyanine dimer, the resulting structures of the conjugate revealed the existence of the $K_4[ZnTCPc]_2$ dimer and formation of new Zn←N coordinate (← represents coordinate bond) and crown ether-NH_3^+ bonds (Figure 4.14). The center-to-center distance between zinc to the center of C_{60}, R_{CC} was estimated to be ~10.4 Å while the edge-to-edge distance, $R_{Ed\text{-}Ed}$ was found to be ~7.5 Å.

As envisioned, the adopted ‗two-point' binding strategy involving axial coordination and alkyl ammonium-crown ether binding resulted in complexes of defined distance and orientation.

Electrochemical Studies.

Electrochemical studies using cyclic voltammetric technique were performed to evaluate the redox potentials and also to probe the integrity of the supramolecular complex. As shown in Figure 5, the cyclic voltammograms of the monomer, ZnTCPc revealed the first oxidation and the first reduction processes located at $E_{1/2}$ = -0.08 and E_{pc} = -1.80 V vs. Fc/Fc^+, respectively (curve i). Upon forming the dimer, $K_4[ZnTCPc]_2$ by the addition of K^+ to the solution of ZnTCPc, the oxidation peaks revealed splitting as a consequence of strongly interacting phthalocyanine macrocycles.[128e,134] The split oxidation processes were located at $E_{1/2}$ = -0.20 and 0.05 V, respectively, while the reduction peak was located at E_{pc} = -1.71 V vs. Fc/Fc^+ (curve ii). Addition of 2 equivalents of $pyC_{60}NH_3^+$ (to form the tetrad as shown in Scheme 4.2) to the $K_4[ZnTCPc]_2$ dimer solution revealed additional changes in the peak potentials; however, the split oxidation peaks, signatures for keeping dimer in solution, were still retained (curve iii). The potentials of the split oxidation processes were located at $E_{1/2}$ = -0.18 and 0.02 V while the reduction was located at E_{pc} = -1.62 V. In addition to this, peaks at $E_{1/2}$ = -1.02 and -1.41 V vs. Fc/Fc^+ corresponding to the reduction of $pyC_{60}NH_3^+$ were also observed. The lower currents observed

for $K_4[ZnTCPc]_2$:$(pyC_{60}NH_3^+)_2$ is due to solution dilution. These results demonstrate the existence of the supramolecular donor-acceptor conjugate, $K_4[ZnTCPc]_2$:$(pyC_{60}NH_3^+)_2$, as depicted in Scheme 4.2.

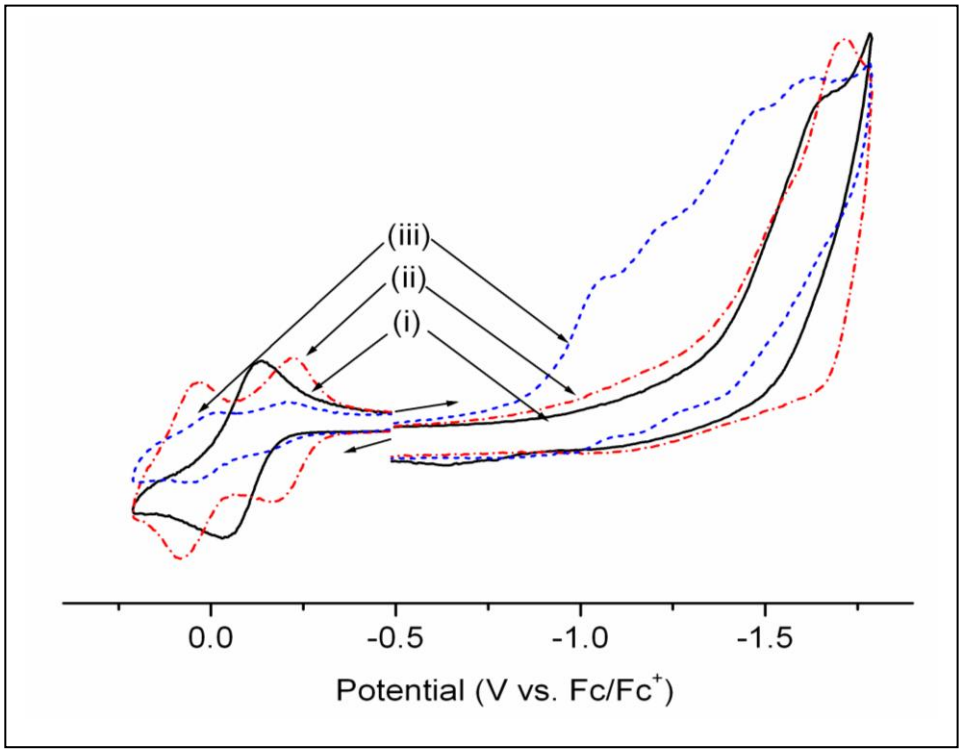

Figure 4.15. Cyclic voltammograms of (i) ZnTCPc, (ii) $K_4[ZnTCPc]_2$ and (iii) $K_4[ZnTCPc]_2$:$(pyC_{60}NH_3^+)_2$ obtained by the addition of 2 eq. $pyC_{60}NH_3^+$ in benzonitrile, 0.1 M $(n\text{-}C_4H_9)_4NClO_4$. San rate = 100 mV/s. The concentration of porphyrins was ~ 0.1 mM, and the potassium tetrakis(4-chlorophenylborate) used to induce dimerization was ~ 5 mM.

The free-energy changes for charge separation ($-\Delta G_{CS}$) via $K_4{}^1[ZnTCPc]_2{}^*$ and charge recombination ($-\Delta G_{CR}$) calculated from the electrochemical redox and emission data of ($E_{0\text{-}0}$ = 1.83 eV for $K_4[ZnTCPc]_2$) were found to be -1.00 eV

and -0.83 eV, respectively, for the supramolecular tetrad. In these calculations the electrostatic term was neglected since the positive and negative charges in the charge separated state are highly delocalized over the donor and acceptor macrocycles. The magnitude of $-\Delta G_{CS}$ suggests charge separation process to be located in the lower half of the normal Marcus curve.[111] Interestingly, the magnitude of $-\Delta G_{CR}$ suggests it to be in the upper half of the inverted Marcus curve.[11,111] That is, lower values of k_{CS} and relatively faster k_{CR} are expected from the free-energy calculations. However, as discussed in the subsequent section, the k_{CR} might further slow down due to rigidity of the phthalocyanine macrocycle which is expected to lower the re-organization energy.

Steady-state and Time-resolved Emission Studies.

Steady-state fluorescence spectrum of ZnTCPc showed two emission bands in benzonitrile located at 684 and 753 nm, respectively. In agreement with the earlier reports,[127e-f] addition of K^+ leading into the formation of the dimer, $K_4[ZnTCPc]_2$, the fluorescence of zinc phthalocyanine was quenched over 90 % of its original intensity as a consequence of static quenching (Figure 4.16). Further, as shown in the inset of Figure 4.16, a plot of emission intensity of the 684 nm band versus the number of equivalents of K^+ revealed a break at 2, a value expected for the 2:1 stoichiometric ratio between K^+ and ZnTCPc of the $K_4[ZnTCPc]_2$ complex, in agreement with the earlier discussed absorbance data (Figure 4.11).

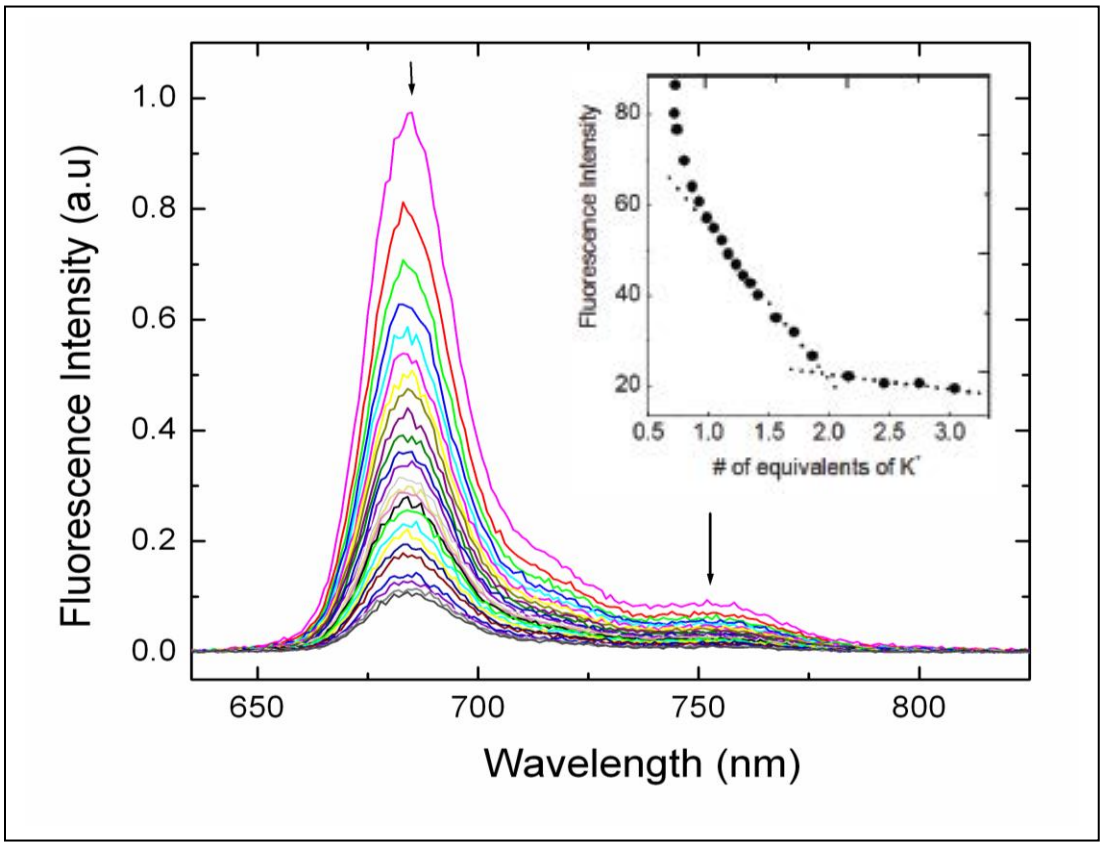

Figure 4.16: Effect of K^+ addition on the fluorescence emission of ZnTCPc (5 μM) in benzonitrile. λ_{ex} = 610 nm. Potassium tetrakis(4-chlorophenyl) borate (0.1 equiv each addition) was used as K^+ source. Figure inset shows a plot of emission intensity of the 684 nm band versus number of equivalents of K^+ added to arrive at the K^+:ZnTCPc stoichiometry. A break at 2 represents $K_4[ZnTCPc]_2$ formation.

It may also be mentioned here that the addition of size appropriate Na^+ for 15-crown-5 entities, leading into the formation of $Na_4[ZnTCPc]$ monomer, had no significant changes in the emission behavior, that is, no fluorescence

quenching was observed. Further, addition of $pyC_{60}NH_3^+$ to the the dimer solution to form the supramolecular conjugate caused additional quenching of the already quenched $K_4[ZnTCPc]_2$ emission to over 98%.

Time-resolved Emission Studies.

Figure 4.17 shows emission decay profiles of ZnTCPc under different solution conditions. The tetra crown substituted ZnTCPc revealed mono-exponential decay with a lifetime of 5.2 ns, close to that reported for zinc phthalocyanines in the literature.[127e-f] The dimer, $K_{4,}[ZnTCPc]_2$ formed by the addition of K^+ also revealed a mono-exponential decay with a lifetime of 7.4 ns, which was almost similar to that of ZnTCPc (Figures 4.17a and b).

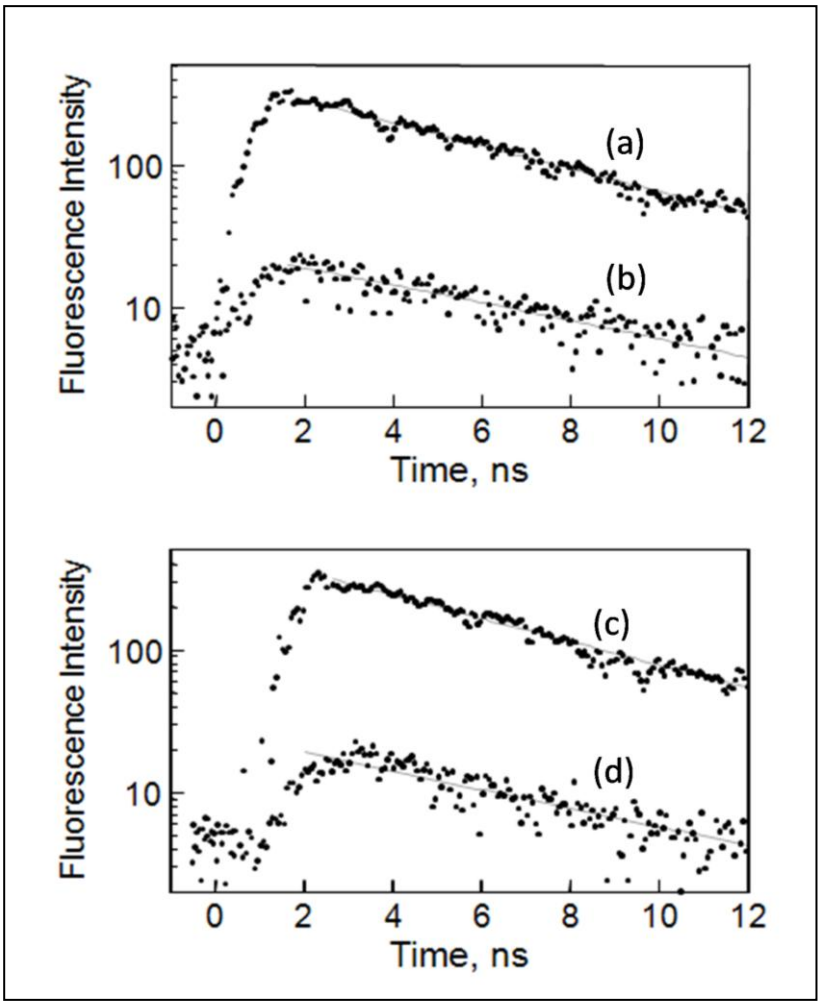

Figure 4.17. Time-resolved fluorescence spectrum of (a) ZnTCPc, (b) $K_4[ZnTCPc]_2$ formed by the addition of K^+ to ZnTCPc (1:4 equivalents), (c) ZnTCPc + $pyC_{60}NH_3^+$ (1:1 equivalent), and (d) tetrad, $K_4[ZnTCPc]_2$:$(pyC_{60}NH_3^+)_2$ in benzonitrile. The excitation wavelength was 410 nm and the decay was monitored at 687 nm. Potassium tetrakis(4-chlorophenyl)borate was used as K^+ source.

The slight increase in lifetime could be attributed to the de-aggregation of the zinc phthalocyanine upon addition of K^+. This observation supports the static quenching observed under steady state conditions shown in Figure 6. Surprisingly, the ZnTCPc:$pyC_{60}NH_3^+$ formed by mixing 1:1 equivalents of the monomer ZnTCPc and $pyC_{60}NH_3^+$, and the tetrad, K_4[ZnTCPc]$_2$:($pyC_{60}NH_3^+$)$_2$ also revealed mono-exponential decays with lifetimes of 5.0 and 6.9 ns, respectively (Figure 4.17c and d). These results suggest absence of any photoinduced processes originating from the singlet excited state of ZnTCPc. To confirm such a process, further femtosecond transient absorption studies were performed, as discussed below.

Femtosecond Transient Absorption Spectral Studies.

The absence of photoinduced electron transfer from the singlet excited state of both monomeric and dimeric forms of ZnTCPc in the presence of bound fullerene was confirmed from these studies. As shown in Figure 4.18a for ZnTCPc, the transient features were that of the excited singlet state undergoing intersystem crossing within 190 ps (Figure 4.18d).[111] The transient features observed for the dimer, K_4[ZnTCPc]$_2$ were not significantly different. The transient observed at 564 nm decayed within 210 ps (Figure 4.18e). Interestingly, the tetrad, K_4[ZnTCPc]$_2$:($pyC_{60}NH_3^+$)$_2$ had a significantly faster decay component of 34 ps (41 %) and a slow decay component of 200 ps (59 %) as shown in Figure 8f. The lifetime of the slow component is the same as that of

$K_4[ZnTCPc]_2$. Thus, the fast component corresponds to the quenching of the singlet excited state of $K_4[ZnTCPc]_2$ by $pyC_{60}NH_3^+$ in the tetrad, $K_4[ZnTCPc]_2$:$(pyC_{60}NH_3^+)_2$. This is supported by the agreement of the percentage of the fast component (41%) with the percentage of the tetrad formation (41%) estimated from the $K_{complex}$ value $(2.7 \pm 0.6) \times 10^3$ M^{-1}) under the experimental conditions in Figure 8f where concentration of $pyC_{60}NH_3^+$ is 2.6 x 10^{-4} M. A similar observation was made for the dyad, ZnTCPc:$pyC_{60}NH_3^+$.

A careful examination of the spectral data in Figure 4.18c clearly shows absence of transient bands corresponding to either the $ZnPc^{+\cdot}$ around 860 nm or $C_{60}^{\bullet -}$ around 1000 nm within allowed time scale of 3000 ps of our instrument. These results suggest occurrence of a much slower electron transfer process, if any, as predicted by the free-energy calculations, perhaps originating from the triplet excited state of ZnTCPc. To confirm this and identify the electron transfer products, transient absorption studies using nanosecond laser flash photolysis have been performed (*vide infra*).

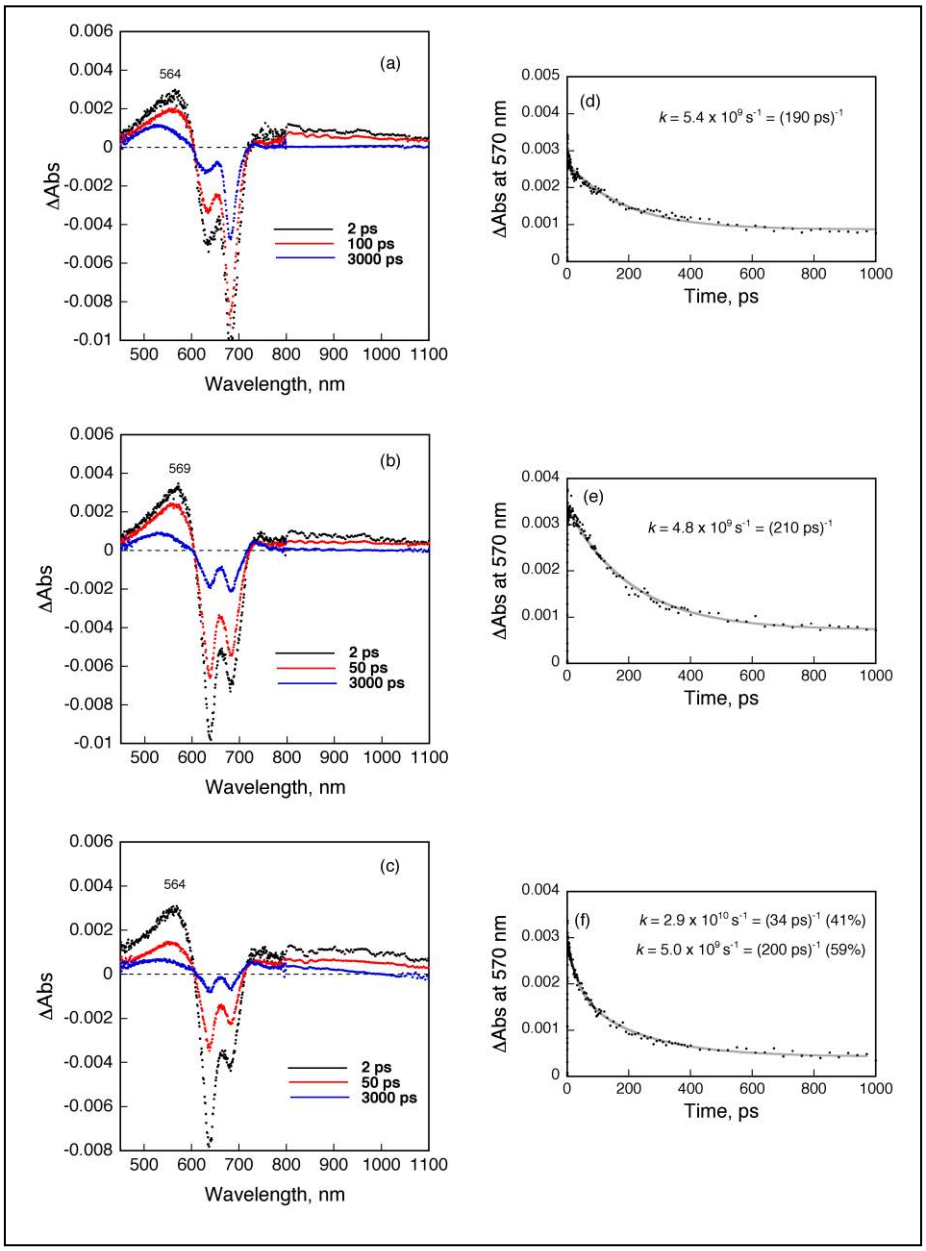

Figure 4.18. Femtosecond transient absorption spectrum recorded at different time intervals for (a) ZnTCPc (2.5×10^{-4} M), (b) ZnTCPc + K^+ to form the cofacial dimer, $K_4[ZnTCPc]_2$, and (c) tetrad, $K_4[ZnTCPc]_2$:$(pyC_{60}NH_3^+)_2$ (1.3×10^{-4} M) constructed by mixing ZnTCPc with two equivalents of K^+ and one equivalent of

$pyC_{60}NH_3^+$ in benzonitrile. λ_{ex} = 410 nm. The panels (d, e, and f) at the right show the first-order decay monitored at 570 nm.

Nanosecond Transient Absorption Spectral Studies.

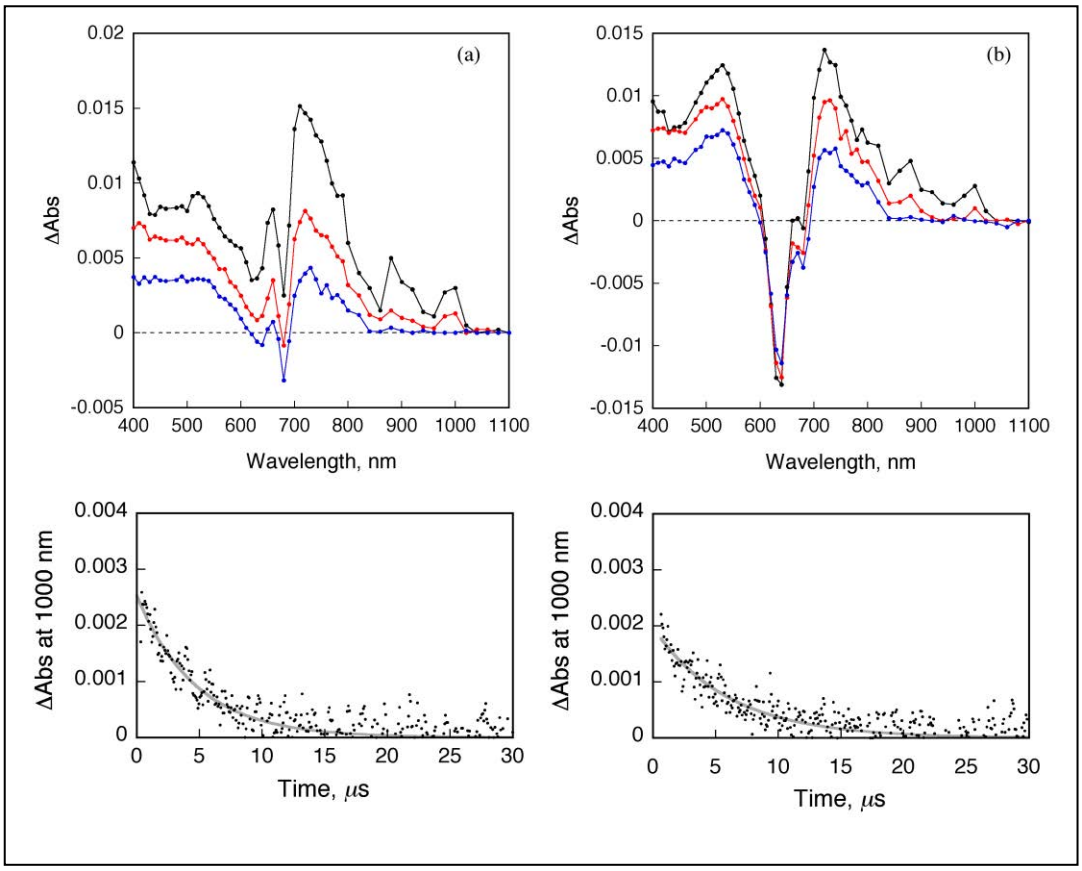

Figure 4.19: Nanosecond transient absorption spectra of (a) dyad, ZnTCPc:$pyC_{60}NH_3^+$ (1.0×10^{-4} M) formed by mixing equimolar ZnTCPc and $pyC_{60}NH_3^+$ and (b) tetrad, $K_4[ZnTCPc]_2$:$(pyC_{60}NH_3^+)_2$ (5.0×10^{-5} M) observed by 430 nm laser irradiation at 1, 4 and 10 μs time intervals in benzonitrile. The lower panel shows time profiles of fullerene anion radical peak at 1000 nm. The first-order decay is fitted by the solid line.

The confirmation of the charge-separated (CS) state and the role of phthalocyanine dimer in stabilizing the CS state were evident from these studies. As shown in Figure 4.19a, the transient absorption spectra of the dyad, ZnTCPc:py$C_{60}NH_3^+$, formed by complexing equimolar py$C_{60}NH_3^+$ and ZnTCPc in the absence of K^+, revealed bands at 870 and 1000 nm corresponding to the formation of $ZnTCPc^{+\cdot}$ and $C_{60}^{\bullet-}$, respectively.[39,60,126] Additional bands around 500 and 700 nm were also observed corresponding to the triplet excited state of fullerene entity ($^3C_{60}^*$).[126] The decay time profile of the absorption at 500 and 700 nm due to $^3C_{60}^*$ is clearly different from the decay of the absorption at 870 and 1000 nm due to the CS state, and the lifetime agrees with that of $^3C_{60}^*$. Thus, the transient absorption at 500 and 700 nm is assigned to the triplet excited state of unbound py$C_{60}NH_3^+$. The quantum yields of charge-separated state are determined as 0.50 $\pm$ 0.08 for ZnTCPc:py$C_{60}NH_3^+$ and 0.29 $\pm$ 0.06 for K_4[ZnTCPc]$_2$:(py$C_{60}NH_3^+$)$_2$ from the absorption of monofunctionalized fullerene at 1000 nm (ε_{1000} = 4700 M^{-1} cm^{-1})[33], using the absorbance of the triplet-triplet absorption of free base tetraphenylporphyrin, ε_{690} = 3500 M^{-1} cm^{-1} as a reference.[41d] These quantum yields agree within experimental errors with the percentages of ZnTCPc:py$C_{60}NH_3^+$ (56 $\pm$ 5 %) and K_4[ZnTCPc]$_2$:(py$C_{60}NH_3^+$)$_2$ (21 $\pm$ 4 %) estimated from the formation constants (1.25 x 10^4 M^{-1} and 2.7 x 10^3 M^{-1}, respectively) under the experimental conditions in Figure 4.19 where concentration of py$C_{60}NH_3^+$ is 1.0 x 10^{-4} M. Unfortunately the concentration of py$C_{60}NH_3^+$ for the nanosecond laser flash photolysis measurements is limited

due to the absorbance at the excitation wavelength, precluding attaining higher quantum yields.

The decay of the absorption at 870 and 1000 nm due to the CS state obeys first-order kinetics. This indicates that the charge recombination occurs in the supramolecular complex. The rate of charge recombination, k_{CR} obtained by monitoring the decay of $C_{60}^{\bullet-}$ was found to be 2.1 x 10^5 s^{-1} which resulted into a lifetime 4.8 μs for the CS state. Upon forming the supramolecular tetrad, that is, coordinating of two equivalent of $pyC_{60}NH_3^+$ to $K_4(ZnTCPc)_2$, the transient spectral features were almost similar to that observed for the dyad. That is, diagnostic bands corresponding to the formation of $ZnTCPc^{\bullet+}$ and $C_{60}^{\bullet-}$ were observed at the expected wavelengths (Figure 4.19b). The calculated k_{CR} was found to be 1.5 x 10^5 s^{-1} resulting into a lifetime of 6.7 μs for the CS state. This lifetime is significantly longer than the value (50 ns) reported for the corresponding tetrad using a zinc porphyrin dimer.[61] Such drastically increased lifetime of the CS state in the phthalocyanine dimer-C_{60} supramolecular complex, $K_4[ZnTCPc]_2$:$(pyC_{60}NH_3^+)_2$, as compared to the corresponding porphyrin dimer complex may result from a smaller reorganization energy of electron transfer for the more π-expanded phthalocyanine macrocycle relative to the porphyrin macrocycle.[136] Such a small reorganization energy of electron transfer also results in the much slower charge separation from the singlet excited state

(^{1}ZnTCPc*) as compared to the intersystem crossing to afford the triplet excited state (^{3}ZnTcPc*), as discussed below.

The energy diagram of the dyad (ZnTCPc:py$C_{60}NH_3^+$) and the tetrad (K_4[ZnTCPc]$_2$:(py$C_{60}NH_3^+$)$_2$) is shown in Figure 4.20, where the ZnPc and C_{60} denote the zinc phthalocyanine and fullerene moieties, respectively. Upon photoexcitation of the supramolecular complex, the singlet excited state (^{1}ZnPc*) is formed, which undergoes the intersystem crossing to afford the triplet excited state (^{3}ZnPc*-C_{60}) as shown in Figure 4.18.[137]

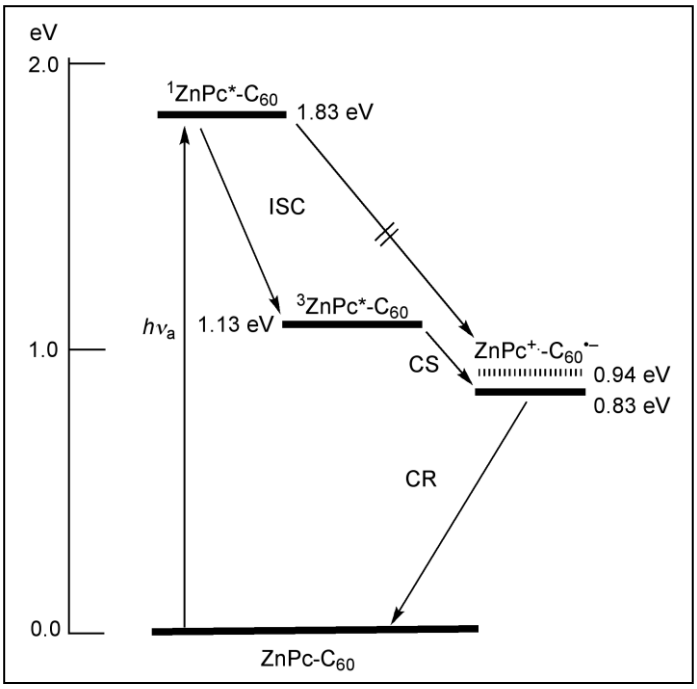

Figure 4.20: Energy level diagram showing the different photochemical events in the present supramolecular cofacial phthalocyanine dimer-fullerene conjugate (abbreviated as ZnPc-C_{60} for simplicity). The dotted line represents the energy level of the CS state of the monomeric phthalocyanine-fullerene dyad.

The driving force of charge separation (0.89 and 1.00 eV for the dyad and tetrad, respectively) is significantly larger than the reorganization energy of electron transfer judging from the reorganization energy of electron transfer of the porphyrin supramolecular complex (0.54 eV).[138] In such a case, the charge separation from $^1ZnPc^*$ is deeply in the Marcus inverted region,[111,135] where the CS rate is too slow to compete with the intersystem crossing. Then, the CS state is formed via electron transfer from $^3ZnPc^*$ as shown in Figure 4.19.[139] Unfortunately the CS rate from $^3ZnPc^*$ was too slow to be determined by femtosecond laser flash photolysis but too fast to be determined by nanosecond laser flash photolysis. The CS time scale is roughly estimated in the range between 3 ns and 100 ns. As a result of small reorganization energy of the relatively rigid phthalocyanine macrocycle in addition to that of fullerene,[140] long-lived CS states were attained as shown in Figure 4.19. The longer CS lifetime of the phthalocyanine dimer-C_{60} supramolecular complex, $K_4[ZnTCPc]_2$:$(pyC_{60}NH_3^+)_2$ (6.7 μs) as compared to that of the monomer complex, ZnTCPc:$pyC_{60}NH_3^+$ (4.8 μs) despite the smaller driving force of electron transfer in the Marcus inverted region may result from the smaller reorganization energy of electron transfer of the phthalocyanine dimer (0.83 eV) than the monomer (0.94 eV). The long CS lifetime with the driving force of 0.83 and 0.94 eV is consistent with no observation of the CS process from $^1ZnPc^*$ with the driving force of 0.89 and 1.00 eV, when the ISC process is much faster than the CS process.

4.4 Summary

An outstanding supramolecular tetrad as photosynthetic reaction center mimic of ‗special pair' dimer self-assembled to electron acceptors has been assembled using zinc phthalocyanine as electron donor and fullerene as electron acceptor. This methodology, fully based on well-defined self-assembly methods without utilization of covalent bonding to link the different entities, resulted into the formation of discrete supramolecular donor-acceptor conjugate. The structure of this supramolecule was deduced from spectroscopic, computational and electrochemical methods. Based on detailed analysis of the kinetic data from the time resolved emission and transient absorption spectroscopy of different time scales, it was found that the charge separation occurs from the triplet excited state of the ZnPc moiety to the C_{60} moiety rather than the singlet excited state to afford the long-lived CS state of the supramolecular complex. The longer CS lifetime of the phthalocyanine dimer-C_{60} supramolecular complex, $K_4[ZnTCPc]_2$:$(pyC_{60}NH_3^+)_2$ (6.7 μs) has been attained as compared to that of the monomer complex, ZnTCPc:$pyC_{60}NH_3^+$ (4.8 μs) despite the smaller driving force of back electron transfer because of a smaller reorganization energy of the phthalocyanine dimer; clearly delineating the role of the co-facial phthalocyanine dimer in stabilizing the CS state in donor-acceptor systems.

CHAPTER 5

Photo-induced Energy Transfer Followed by Electron Transfer in Donor-Accepor Conjugates

(A) Photosynthetic Antenna-Reaction Center Mimicry: Sequential Energy- and Electron Transfer in a Self-assembled Supramolecular Triad Composed of Boron Dipyrrin, Zinc Porphyrin and Fullerene

5.1 Introduction

The photochemical process of natural photosynthesis involves two major steps, namely, absorption and transportation of light energy of appropriate wavelength by the antenna light harvesting molecules to the reaction center and occurrence of photoinduced electron transfer (PET) to generate charge-separated entities by using the electronic excitation energy.[2] The light energy harvesting antenna system consists of chromophore arrays which transport energy via a singlet-singlet energy transfer mechanism among the chromophores. The antenna pigments, different for different organisms, are optimized for the quality of light in a particular environment and are effectively coupled to the reaction center. The reaction center absorbs the excitation energy and converts it to chemical energy in the form of transmembrane charge separation via a multistep electron transfer reaction. The stored electrochemical

energy in the form of charge-separated species is later converted into other forms, e.g., proton motive force, of biological useful forms of energy. Mimicry of the photosynthetic events by using synthetic model compounds is vital to further our understanding of the complex processes of bioenergetics. Research in this area also holds promise for technological advances in light energy harvesting, building molecular optoelectronics, and to develop photocatalysts capable of producing hydrogen.[141] In this regard, several studies using synthetic models focused on mimicking the reaction center where photoinduced electron transfer from the excited donor to acceptor occurs have been reported.[3f,12a,91,41a,b,d,92,98,119a,142,143] In the majority of these studies porphyrin has been used as an electron donor due to its close resemblance to the photosynthetic pigment, chlorophyll, and the established synthetic manipulations. The efficiency of charge separation in some of the donor-acceptor systems has been comparable to those found in natural reaction centers.[65,144] To mimic the antenna functionality, singlet-singlet energy transfer between two or more covalently linked or self-assembled porphyrins, or other chromophores, has been studied extensively.[20,145] Some of these molecular/supramolecular systems have revealed potentials for constructing photonic, photocatalytic, and optoelectronic devices. Although a number of studies dealing either with the reaction center or the antenna mimicry have been reported,[41a,b,c,91,92,98] a molecular/supramolecular complex performing combined antenna and reaction center functions has been scarce. A very few elegantly designed molecular/supramolecular systems involving two or more fluorophores and an electron acceptor like fullerene have

been developed and the occurrence of stepwise energy and electron transfer events has been demonstrated.[146] In the present study, we report a self-assembled supramolecular complex to perform the combined antenna-reaction center photochemical events. The structure of the model system is shown in Figure 5.1.

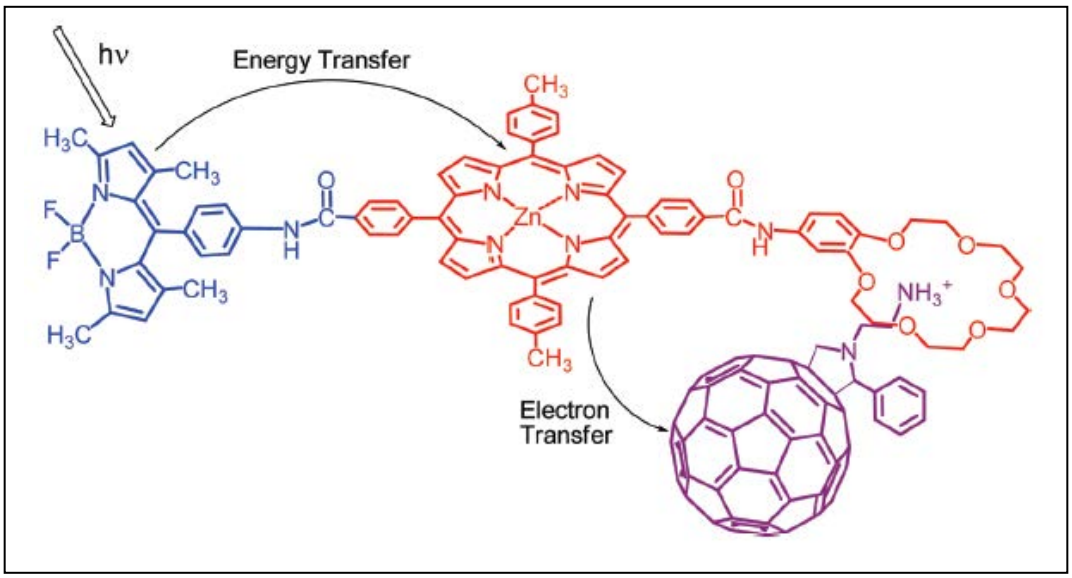

Figure 5.1: Structure of the presently constructed supramolecular triad composed of boron dipyrrin-zinc porphyrin-crown ether bound to an alkyl ammonium functionalized fulleropyrrolidine to probe ~~a~~ntenna-reaction center" functionalities.

Here, boron dipyrrin[147a] (also known as BODIY, abbreviated as BDP) acts as an energy absorbing and transferring antenna to the light energy acceptor,

zinc porphyrin. That is, when excited in the 480-515 nm wavelength region, selective excitation of BDP occurs, and due to good spectral overlap between BDP emission and zinc porphyrin absorption spectra, efficient singlet-singlet energy transfer to the zinc porphyrin takes place. When the crown ether receptor site of the dyad binds to an electron acceptor, an alkyl ammonium bearing fulleropyrrolidine,[59,129,148] photoinduced electron transfer from the singlet excited porphyrin to fulleropyrrolidine subsequently occurs. The easily oxidizable BDP unit in the present system is also involved to some extent in stabilizing the charge separated state. The stronger crown ether-crown binding approach permits us to perform the investigations in an electron transfer favoring solvent such as polar benzonitrile.[59,129,148] Systematic spectral, computational, electrochemical, and photochemical studies have been performed to unravel sequential energy and electron transfer in the newly built supramolecular triad.

5.2 Experimental section

Synthesis of Boron Dipyrrin-Zinc Porphyrin-Crown Ether Dyad.

5-(4-Methoxycarbonylphenyl)dipyrromethane (15). This compound was prepared according to the general procedure outlined for the synthesis of dipyrromethanes by Lindsey et al.[149] To a pyrrole (68 mL, 0.98 mol) was added methyl 4-formyl benzoate (4 g, 0.024 mol) and the solution was purged with argon for 15 min. Then trifluoroacetic acid (190 µL, 0.0024 mmol) was added and

the mixture was stirred at room temperature for 15 min. The mixture was then diluted with CH_2Cl_2 and NaOH (100 mL, 0.1 M) was added, then the organic layer was extracted over Na_2SO_4. The compound was purified by flash column chromatography on silica gel with hexanes: ethyl acetate (60:40 v/v) as eluent. Evaporation of the solvent yielded a pale-yellow solid. Yield 2 g (30%). ^{1}H NMR ($CDCl_3$) δ (ppm) 8.05-7.90 (m, 4H, pyrrole *NH* and phenyl *H*), 7.28 (d, 2H, phenyl *H*), 6.75-6.65 (m, 2H, pyrrole *H*), 6.18-6.12 (m, 2H, pyrrole *H*), 5.92-5.87 (m, 2H, pyrrole *H*), 5.54 (s, 1H, -CH-), 3.90 (s, 3H, -$COOCH_3$).

H_2-5,15-Di(p-methoxycarbonylphenyl)-10,20-di(p-tolyl)porphyrin(16). This compound was prepared according to Luo et al.[62] A solution of **15** (1.6 g, 5.71 mmol) was added to *p*-tolylaldehyde (675 μL, 5.71 mmol) in $CHCl_3$, and the reaction mixture was stirred under argon for 1 h. Then $BF_3.O(Et)_2$ (724 μL, 5.71 mmol) was added, and the reaction mixture was stirred in the dark for 2 h. *p*-Chloranil (2.11 g, 8.57 mmol) was added to the reddish-black reaction mixture, and the resulting mixture was stirred for 18 h. Triethylamine (2.4 mL, 17.25 mmol) was added, and the reaction mixture was stirred for 1 h and then concentrated. Column chromatography on silica gel with chloroform as eluent gave a mixture of five porphyrins including the titled compound. Subsequent column chromatography of this fraction on silica gel with toluene:$CHCl_3$ (70:30 v/v) as eluent yielded the titled compound as the third band. Evaporation of the solvent yielded the desired compound as a purple solid. Yield 208 mg (5%). ^{1}H

NMR ($CDCl_3$) δ (ppm) 8.82 (dd, 8H, -pyrrole *H*), 8.42 (d, 4H, phenyl *H*), 8.25 (d, 4H, phenyl *H*), 8.10 (d, 4H, phenyl *H*), 7.58 (d, 4H, phenyl *H*), 4.12 (s, 6H, -$COOCH_3$) 2.7 (s, 6H, -CH_3), -2.80 (s, br, 2H, -NH). ESI mass (in CHCl3) calcd 758.8, found [M + 1] 759.9.

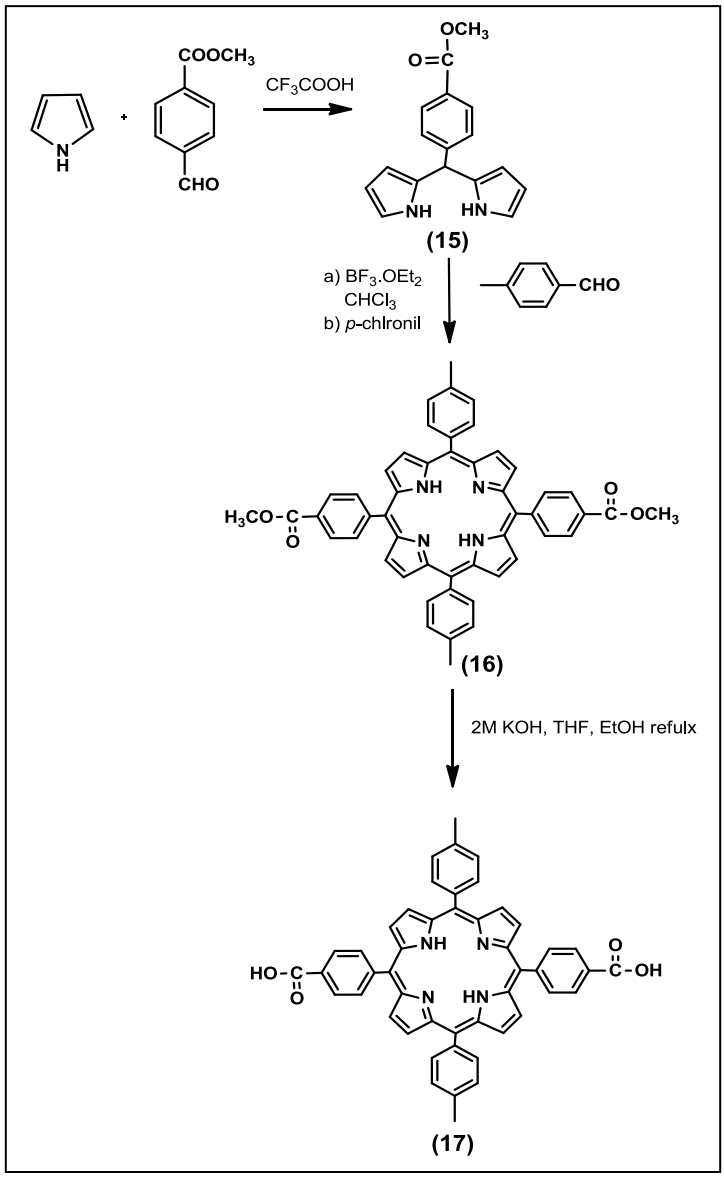

Scheme 5.1: Synthetic scheme adopted for H_2-5,15-di(p-carboxyphenyl)-10,20-di(*p*-tolyl)porphyrin

H_2-5,15-di(p-carboxyphenyl)-10,20-di(*p*-tolyl)porphyrin (17).[62] A suspension of **16** (200 mg, 0.264 mmol) in THF:ethanol (1:1) was taken in a 250 mL round-bottomed flask and potassium hydroxide (1.5 g, 0.027 mol) dissolved in water (12 mL) was added to it. The reaction mixture was refluxed for 8 h. After cooling, the solvent was evaporated; the residue was diluted with water (100 mL) and then filtered. The desired compound was obtained as the dipotassium salt. The aqueous suspension of porphyrin dipotassium salt was acidified with concentrated HCl (pH 2) and then filtered. The title compound was obtained as a purple powder and used without further purification. Yield 85 mg (44%). 1H NMR (DMSO-*d*) δ (ppm) 8.8 (dd, 8H, -pyrrole *H*), 8.38 (d, 8H, phenyl *H*), 8.18-8.10 (d, 4H, phenyl *H*), 7.65-7.55 (d, 4H, phenyl *H*), 2.55 (s, 6H, $-CH_3$), -2.40-2.95 (s, br, 2H, -NH).

1-(Difluoroboryl)-2-[(Z)-(3,5-dimethyl-2H-pyrrol-2-ylidene)(4-nitrophenyl)methyl]-3,5-dimethyl-1H-pyrrole (18).[146d] 2,4-Dimethylpyrrole (1.08 mL, 10.5 mmol) and 4-nitrobenzaldehyde (0.93 g, 6.2 mmol) were added to CH_2Cl_2 (600 mL) and purged with N_2, then trifluoroacetic acid (0.09 mL, 1.23 mmol) was added and the mixture was stirred for 2 h. The resulting solution was washed with 0.1 M NaOH (200 mL) and then water, dried over anhydrous Na_2SO_4, and filtered, then the solvent was evaporated. Next the product was redissolved in methylene chloride, and *p*-chloranil (1.36 g, 5.5 mmol) was added to the mixture. The resulting mixture was stirred for 10 min, then triethylamine (4

mL) and born trifluoride etherate (3.5 mL) were added to the mixture. After 1 h of stirring, the resulting solution was poured into water and the compound was extracted with methylene chloride. The compound was purified by flash column chromatography on silica gel with hexanes:$CHCl_3$ (60:40 v/v) as eluent. Evaporation of the solvent yielded 900 mg of the desired product. ^{1}H NMR ($CDCl_3$) δ (ppm) 8.39 (d, 2H, phenyl *H*), 7.55 (d, 2H, phenyl *H*), 6.02 (s, 2H, pyrrole *H*), 2.55 (s, 6H, -CH_3), 1.37 (s, 6H, -CH_3). ESI mass (in CH_2Cl_2) calcd 369.2, found [M + 1] 370.5.

1-(Difluoroboryl)-2-[(Z)-(3,5-dimethyl-2H-pyrrol-2-ylidene)(4-aminophenyl)methyl]-3,5-dimethyl-1H-pyrrole (19). A solution of **18** (100 mg) in THF (40 mL) was hydrogenated over 5% Pd on charcoal (300 mg) at room temperature and atmospheric pressure. Then, the catalyst was removed by filtration with use of Celite, and the filtrate was evaporated. The compound was purified by flash column chromatography on silica gel with toluene as eluent. Evaporation of the solvent yielded 36 mg of **19**, 40%. 1H NMR($CDCl_3$) δ (ppm) 7.00 (d, 2H, phenyl *H*), 6.78 (d, 2H, phenyl *H*), 5.96 (s, 2H, pyrrole *H*), 3.47 (br s, 2H, -NH_2), 2.55 (s, 6H, -CH_3), 1.49 (s, 6H, -CH_3). ESI mass (in CH_2Cl_2) calcd 339.2, found [M + 1] 340.3.

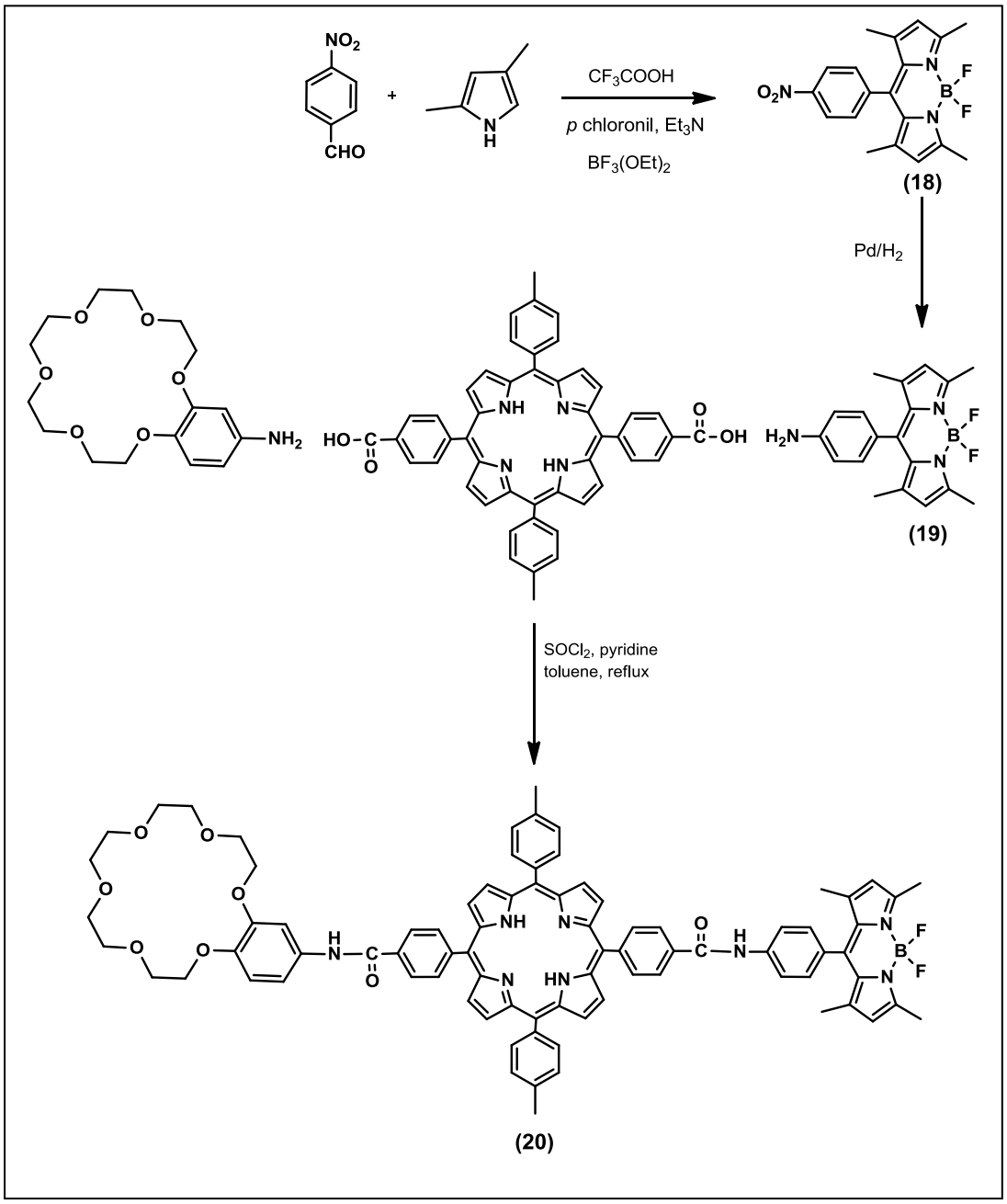

Scheme 5.2: Synthethic scheme adopted for compound **20**

H_2-5-{4-[2-(4-benzo-[18-crown-6])amido]phenyl}-15-{4-[2-(4-difluoroboron dipyrrinylphenyl)amido]phenyl}-10,20-di(ptolyl) porphyrin (20). Compound **17** (40 mg, 0.05 mmol) was taken in dry toluene (20 mL) then thionyl chloride (80 μL, 1.1 mmol) and pyridine (80 μL) were added and the reaction mixture was refluxed under argon for 3 h. After cooling, the solvent was evaporated and the resulting green compound was redissolved in dry toluene (25 mL). Then, pyridine (210 μL) was added followed by **19** (18 mg, 0.05 mmol) and 4′-amino benzo-[18-crown-6] (18 mg, 0.05 mmol). The reaction mixture was allowed to stir at room temperature under argon for 12 h. The solvent was evaporated and the crude compound was purified by column chromatography on silica gel with hexanes:$CHCl_3$ (10:90 v/v). Evaporation of the solvent yielded the desired compound (24 mg). ^{1}H NMR ($CDCl_3$) δ (ppm) 8.95-8.75 (m, 8H, -pyrrole *H*), 8.40-8.18 (m, 8H, phenyl *H*), 8.10 (d, 4H, phenyl *H*), 7.85 (d, 2H, BDP phenyl *H*), 7.56 (d, 4H, phenyl *H*), 7.35-7.28 (m, 1H, benzo-crown phenyl *H*), 7.12-7.05 (m, 1H, benzo-crown phenyl *H*), 6.90 (d, 1H, benzo-crown phenyl *H*), 6.02 (s, 2H, pyrrole *H*), 4.30-4.18 (m, 4H, crownethylene *H*), 4.00-3.90 (m, 4H, crownethylene *H*), 3.82-3.70 (m, 12H, crownethylene *H*), 2.70 (s, 6H, phenyl CH_3), 2.60 (s, 6H, pyrrole CH_3), 1.65 (s, 6H, pyrrole CH_3), -2.78 (s, br, 2H, -NH). ESI mass (in $CHCl_3$) calcd 1400.3 (with K^+), found [M + 1] (with K^+) 1401.2.

5-{4-[2-(4-benzo-[18-crown-6])amido]phenyl}-15-{4-[2-(4-difluoroboron dipyrrinylphenyl)amido]phenyl}-10,20-di(ptolyl)porphyrinato Zinc(II) (21). The free-base porphyrin **20** (20 mg) was dissolved in $CHCl_3$ (10 mL) then a saturated solution of zinc acetate in methanol was added to the solution, and the resulting mixture was refluxed for 2 h until the 515 nm band of free-base porphyrin had disappeared. At the end, the reaction mixture was washed with water and dried over anhydrous Na_2SO_4. Chromatography on silica gel column by using hexanes:$CHCl_3$ (10:90 v/v) gave the title compound. Yield 20 mg (90%). ^{1}H NMR ($CDCl_3$) δ (ppm) 9.00-8.80 (m, 8H, -pyrrole *H*), 8.43-8.21 (m, 8H, phenyl *H*), 8.12 (d, 4H, phenyl *H*), 7.88 (d, 2H, BDP phenyl *H*), 7.58 (d, 4H, phenyl *H*), 7.35-7.28 (m, 1H, benzo-crown phenyl *H*), 7.07-7.00 (m, 1H, benzo-crown phenyl *H*), 6.85 (d, 1H, benzo-crown phenyl *H*), 6.01 (s, 2H, pyrrole *H*), 4.28-4.15 (m, 4H, crownethylene *H*), 4.38-3.87 (m, 4H, crownethylene *H*), 3.79-3.76 (m, 12H, crownethylene *H*), 2.70 (s, 6H, phenyl CH_3), 2.62 (s, 6H, pyrrole CH_3), 1.69 (s, 6H, pyrrole CH_3). ESI mass (in $CHCl_3$) calcd 1463.7 (with K^+), found [M + 1] (with K^+) 1464.6.

5.3 Results and discussion

Ground State Properties of the Boron Dipyrrin-Zinc Porphyrin Dyad.

Figure 5.2 shows the optical absorption spectrum of the dyad along with the spectra of control compounds in benzonitrile. 1-(Difluoroboryl)-2-[(*Z*)-(3,5-dimethyl-2*H*-pyrrol-2-ylidene)(4-tolyl)methyl]-3,5-dimethyl-1*H*-pyrrole as BDP control and 5-{[4-(benzo-[18-crown-6])amido] phenyl}-10,15,20-tri(*p*-tolyl)porphyrinatozinc(II) as zinc porphyrin-crown ether control were used. The absorption bands located at 431, 559, and 602 nm correspond to zinc porphyrin while the band at 495 nm corresponds to the boron dipyrrin entity (plot i in Figure 5.2). The absorption band corresponding to BDP revealed ~2 nm red shift in the dyad, indicating some ground state interactions between the two chromophores. Importantly, the absorption of boron dipyrrin at 504 nm had no appreciable overlap with the ZnP-crown ether control or C_{60} ammonium cation absorption at these wavelengths (plots ii and iv in Figure 5.2). Hence, irradiation of the dyad at the 500 nm region is expected to a large extent to selectively excite the boron dipyrrin moiety of the dyad.

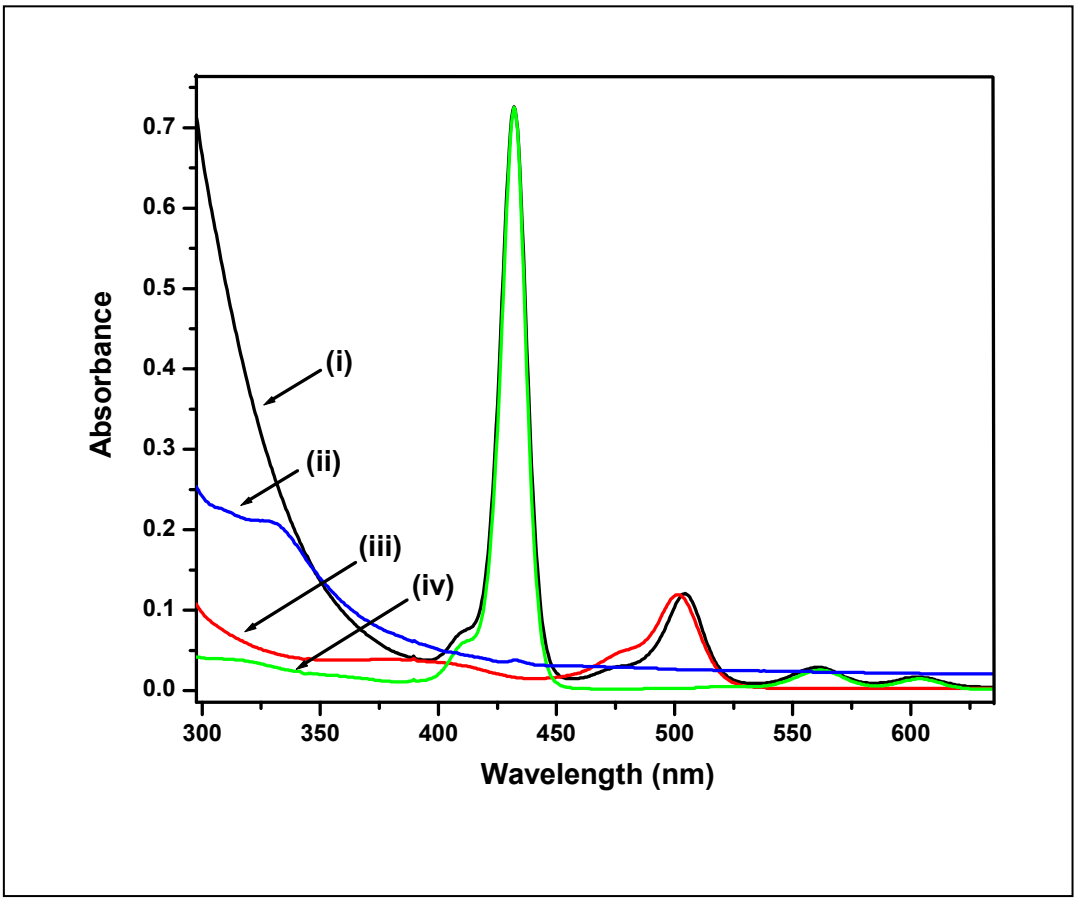

Figure 5.2: UV-visible spectra of (i) BDP-zinc porphyrin-crown ether dyad (0.32 μM), (ii) C_{60} ammonium cation (0.12 mM), (iii) *p*-tolyl boron dipyrrin (BDP control, 0.32 μM), and (iv) zinc porphyrin-crown ether (0.32 μM) in benzonitrile.

The fluorescence emission spectrum of the BDP-zinc porphyrin dyad, excited at 495 nm corresponding to BDP excitation, is shown in Figure 5.3 along with the emission of control compounds. An emission band at 515 nm corresponding to the emission of BDP was observed in addition to the zinc

porphyrin emission bands at 614 and 662 nm (Figure 5.3, plot i). The area under the 515 nm band was found to be quenched over 93% compared to BDP control (plot ii in Figure 5.3). In a control experiment, the emission spectrum of BDP control in the presence of an equimolar amount of zinc porphyrin-crown ether control was recorded. Under these conditions, the presence of zinc porphyrin had no effect on the BDP emission intensity; in addition, no significant emission corresponding to zinc porphyrin was observed. In separate control experiments, when ZnP-crown ether control and C_{60} ammonium cation were excited at 514 nm, no significant emission at 614 and 662 nm corresponding to ZnP in the former case or at 720 nm corresponding to fulleropyrrolidine in the latter case were observed (Figure 5.3, plots iii and iv). These results suggest the absence of simultaneous excitation of the different chromophores used to build the triad in Figure 5.1 when excited at 514 nm corresponding to BDP excitation, an important criteria to visualize sequential energy and electron transfer in ~~a~~ntenna-reaction center" mimics.

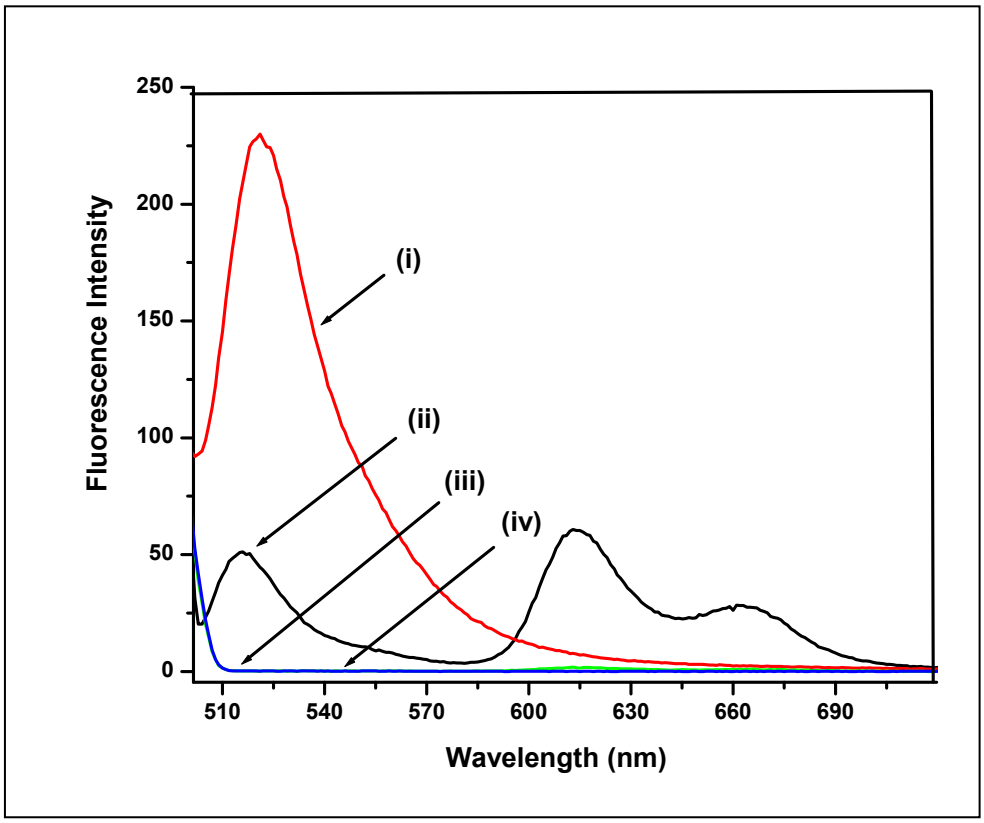

Figure 5.3: Fluorescence spectra of (i) BDP control (0.32 mM), (ii) BDP-zinc porphyrin-crown ether dyad (0.32 μM), (iii) zinc porphyrin-crown ether control (0.32 μM), and (iv) C_{60} ammonium cation (0.12 mM) in benzonitrile. The compounds were excited at λ_{ex} = 495 nm.

The occurrence of singlet excited energy transfer from BDP to zinc porphyrin in the dyad was also confirmed by recording the excitation spectrum of the dyad while holding the emission monochromator at 662 nm corresponding to zinc porphyrin emission. Such a spectrum shown in Figure 5.4 revealed the excitation band of not only the zinc porphyrin entity but also that of the BDP entity

of the dyad indicating energy transfer from BDP to zinc porphyrin. An estimation of energy transfer was performed by calculating the intensity ratio of the BDP band at 504 nm to the zinc porphyrin visible band at 559 nm (S_o to S_1 transition) in the absorption spectrum of the dyad in Figure 5.2, and in the excitation spectrum of the dyad in Figure 5.4. The peak intensity ratio from the absorption spectrum was found to be 4.1 while for the excitation spectrum this ratio was 4.05 amounting to an energy transfer efficiency of about 97%. These observations suggest excited energy transfer as the exclusive quenching mechanism in the BDP-zinc porphyrin dyad.

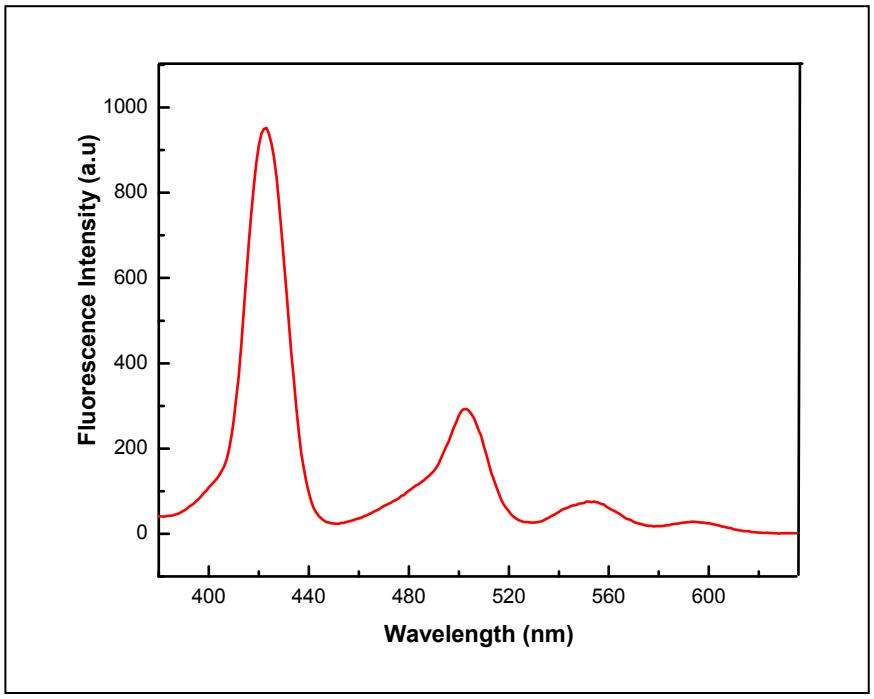

Figure 5.4: Excitation spectrum collected at 662 nm of the boron dipyrrin-zinc porphyrin dyad in benzonitrile.

Formation of the Supramolecular BDP-ZnP-Fullerene Triad

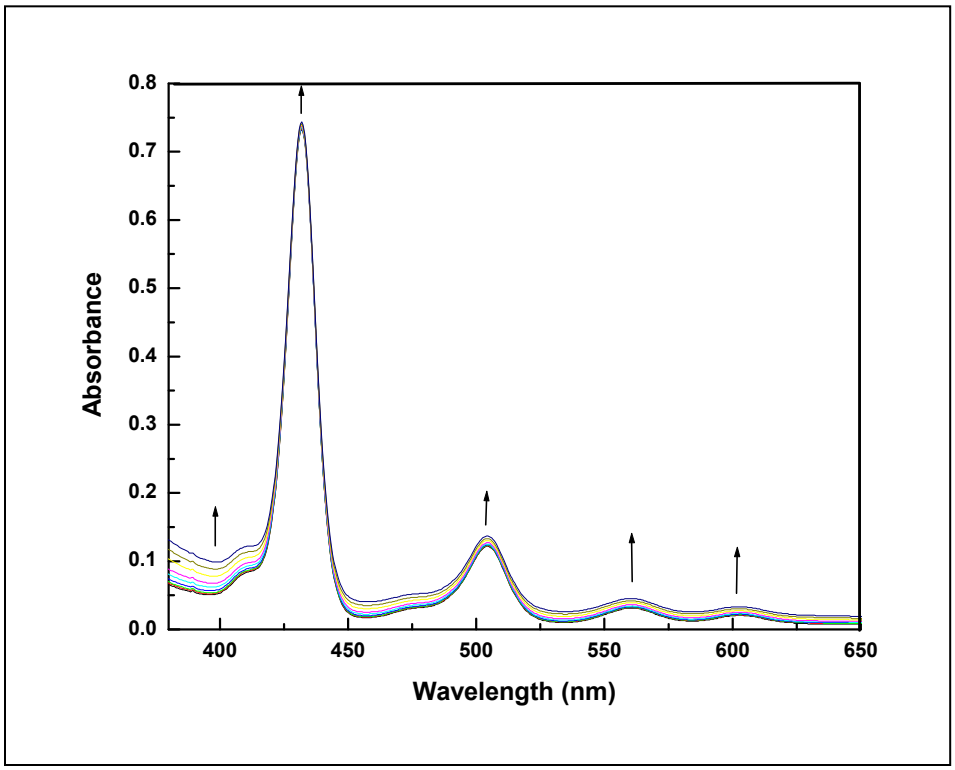

Figure 5.5: Absorption spectral changes observed during titration of BDP-zinc porphyrin-crown ether (3.6×10^{-6} M) binding to C_{60} ammonium cation (2.4×10^{-4} M each addition) in benzonitrile.

The formation of the supramolecular triad was initially followed by optical absorption and steady-state fluorescence methods. Figure 5.5 shows the spectral changes observed during the addition of C_{60} alkyl ammonium cation to the BDP-ZnP crown ether dyad in benzonitrile. The absorption bands corresponding to both the zinc porphyrin and BDP entities revealed a slight

increase in their intensity without any noticeable changes in the peak position. The increase in absorption in the 350 nm region is due to the presence of fulleropyrrolidine in solution. Extending the absorption wavelength well into the near-IR region revealed no new bands corresponding to any charge transfer complex. These observations suggest little, if any, interactions between the fullerene and either the zinc porphyrin or BDP entities. That is, a nonperturbed electronic structure of the zinc porphyrin and BDP chromophores upon formation of the triad via crown ether-alkyl ammonium binding is borne out from this study.

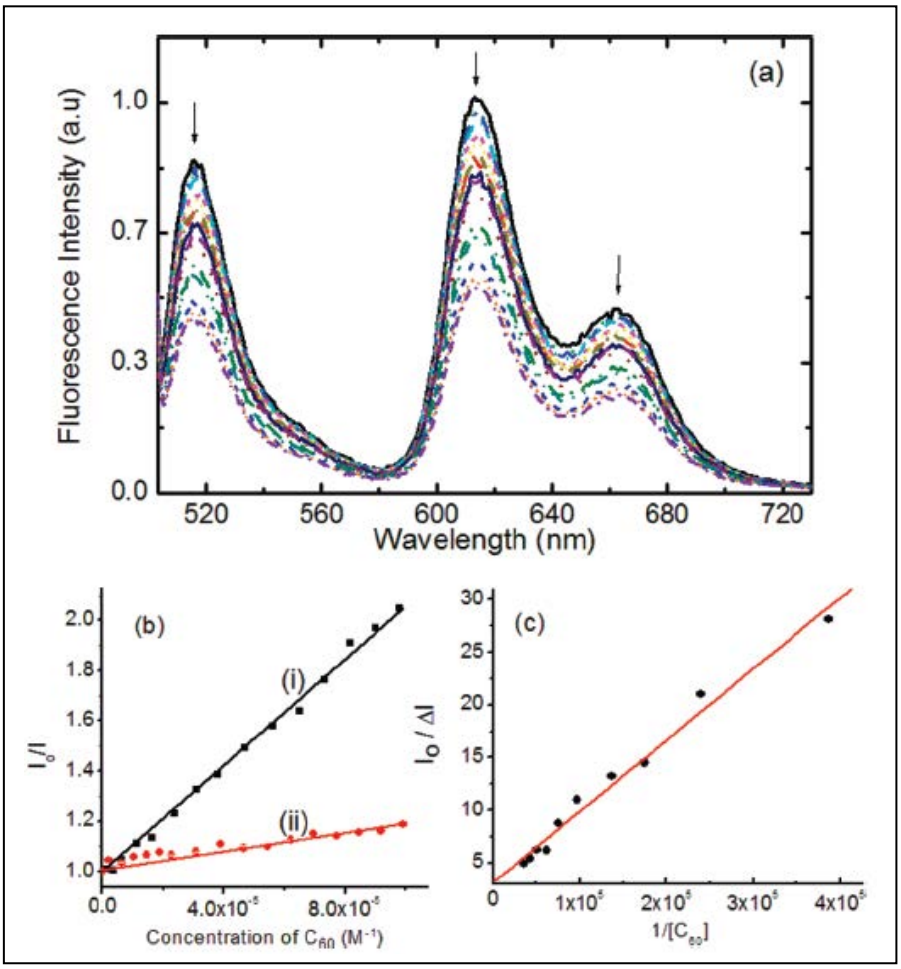

Figure 5.6: (a) Fluorescence spectral changes observed during increasing addition of C_{60} ammonium cation (0.24 mM each addition) to a solution of BDP-zinc porphyrin-crown ether to form the triad in benzonitrile. λ_{ex} = 495 nm. (b) Stern-Volmer plots constructed for (i) C_{60} ammonium cation and (ii) 2-phenyl fulleropyrrolidine quenching of BDP-zinc porphyrin-crown ether in benzonitrile (emission intensity of the 614 nm band of zinc porphyrin was monitored). (c) Benesi-Hildebrand plot constructed by monitoring the emission intensity at 614 nm band for calculating the binding constant. The abbreviations I_o and I

represent fluorescence intensity in the absence and presence of fullerene, and ΔI is the change of fluorescence intensity upon addition of fullerene.

The fluorescence spectrum recorded during the formation of the supramolecular triad revealed drastic quenching effects. As shown in Figure 5.6a, increasing addition of fulleropyrrolidine to the BDP-zinc porphyrin dyad solution quenched the fluorescence of not only the zinc porphyrin but also that of BDP suggesting the occurrence of excited state events. In a control experiment, the emission of BDP-zinc porphyrin dyad was monitored by increasing the addition of 2-phenylfulleropyrrlidine, that is, fulleropyrrolidine bearing no alkyl ammonium functionality. Stern-Volmer plots of zinc porphyrin quenching monitored at 614 nm were constructed as shown in Figure 5.6b; a higher slope was obtained for C_{60} alkyl ammonium cation binding to the dyad. The calculated Stern-Volmer constant, K_{SV}, was found to be 1.06×10^5 M^{-1} for C_{60} alkyl ammonium cation binding to the dyad, which compared with a value of 1.9×10^3 M^{-1} for 2-phenylfulleropyrrolidine binding to the dyad. The higher K_{SV} value for the former case unanimously proves C_{60} alkyl ammonium binding to the crown ether induced intramolecular quenching. The magnitude of K_{SV} for 2-phenyl-fulleropyrrolidine quenching is slightly larger than that predicted for a biomolecular quenching process.[9] This could be rationalized by the weaker porphyrin-fullerene and fullerene-crown ether interactions reported earlier.[150] To calculate the binding constant of crown ether-alkyl ammonium cation binding, the quenching data were analyzed by using the Benesi-Hildebrand method.[93] Such

analysis yielded a straight line plot indicating a 1:1 complex formation (Figure 5.6c) and a binding constant, *K*, of 4.6 × 10^4 M^{-1}. The magnitude of the binding constant is comparable to the *K* values reported earlier for other crown ether-alkyl ammonium binding[59,129,148] suggesting stable complex formation in the studied benzonitrile solvent.

Geometry Optimization by Computational Calculations.

The structure of the supramolecular triad was visualized by performing computational studies at the B3LYP/3-21G(*) level.[94] Figure 5.7 shows the optimized structures in two orientations of the triad in which two forms, viz., ~~c~~lose" and ~~e~~xtended", were visualized. Both of the structures were energetically stable as they revealed minima on a Born-Oppenheimer potential energy surface. The ~~c~~lose" form was energetically favored by ~7.6 kcal/mol, which could be attributed to the spontaneous attraction between porphyrin and fullerene31 and the flexible nature of the benzo-18-crown-6 entity. However, this energy could be an overestimation due to a large Basis Set Superposition Errors (BSSE) as a result of the low-level B3LYP/3-21G(*) basis set.[151] In the ~~c~~lose" form of the triad, the distance between the boron atom of BDP and the zinc of ZnP was 18.77 Å while the distance between the zinc and the center of C_{60} was found to be 5.59 Å suggesting closely disposed donor-acceptor entities. Similarly, the distance between boron and the center of C_{60} was found to be 20.47 Å being sufficiently far from the electron acceptor fullerene. In the ~~e~~xtended" form, the

distance between the boron atom of BDP and the zinc of ZnP was 18.68 Å while the distance between the zinc and the center of C_{60} was found to be 18.59 Å suggesting distantly disposed donor-acceptor entities. The distance between boron and the center of C_{60} was found to be 35.03 Å being far from the electron acceptor fullerene. It is interesting to note that the boron dipyrrin and porphyrin macrocycles were in the same plane for both forms of the structures, which may facilitate energy transfer due to favorable macrocycle orientation.

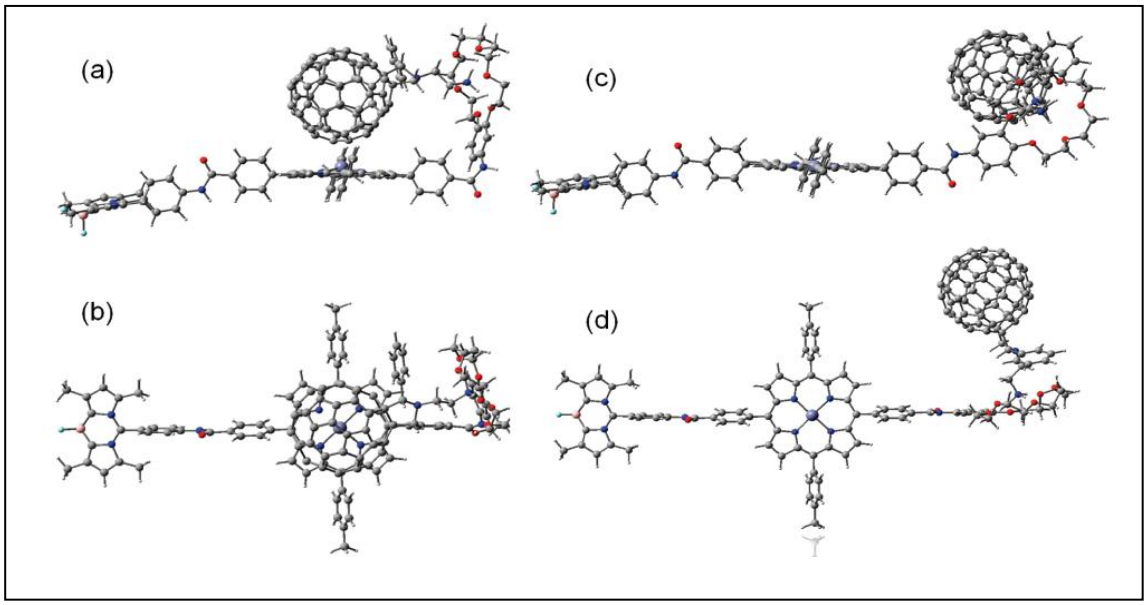

Figure 5.7: B3LYP/3-21G(*) optimized structures of supramolecular triad comprised of boron dipyrrin-zinc porphyrin-crown ether bound to C_{60} alkyl ammonium cation in the close (a and b) and extended (c and d) forms.

Cyclic Voltammetry Studies and Estimation of Energy Levels.

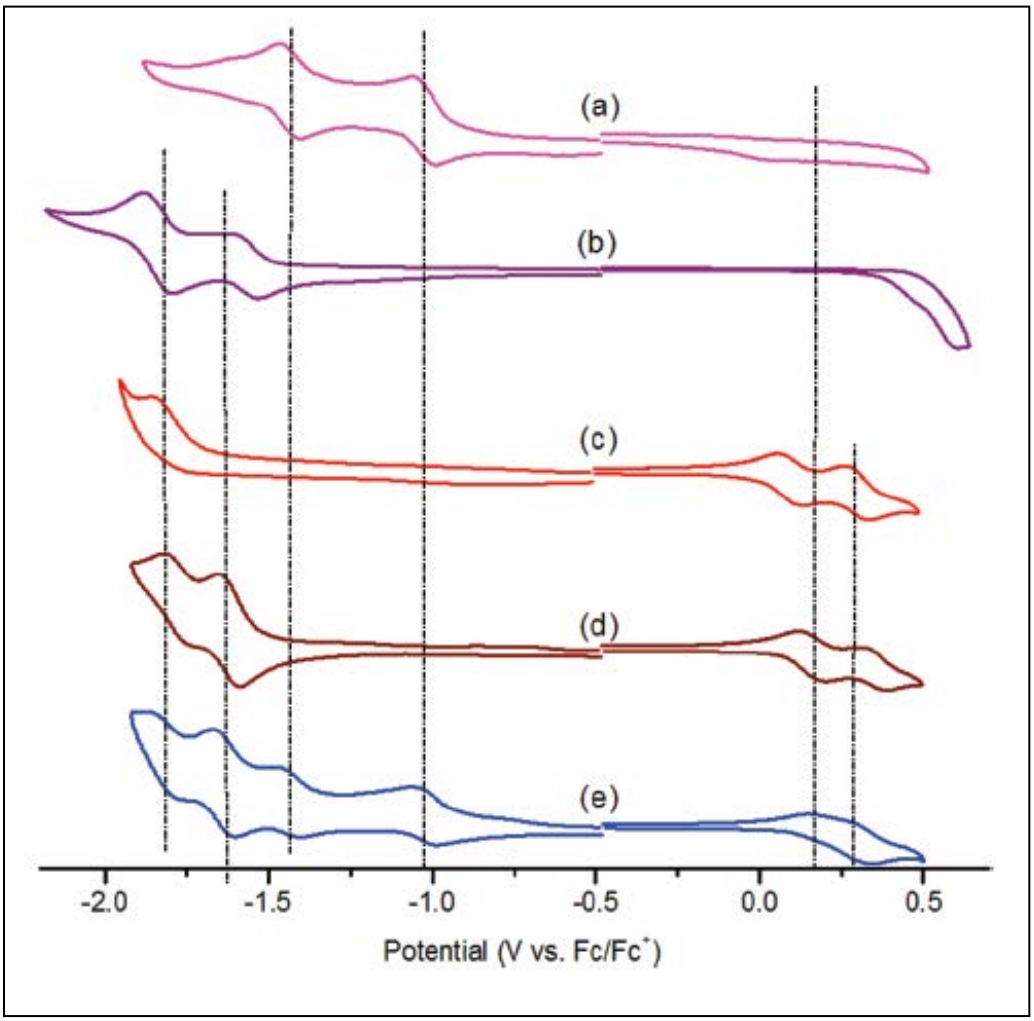

Figure 5.8: Cyclic voltammograms of (a) C_{60} alkyl ammonium cation, (b) *p*-tolyl boron dipyrrin (BDP control) (c) zinc porphyrin-crown ether, (d) BDP-zinc porphyrin-crown ether dyad, and (e) BDP-zinc porphyrin-crown ether-fullerene triad in benzonitrile containing 0.1 (TBA)ClO_4. Scan rate) 0.1 V/s.

Electrochemical studies using the cyclic voltammetric technique were performed to arrive at the redox potentials of the newly assembled supramolecular triad. Figure 5.8 shows cyclic voltammograms of the investigated compounds along with the control compounds during both negative and positive scanning of the potential. The first two reductions of the C_{60} alkyl ammonium cation were located at $E_{1/2}$ = -1.03 and -1.45 V vs. Fc/Fc^+, respectively (Figure 6a).[129b]

The peak-to-peak separation and plots of peak current versus square root of scan rate indicated both electroreductions to be one-electron reversible processes.[152] The one-electron reductions of the BDP control were located at $E_{1/2}$ = -1.56 and -1.83 V vs. Fc/Fc^+ while its irreversible oxidations were located at E_{pa} = 0.46 and 0.61 V vs. Fc/Fc^+ (Figure 5.8b), respectively. The first two reversible oxidations of the zinc porphyrin-crown ether were located at $E_{1/2}$ = 0.11 and 0.29 V vs. Fc/Fc^+ while the first irreversible reduction was located at E_{pc} = -1.85 V vs. Fc/Fc^+, respectively (Figure 5.8c). As shown in Figure 5.8d, the first two reversible oxidations of the BDP-zinc porphyrin crown ether dyad were located at $E_{1/2}$ = 0.17 and 0.36 V vs. Fc/Fc^+ while the first two reversible reductions were located at $E_{1/2}$ = -1.61 and -1.71 V vs. Fc/Fc^+, respectively. Control experiments involving pristine BDP and zinc porphyrin indicated that both these oxidations involve porphyrin macrocycle and not the BDP entity. By

comparison of the redox potentials of starting control compounds in Figure 5.8a-c, the first reduction of the BDP-ZnPcrown ether dyad at -1.61 V was ascribed to the reduction of the BDP entity while the first oxidation at 0.17 was ascribed to the zinc porphyrin entity, respectively. Addition of the C_{60} alkyl ammonium cation to the BDP-ZnPcrown ether dyad solution to form the supramolecular triad revealed noticeable changes in the redox potentials. That is, the first oxidation process of the zinc porphyrin revealed a slight positive shift and the second oxidation a slight negative shift, located at $E_{1/2}$ = 0.20 and 0.28 V vs. Fc/Fc^{+}, respectively (Figure 5.8e). The small anodic shift of zinc porphyrin upon the formation of the triad suggests intramolecular interactions between the fullerene and zinc porphyrin entities, a result that readily agrees with the predictions of the earlier discussed computational results. As discussed earlier, our attempts to locate a new absorption band corresponding to charge transfer interactions in the near-IR region were not successful. Perhaps the extinction coefficient for such absorption band is too small to be detected even at relatively higher concentrations. The first two reductions of the supramolecular triad were located at $E_{1/2}$ = -1.00 and -1.44 V vs. Fc/Fc^{+}, and by comparison with the redox potentials of the control compounds both processes were assigned to the one-electron reduction of the C_{60} alkyl ammonium cation. These values are close to that reported for similar fulleropyrrolidine derivatives in benzonitrile.[59,129,148] The third reduction process of the triad located at -1.62 V corresponding to BDP reduction revealed no significant changes as compared to the corresponding reductions of the dyad.

By using the electrochemical data, excited energies and distances between the chromophores, the free energies of charge separation (ΔG_{CS}), and charge recombination (ΔG_{CR}) were calculated, using eqs 5.1 and 5.2, by Weller's approach.

$$\Delta G_{CR} = e(E_{ox} - E_{red}) + \Delta G_S \quad \textbf{(5.1)}$$

where $\Delta G_S = -e^2/(4\pi\varepsilon_0\varepsilon_R R_{Ct\text{-}Ct})$ and ε_0 and ε_R refer to vacuum permittivity and dielectric constant of benzonitrile.

$$-G_{CS} = \Delta E_{0-0} - \Delta G_{CR} \quad \textbf{(5.2)}$$

where $\Delta E_{0\text{-}0}$ is the energy of the lowest excited state of ZnP (2.05 eV). Such calculations revealed a ΔG_{CS} value of -0.82 eV for electron transfer from the singlet excited zinc porphyrin to fullerene, and a ΔG_{CR} value of -1.18 eV for the charge recombination process, for both "close" and "extended" forms of the structures. For comparison purposes, the ΔG_{CS} and ΔG_{CR} values for charge separation within the BDP-zinc porphyrin, donor-acceptor dyad were also calculated. The ΔG_{CS} and ΔG_{CR} originating from the ^{1}ZnP*-BDP were found to be -0.41 and -1.63 eV, respectively. These studies, in addition to the thermodynamic feasibility of the occurrence of electron transfer, also indicate fullerene being the superior electron acceptor in the supramolecular triad.

Time-Resolved Emission and Transient Absorption Studies

The photodynamics of the energy and charge transfer of the newly developed dyad and triad was studied by pico- and femtosecond optical spectroscopy techniques. The emission decays measured by using the time-correlated single photon counting (TCSPC) method are shown in Figure 5.9. The boron dipyrrin-zinc porphyrin dyad in benzonitrile was excited at 485 nm. At this wavelength boron dipyrrin was mainly excited. The emission decays were monitored at 520 and 620 nm corresponding to the emission wavelengths of boron dipyrrin and zinc porphyrin fluorescence, respectively. The data could be fitted by using a three-exponential model. The major fast component had a lifetime of approximately 60 ps, and appeared as fast emission decay at 520 nm and concurrent emission growth at 620 nm, respectively.

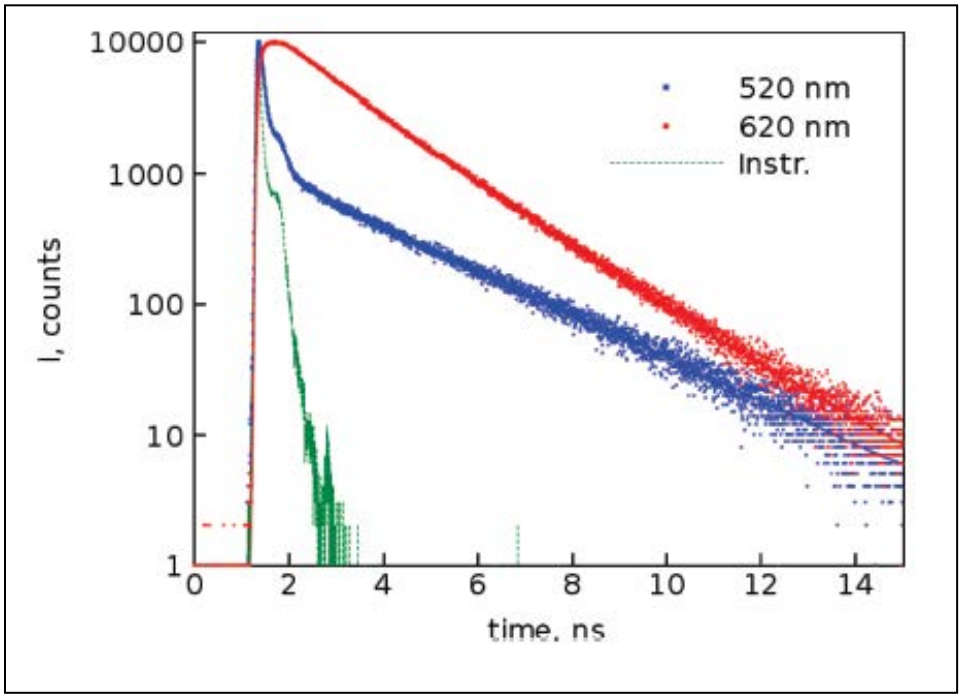

Figure 5.9. Emission decays of BDP-ZnP dyad in benzonitrile at 620 and 520 nm. The excitation wavelength was 485 nm. These measurements were carried out by using the TCSPC technique. The dashed line is the instrument response function.

This component can be associated with the energy transfer from the singlet excited boron dipyrrin to zinc porphyrin. However, the lifetime determined by this method may not be very accurate as it is approaching the time resolution of the instrument (65 ps, fwhm). The second component with a lifetime of 1.6 ns was only observed at 620 nm corresponding to the fluorescence lifetime of zinc

porphyrin. In addition, a very weak longest lived component with a lifetime of 2.8 ns was seen only at 520 nm attributed to BDP. A better time resolution was achieved by using the up conversion method for the emission decay measurements. Unfortunately, for this method the only available excitation wavelength was 400 nm, at which both the BDP and ZnP chromophores have appreciable absorption. However, the quenching of the BDP chromophore at 520 nm was clearly seen as presented in Figure 5.10. The best fit of the data was achieved by using a three-exponential model.

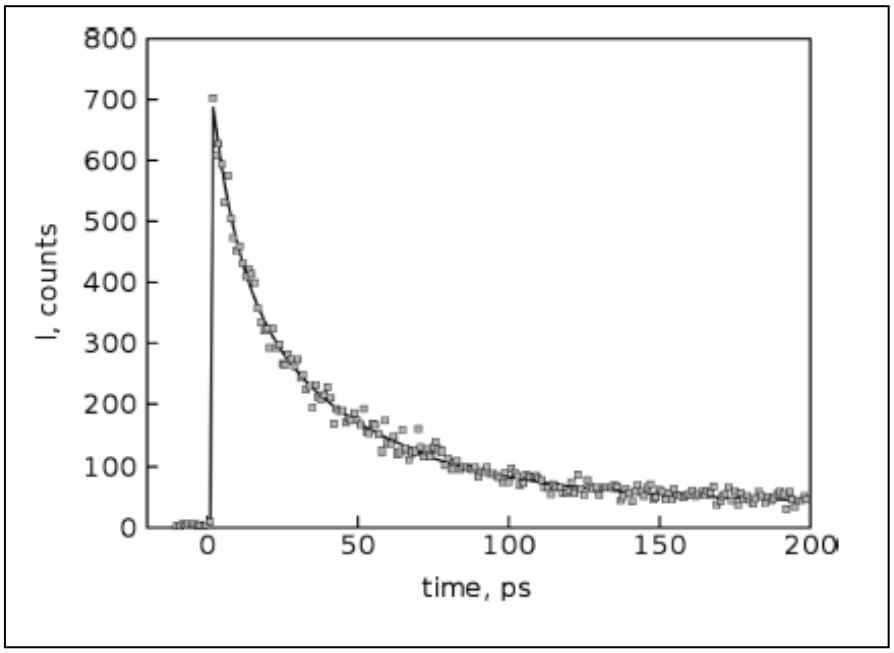

Figure 5.10: Emission decay of the BDP-ZnP dyad monitored at 520 nm by the up-conversion method in benzonitrile. The solid line presents the data fit (see text). Excitation wavelength was 400 nm.

The two fast decay components had almost equal relative intensities, 40% and 54%, with lifetimes of 9 and 40 ps, respectively. The third longer lived component was a minor one with contribution less than 6%. The two fast decay components indicate that two conformers of the BDP-ZnP dyad coexist in solution with somewhat different mutual orientations.

The transient absorption measurements with the use of femtosecond pump-probe methods also confirmed the occurrence of efficient energy transfer from BDP to ZnP, as presented in Figure 5.11.

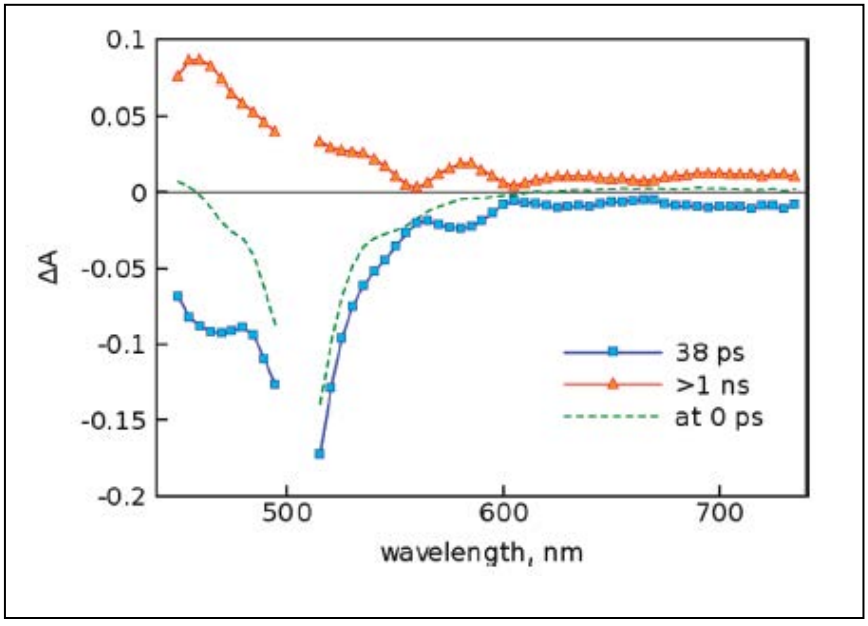

Figure 5.11: Transient absorption component spectra of BDP-ZnP dyad in benzonitrile (lines with symbols), and time-resolved spectrum right after excitation (dotted line). Excitation wavelength was 500 nm.

The experiments were carried out with an excitation wavelength of 500 nm to populate the BDP singlet excited state selectively, and analyzed by using a global biexponential fitting of the data. The initial transient absorption spectrum of the dyad (at 0 ps delay time, shown by the dotted line in Figure 5.11) had characteristic features of the bleached ground state absorption of the BDP chromophore. With a time constant close to 40 ps, the transient absorption spectrum turned into one with characteristic features of the porphyrin singlet excited state (the longest lived component in Figure 5.11). The transition time correlates well with the emission decay lifetime at 520 nm. By applying a three-exponential fit to the transient absorption measurements the fit quality was slightly improved and the calculated lifetimes, 18 and 52 ps, matched well with those obtained from up-conversion measurements. An example of fit is presented in Figure 5.12 for the transient absorption measured at 530 nm.

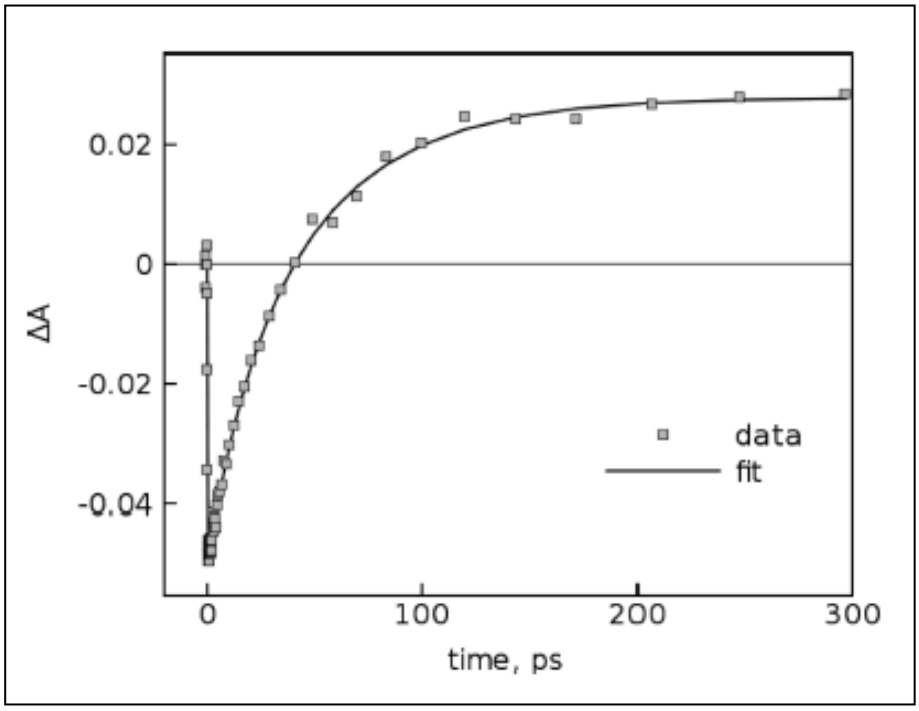

Figure 5.12: Transient absorption time profile of BDP-ZnP dyad in benzonitrile at 530 nm (squares). The data fit is shown by the solid line. Excitation wavelength was 500 nm.

At this wavelength the relative intensities of the fast component were 26% and 74%, respectively. The absorption maximum of ZnP is located at 431 nm, which could be used for selective excitation of the porphyrin chromophore. Unfortunately this wavelength was not available for excitation for the pump-probe

instrument used. The closest available wavelength was 410 nm, at which some fraction of BDP chromophore was also excited. The time-resolved transient absorption spectra obtained with the 410 nm excitation for the BDP-ZnP dyad are presented in Figure 5.13.

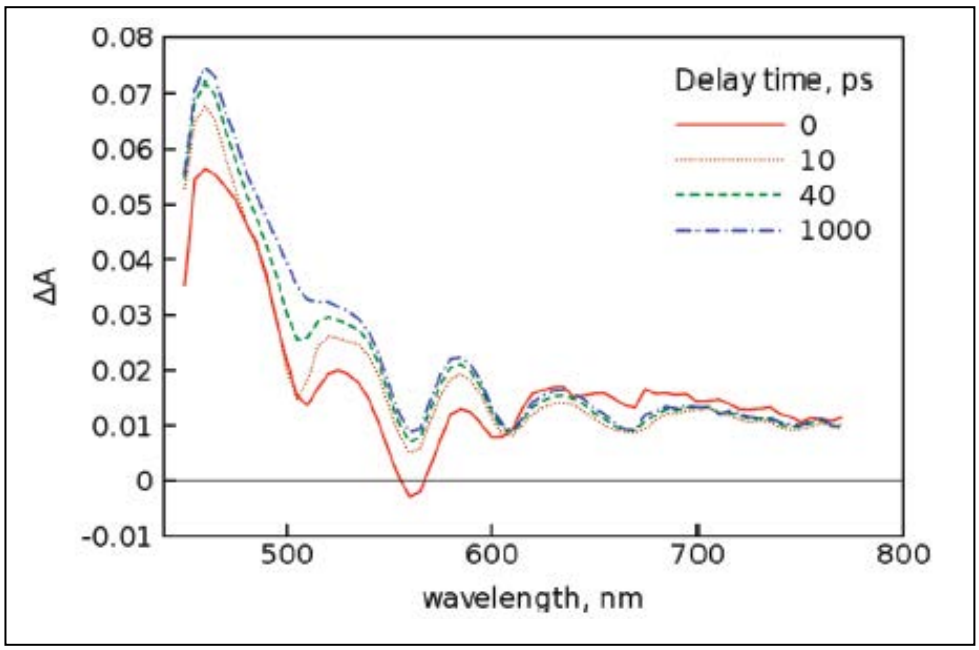

Figure 5.13: Time resolved transient absorption spectra of BDP-ZnP dyad in benzonitrile. The delay times are indicated in the plot. The excitation wavelength was 410 nm.

The spectrum at zero delay time (right after excitation) revealed characteristic features of both BDP and ZnP singlet excited states. A dip in the absorbance at 500 nm due to the bleaching of the BDP chromophore ground state was observed indicating that some fraction of the chromophore is in the

excited state. The appearance of the 460 nm peak and the bleaching at 560 and 600 nm are typical features of the porphyrin singlet excited state.

As the delay time increased, the dip at 500 nm disappeared and the absorption at 460 nm increased indicating the energy transfer from BDP to ZnP chromophore. Upon addition of C_{60} to the solution to form the supramolecular triad, the shapes of the spectra recorded after a few picoseconds and longer delay times changed significantly, as presented in Figure 5.14.

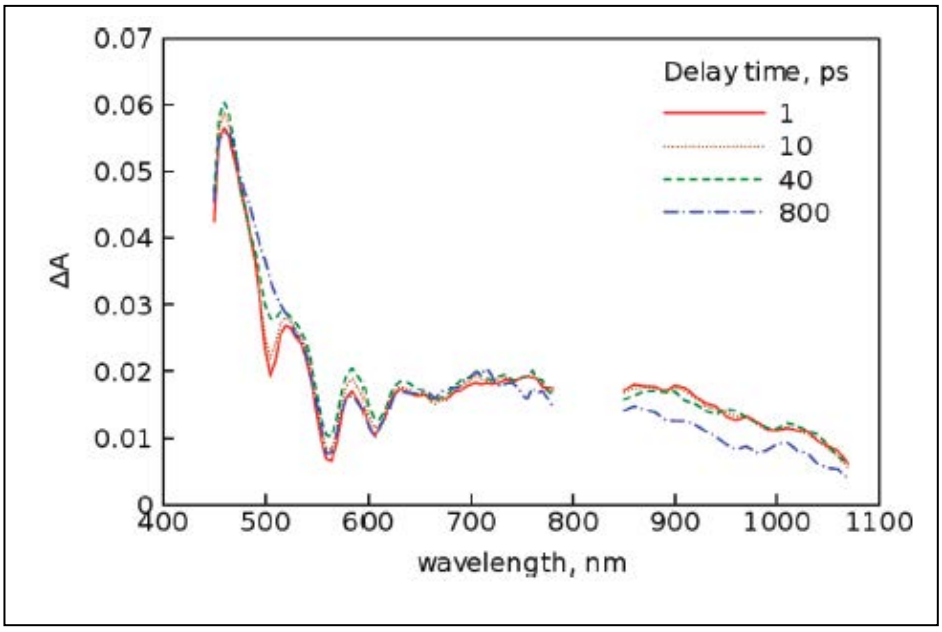

Figure 5.14: Time resolved transient absorption spectra of BDP-ZnP dyad upon addition of C_{60} (0.6 mM) in benzonitrile. The delay times are indicated in the plot. The excitation wavelength was 410 nm.

The noteworthy difference is rather strong absorption at the red part of the spectrum (670-750 nm), which is characteristic for the porphyrin cation radical. At the same time in the near-infrared part of the spectrum, the absorption features were broad and rather featureless at the beginning, but at longer delays a band at 1020 nm was noticed (the spectrum at 800 ps in Figure 5.13), which is indicative of the fullerene anion radical formation. This type of behavior can be explained by a fast formation of the porphyrin-fullerene exciplex, which then relaxes to the charge-separated state, $ZnP^{+\bullet}$-$C_{60}^{-\bullet}$. The formation of an exciplex is conceivable due to close positioning of zinc porphyrin and fullerene entities in the supramolecular triad as shown in Figure 5.7a,b. To gather quantitative information on excited state electron transfer, a global fitting of the transient absorption data was employed. A four-exponential model gave a reasonably small mean square deviation value (ζ) 0.001), and it was possible to extract three lifetimes in the time scale of the measurements, 0.6, 20, and 700 ps, and a long lifetime extended to nanosecond time domain. The spectra of the decay components are presented in Figure 5.15. The fast component, 0.6 ps, is most probably due to the internal conversion of the second singlet excited state of ZnP to the first singlet excited state. The second component, 20 ps, showed recovery of the BDP ground state (negative peak at 500 nm), but at the same time it had relatively strong negative intensity in the red part of the spectrum and around 1000 nm, which are characteristic for the formation of the charge-separated state. It seems that two reactions are taking place in the same time domain, that is, the energy transfer from BDP to ZnP and the electron transfer from ZnP to

C_{60}. The former is associated with relatively big spectral changes, as can be seen from Figure 5.11, and the latter has a rather moderate effect on the transient spectra. Although the relative contribution of the excited BDP chromophores was smaller than that of ZnP, the electron transfer time constant from the directly excited ZnP to fullerene was difficult to accurately determine since it interfered strongly with the energy transfer time constant. However, the calculated time constant, 20 ps, was shorter than that for "pure" energy transfer in the BDP-ZnP dyad indicating that porphyrin-fullerene charge separation was somewhat faster than the energy transfer. The latter makes the determination of the charge separation time constant even more difficult when the BDP chromophore was excited (at 500 nm), since in the sequential series of reactions, BDP*-ZnP-C_{60} BDP-ZnP*-C_{60} BDP-$ZnP^{+\bullet}$-$C_{60}^{-\bullet}$, population of the BDP-ZnP*-C_{60} intermediate state is never high, i.e., this state is practically unobservable. Hence the transient spectra at a time delay of a few hundred picoseconds had virtually the same shapes at excitation wavelengths of both 410 and 500 nm. The spectrum of the longest lived component in Figure 5.15 corresponds to the charge-separated state, BDP-$ZnP^{+\bullet}$-$C_{60}^{-\bullet}$.The lifetime of this state is much longer than the maximum delay time of the pump-probe instrument used (<1 ns). To gather additional information on the CS state lifetime, nanosecond flash photolysis was performed. Since the sample was prepared in an excess of fullerene, two states can be observed in the microsecond time domain: the triplet excited state of fullerene and the CS state. To distinguish between them the transient absorption decays were measured for a number of

wavelengths and fitted globally. The results of the fit are presented in Figure 5.16.

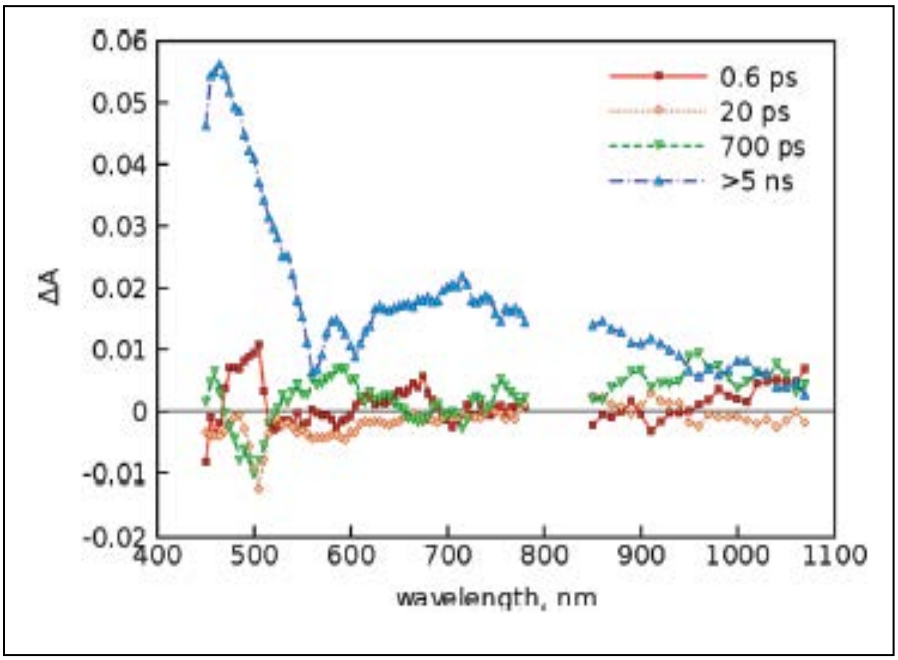

Figure 5.15: Transient absorption decay component spectra of BDP-ZnP dyad in the presence of C_{60} (0.6 mM) in benzonitrile. The component lifetimes are indicated in the plot. The excitation wavelength was 410 nm.

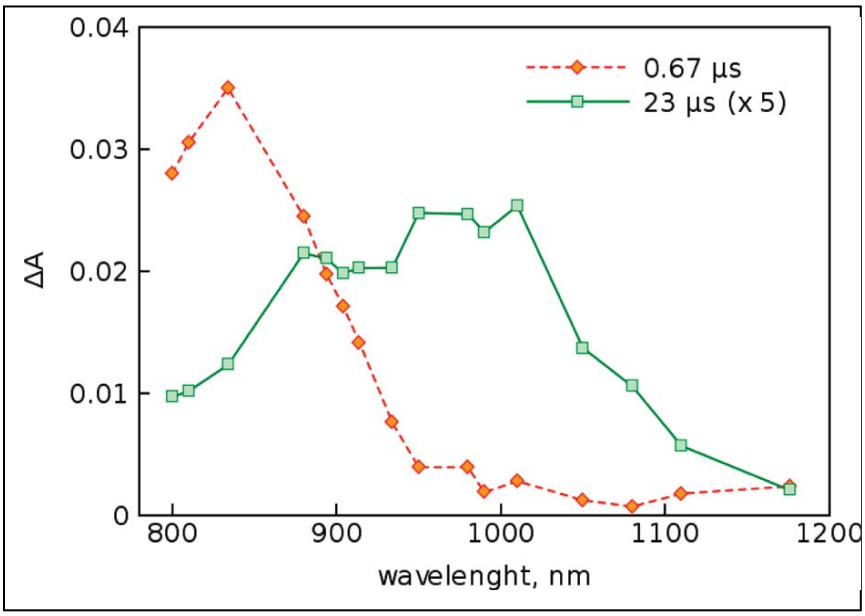

Figure 5.16: Transient absorption component spectra of BDP-ZnP dyad in the presence of C_{60} (0.6 mM) in benzonitrile obtained by nanosecond laser flash photolysis.

The component with lifetime 0.67 μs was attributed to the fullerene triplet state (notice that the measurements were carried out with air saturated solution, and the reference measurements of a pure fullerene sample had virtually the same lifetime as the fullerene triplet state), and the component with the 23 μs lifetime was attributed to the CS state. The decay traces at two characteristic wavelengths are presented in Figure 5.17. The lifetime of the CS state for the present triad is comparable to the supramolecular triad involving covalently linked ferrocene-zinc porphyrin-crown ether binding to the alkyl ammonium

functionalized cation supramolecular triad (lifetime of CS state was 6.2 μs)[102b] suggesting charge stabilization to some extent.

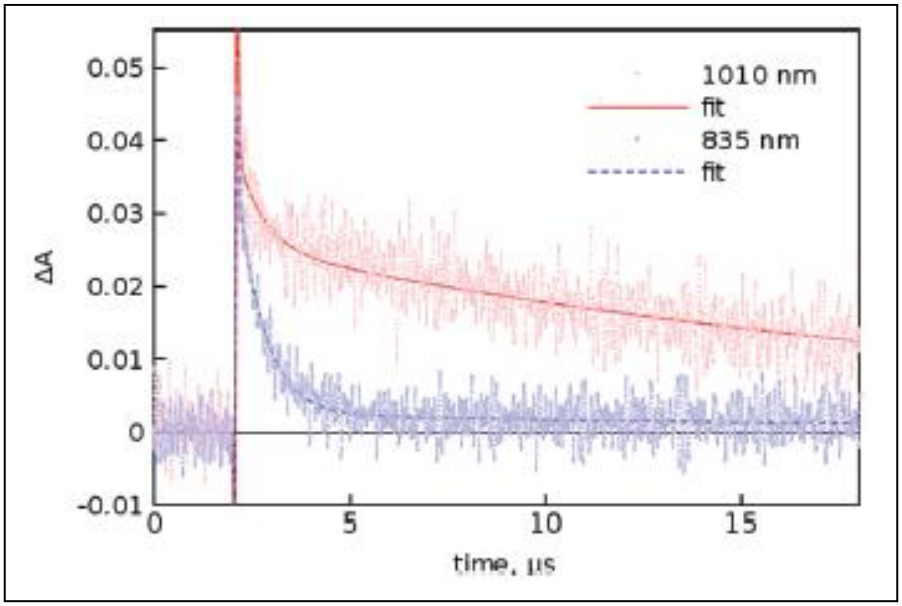

Figure 5.17: Time profiles of the transient absorption bands of the BDP-ZnP-C_{60} triad (0.6 mM) in benzonitrile at two selected wavelengths.

Energy Level Diagram.

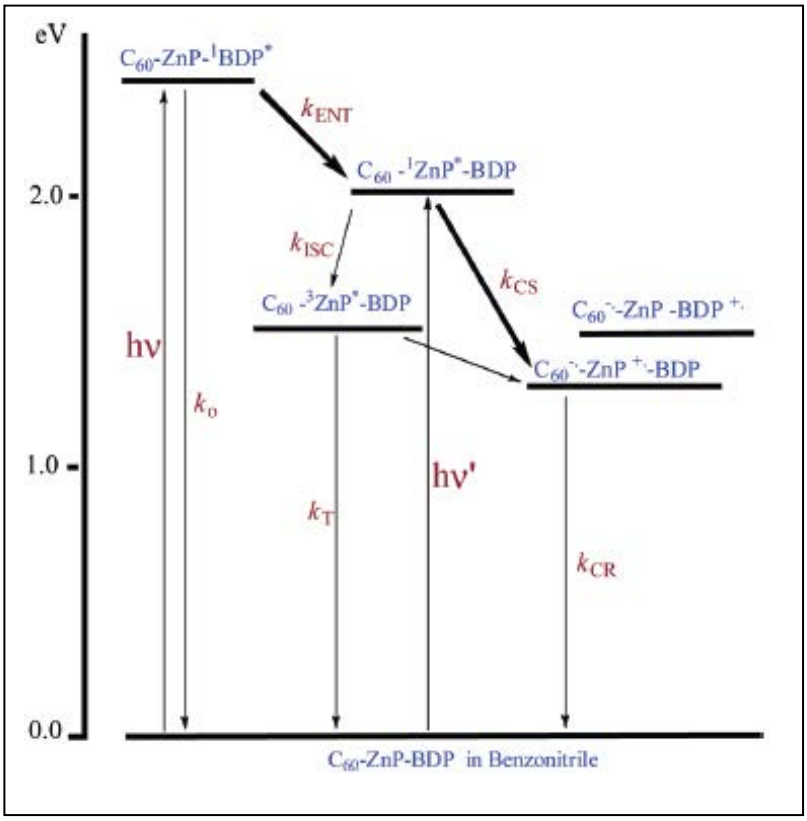

Figure 5.18: Energy level diagram showing the different photochemical events of the supramolecular C_{60}-ZnP-BDP triad after excitation of either the BDP or ZnP moieties. The thick arrows indicate the major photochemical process and the thin arrows represent the minor photochemical process.

The results of the present investigation along with all of the control experiments clearly show the occurrence of efficient energy transfer followed by electron transfer in the studied supramolecular triad. The combination of optical absorption, steady-state fluorescence emission, molecular modeling,

electrochemistry, and time-resolved emission and transient absorption studies has permitted the extraction of the needed energetic and kinetic information. The different photochemical events observed in the triad are depicted in Figure 5.18 in the energy level diagram. Energies of the excited states of the different entities were calculated from the fluorescence peaks while the triplet state energy of ZnP was cited from the literature.[153] The driving forces for the occurrence of electron transfer from the different excited chromophores of the triad used were as discussed earlier. It is also important to note that the difference in free energy change of charge separation for the "close" and "extended" forms of the triad is considered to be negligible. In the energy level diagram, the thick arrows indicate the major processes and the thin arrows are minor processes. On the basis of distance and energetic considerations, an electron transfer from singlet excited BDP to C60 is considered to be an inefficient process.

5.4 Summary

A novel supramolecular triad to mimic the "antenna-reaction center" functionality of the photosynthetic reaction center has been successfully constructed. The antenna mimic, a boron dipyrrin entity, was covalently linked to the reaction center electron donor mimic, a zinc porphyrin possessing a 18-crown-6 entity, as the opposite side of the macrocycle. Both steady-state and time-resolved emission as well as transient absorption studies decidedly proved the occurrence of efficient singlet-singlet energy transfer from BDP to zinc porphyrin with the

time scale of 10-50 ps. Next, the reaction center electron acceptor mimic, a fulleropyrrolidine appended with an alkyl ammonium chain, was self-assembled via crown-ether-alkyl ammonium binding to form the supramolecular triad. The structural integrity of the supramolecular triad was derived by optical, computational, and electrochemical studies. Computational studies revealed two possible structures as extreme cases of the supramolecular triad. Energy calculations revealed the possibility of photoinduced electron transfer from singlet excited zinc porphyrin to fullerene. Further time-resolved emission and transient absorption studies demonstrated the occurrence of sequential energy transfer from ^{1}BDP* to ZnP followed by electron transfer from ^{1}ZnP* to fullerene in the supramolecular triad. Nanosecond transient absorption studies revealed the existence of long-lived charge separated species of $ZnP^{+\bullet}$-$C_{60}^{-\bullet}$, suggesting that the BDP is also involved in the charge stabilization process due to its facile oxidation.

(B) Electronic Energy Harvesting Multi BODIPY – Zinc Porphyrin Dyads Accommodating Fullerene as Photosynthetic Composite of Antenna-Reaction Center

5.1 Introduction

In photosynthetic organisms, light energy harvesting antenna (LH) complexes composed of large number of chlorophyll and carotenoid molecules are essential for effective capturing of solar energy and deliver that to the reaction center (RC) with minimal loss of energy.[154] The LH systems (LH1 and LH2) of purple bacteria have been characterized at atomic resolution and photophysical events have been probed using ultrafast spectroscopic techniques.[2f,155] In this bacterial system, electronic energy transfer occurs from LH2 to LH1, and finally to the special pair in the RC where electron transfer occurs to produce a stable charge-separated state leading to ATP synthesis by means of transmembrane proton-motive force.[154e] Mimicking the complex photochemical events of the photosynthetic systems using synthetic model compounds is important not only to understand the natural systems but also for technological advances in solar energy conversion, a promising solution for global energy demands and environmental issues. Consequently, a number of researchers have built various synthetic models of LH, RC, and their combined architectures and reported light induced electronic energy and electron transfer events.

Porphyrin and other related tetrapyrroles have been widely employed as energy capturing antenna or electron donor units in artificial model compounds due to their structural resemblance to natural chlorophylls.[3f,j,12a,64,98,119,156] Similarly, fullerene, C_{60} owing to its facile reduction potential and low-reorganization energy in electron transfer reactions, has been widely used as an electron acceptor.[3f,j,12a,64,98,119,156] In fact, in recent years the use of fullerene has minimized the utilization of two-dimensional electron acceptors like quinone, methyl viologin, etc., in donor-acceptor systems. In a few studies reporting combined ‗antenna-reaction center' functionalities; fluorophores with appropriate spectral and redox properties have been liked to RC electron donor-acceptor dyads. Sequential energy transfer followed by electron transfer in these model compounds has been successfully demonstrated.

Boron dipyrrin, BODIPY® or BDP, is a well known photosensitizer that has been widely used in the development of fluorescent chemosensors for various analytes and tags to detect biomolecules.[147a,157] When linked to appropriate electron/energy donor/acceptor entity, it can act as an electron/energy acceptor/donor, respectively.[19,22,23,66,67,146d,158] Interestingly, BDP can also be used as an energy absorbing and transferring antenna molecule in artificial photosynthetic antenna-reaction center mimics.[66,146d] Few elegant systems including covalently linked BDP-porphyrin dyads have been reported in the literature taking advantage of BDP's ability to act as an antenna molecule.

[19,22,23,66,67,146d,158] In the present study, we have further exploited utilization of such dyads by synthesizing zinc porphyrin covalently linked to 1, 2 or 4 number of BDP to investigate the effect of number of antenna units on the overall excitation energy transfer efficiency (Chart 1). Further, zinc porphyrin in these dyads has been axially coordinated to an electron acceptor, an imidazole functionalized fullerene, C_{60}Im, to form an electron donor-acceptor pair in the supramolecular complex. Formation, and energy and electron transfer in these novel triads have been systematically investigated using computational, electrochemical, spectroscopic and time-resolved photochemical techniques.

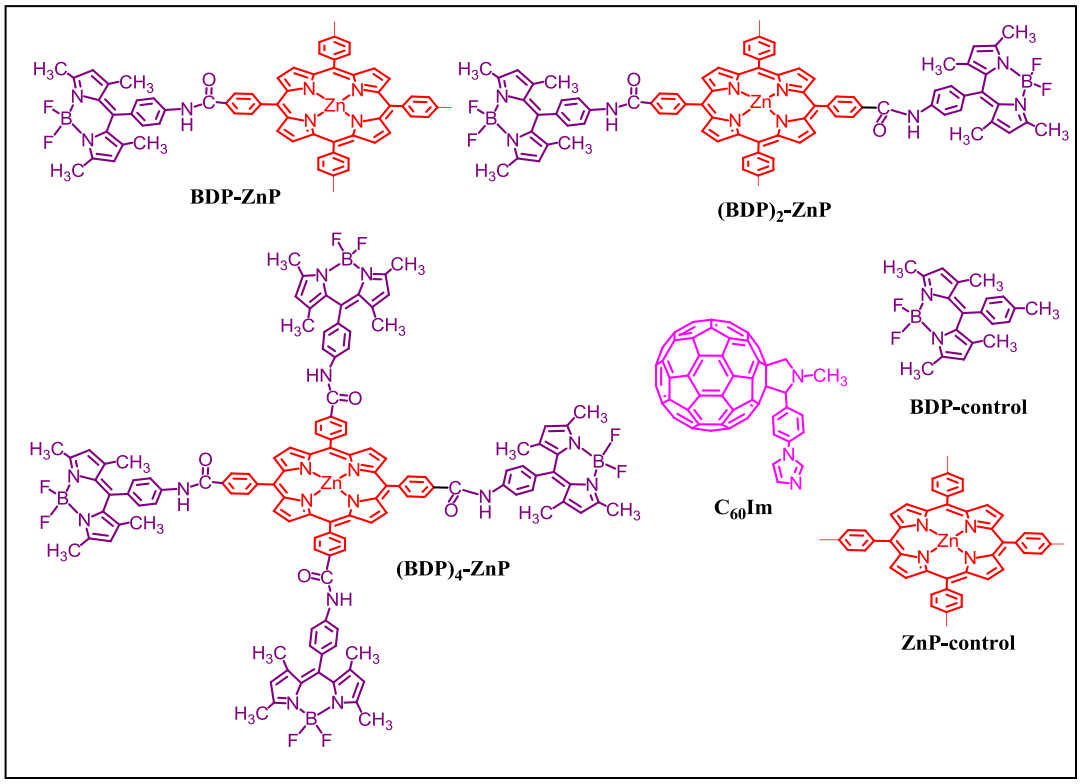

Chart 5.1: Structure of the $(BDP)_n$-ZnP dyads (n = 1, 2, or 4), imidazole appended C_{60}, C_{60}Im, and the control compounds employed in the present study to probe excitation energy and electron transfer events.

5.2 Experimenatl section

Synthesis of mono BDP-zinc porphyrin dyad

H_2-5-(p-carboxyphenyl)-10,15,20-tri(p-tolyl)porphyrin (22)

4-carboxybenzaldehyde (1.0 g, 0.006 mol) was dissolved in propaonic acid (120 mL) and pyrrole (0.027 mol, 1.85 mL) was followed by *p*-tolualdehyde (2.35 mL, 0.019 mol). The mixture was refluxed for 4 h. The propanoic acid was removed under reduced pressure and the compound was purified by using a basic alumina column with $CHCl_3$:MeOH (96:4 v/v) as eluent. Evaporation of the solvent yielded the desired compound as a purple solid. Yield: 450 mg (10 %).

^{1}H NMR ($CDCl_3$) δ (ppm) 9.00-8.78 (m, 8H, β pyrrole *H*), 8.51 (d, 2H, phenyl *H*), 8.35 (d, 2H, phenyl *H*), 8.14 (d, 6H, tolyl *H*), 7.61 (d, 6H, tolyl *H*), 3.76 (s, 9H, 3-CH_3), -2.78 (s, br, 2H, -NH).

1-(Difluoroboryl)-2-[(Z)-(3,5-dimethyl-2H-pyrrol-2-ylidene)(4-nitrophenyl)methyl]-3,5-dimethyl-1H-pyrrole (18)

2,4-Dimethylpyrrole (1.08 mL, 10.5 mmol) and 4-nitrobenzaldehyde[146d] (0.93 g, 6.2 mmol) were added to distilled CH_2Cl_2 (600 mL) and purged with N_2, then trifluoroacetic acid (0.09 mL, 1.23 mmol) was added and the mixture was stirred for 2 h. The resulting solution was washed with 0.1 M NaOH (200 mL) and then water, dried over anhydrous Na_2SO_4, and filtered, then the solvent was

evaporated. Next the product was redissolved in methylene chloride, and *p*-chloranil (1.36 g, 5.5 mmol) was added to the mixture. The resulting solution was stirred for 10 min, then triethylamine (4 mL) and boron trifluoride etherate (3.5 mL) were added to the mixture. After 1 h of stirring, the resulting solution was poured into water and extracted with CH_2Cl_2. The organic layer was extracted with water, and the solvent was evaporated. The compound was purified by flash column chromatography on silica gel with hexanes:$CHCl_3$ (60:40 v/v) as eluent. Evaporation of the solvent yielded 900 mg (40%) of the desired product.

^{1}H NMR ($CDCl_3$) δ (ppm) 8.39 (d, 2H, phenyl *H*), 7.55 (d, 2H, phenyl *H*), 6.02 (s, 2H, pyrrole *H*), 2.55 (s, 6H, -CH_3), 1.37 (s, 6H, -CH_3). ESI mass (in CH_2Cl_2) calcd 369.2, found [M + 1] 370.5.

1-(Difluoroboryl)-2-[(Z)-(3,5-dimethyl-2H-pyrrol-2-ylidene)(4-aminophenyl)methyl]-3,5-dimethyl-1H-pyrrole (19)

A solution of **2** (120 mg) in THF (30 mL) was hydrogenated over 5% Pd on charcoal (300 mg) at room temperature and atmospheric pressure. Then, the catalyst was removed by filtration with use of Celite, and the filtrate was evaporated. The compound was purified by flash column chromatography on silica gel with hexane:CH_2Cl_2 (60:40 v/v) as eluent. Evaporation of the solvent yielded 44 mg of **3**, 40%.

^{1}H NMR($CDCl_3$) δ (ppm) 7.00 (d, 2H, phenyl *H*), 6.78 (d, 2H, phenyl *H*), 5.96 (s, 2H, pyrrole *H*), 3.47 (br s, 2H, -NH_2), 2.55 (s, 6H, -CH_3), 1.49 (s, 6H, -CH_3). ESI mass (in CH_2Cl_2) calcd 339.2, found [M + 1] 340.3.

H_2-5-{4-[2-(4-difluoroborondipyrrinylphenyl)amido]phenyl}-10,15,20-tri(p-tolyl)porphyrin (23)

Compound **22** (36 mg, 0.05 mmol) was taken in dry toluene (20 mL) then thionyl chloride (80 μL, 1.1 mmol) and pyridine (80 μL) were added and the reaction mixture was refluxed under argon for 3 h. After cooling, the solvent was evaporated and the resulting green compound was redissolved in dry toluene (25 mL). Then, pyridine (260 μL) was added followed by **19** (17 mg, 0.05 mmol). The reaction mixture was allowed to stir at room temperature under argon for 12 h. The solvent was evaporated and the crude compound was purified by column chromatography on silica gel with hexanes:$CHCl_3$ (60:40 v/v). Evaporation of the solvent yielded the desired compound (28 mg).

^{1}H NMR ($CDCl_3$) δ (ppm) 8.95-8.76 (m, 8H, β pyrrole *H*), 8.39 (d, 2H, phenyl *H*), 8.30 (d, 2H, phenyl *H*), 8.11 (d, 6H, tolyl *H*), 7.98 (d, 2H, BDP phenyl *H*), 7.48 (d, 2H, tolyl *H*), 7.39 (d, 2H, BDP phenyl *H*), 6.04 (s, 2H, pyrrole *H*), 2.71 (s, 9H, tolyl CH_3), 2.58 (s, 6H, pyrrole CH_3), 1.58 (s, 6H, pyrrole *H*), -2.78 (s, br, 2H, -NH). ESI mass (in CH_2Cl_2) calcd 1021.0, found [M + 1] 1022.2.

5-{4-[2-(4-difluoroborondipyrrinylphenyl)amido]phenyl}-10,15,20-tri(p-tolyl) porphyrinato zinc(II) (24)

Compound **23** (30 mg) was dissolved in $CHCl_3$ (15 mL) then zinc acetate in methanol was addhnuhjed to the chloroform solution, and the resulting mixture was refluxed for 2 h until the 515 nm band of free-base porphyrin had disappeared. At the end, the organic layer was washed with water and dried over anhydrous Na_2SO_4. Chromatography on silica gel column by using hexanes: $CHCl_3$ (50:50 v/v) gave the title compound. Yield 30 mg (93%).

^{1}H NMR ($CDCl_3$) δ (ppm) 9.00-8.82 (m, 8H, β pyrrole *H*), 8.39 (d, 2H, phenyl *H*), 8.22 (d, 2H, phenyl *H*), 8.11 (d, 6H, tolyl *H*), 7.92 (d, 2H, BDP phenyl *H*), 7.55 (d, 2H, tolyl *H*), 7.35 (d, 2H, BDP phenyl *H*), 6.02 (s, 2H, pyrrole *H*), 2.71 (s, 9H, tolyl CH_3), 2.60 (s, 6H, pyrrole CH_3), 1.53 (s, 6H, pyrrole *H*), ESI mass (in CH_2Cl_2) calcd 1085.4, found [M + 1] 1086.8.

Synthesis of $(BDP)_2$-ZnP dyad

5-(4-Methoxycarbonylphenyl)dipyrromethane (15)

This compound was prepared according to the general procedure outlined for the synthesis of dipyrromethanes by Lindsey et al.[149] To a pyrrole (68 mL, 0.98 mol) was added methyl 4-formyl benzoate (4.0 g, 0.024 mol) and the solution was purged with argon for 15 min. Then trifluoroacetic acid (190 μL, 0.0024 mmol) was added and the mixture was stirred at room temperature for 15 min. The mixture was then diluted with CH_2Cl_2 and NaOH (100 mL, 0.1 M) was added,

then the organic layer was extracted over Na_2SO_4. The compound was purified by flash column chromatography on silica gel with hexanes:ethyl acetate (60:40 v/v) as eluent. Evaporation of the solvent yielded a pale-yellow solid. Yield 2 g (30%).

^{1}H NMR ($CDCl_3$) δ (ppm) 8.05-7.90 (m, 4H, pyrrole *NH* and phenyl *H*), 7.28 (d, 2H, phenyl *H*), 6.75-6.65 (m, 2H, pyrrole *H*), 6.18-6.12 (m, 2H, pyrrole *H*), 5.92-5.87 (m, 2H, pyrrole *H*), 5.54 (s, 1H, -CH-), 3.90 (s, 3H, -$COOCH_3$).

H_2-5,15-Di(p-methoxycarbonylphenyl)-10,20-di(p-tolyl)porphyrin(16)

This compound was prepared according to Luo et al.[62] A solution of **15** (1.6 g, 5.71 mmol) was added to *p*-tolylaldehyde (675 μL, 5.71 mmol) in $CHCl_3$, and the reaction mixture was stirred under argon for 1 h. Then $BF_3{\cdot}O(Et)_2$ (724 μL, 5.71 mmol) was added, and the reaction mixture was stirred in the dark for 2 h. *p*-Chloranil (2.11 g, 8.57 mmol) was added to the reddish-black reaction mixture, and the resulting mixture was stirred for 18 h. Triethylamine (2.4 mL, 17.25 mmol) was added, and the reaction mixture was stirred for 1 h and then concentrated. Column chromatography on silica gel with chloroform as eluent gave a mixture of five porphyrins including the titled compound. Subsequent column chromatography of this fraction on silica gel kwith toluene:$CHCl_3$ (70:30 v/v) as eluent yielded the titled compound as the third band. Evaporation of the solvent yielded the desired compound as a purple solid. Yield 208 mg (5%).

^{1}H NMR ($CDCl_3$) δ (ppm) 8.82 (dd, 8H, pyrrole *H*), 8.42 (d, 4H, phenyl *H*), 8.25 (d, 4H, phenyl *H*), 8.10 (d, 4H, phenyl *H*), 7.58 (d, 4H, phenyl *H*), 4.12 (s, 6H, -$COOCH_3$).

H_2-5,15-Di(p-carboxyphenyl)-10,20-di(p-tolyl)porphyrin (17)

A suspension of **16** (200 mg, 0.264 mmol) in THF:ethanol (1:1) was taken in a 250 mL round-bottomed flask and potassium hydroxide (1.5 g, 0.027 mol) dissolved in water (12 mL) was added to it. The reaction mixture was refluxed for 8 h. After cooling, the solvent was evaporated; the residue was diluted with water (100 mL) and then filtered. The desired compound was obtained as the dipotassium salt. The aqueous suspension of porphyrin dipotassium salt was acidified with concentrated HCl (pH 2) and then filtered. The titled compound was obtained as a purple powder and used without further purification. Yield 85 mg (44%).

^{1}H NMR (DMSO-*d*) δ (ppm) 8.8 (dd, 8H, pyrrole *H*), 8.38 (d, 8H, phenyl *H*), 8.18-8.10 (d, 4H, phenyl *H*), 7.65-7.55 (d, 4H, phenyl *H*), 2.55 (s, 6H, -CH_3), -2.95 (s, br, 2H, -NH).

H_2-5,15-Di{4-[2-(4-difluoroborondipyrrinylphenyl)amido]phenyl}-10,20-di(p-tolyl) porphyrin (25)

Porphyrin diacid **17** (30 mg, 0.03 mmol) was taken in dry toluene (20 mL) then thionyl chloride (56 μL, 0.76 mmol) and pyridine (56 μL) were added and the reaction mixture was refluxed under argon for 3 h. After cooling, the solvent was

evaporated and the resulting green compound was redissolved in dry toluene (25 mL). Then, pyridine (56 μL) was added followed by **19** (28 mg, 0.08 mmol). The reaction mixture was allowed to stir at room temperature under argon for 12 h. The solvent was evaporated and the crude compound was purified by column chromatography on silica gel with hexanes:$CHCl_3$ (75:25 v/v).

^{1}H NMR ($CDCl_3$) δ (ppm) 8.96-8.77 (m, 8H, β pyrrole *H*), 8.42-8.22 (m, 8H, phenyl *H*), 8.12 (d, 4H, phenyl *H*), 8.00-7.92 (dd, 4H, phenyl *H*), 7.58 (d, 4H, phenyl *H*), 7.42-7.34 (dd, 2H, phenyl *H*), 7.18 (d, 4H, phenyl *H*), 6.03 (s, 4H, pyrrole *H*), 2.54 (s, 6H, tolyl CH_3), 2.52 (s, 12H, pyrrole CH_3), 1.56 (s, 12H, pyrrole *H*), -2.79 (s, br, 2H, -NH). ESI mass (in CH_2Cl_2) calcd 1373.0, found [M + 1] 1373.8.

5,15-Di{4-[2-(4-difluoroboron dipyrrinylphenyl)amido]phenyl}-10,20-di(p-tolyl) Porphyrinato Zinc(II) (26)

The free-base porphyrin **25** (25 mg) was dissolved in $CHCl_3$ (10 mL) then a saturated solution of zinc acetate in methanol was added to the solution, and the resulting mixture was refluxed for 2-3 h until the 515 nm band of free-base porphyrin had disappeared. At the end, the reaction mixture was washed with water and dried over anhydrous Na_2SO_4. Chromatography on silica gel column by using hexanes: $CHCl_3$ (70:30 v/v) gave the title compound. Yield 25 mg (90%). ^{1}H NMR ($CDCl_3$) δ (ppm) 9.05-8.98 (m, 8H, β pyrrole *H*), 8.40-8.35 (m, 8H, phenyl *H*), 8.11 (d, 4H, phenyl *H*), 8.01-7.93 (dd, 4H, phenyl *H*), 7.60 (d, 4H,

phenyl *H*), 7.42-7.34 (dd, 2H, phenyl *H*), 7.18 (d, 4H, phenyl *H*), 6.01 (s, 4H, pyrrole *H*), 2.78 (s, 6H, tolyl CH_3), 2.61 (s, 12H, pyrrole CH_3), 1.56 (s, 12H, pyrrole *H*), ESI mass (in CH_2Cl_2) calcd 1436.4, found [M + 1] 1437.3.

Synthesis of $(BDP)_4$-ZnP dyad

H_2-5,20,15,20-tetra{4-[2-(4-difluoroborondipyrrinylphenyl)amido]phenyl} porphyrin (27)

Commercially available *meso*-tetra(4-carboxyphenyl)porphyrin (14 mg, 0.01 mmol) was taken in dry toluene (20 mL) then thionyl chloride (22 μL, 0.29 mmol) and pyridine (25 μL) were added and the reaction mixture was refluxed under argon for 3 h. After cooling, the solvent was evaporated and the resulting green compound was redissolved in dry toluene (20 mL). Then, pyridine (81 μL) was added followed by **19** (22 mg, 0.05 mmol). The reaction mixture was allowed to stir at room temperature under argon for 12 h. The solvent was evaporated and the crude compound was purified by column chromatography on silica gel with hexanes:$CHCl_3$ (40:60 v/v).

^{1}H NMR ($CDCl_3$) δ (ppm) 8.95-8.80 (s, 8H, β pyrrole *H*), 8.42-8.25 (dd, 16H, phenyl *H*), 7.95 (d, 8H, phenyl *H*), 7.39 (d, 8H, phenyl *H*), 6.02 (s, 8H, pyrrole *H*), 2.58 (s, 24H, pyrrole CH_3), 1.55 (s, 24H, pyrrole CH_3), -2.89 (s, br, 2H, -NH). ESI mass (in CH_2Cl_2) calcd 1058.0, found [M + 1] 1059.4.

5,20,15,20-tetra{4-[2-(4-difluoroboron dipyrrinylphenyl)amido]phenyl}porphyrinato zinc(II) (28)

To a solution of **27** (20 mg) dissolved in chloroform was added zinc acetate dissolved in methanol, and the solution was stirred for 2 h. The solution was washed with water and evaporated under reduced pressure. The compound was purified over silica gel column hexanes:$CHCl_3$ (30:70 v/v) as eluent. Yield 20 mg.

^{1}H NMR ($CDCl_3$) δ (ppm) 8.90 (s, 8H, β pyrrole *H*), 8.45-8.20 (dd, 16H, phenyl *H*), 7.95 (d, 8H, phenyl *H*), 7.39 (d, 8H, phenyl *H*), 6.02 (s, 8H, pyrrole *H*), 2.59 (s, 24H, pyrrole CH_3), 1.57 (s, 24H, pyrrole CH_3) ESI mass (in CH_2Cl_2) calcd 1121.3, found [M + 1] 1122.4

In the first part of this chapter, we discuss the excitation energy transfer in the multi-BDP appended zinc porphyrin dyads and in the second part electron transfer in supramolecular triads formed by axial coordination of C_{60}Im to the zinc center of $(BDP)_n$-ZnP dyads is discussed.

5.3 Results and discussion

Excitation energy transfer in the multi-BDP appended zinc porphyrin dyads

Optical absorption and fluorescence emission studies of $(BDP)_n$-ZnP dyads

Figure 5.19 shows the optical absorption spectra of the $(BDP)_n$-ZnP dyads in *o*-dichlorobenzene (DCB), normalized to their Soret band along with a control compound, *meso*-tolyl boron dipyrromethane (BDP-control). In the dyads, the bands at 426, 550 and 590 nm correspond to zinc porphyrin while the band at

505 nm corresponds to the boron dipyrrin entity.[146d] As expected, the 505 nm band revealed an increase with increasing number of BDP units, although the dependence is no strictly linear. The absorption bands of $(BDP)_4$-ZnP were red shifted by 1-2 nm compared to the other two dyads. Importantly, the absorption of BDP at 505 nm in the control compound had no appreciable overlap with the ZnP, suggesting that irradiation of the dyads at this wavelength would selectively excite the boron dipyrrin entity(ies) of the dyads.

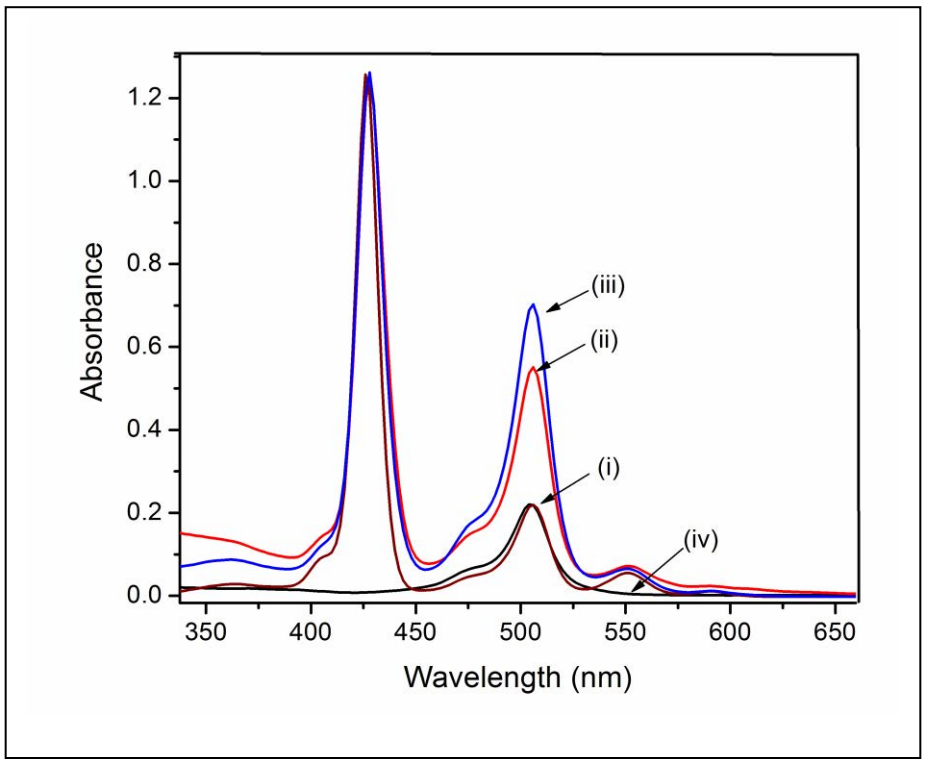

Figure 5.19: Absorption spectra of (i) BDP-ZnP, (ii) $(BDP)_2$-ZnP, (iii) $(BDP)_4$-ZnP and (iv) BDP in DCB, normalized to the porphyrin Soret band.

The fluorescence emission spectrum of the BDP-zinc porphyrin dyad, excited at 495 nm corresponding to BDP excitation, is shown in Figure 5.20 along with the emission of BDP-control compound. In case of the dyads, a weak band in the range of 517-525 nm corresponding to the emission of BDP was observed in addition to the zinc porphyrin emission bands at 602 and 650 nm. [15a] The BDP emission band in the dyads was found to be quenched substantially compared to the BDP-control having no covalently linked ZnP. The amount of quenching was found to be 96%, 93% and 91%, for BDP-ZnP, $(BDP)_2$-ZnP and $(BDP)_4$-ZnP dyads, respectively. In a control experiment, equimolar mixture of ZnP and BDP compounds was excited at the wavelength of the BDP absorption band, 495 nm, and no significant emission of ZnP was detected. The quenching of BDP emission and occurrence of ZnP emission indicate singlet-singlet energy transfer in the studied dyads.

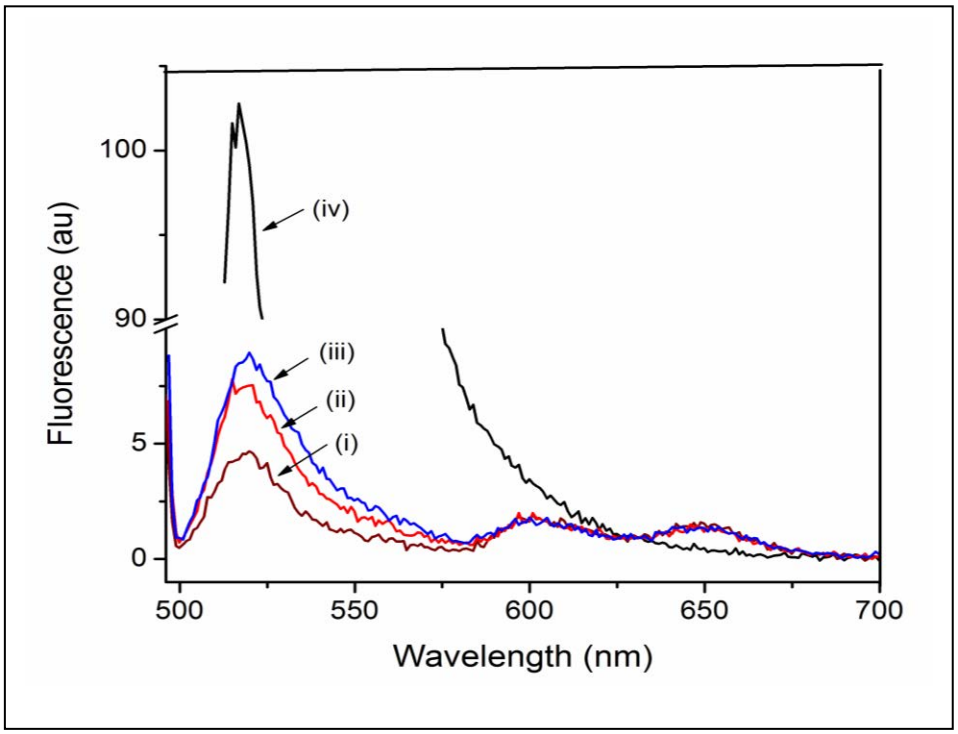

Figure 5.20: Fluorescence spectra of (i) BDP-ZnP, (ii) $(BDP)_2$-ZnP, (iii) $(BDP)_4$-ZnP and (iv) BDP in DCB. The concentration of BDP was held constant by fixing the optical density of BDP at 505 nm to 0.1. λ_{ex} = 495 nm.

The occurrence of singlet excited energy transfer from BDP to zinc porphyrin in the dyads was also confirmed by recording the excitation spectra of the dyads while holding the emission monochromator at 662 nm corresponding to zinc porphyrin emission. Such spectra are shown in Figure 5.21 and revealed excitation band of not only zinc porphyrin entity but also that of BDP entity of the dyad indicating energy transfer from BDP to zinc porphyrin. Generally, the intensity of BDP excitation band increased with increasing their numbers,

suggesting higher probability of excitation energy transfer with increasing the number of antenna BDP units.

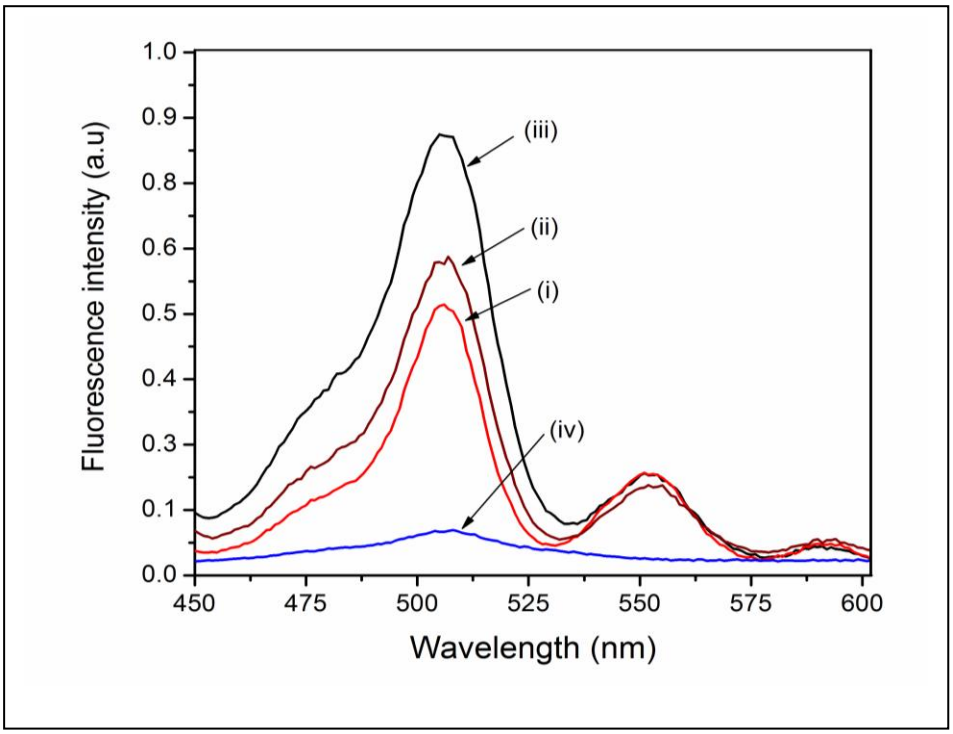

Figure 5.21: Excitation spectra of equimolar concentrations of (i) BDP-ZnP, (ii) $(BDP)_2$-ZnP, (iii) $(BDP)_4$-ZnP, and (iv) BDP in DCB. The excitation was scanned by holding the emission monochromator at 650 nm corresponding to ZnP emission.

Computational and electrochemical studies of $(BDP)_n$-ZnP dyads

Since the relative orientation of the donor and acceptor dipoles in the dyads is crucial for energy transfer efficiency, the structure of the dyads were visualized by performing computational studies at the B3LYP/3-21G(*) level.[94,95] Figure 5.22 shows the structures of the dyads energy optimized on Born-

Oppenheimer potential energy surfaces. The appended BDP macrocycle(s) were found to be almost in the same plane of zinc porphyrin. That is, the dihedral angle between the two macrocycles was found to be less than 10^{o} irrespective of the number of BDP entities on the ZnP macrocycle. The center-to-center (boron to zinc) and edge-to-edge (between *meso* carbon atoms of the macrocycles) distances between the BDP and ZnP macrocycles were found to be 18.8 Å and 12.3 Å, respectively. That is, no steric crowding between the macrocycles was observed. The B-B distance between the two BDP units of $(BDP)_2$-ZnP was found to be ~37 Å. In the case of $(BDP)_4$-ZnP, the four BDP units were arranged in an rectangular fashion around ZnP for which the B-B distance between the adjacent BDP entities was found to be ~25 Å. The positioning of the both the BDP and ZnP macrocycles in the same plane is expected to facilitate energy transfer owing to better orientation factor of the dipoles.[9] It may be mentioned here that we have not further attempted to evaluate the orientation of the dipoles of the two macrocycles due to flexible nature and limited computational facility.

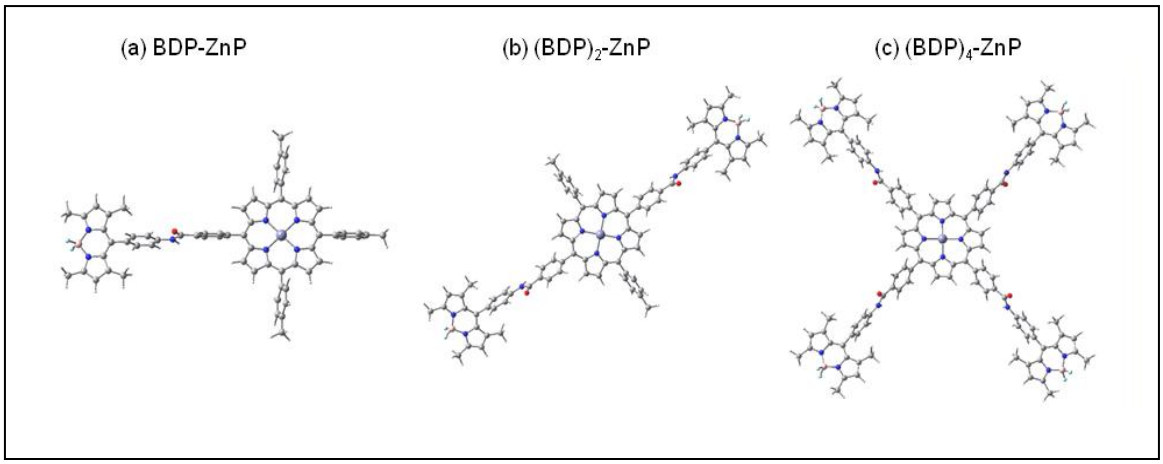

Figure 5.22: B3LYP/3-21G(*) optimized structures of (i) BDP-ZnP, (ii) $(BDP)_2$-ZnP, and (iii) $(BDP)_4$-ZnP dyads.

Further electrochemical studies were performed to evaluate the redox potentials and establish the energy states. The one-electron reduction of the BDP control was located at $E_{1/2}$ = -1.96 vs. Fc/Fc^+ while its irreversible oxidation was located at E_{pa} = 0.54 V vs. Fc/Fc^+. The first two reversible oxidations of the zinc porphyrin were located at $E_{1/2}$ = 0.23 and 0.57 V vs. Fc/Fc^+ while the first two reversible reductions were located at E_{pc} = -1.95 and -2.22 V vs. Fc/Fc^+, respectively. That is, the first reduction potential of ZnP and BDP were almost the same. The first three reductions of the C_{60}Im were located at $E_{1/2}$ = -1.11 - 1.55, and -2.09 V vs. Fc/Fc^+, respectively. The peak-to-peak separation and plots of peak current versus square root of scan rate indicated all of the electroreductions to be one-electron reversible processes. For the BDP-ZnP dyad, three electrooxidations located at 0.25, 0.58, and 0.78 V vs. Fc/Fc^+ were observed, the latter being an irreversible process (Figure 5.23).

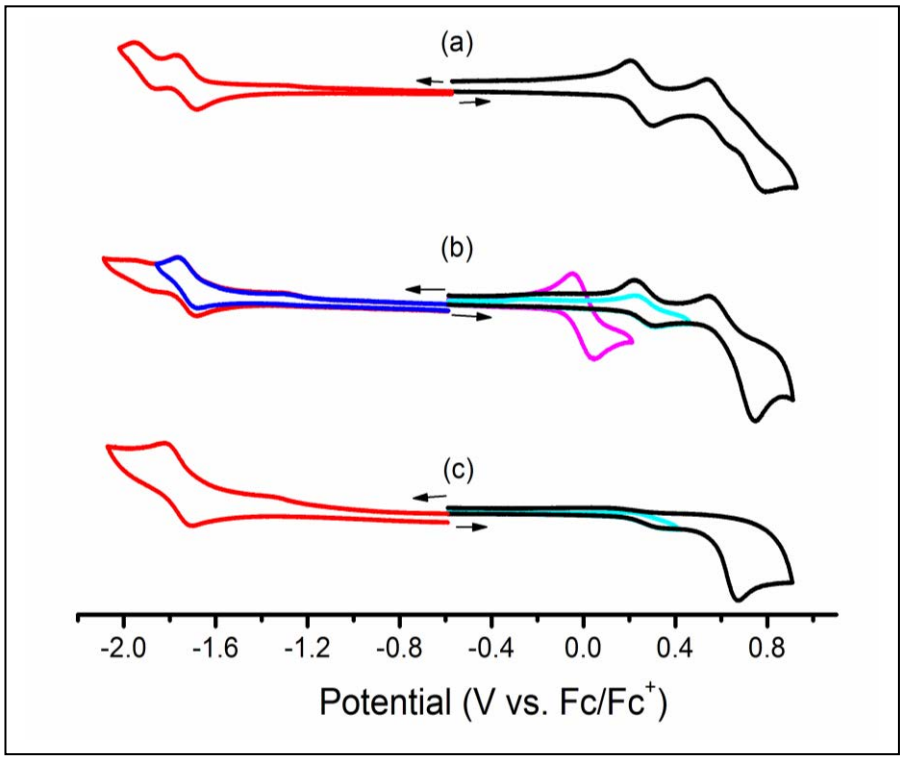

Figure 5.23: Cyclic voltammograms of the investigated (a) BDP-ZnP (b) $(BDP)_2$-ZnP and (c) $(BDP)_4$-ZnP dyads (~0.5 mM) in DCB containing 0.1 M (TBAP)ClO_4. Scan rate = 100 mV/s. The ferrocene oxidation, used as an internal standard, is shown in (b) (pink line).

Two electroreductions were also observed at -1.73 and -1.92 V, the former being the overlapping first electroreductions of BDP and ZnP entities. Interestingly, for the $(BDP)_2$-ZnP and $(BDP)_4$-ZnP dyads, almost similar redox behavior was observed, however, the peak currents corresponding to BDP electrooxidation and electroreduction were higher. That is, peak currents twice as much as ZnP in $(BDP)_2$-ZnP and four times as much as of ZnP in $(BDP)_4$-ZnP

were observed. The relatively difficult oxidation of BDP and almost similar reduction of BDP in the dyads suggest it being a poor electron donor or acceptor in the dyads.

Using the electrochemical, computational, and excited energy data, the free-energies of charge-separation (ΔG_{CS}) were calculated using following equations by Weller's approach.[96a]

$$-\Delta G_{CS} = \Delta E_{0\text{-}0} - e(E_{ox} - E_{red}) + \Delta G_S$$

where $\Delta E_{0\text{-}0}$ is the energy of the lowest excited state of ZnP (2.06 eV), $\Delta G_S = -e^2/(4\pi\varepsilon_0\varepsilon_R R_{Ct\text{-}Ct})$ and ε_0 and ε_R refer to vacuum permittivity and dielectric constant of DCB.

The calculations revealed ΔG_{CS} values to be endothermic by 0.1-0.2 eV for electron transfer from the singlet excited Zn porphyrin to BDP suggesting less likely occurrence of such reactions in the studied dyads.

Excited energy transfer in the $(BDP)_n$-ZnP dyads probed by pump-probe technique

As pointed out earlier, excitation of the BDP in the 495-505 nm range to a large extent selectively excites the antenna unit, BDP, thus allowing us to monitor energy transfer to the acceptor, ZnP, without it being directly getting excited. Both steady-state emission and excitation spectra confirm occurrence of excited

energy transfer in the dyads. Further evidence for the energy transfer and kinetics of such process is obtained from studies involving pump-probe technique. Here, an excitation wavelength was 500 nm, achieved by optical parameter amplifier with the time resolution of the instrument of 150-200 ps (FWHM of the instrument response). Measurements were carried out in three wavelength ranges, 440-660, 520-740 and 870-1090 nm. Since the excitation interfered with the signal around 500 nm, in some measurements in a small wavelength range around 500 nm was ignored. In most cases a global fit was used to achieve coherent analysis of the data at all wavelengths.

Transient absorption spectra of BDP-ZnP in DCB are presented in Figure 5.24 for which the most informative part of the spectrum was the visible part. At least three exponential fit had to be used. With the excitation wavelength of 500 nm mainly exciting the BDP chromophore, right after excitation a bleached band at 505 nm was clearly observed. The main lifetime for this bleached band was 48±9 ps. At longer delay time (>100 ps), the time resolved spectrum of the dyad corresponded to the differential spectrum of the first excited state of ZnP. Lifetime of this excited state was too long to be resolved with pump-probe measurements. A relatively minor fast component with time constant of 6 ps observed for BDP-ZnP was attributed to originate from more than one process.

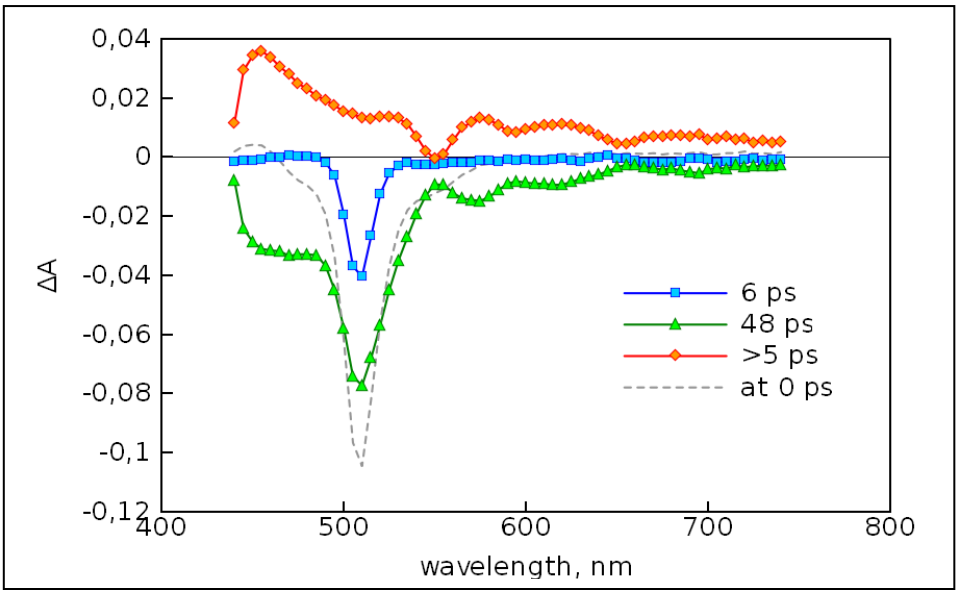

Figure 5.24: Transient absorption decay component spectra of the BDP-ZnP dyad in *o*-dichlorobenzene. The dashed line shows the differential absorption spectrum right after excitation (at 0 ps delay time).

That is, vibrational relaxation and solvent dynamics of BDP could be main contributors to this component. The ZnP internal conversion can be ruled out since the probe, ZnP is not excited to the second excited state at the excitation wavelength of 500 nm.

Transient absorption spectra of $(BDP)_2$-ZnP and $(BDP)_4$-ZnP in o-DCB were similar to that of the BDP-ZnP dyad (Figure 5.25). The lifetime of excited state of BDP moiety in $(BDP)_2$-ZnP and $(BDP)_4$-ZnP were 44±17 and 16±5 ps, respectively, though a bi-exponential fit was used for the latter dyad. The long-lived component (>> 3 ns) in Fig. 5.25a corresponded to that of the excited state

of porphyrin and couldn't be determined accurately with pump-probe method. The fastest component can be explained similar to the BDP-ZnP sample.

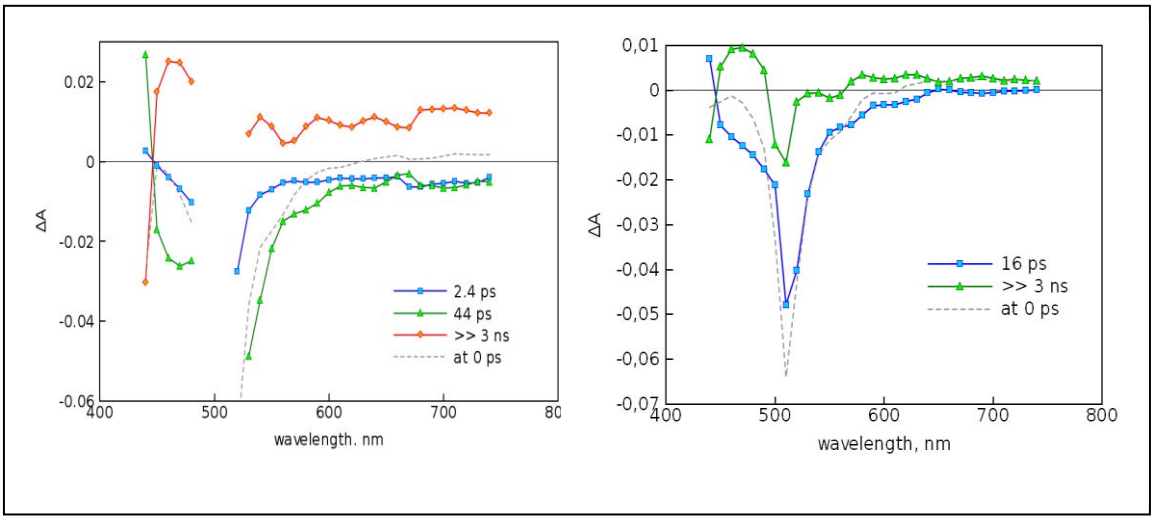

Figure 5.25: Transient absorption decay component spectra of (a) $(BDP)_2$-ZnP and (b) $(BDP)_4$-ZnP in *o*-dichlorobenzene. The dashed line shows the differential absorption spectrum right after excitation (at 0 ps delay time).

The results of pump-probe method suggest occurrence of ultrafast excitation energy transfer in the studied dyads, and a decrease in time constants for energy transfer with increasing the number of BDP units. That is, better antenna effect for dyads with multiple BDP units is realized not only by increased absorption of the compound but also by a faster energy transfer to the acceptor, porphyrin unit.

Formation and study of electron transfer of supramolecular triads.

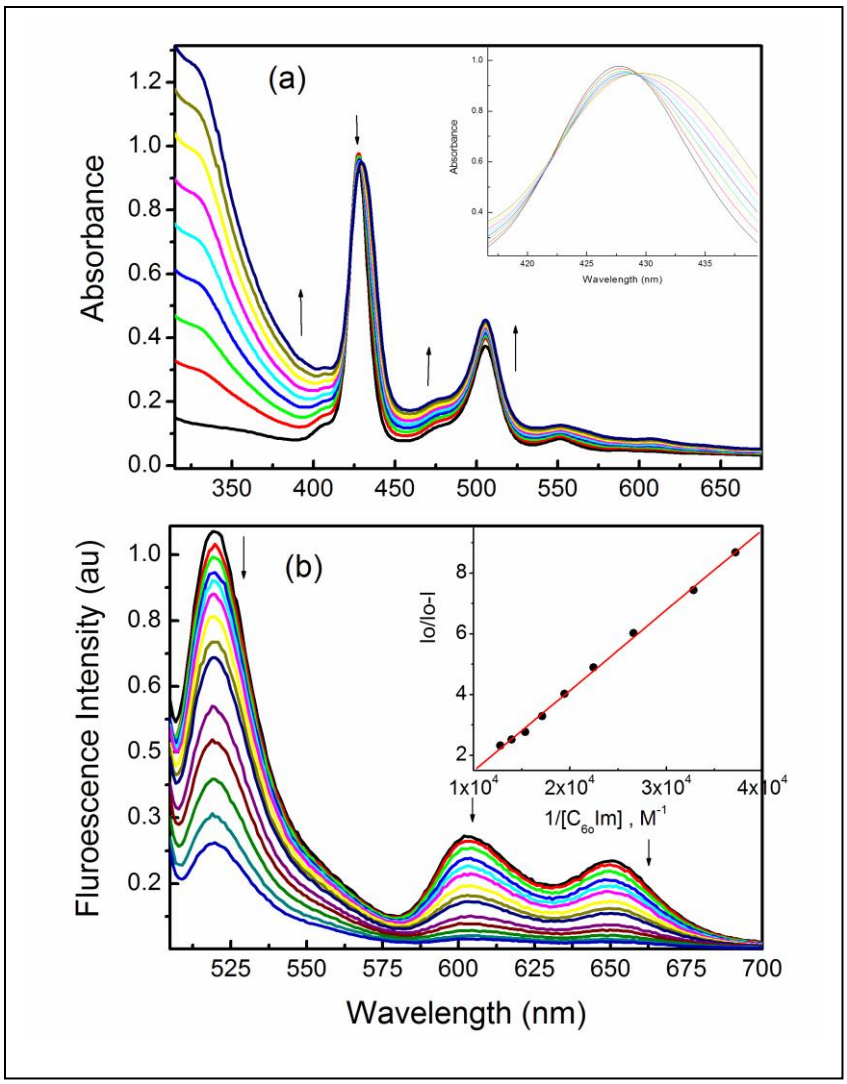

Figure 5.26: (a) Absorption spectral changes observed for $(BDP)_2$-ZnP (1.40 μM) binding to C_{60}Im (1.13 μM each addition) in DCB. (b) Fluorescence spectral changes observed during increasing addition of C_{60}Im (1.13 μM each addition) to the solution of $(BDP)_2$-ZnP to form the triad in DCB. λ_{ex} = 495 nm. The figure

inset shows Benesi-Hildebrand plot constructed by monitoring the emission intensity of the at 520 nm band for calculating the binding constant.

First, the formation and characterization of the supramolecular triads by axial coordination of C_{60}Im to $(BDP)_n$-ZnP dyads in DCB was performed using spectroscopic and electrochemical methods. The formation of the supramolecular triad was followed by optical absorption spectral methods. Figure 5.26a shows the spectral changes observed during the addition of C_{60}Im to the $(BDP)_2$-ZnP dyad in DCB. The Soret band at 426 nm first, decreased in intensity and then increased with a red shift to 431 nm. Isosbestic points at 422 and 429 nm were observed indicating the occurrence of an equilibrium process in solution (see Fig. 5.26a inset). It may be mentioned here that the band at 505 nm corresponding to the boron dipyrrin moiety revealed no peak shift during the course of the titration indicating no significant interactions with the fullerene; increase in the absorbance at 505 nm is attributed to the absorption of added fulleropyrrolidine. Independent control experiments performed in the presence of BDP control and C_{60}Im also revealed no spectral changes. These results suggest that only the zinc porphyrin is involved in axial coordination and not the boron dipyrrin of the dyad.

Figure 5.26b shows the fluorescence spectra of the $(BDP)_2$-ZnP dyad in the presence of increasing amounts of C_{60}Im at the excitation wavelength of 495 nm corresponding to the excitation of the BDP entity. The emission bands

corresponding to both boron dipyrrin and zinc porphyrin revealed quenching. Similar quenching was also observed when ZnP was directly excited at 550 nm in the triads. This quenching process in the $(BDP)_2$-ZnP:ImC_{60} triad clearly indicates the occurrence of electron transfer from the singlet excited zinc porphyrin to the coordinated fulleropyrrolidine.

The binding constant was evaluated by constructing Benesi-Hildebrand plot[93] (Fig. 5.26b inset). The calculated binding constant was found to be 3.0 x 10^4, 4.4 x 10^3, and 3.9 x 10^3 M^{-1}, respectively, for the mono, bis and tetra BDP appended ZnP. These results indicate moderately stable supramolecular triad formation by the axial ligation approach. The slightly lower stability for triads with higher number of BDP could be attributed to the steric and electronic effects.

Computational and electrochemical studies of the $(BDP)_n$-ZnP:ImC_{60} triads

The geometry of the triads was also visualized by performing computational studies. Figure 5.27 shows the optimized structures of the triads in which coordination of imidazole of C_{60}Im to Zn of ZnP was evident. Minimal structural changes of the $(BDP)_n$-ZnP dyads upon coordination of C_{60}Im were seen. Importantly, no direct interaction between the fullerene and BDP entity(ies) was observed. That is, the BDP and C_{60} units were separated by over 6.2 Å in these triads. The center-to-center and edge-to-edge distance between the fullerene and ZnP macrocycles were found to be 13.0 Å and 8.1 Å, respectively. The frontier HOMO and LUMO orbitals were also generated for the optimized

structures. In all these triads, the HOMO was located on the ZnP entity while the LUMO was located on the fullerene entity. That is, formation of $ZnP^{+\cdot}$:$ImC_{60}^{-\cdot}$ as the initial electron transfer product was visualized from these results. The localization of HOMO and LUMO also agree well with electrochemical results discussed earlier.

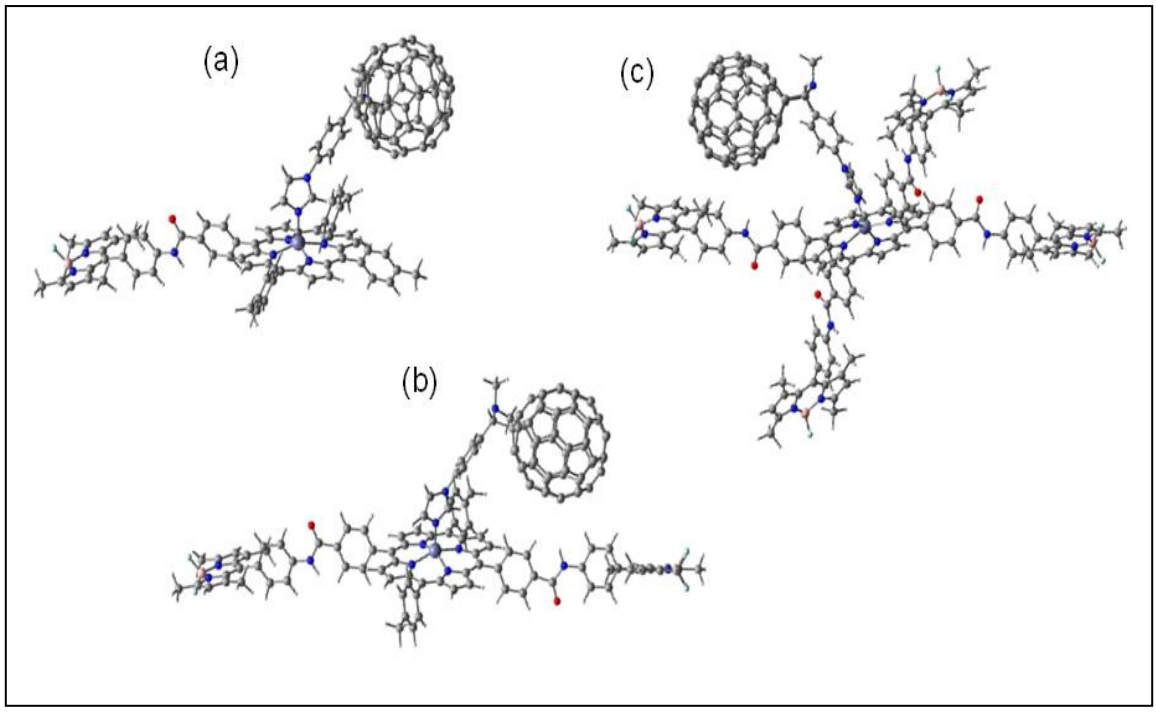

Figure 5.27: B3LYP/3-21G(*) optimized structures of (i) BDP-ZnP:ImC_{60}, (ii) $(BDP)_2$-ZnP:ImC_{60}, and (iii) $(BDP)_4$-ZnP:ImC_{60}.

Cyclic voltammetric studies were performed to arrive at the redox potentials of the investigated triads. Figure 5.28 shows voltammograms of BDP-ZnP dyad upon increasing additions of C_{60}Im. The first oxidation peak of ZnP

revealed a cathodic shift of about 60 mV upon axial coordination of C_{60}Im. However, no significant changes in the oxidation and reduction potentials of BDP or C_{60}Im were observed indicating little or no electronic perturbation of these macrocycles upon formation of the triads. Importantly, fulleropyrrolidine being better electron acceptor in terms of reduction potential in the triads was evident from these studies. From these electrochemical data on adding the excited energies and distances between the chromophores (*vide supra*), the free-energies of charge-separation (ΔG_{CS}) and charge-recombination (ΔG_{CR}) were calculated using the Weller equation.[95a] Such calculations revealed photoinduced electron transfer from the $^1ZnP^*$ to coordinated fullerene to be exothermic by ~0.80 eV for the triads while for charge recombination, the ΔG_{CR} values were ~1.26 eV.

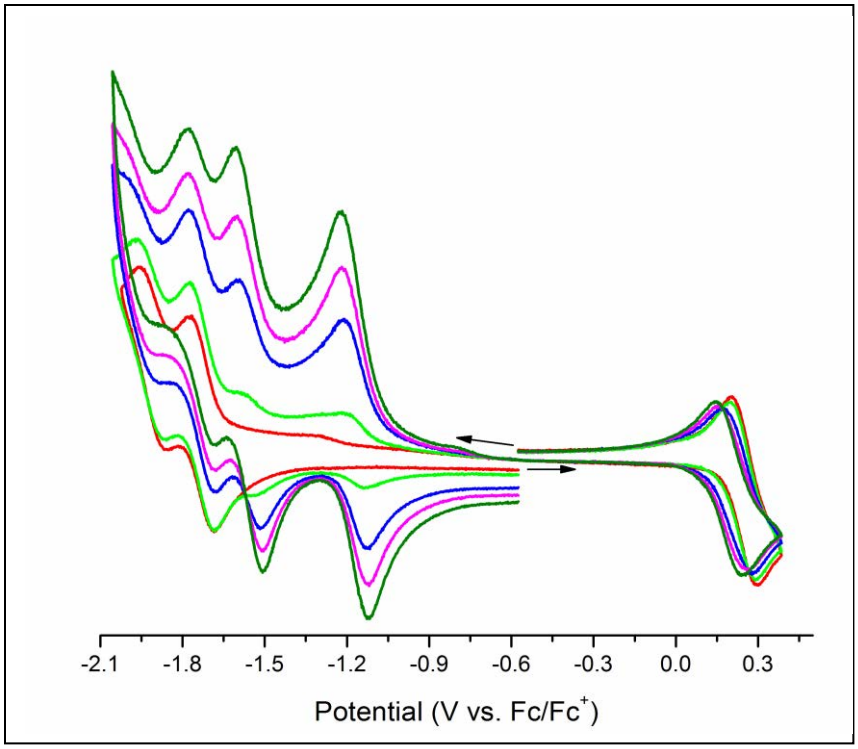

Figure 5.28: Cyclic voltammograms of the ZnP-BDP dyad upon increasing addition of C_{60}Im (0.2, 0.6, 0.8 and 1.0 eq) in *o*-dichlorobenzene, 0.1 M (TBA)ClO_4. Scan rate = 100 mV/s.

Photoinduced electron transfer in the $(BDP)_n$-ZnP:ImC_{60} triads probed by transient spectral studies

Transient absorption decay component spectra and data fitting using four exponential model of the BDP-ZnP:ImC_{60} supramolecular triad in DCB are presented in Figure 5.29.

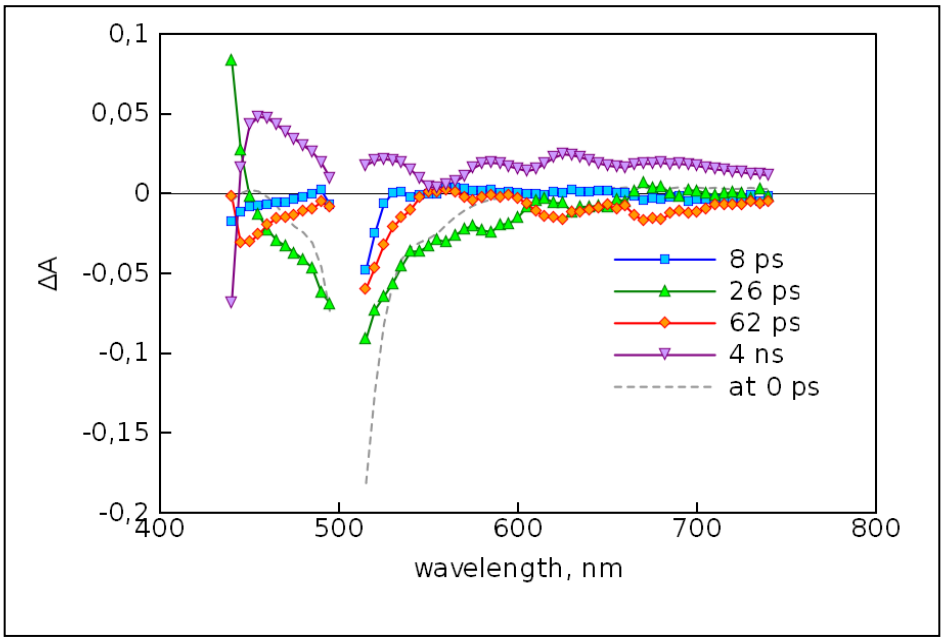

Figure 5.29: Transient absorption decay component spectra of BDP-ZnP:ImC_{60} complex in DCB. The dashed line shows the differential absorption spectrum right after excitation (at 0 ps delay time).

Same components of pure BDP-ZnP dyad are seen for triad complex. In analogous to (BDP)-ZnP spectrum, the fastest component observed in the triad spectrum, 8 ps, probably originates from the solvent and vibrational relaxation. A second component with lifetime of 26 ps can be attributed to the excitation relaxation of the BDP chromophore, since it has spectral features similar to that of 48 ps component of BDP-ZnP dyad. Qualitatively the decrease in the lifetime of the BDP excited state is in agreement with steady state emission measurements, showing lower fluorescence intensity of BDP unit upon addition of ImC_{60}. The longest-lived component at 4 ns, has been attributed to the charge separated state, $ZnP^{+\bullet}$: $ImC_{60}^{-\bullet}$, though it is rather similar to the longest-lived component of BDP-ZnP dyad. However, the main difference is in the shapes of transient absorption spectra where an increased intensity in the range of 600-700 nm for the BDP-ZnP:ImC_{60} triad due to the presence of ZnP radical cation was clearly observed. The component with lifetime of 62 ps can be attributed to the formation of charge separated state, since it shows some increase in transient absorption in the 600-700 nm range (area of porphyrin cation absorption).

Typically the transient absorption responses of porphyrin-fullerene dyads in the near infrared region are lower than that in the visible part of the spectrum since the molar absorbances of the transient states are lower. However a characteristic fullerene anion band can be observed around one micron wavelength to confirm the formation of the charge separated state. Transient

absorption decay component spectra and data fitting for the near IR-region are presented in Figure 5.30.

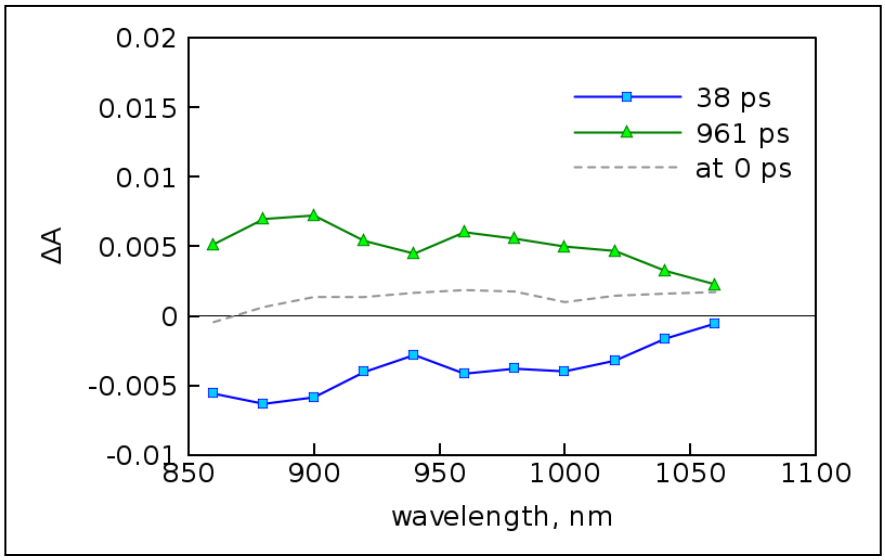

Figure 5.30: Transient absorption decay component spectra of (BDP)-ZnP:ImC_{60} complex in *o*-dichlorobenzene calculated for a bi-exponential model. The dashed line shows the differential absorption spectrum right after excitation (at 0 ps delay time).

Although three-exponential fit was used for the data in the visible part of spectrum, the bi-exponential fit is statistically sufficient for the IR part of the spectrum. The mean square deviations were 0.00095 and 0.00092 for bi- and three-exponential fits, respectively. The important feature of the transient absorption response in the IR region is that the absorption right after excitation was close to zero through the whole region, indicating that the fullerene is not

affect by the excitation pulse. The signal grew with time constant of roughly 40 ps and could be attributed to the formation of the charge separated state, although one cannot exclude presence of some amount of the fullerene excited state formed as the result of energy transfer. However a –pure" energy transfer can be excluded since the porphyrin is not in the ground state even at hundred picosecond delay time as clearly seen from the transient absorption data in the visible part of the spectrum.

The signal of $(BDP)_2$-ZnP:ImC_{60} and $(BDP)_4$-ZnP:ImC_{60} triads were much weaker due to solubility issue and as the result lower absorption at excitation wavelength, 500 nm, though the number BDP units per molecule is increased for this compounds. Signal-to-noise ratio was much poorer and the CS state is not clearly visible from the results though results show quenching of the lifetime of BDP chromophore. Hence, no further studies on these triads using pump-probe technique were performed.

The kinetics of electron transfer for the present triads is in good agreement with the previous studies involving triads made out of these entities but with different linkers and geometries.[66,146d] For BDP-ZnP:ImC_{60} triad, the CS time constant is roughly 60 ps, and the lifetime of the CS state is extended into nanosecond time domain. For $(BDP)_2$-ZnP:ImC_{60} triad such a claim can also be made due to similarities of the long-lived spectra and due to the strong overlap of energy transfer and electron transfer processes in time domain (both takes place in a few tens of picoseconds).

Energy level diagram

The results of the present investigation along with all of the control experiments clearly show occurrence of efficient energy transfer and electron transfer in the newly built supramolecular triads. The combination of optical absorption, steady-state fluorescence emission, and computational modeling, electrochemistry, and pump-probe transient absorption studies has allowed extraction of the needed energetic and kinetic information.

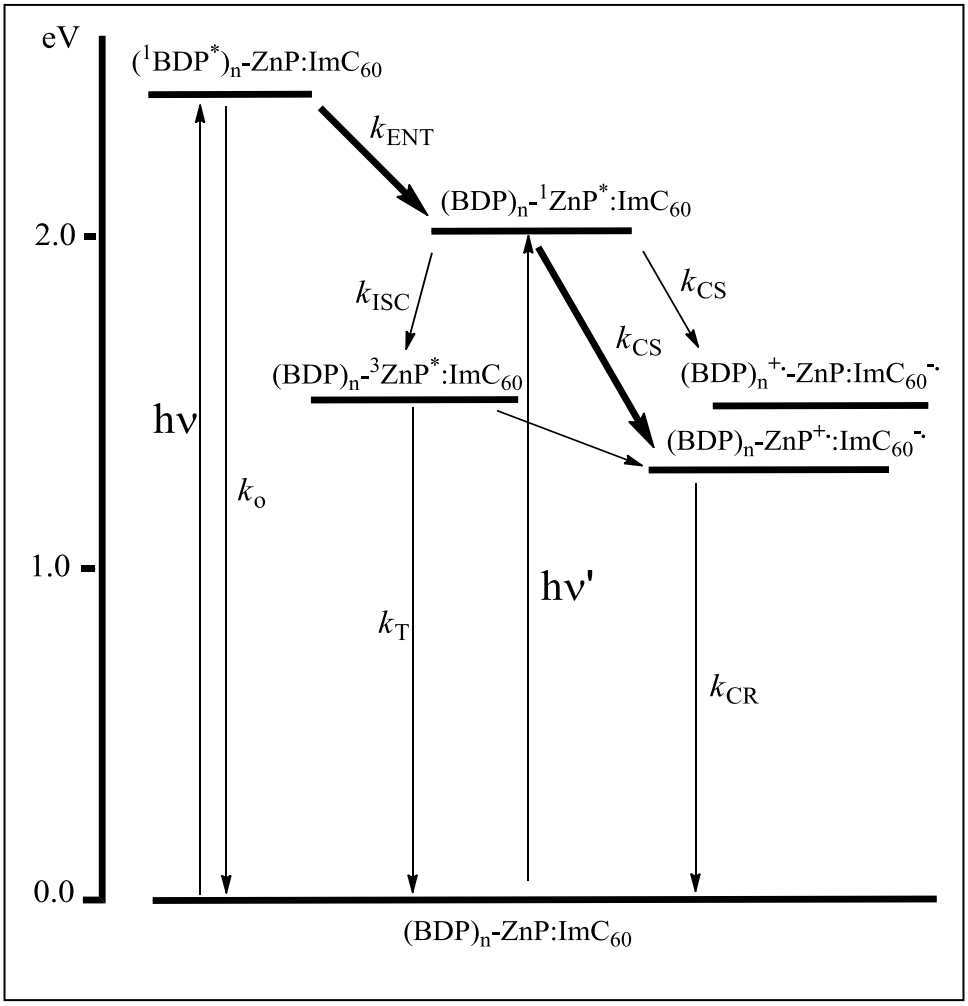

Figure 5.31: Energy level diagram showing the different photochemical events of the supramolecular $(BDP)_n$-ZnP:ImC_{60} triads after excitation of either the BDP or ZnP moieties. The thick arrows indicate major photochemical process and thin arrow represents minor photochemical process.

The different photochemical events observed in the triads are depicted in Figure 5.31 in the energy level diagram. Energies of the excited states of the different entities were calculated from the fluorescence peaks while the triplet state energy of ZnP was cited from the literature. The driving forces for the occurrence of electron transfer from the different excited chromophores of the triads used as discussed earlier. In the energy level diagram, the thick arrows indicate the major photochemical processes while thin arrows reveal minor processes. Based on the distance and energetic considerations, an electron transfer from singlet excited BDP to C_{60} is considered to be an inefficient process.

5.4 Summary

Novel supramolecular triads to mimic the ‗antenna-reaction center' functionality of photosynthetic reaction center have been successfully developed. The antenna mimic, boron dipyrrin entities were covalently linked to the reaction center electron donor mimic, a zinc porphyrin. Both steady-state and time-resolved emission as well as transient absorption studies clearly proved occurrence of efficient singlet-singlet energy transfer from BDP to zinc porphyrin

with the time scale of 28-48 ps, and a decrease in time constants for energy transfer with increasing the number of BDP units. That is, better antenna effect for dyads with higher numbers of BDP entities is realized from the present study. Next, the reaction center electron acceptor mimic, a fulleropyrrolidine appended with an imidazole ligand was coordinated to the zinc porphyrin to form the supramolecular triads. The structural integrity of the supramolecular triad was arrived by optical, computational and electrochemical studies. Energy calculations revealed possibility of photoinduced electron transfer from singlet excited zinc porphyrin to fullerene. Further transient studies involving pump-probe technique demonstrated occurrence of electron transfer from ^{1}ZnP* to fullerene in the supramolecular triads.

CHAPTER 6

Photo-induced Electron Transfer in Donor-Accepor Nanoconjugates

(A) Sensitive Efficiency of Photoinduced Electron Transfer to Band Gaps of Semiconductive Single-Walled Carbon Nanotubes with Supramolecularly Attached Zinc Porphyrin Bearing Pyrene Glues

6.1 Introduction

In recent years, major research effort has been devoted to understanding the physicochemical properties of carbon nanotubes, a new allotropic form of carbon,[159] with the intention of developing nanomaterial-based devices that could outline future technologies.[160-162] In this context, single-walled carbon nanotubes (SWNTs) have emerged as attractive candidates because of their outstanding physical, chemical, and mechanical properties.[160] The SWNTs consist of graphitic layers wrapped seamlessly into cylinders that originate from defined sections of two-dimensional graphene sheets. The structure of SWNTs relates to a pair of indices (*n*,*m*), referring to their diameter and chirality.[163] SWNTs are semiconducting, except for those in which the difference between *n* and *m* is a multiple of 3, and those are metallic. Recent efforts involving noncovalent chemical functionalization and physical techniques have resulted in the separation of metallic and semiconducting SWNTs according their (*n*,*m*)

index.[164-167] Among the different applications of SWNTs, the unique structure and the presence of extended π-delocalization have made them attractive candidates to develop light-energy harvesting and photovoltaic materials.[119b,168] Consequently, incorporation of SWNTs into donor-acceptor ensembles for the study of light-induced electron transfer has become an active area of research. Accordingly, various elegant covalently linked and non-covalently assembled donor-acceptor hybrids containing SWNT have been reported.[83,88-90,119b,168-171] However, all of these studies used mixture of SWNTs that were both metallic and semiconducting, with different (*n*,*m*) indices, making it impossible to derive meaningful and conclusive structure-reactivity relationships.

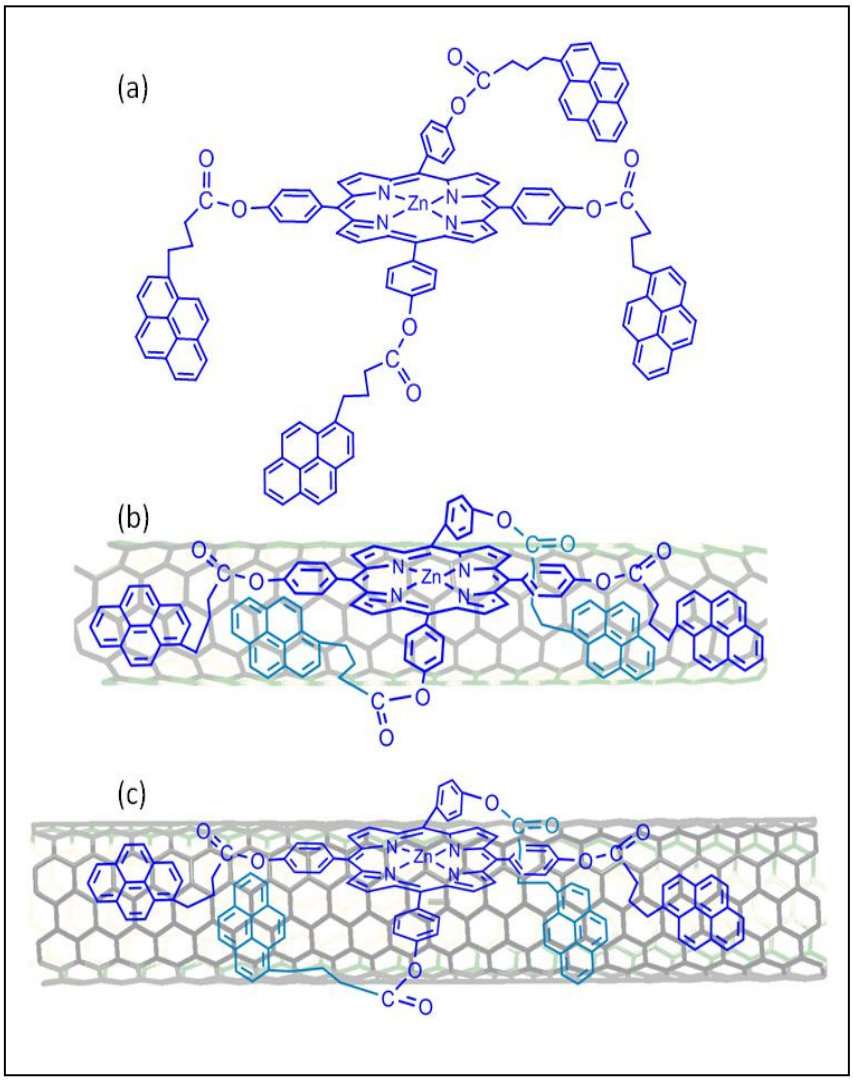

Figure 6.1: (a) Structure of the pyrene-appended zinc porphyrin donor. (b) $ZnP(pyr)_4$/(6,5)-SWNT and (c) $ZnP(pyr)_4$/(7,6)-SWNT donor-acceptor hybrids obtained as a result of $\pi-\pi$ interactions of the entities.

In the present study, we have overcome this barrier by constructing donor-acceptor hybrids made from semiconducting SWNTs of largely a single (*n*,*m*) index type; that is, two types of semiconducting nanotubes, viz., (6,5) and (7,6),

having different band gaps (difference up to 0.1 eV) have been utilized. Additionally, non-covalent self-assembly involving $\pi-\pi$ interactions between the donor-acceptor entities has been employed since this method would not destroy the electronic structure of nanotubes significantly.[172] To accomplish this, the donor, zinc porphyrin, has been functionalized with four pendant pyrene entities (Figure 6.1; ZnP(pyr)$_4$). Due to the presence of four interacting pyrene entities on the nanotubes' surface, stable ZnP(pyr)$_4$/SWNT hybrids are expected to form. As demonstrated here, this is indeed the case; additionally, the newly formed ZnP(pyr)$_4$/SWNT hybrids have allowed us to investigate the photoinduced electron transfer and to compare the electron acceptor behavior of the two types of nanotubes employed. Finally, photoelectrochemical responses of these ZnP(pyr)$_4$/SWNT nanohybrids have been tested.

6.2 Experimental section

Synthesis of Pyrene Functionalized Zinc Porphyrin

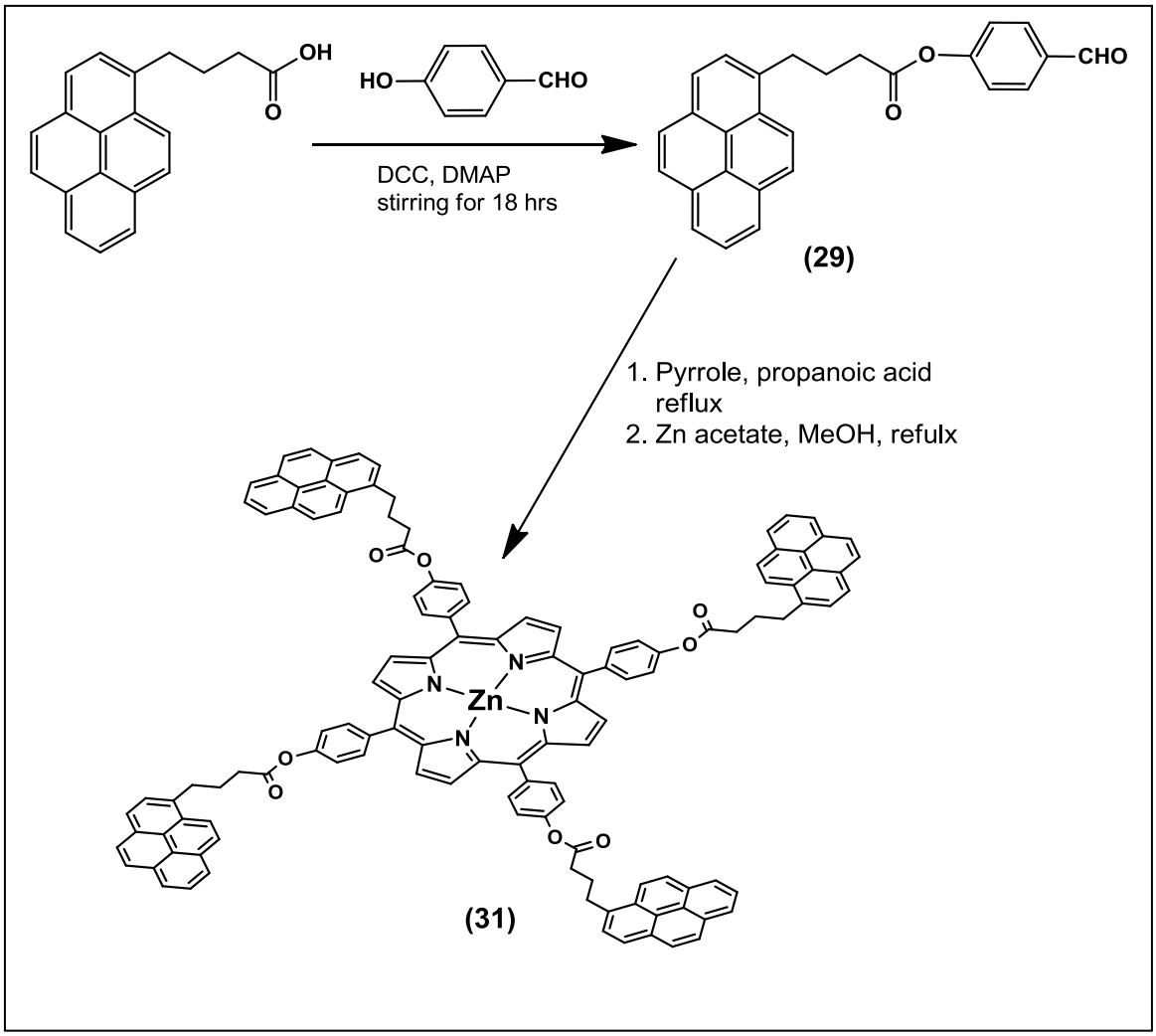

Scheme 6.1: Synthetic scheme adopted for compound **31**

(***4-Formyl)-phenyl-4-pyenylbutanoate, (29):*** 1-Pyrene butyric acid (590 mg, 2.05 mmol) and 4-hydroxy benzaldehyde (750 mg, 6.00 mmol) were

dissolved in 150 mL of dry CH_2Cl_2. Then 1,3-dicyclohexycarbodiimide (600 mg, 2.25 mmol) and 4-(dimethylamino)pyridine (32 mg, 0.524 mmol) were added, and the reaction mixture was stirred for 18 hrs. Then, the solvent was evaporated under the reduced pressure, and the crude compound was purified on silica gel column using hexane:CH_2Cl_2 (94:6 v/v) as eluent. Yield: 170 mg (20 %). ^{1}H NMR (400 MHz, $CDCl_3$) (in ppm) : δ 9.99 (s, 1 H, -CHO), 8.33-7.83 (m, 13H, pyrene *H* and phenyl *H*), 3.50 (t, 2 H, -CH_2-), 2.75 (t, 2H, -CH_2-), 2.33 (m, 2H, -CH_2-), Mass (APCI mode in CH_2Cl_2): calcd, 392.45; found 393.80.

H_2-5,10,15,20-tetra(phenyl-4-pyrenylbutanoate)porphyrin, (30): The title compound was synthesized according to Lindsey et al.[22] Pyrrole (100 μL, 1.42 mmol), and **29** (558 mg, 1.42 mmol) were dissolved in 200 mL of dry $CHCl_3$ and the resultant mixture was stirred under argon for 1.5 hr. Then $BF_3.O(Et)_2$ (60 μL, 0.473 mmol) was added. Porphyrin formation leveled off after 1 hr. *p*-chloronil (265 mg, 1.07 mmol) was then added to reddish-black reaction mixture and the resultant mixture was stirred at room temperature for 1 hr. Triethylamine (66 μL, 0.473 mmol) was added, and the reaction mixture was stirred for 8 hrs and then concentrated. Column chromatography on silica gel using hexane:$CHCl_3$ (60:40 v/v) as eluent gave the titled compound. Yield: 52 mg (5%). ^{1}H NMR (400 MHz, $CDCl_3$) (in ppm) : δ 8.89 (s, 8 H, β pyrrole), 8.49-7.50 (m, 52H, pyrene *H* and phenyl *H*), 3.61 (t, 8 H, -CH_2-), 2.90 (t, 8H, -CH_2-), 2.41 (m, 8H, -CH_2-), -2.81 (s, 2H, -NH-). Mass (APCI mode in CH_2Cl_2): calcd, 1760.03 ; found 1761.0.

5,10,15,20-tetra(phenyl-4-pyrenylbutanoate)porphyrinatozinc(II), (31): The free-base porphyrin **(30)** (25 mg) was dissolved in $CHCl_3$ (10 mL), a saturated solution of zinc acetate in methanol was added to the solution, and the resulting mixture was refluxed for 2 hrs.[23] The course of the reaction was followed spectrophotochemically by monitoring the disappearance of 521 nm band of **30**. At the end, the reaction was washed with water and dried over anhydrous Na_2SO_4. Chromatography on silica gel column was $CHCl_3$ as eluent gave the title compound. Yeild 90%. ^{1}H NMR (400 MHz, $CDCl_3$) (in ppm) : δ 9.00 (s, 8 H, β pyrrole), 8.41-7.21 (m, 52H, pyrene *H* and phenyl *H*), 3.60 (t, 8 H, -CH_2-), 2.88 (t, 8H, -CH_2-), 2.46 (m, 8H, -CH_2-), Mass (APCI mode in CH_2Cl_2): calcd, 1823.43 ; found 1824.8.

Preparation of ZnP(pyr)$_4$/SWNT(6,5) and ZnP(pyr)$_4$/SWNT(7,6) nanohybrids

A 1.0 mg sample of SWNT [(6,5) or (7,6) chirality] was added to 2.10 mg of ZnP(pyr)$_4$ dissolved in 15 mL of dry DMF and the reaction mixture was stirred for 48 hrs at room temperature. The resulting mixture was sonicated (Fisher Scientific, 60 Hz, 40 W) for 6 hrs at 20°C followed by centrifugation (Fisher Scientific, 50/60 CY) for 2 hrs. The excess of porphyrin was removed by separating the centrifugate from the black precipitate. Further purification is carried out by dissolving the black mixture in 5 mL of fresh DMF, sonicating for 30 min at 20 °C, followed by centrifugation for 1 hr, and removal of unadsorbed

porphyrin by separating from the black centrifugate. This process was repeated (at least twice) until the solution in the centrifuge tube turned colorless. At the end, 10 mL of fresh solvent was added to the resulting deposit and was sonicated for 15 min at 20 °C. This homogenous black dispersion was used for mentioned studies.

6.3 Results and discussion

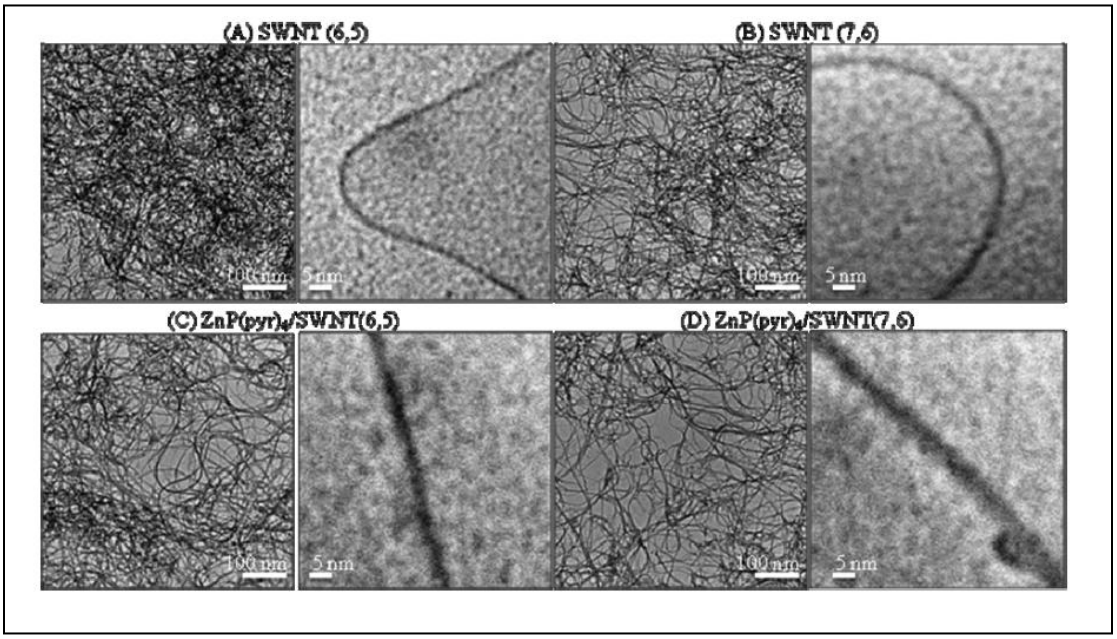

Figure 6.2: TEM images of (A) (6,5)-SWNT, (B) (7,6)-SWNT, (C) $ZnP(pyr)_4$/(6,5)-SWNT, and (D) $ZnP(pyr)_4$/(7,6)-SWNT at two magnification scales; white bar (left) 100 nm and (right) 5 nm.

The $ZnP(pyr)_4$/(6,5)-SWNT and $ZnP(pyr)_4$/(7,6)-SWNT hybrids were prepared by treating zinc porphyrin appended with pyrene entities, ZnP(pyr)4,

with SWNTs. Figure 6.2 shows transmission electron microscopy (TEM) images of the $ZnP(pyr)_4$-bound (6,5)- and (7,6)-SWNTs. The SWNT bundles were found to be loosened upon treatment with $ZnP(pyr)_4$, although intertwining during TEM sample preparation was observed. This suggests an appreciable decrease in SWNT stacking as compared with that in the untreated pristine SWNT samples. Each SWNT appeared thickened with a blur, probably by the adsorbed molecules. To a large extent, $ZnP(pyr)_4$/(6,5)-SWNT and $ZnP(pyr)_4$/(7,6)-SWNT hybrids were found to be free from impurities.

The samples were also characterized using laser Raman spectroscopy to obtain spectroscopic insight into the electronic structure of the SWNT in the $ZnP(pyr)_4$/(6,5)-SWNT and $ZnP(pyr)_4$/(7,6)-SWNT nanohybrids. In the Raman spectra of (6,5)-SWNT and (7,6)-SWNT, the characteristic radial breathing mode (RBM) bands in the 100-400 cm^{-1} region, disorderinduced D-mode in the 1350 cm^{-1} region, and Raman-allowed tangential G-bands in the 1500-1600 cm^{-1} region were expected.[173] As shown in Figure 6.3, the pristine (6,5)- and (7,6)-SWNTs revealed all of these Raman bands, and their values agreed well with the literature reports.[174] Interestingly, the Raman spectra of the noncovalently functionalized $ZnP(pyr)_4$/(6,5)-SWNT and $ZnP(pyr)_4$/(7,6)-SWNT revealed no significant shift on the peak position, only changing the relative intensities (300 vs 1570 cm^{-1} for (6,5)-SWNT and 170 vs 1570 cm^{-1} for (7,6)-SWNT). This implies that the electronic structures of the (6,5)-SWNT and (7,6)-SWNT are intact after being noncovalently functionalized with $ZnP(pyr)_4$.

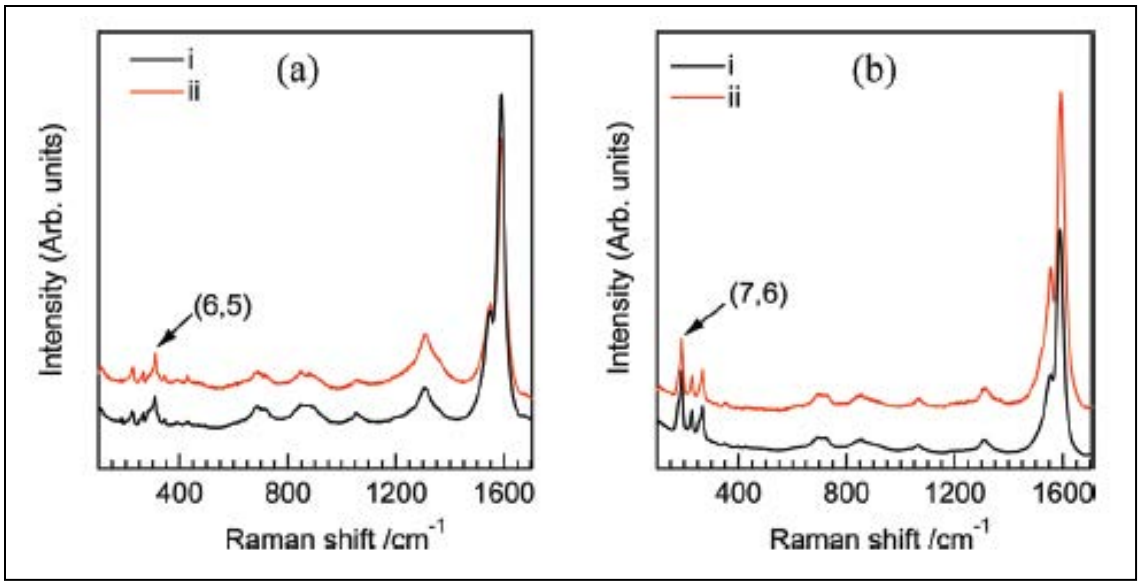

Figure 6.3: Raman spectra of (a) (i) $ZnP(pyr)_4$/(6,5)-SWNT and (ii) SWNT(6,5) and (b) (i) $ZnP(pyr)_4$/(7,6)-SWNT and (ii) SWNT(7,6) at the laser excitation wavelength of 632.8 nm.

Optical Absorption and Emission Studies.

Figure 6.4 shows the optical absorption spectra of $ZnP(pyr)_4$/(6,5)-SWNT and $ZnP(pyr)_4$/(7,6)-SWNT in the UV-vis region in dimethylformamide (DMF). Absorption bands of the semiconducting (6,5)-SWNTs in the hybrids are at 583 and 1022 nm, and those of the (7,6)-SWNTs are at 667 and 1170 nm, respectively, showing red-shifts by 400-600 cm^{-1} from the pristine peaks,24 due to their interaction with a π-electron of $ZnP(pyr)_4$. From the longest absorption edges, the band gap can be evaluated to be 1.21 and 1.05 eV, respectively,

which also showed narrowing of 0.06-0.08 eV, due to the interaction with a π-electron of $ZnP(pyr)_4$. The $ZnP(pyr)_4$/(6,5)-SWNT and $ZnP(pyr)_4$/(7,6)-SWNT hybrids also showed Soret and Q bands of ZnP in the 420 and 550 nm regions, with UV bands corresponding to the pyrene moieties.[167e] As for the Soret band of the ZnP units at 420 nm, peak position shows appreciable shift, and spectral broadenings, suggesting weak interaction with SWNT.

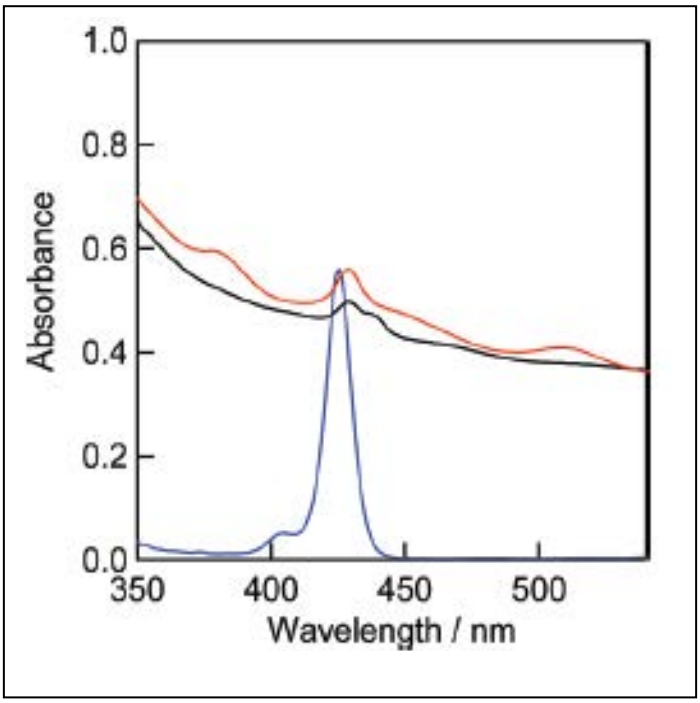

Figure 6.4: Steady-state absorption spectra in the Soret region of $ZnP(pyr)_4$/(6,5)-SWNT (black line), $ZnP(pyr)_4$/(7,6)-SWNT (red line), and $ZnP(pyr)_4$ (blue line) in DMF.

Several studies have attempted to estimate the redox potentials (E_{ox} and E_{red}) of nanotubes using techniques such as scanning tunneling spectroscopy, redox titrimetry, photoluminescence, and spectroelectrochemistry. Nakashima and co-workers[175] reported redox potentials of 15 isolated individual SWNTs having their own chirality indices based on Nernst analysis of the *in situ* spectroelectrochemical data. The work function of the SWNTs obtained experimentally agreed well with those calculated on the basis of first-principles.[175] The reported E_{ox} and E_{red} for the (6,5)-SWNT were 5.08 and 4.01 V vs vacuum, corresponding to a HOMO-LUMO gap of 1.07 eV. The E_{ox} and E_{red} for the (7,6)-SWNT were 4.94 and 4.03 V vs vacuum, with a HOMO-LUMO gap of 0.91 eV. The wider band gaps for (6,5)-SWNT than for (7,6)-SWNT estimated from the absorption bands is supported by these reported HOMO-LUMO gaps.

Steady-State Fluorescence Studies.

The formation of the ZnP(pyr)$_4$/(6,5)-SWNT and ZnP(pyr)$_4$/(7,6)-SWNT hybrids was also confirmed by fluorescence measurements, which also gave information about the excited state events in the hybrids. Figure 6.5 shows the steady-state fluorescence spectra (normalized to the intensity of the 614 nm band) of ZnP(pyr)$_4$, observed by the predominant excitation of the ZnP moiety (blue line), exhibiting a main peak around 614-620 nm with an additional 660 nm peak in DMF. Broadening with a slight peak shift was observed for (6,5)-SWNT and (7,6)-SWNT, supporting weak interaction between ZnP units and the SWNT

surface. In the hybrids with SWNT, the ZnP fluorescence intensity was found to be quenched over 80% of its original intensity, suggesting the occurrence of excited-state events such as electron transfer and energy transfer.

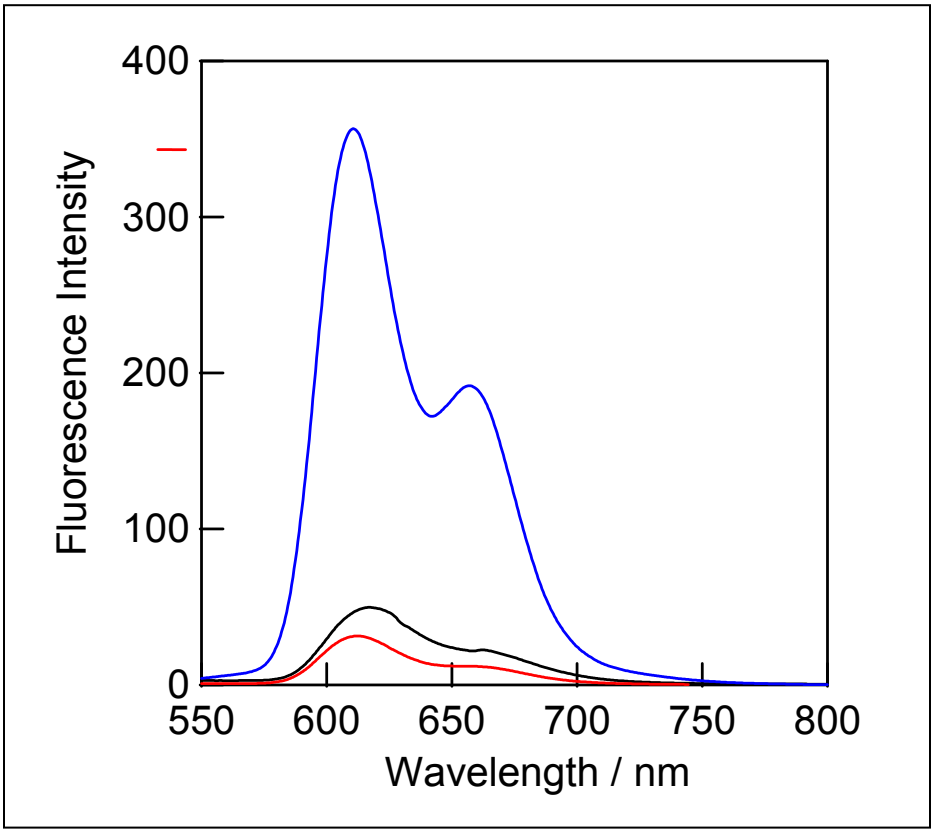

Figure 6.5: Steady-state fluorescence spectra of ZnP(pyr)$_4$/SWNT(6,5) (dark line) ZnP(pyr)$_4$/SWNT(7,6) (red line) and ZnP(Pyr)$_4$ (blue line) in DMF. λ_{ex} = 428 nm.

In order to obtain kinetics data for the singlet excited state of the ZnP moiety (^{1}ZnP*), picosecond time-resolved fluorescence measurements were

performed with the streak-scope method. The time profiles collected in the ZnP fluorescence are shown in Figure 6. 6.

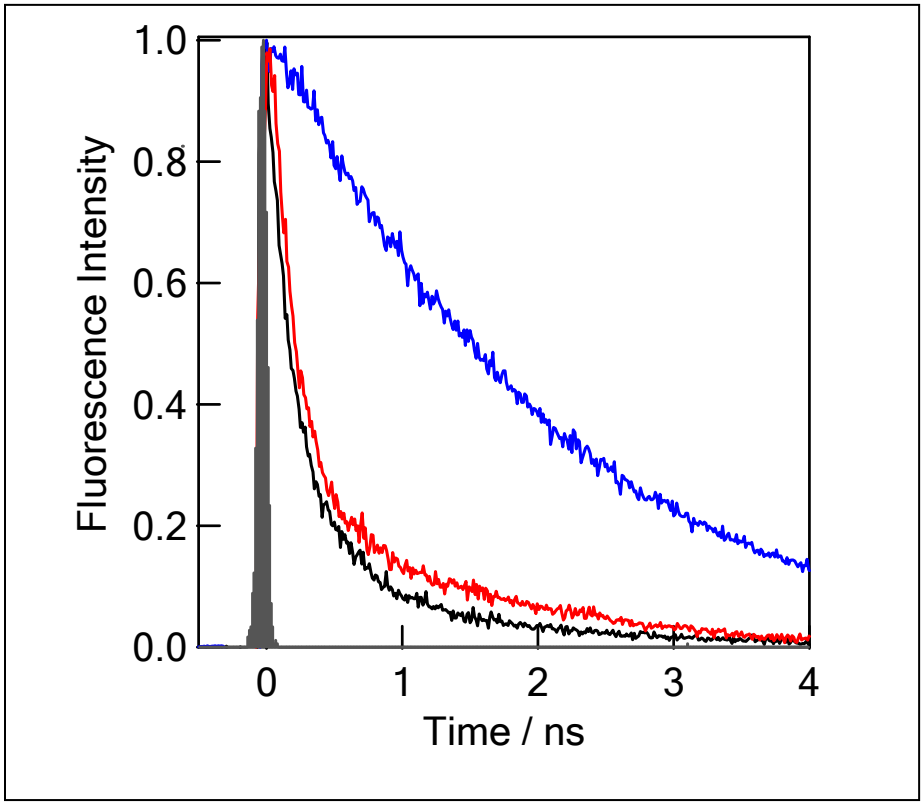

Figure 6.6: Fluorescence decays at monitoring region of 600-660 nm for ZnP(pyr)$_4$/SWNT(6,5) (dark line), ZnP(pyr)$_4$/SWNT(7,6) (red line) and ZnP(Pyr)$_4$ (blue line) in DMF; λ_{ex} = 408 nm.

The ZnP fluorescence followed a monoexponential decay with a lifetime of 2100 ps. Addition of (6,5)-SWNT and (7,6)-SWNT to form the hybrids accelerated the ZnP fluorescence decay, which could be curve-fitted with a

biexponential decay function. The ZnP fluorescence lifetimes evaluated under these conditions were found to be 260 (78%) and 2100 ps (22%) for ZnP(pyr)$_4$/(6,5)-SWNT and 180 (80%) and 2100 ps (20%) for ZnP(pyr)$_4$/(7,6)-SWNT, in which the longer lifetime may be attributed to non-interacting ZnP(pyr)$_4$ with SWNTs. The fast-decaying component provides additional evidence for the formation the hybrids with SWNTs. By assuming that the fast-decaying component is due to electron transfer, the rate of charge separation, k_{CS}, and quantum yield, Φ_{CS}, were evaluated according to eqs 6.1 and 6.2.

$$k_{CS} = (1/\tau_f)_{nanohybrid} - (1/\tau_f)_{ref} \quad (6.1)$$

$$\Phi_{CS} = [(1/\tau_f)_{nanohybrid} - (1/\tau_f)_{ref}] / (1/\tau_f)_{nanohybrid} \quad (6.2)$$

where $(1/\tau_f)_{nanohybrid}$ and $(1/\tau_f)_{ref}$ are the lifetimes of the ^{1}ZnP* moiety in the presence and in the absence of SWNTs, respectively. The evaluated k_{CS} and Φ_{CS} in DMF were found to be 3.4×10^9 s^{-1} and 0.88 (0.69 including interacting fraction), respectively, for ZnP(pyr)$_4$/(6,5)-SWNT, which are slightly smaller than those for ZnP(pyr)$_4$/(7,6)-SWNT, that is, k_{CS}) 5.1×10^9 s^{-1} and Φ_{CS}) 0.91 (0.73 including interacting fraction) in DMF. These findings indicate that (7,6)-SWNT, with a narrower band gap, is more favorable for charge separation via ^{1}ZnP* compared with (6,5)-SWNT with wider band gap. Usually, semiconductors with narrower band gaps possess lower conduction bands having higher electron affinity, as supported by the reported E_{red} values.[175]

Nanosecond Transient Absorption Studies.

Evidence for charge separation and the rate of charge recombination, k_{CR}, has been obtained from the transient absorption spectral studies using a 532-nm laser light, which predominantly excites the ZnP moiety.[176] Figure 6.7 shows the nanosecond transient absorption spectra of ZnP(pyr)$_4$/(7,6)-SWNT nanohybrids in Ar saturated DMF (see Figures 6.8 (a) and (b) for (6,5)- and (7,6)-SWNT in the absence of ZnP).

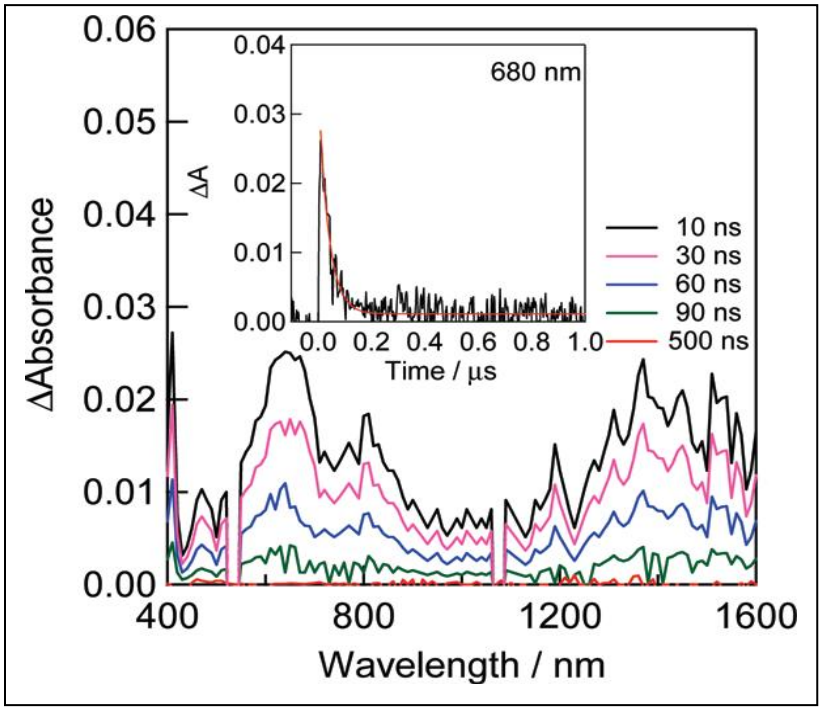

Figure 6.7: Nanosecond transient absorption spectra of ZnP(pyr)$_4$/(7,6)-SWNT bserved upon 532 nm (ca. 3 mJ/pulse) laser irradiation in Ar saturated DMF. Inset: Absorption-time profile.

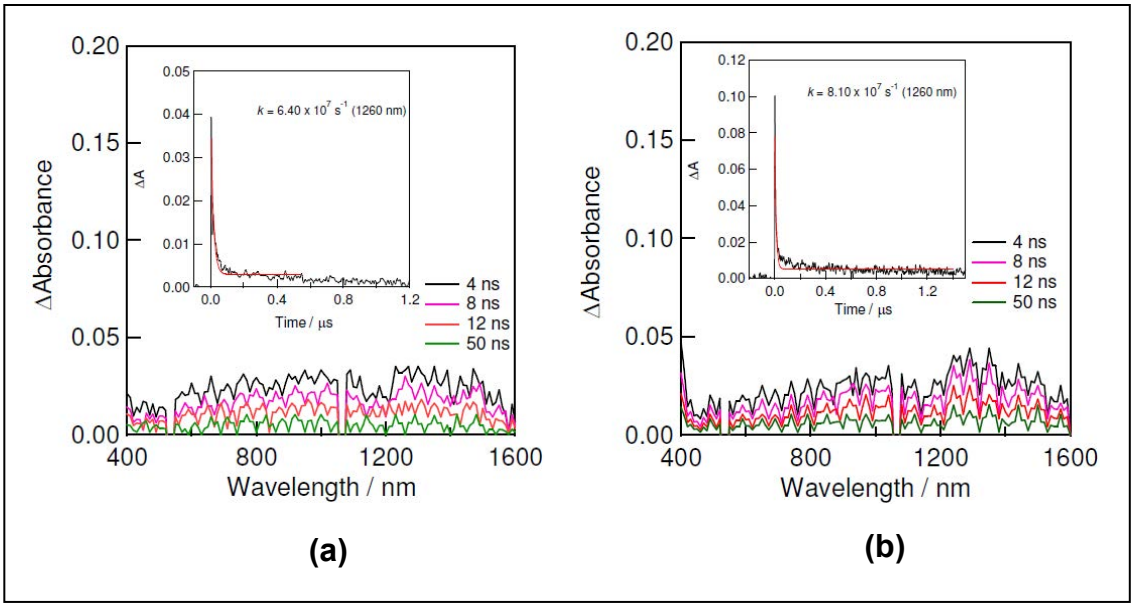

Figure 6.8: (a) Nanosecond transient absorption spectra of (a) SWNT(6,5)pyNH_3 and (b) SWNT(7,6)pyNH_3 observed by 532 nm (ca. 3 mJ/ pulse) laser irradiation in DMF. Inset: Absorption-time profile.

Importantly, a transient absorption peak corresponding to the formation of the ZnP radical cation ($ZnP^{\bullet+}$) around 600-700 nm[90] was observed, although the $ZnP^{\bullet+}$ absorption may show slightly different features from the isolated ones because of appreciable perturbation from the near-by π-interacting SWNTs. In addition, the absorption bands in the near-IR region probably correspond to the trapped electron on the SWNTs (expressed as $SWNT^{\bullet-}$). Indeed, broad absorption bands observed around 1400 nm were frequently assigned to $SWNT^{\bullet-}$, although further studies are needed to confirm these assignments. The rise of $ZnP^{\bullet+}$ around 680 nm was estimated to be fast, within the nanosecond laser

pulse (6 ns) (see the time profile in Figure 6.7 (inset), which corresponds to the charge separation within ca. 2 ns as estimated from the ZnP fluorescence decay time profile (Figure 6.6), giving $ZnP^{\bullet+}(pyr)_4$/(7,6)-$SWNT^{\bullet-}$. The decay of $ZnP^{\bullet+}$ mostly finished within 200 ns; from the first-order fitting to the decay curve, the charge recombination rate constant of $ZnP^{\bullet+}(pyr)_4$/(7,6)-$SWNT^{\bullet-}$ was evaluated to be k_{CR}) 2.7 × 10^7 s^{-1}. Using the k_{CR} value, the lifetime of the radical ion pair, τ_{RIP} (= $1/k_{CR}$), was evaluated to be 37 ns, indicating that the radical ion pairs persist for some extent in the supramolecular nanohybrid in DMF.

For the $ZnP(pyr)_4$/(6,5)-SWNT, similar transient absorption spectra were observed (Figure 6.9). From the time profile of $ZnP^{\bullet+}$, k_{CR} = 2.1 × 10^7 s^{-1} and τ_{RIP} = ca. 48 ns in DMF were evaluated. These findings indicate that τ_{RIP} of $ZnP^{\bullet+}(pyr)_4$/(7,6)-$SWNT^{\bullet-}$ is slightly shorter than that of $ZnP(pyr)_4{}^{\bullet+}$/(6,5)-$SWNT^{\bullet-}$

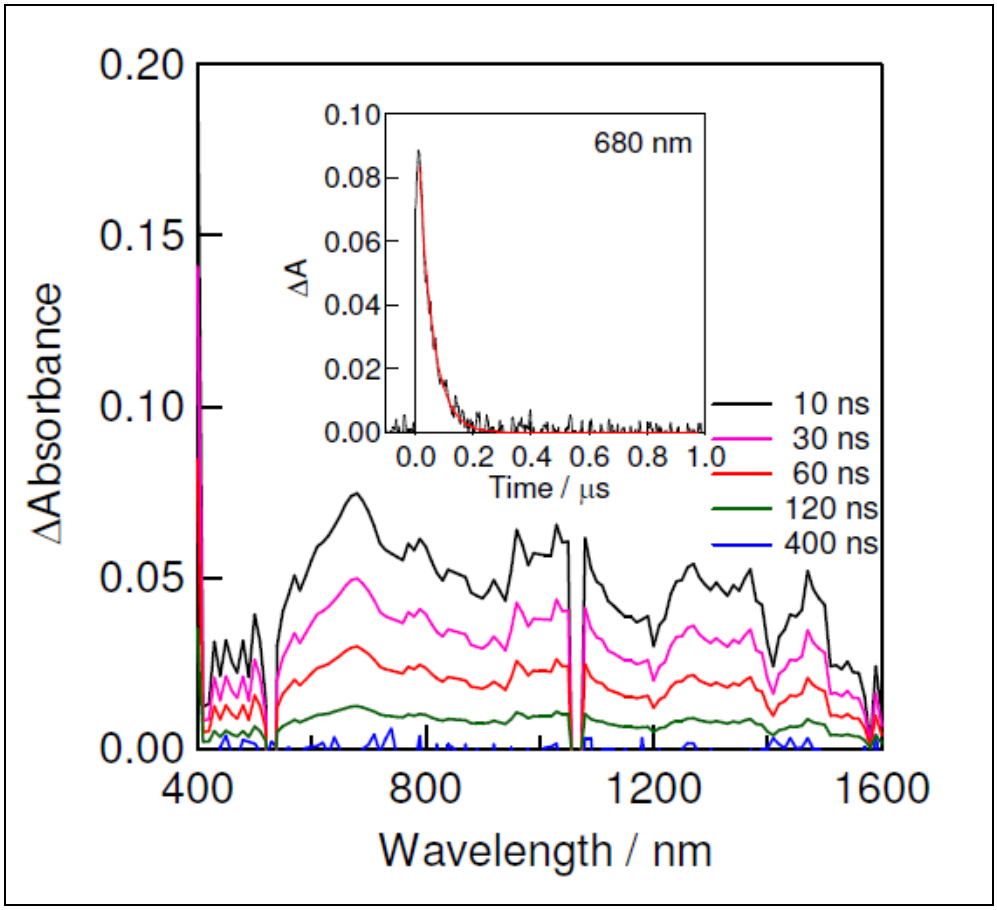

Figure 6.9: Nanosecond transient absorption spectra of ZnP(pyr_4)/SWNT(6,5) observed by 532 nm (ca. 3 mJ/ pulse) laser irradiation in Ar-saturated DMF. Inset: Absorption-time profile.

Electron-Pooling Measurements.

In order to further confirm the occurrence of charge separation leading to the formation of $ZnP^{\bullet+}(pyr)_4/SWNT^{\bullet-}$, additional electron mediation experiments were performed by the addition of the second electron acceptor, hexyl viologen

dication (HV^{2+}), and a sacrificial electron donor, 1-benzyl-1,4-dihydronicotinamide (BNAH), to the nanohybrid solution.[177] By steady-state absorption spectral measurements after repeated laser light irradiation (532 nm), which predominantly excites the ZnP moiety and SWNT but not the additives (HV^{2+} and BNAH), the accumulation of $HV^{\bullet+}$ was observed at 620 nm, as shown in Figure 6.10.

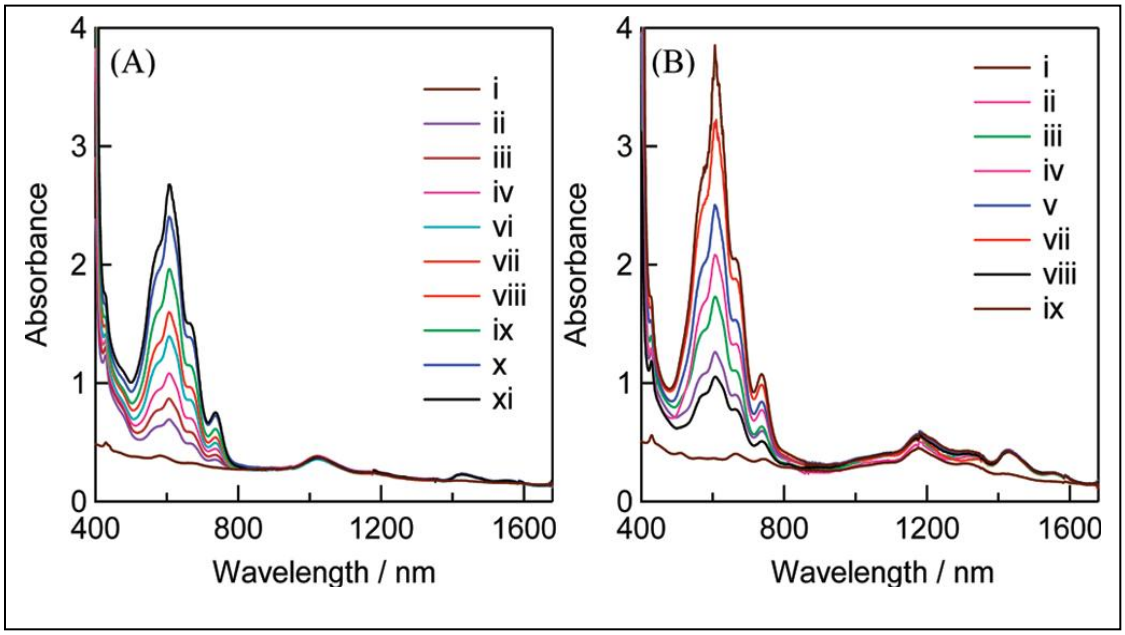

Figure 6.10: Steady-state absorption spectra of (A) $ZnP(pyr)_4$/(6,5)-SWNT and (B) $ZnP(pyr)_4$/(7,6)-SWNT in Ar-saturated DMF solution measured after five laser shots (6 ns pulse width and 3 mJ/pulse) at 532 nm in the presence of HV^{2+} (0.5 mM) and BNAH, (i) 0, (ii) 0.5, (iii) 1.0, (iv) 1.5, (v) 2.0, (vi) 2.5, (vii) 3.0, (viii) 3.5, and (ix) 4.0 mM.

The concentration of accumulated $HV^{\bullet+}$ species increased with increasing BNAH concentration, supporting the role of BNAH as a sacrificial hole-shifting reagent. In Figure 6.10, the overall maximal absorbance of $HV^{\bullet+}$ was observed in the presence of 0.5 mM HV^{2+} and 4.0 mM BNAH; thus, from the absorbance, the maximal concentration of $HV^{\bullet+}$ was evaluated to be 0.2 mM, which amounts to 40% conversion of added HV^{2+} for $ZnP(pyr)_4$/(6,5)-SWNT. For $ZnP(pyr)_4$/(7,6)-SWNT, the accumulation of $HV^{\bullet+}$ was similarly observed at 620 nm, giving the maximal concentration of 0.3 mM and 60% conversion. These observations indicate that $ZnP(pyr)_4$/(7,6)-SWNT is more efficient than ZnP(pyr)4/(6,5)-SWNT for the accumulation of $HV^{\bullet+}$.

The mechanism for this electron-pooling process can be understood on the basis of the ZnP fluorescence quenching and transient absorption spectral measurements, suggesting generation of $ZnP^{\bullet+}$ and probable $SWNT^{\bullet-}$ in the nanohybrids. The electron trapped in SWNT transfers to HV^{2+}, generating $HV^{\bullet+}$ as the electron-pooling product. The hole of $ZnP^{\bullet+}$ irreversibly shifts to BNAH in the nanohybrids, giving $BNAH^{\bullet+}$, which is further converted to 1-benzylnicotinamide cation (BNA^+). The efficient photosensitized charge separation/electron migration/hole shift processes of the $ZnP(pyr)_4$/SWNT nanohybrids are illustrated in Scheme 6.2.

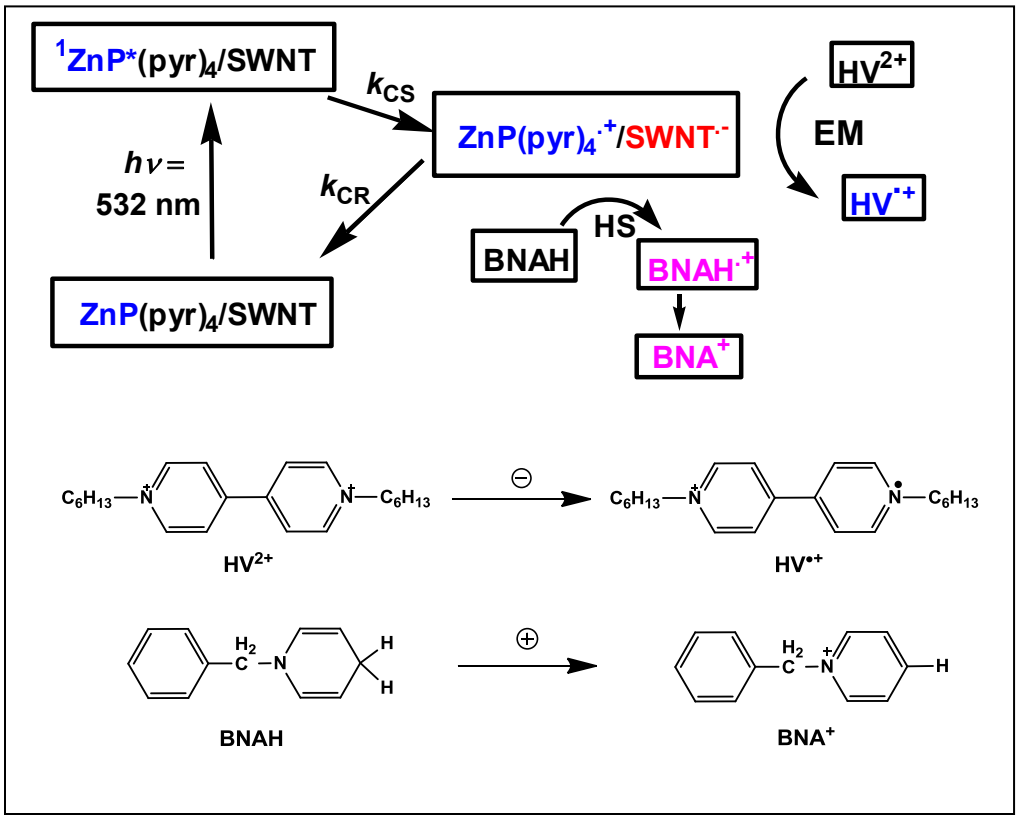

Scheme 6.2: Photocatalysis via electron mediation.

Abbreviations: s-SWNT, semiconductor SWNT; CS, charge separation; CR, charge recombination; EM, electron migration; and HS, hole shift.

The efficiency of the CS process vs the CR process can be evaluated from the ratio of k_{CS}/k_{CR}; the value of 190 for ZnP(pyr)$_4$/(7,6)-SWNT is higher than the value of 160 for ZnP(pyr)$_4$/(6,5)-SWNT, which can be defined as kinetic charge stabilization. This order is in agreement with the $HV^{\bullet+}$ accumulation conversion.

Photocurrent Measurements

A drop-cast method was applied to fabricate the films of $ZnP(pyr)_4$/SWNT adsorbing on the SnO_2 nanoparticles on the optical transparent electrodes (OTE/SnO_2 electrode). The absorption spectrum of OTE/SnO_2/$ZnP(pyr)_4$/ SWNT is almost the same as those of $ZnP(pyr)_4$/SWNT shown in Figure 6.3 (see Figure 6.11), except for the broadening of the absorption bands in the whole region, suggesting aggregation on the electrodes.

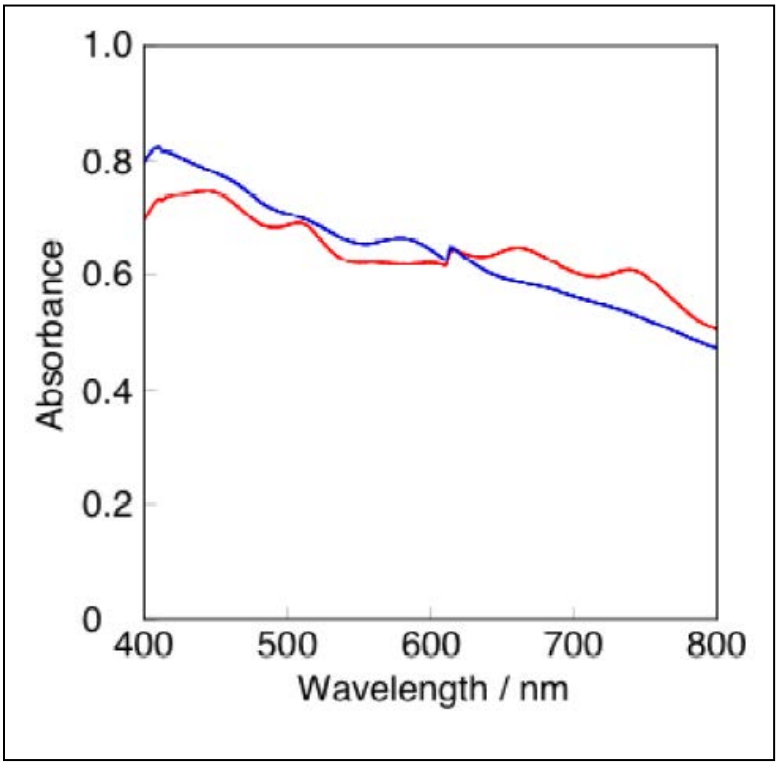

Figure 6.11: Absorption spectra of OTE/SnO_2/ZnP-$(Pyr)_4$:SWNT(6,5) electrode (blue spectrum) and OTE/SnO_2/ZnP-$(Pyr)_4$:SWNT(6,7) electrode (red spectrum).

Photoelectrochemical measurements were performed in a two compartment cell equipped with a potentiostat, using OTE/SnO_2/ZnP(pyr)$_4$/SWNT as the working electrode and Pt wire as the counter electrode. The photocurrent action spectra of OTE/SnO_2/ZnP(pyr)$_4$/SWNT electrodes were measured by examining the wavelength dependence of the incident photon-to-current conversion efficiency (IPCE).[178] The IPCE values are calculated by normalizing the photocurrent densities for incident light energy and intensity in the usual manner.

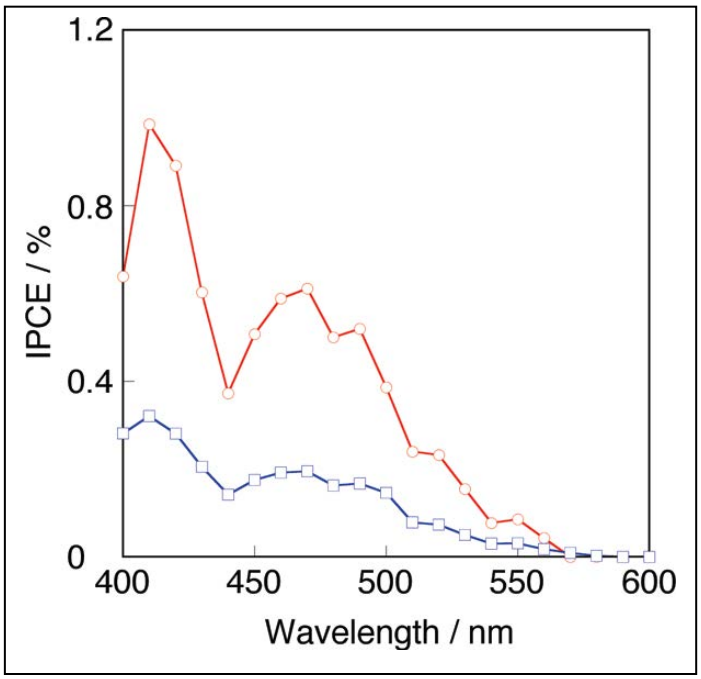

Figure 6.12: Photocurrent action spectra of IPCE: OTE/SnO_2/ZnP(pyr)$_4$/(6,5)-SWNT electrode (blue spectrum) and OTE/SnO_2/ZnP(pyr)$_4$/(7,6)-SWNT electrode (red spectrum). Electrolyte: 0.5 M LiI, 0.01 M I_2 in acetonitrile.

As shown in Figure 6.12, the IPCE of OTE/SnO_2/ZnP(pyr)$_4$/(7,6)-SWNT electrode reaches 1% as a maximal value at 420 nm, with the second maximum near 460 nm, which is about 3 times larger than that of OTE/SnO_2/ZnP(pyr)$_4$/(6,5)-SWNT electrode (0.35% in 400-450 nm region). This order is in agreement with those of the $HV^{\bullet+}$ accumulation conversion and k_{CS}/k_{CR}.

6.4 Summary

Photoinduced electron transfer in selfassembled zinc porphyrin-SWNT hybrids having (7,6)- and (6,5)-enriched carbon nanotubes is documented. The zinc porphyrin, along with four pendant pyrene entities (ZnP(pyr)$_4$), stacked on the SWNT surface due to $\pi-\pi$ interactions, resulting in exfoliation of the semiconducting nanotubes, as revealed by TEM measurements. Raman spectral measurements revealed the electronic structure of the nanotubes to be intact upon hybrid formation. Free-energy calculations suggested the possibility of photoinduced electron transfer in both the (7,6)- and (6,5)-enriched ZnP(pyr)$_4$/SWNT nanohybrids, while steady-state and time-resolved fluorescence studies revealed efficient charge separation quenching via the singlet excited state of zinc porphyrin, as supported by the nanosecond transient absorption technique, which confirmed the porphyrin cation radical. The rates of charge separation, k_{CS}, was found to be slightly higher for (7,6)-nanotube-derived hybrids than for (6,5)-nanotubederived hybrids, while an opposite trend was observed for k_{CR}. The nanohybrids also photocatalytically reduced hexyl viologen

dication (HV^{2+}) and oxidized a sacrificial electron donor in an electron-pooling experiment, offering additional proof for the occurrence of photoinduced charge separation. Finally, solar cells constructed using the $ZnP(pyr)_4$/SWNT hybrids yielded an interesting result, showing that the efficiency of the solar energy conversion was higher for (7,6)-SWNT, with a narrower band gap, compared with (6,5)-SWNT, having a wider band gap, following the same trends observed with charge separation and electron pooling processes.

(B) Band Gap Dependent Electron Transfer in Supramolecular Nanohybrids of (6,5)- or (7,6)-Enriched Semiconducting SWNT as Donors and Fullerene as Acceptor

6.1 Introduction

Carbon nanotubes (SWNT)[159] are emerging new materials for diverse applications including photovoltaics, electronics, composites, and biosensors.[160] The unique structural properties have made them novel materials in nanotechnology, especially in light energy harvesting applications.[168c] Accordingly, a number of studies have reported electron transfer and photovoltaic applications of nanohybrids made out of SWNTs.[168b,179] From these studies, however, no meaningful structure-reactivity relationship could be derived due to the nature of employed SWNT having both metallic and semiconducting tubes with different chirality indices. We overcame this hurdle by constructing previous nanohybrid, porphyrin-SWNT donor-acceptor hybrids using (7,6)- and (6,5)- enriched SWNTs and demonstrated that the former with a larger diameter of 1.0 nm is better for charge separation compared to the latter with a smaller diameter of 0.8 nm.[180]

A quick literature survey shows that in majority of the studies SWNTs acted as good electron acceptors, and only in a very few examples they have been shown to be electron donors.[90] Moreover, no systematic study has ever

been done on enriched semi-conducting SWNT for their ability to be electron donors. In fact, recent electrochemical studies on purified semiconducting SWNTs have shown that their chirality dependent oxidation potential are moderately low,[175,181] and hence, can be employed as electron donors in the presence of suitable electron acceptors. This has been verified in the present study where (6,5)- and (7,6)-enriched SWNT have been noncovalently attached to a well-known electron acceptor, fullerene[179] and demonstrate band gap dependent electron transfer behavior. To accomplish the noncovalent attachment, fullerene was functionalized to possess a pyrene moiety, pyrC_{60} as shown in Figure 6.12. To produce SWNT(n,m)/pyrC_{60} nanohybrids, about 2 mg of pyrC_{60} were mixed with 1 mg of SWNT(*n*,*m*) in 1.5 mL of DMF and purified by repeated sonication and centrifugation.

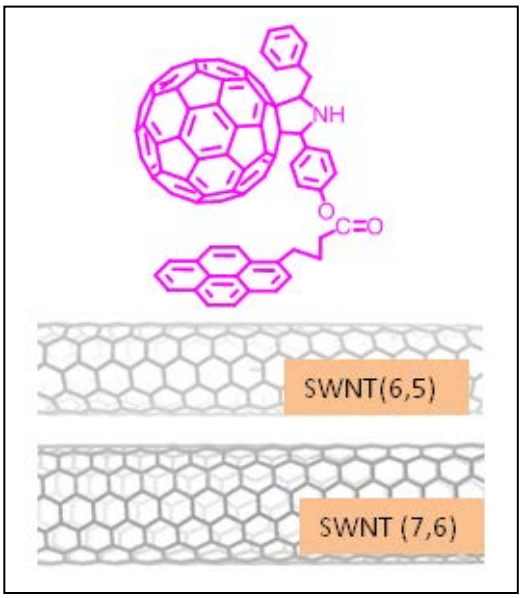

Figure 6.13: SWNT/C_{60} donor-acceptor nanohybrids assembled via $\pi-\pi$ interactions

6.2 Experimental section

Syntheses

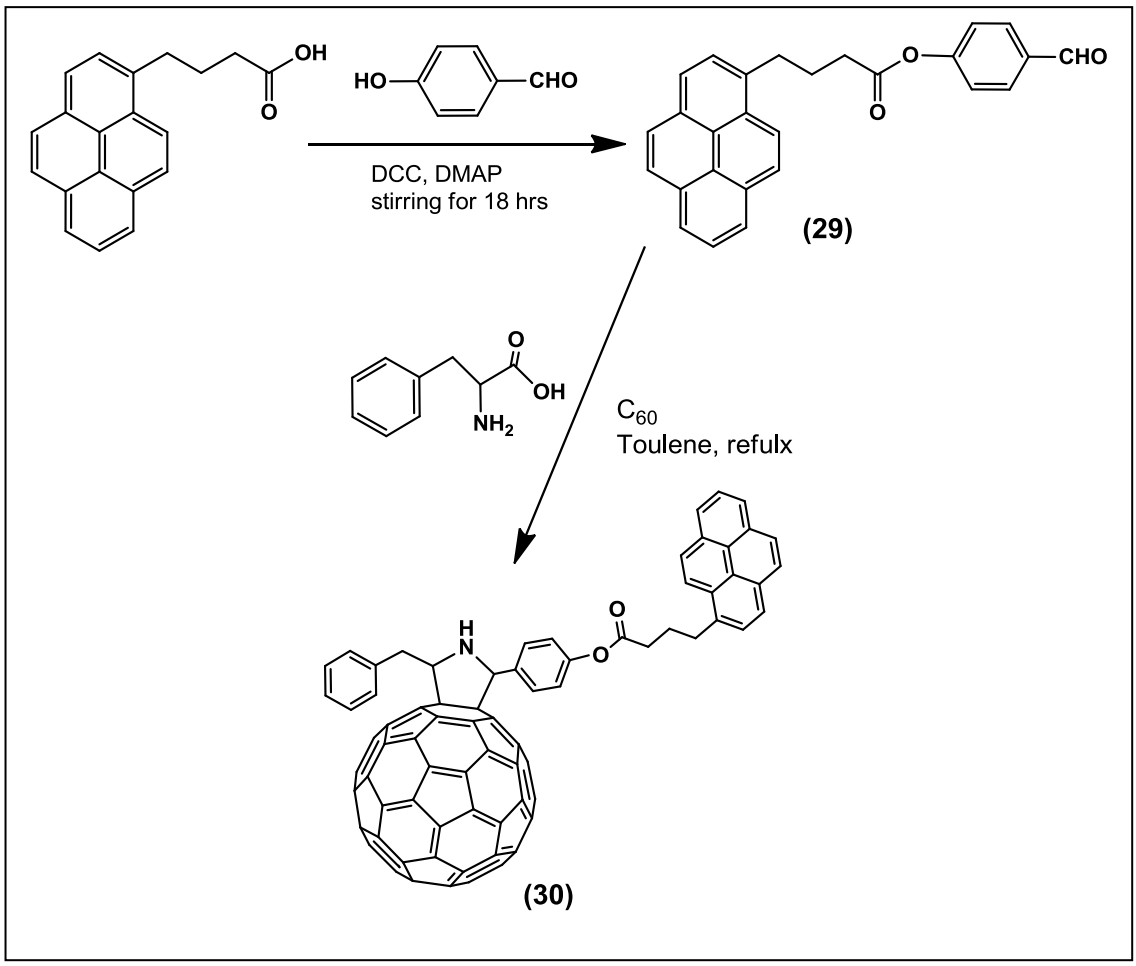

Scheme 6.3: Synthetic scheme adopted for pyrene appended fullerene (**30**)

(***4-Formyl)-phenyl-4-pyenylbutanoate,*** **(29)*:*** 1-Pyrene butyric acid (590 mg, 2.05 mmol) and 4-hydroxy benzaldehyde (750 mg, 6.00 mmol) were dissolved in 150 mL of dry CH_2Cl_2. Then 1,3-dicyclohexycarbodiimide (600 mg, 2.25 mmol) and 4-(dimethylamino)pyridine (32 mg, 0.524 mmol) were added,

and the reaction mixture was stirred for 18 hrs. Then, the solvent was evaporated under the reduced pressure, and the crude compound was purified on silica gel column using hexane:CH_2Cl_2 (94:6 v/v) as eluent. Yield: 170 mg (20 %). ^{1}H NMR (400 MHz, $CDCl_3$) (in ppm) : δ 9.99 (s, 1 H, -CHO), 8.33-7.83 (m, 13H, pyrene *H* and phenyl *H*), 3.50 (t, 2 H, -CH_2-), 2.75 (t, 2H, -CH_2-), 2.33 (m, 2H, -CH_2-), Mass (APCI mode in CH_2Cl_2): calcd, 392.45; found 393.80.

2-(Phenoxy pyrenebutyl)-5-methylphenyl-3,4-fulleropyrrolidine (32): The title compound was synthesized according to Prato et al. A solution of C_{60} (100 mg, 0.138 mmol), phenylalanine (46 mg, 0.277 mmol), and pyrene appended aldehyde **(29)** (164 mg, 0.416 mmol) in toluene (100 mL) was refluxed for 6 h. The crude product was purified by column chromatography (silica gel, hexane/toluene 40:60) to give the product (23.0 mg, 13.6%). ^{1}H NMR (300 MHz, CDCl3): 8.31-7.08 (m, 18H, pyrene *H* and phenyl *H*), 5.68 (s, 1H, -CH- fulleropyrrolidine ring), 5.00 (dd, 1H, -CH-), 4.08 (dd, 1H, -CH-), 3.50 (s, 1H, -CH- fulleropyrrolidine ring) 3.45 (t, 2 H, -CH_2-), 2.91 (broad s, 1H, -NH-) 2.65 (t, 2H, -CH_2-), 2.33 (m, 2H, -CH_2-), Mass (APCI mode in CH_2Cl_2): calcd, 1221.27; found 1222.85

6.3 Results and discussion

Preparation of SWNT(6,5)/pyrC_{60}, and SWNT(7,6)/pyrC_{60} nanohybrids

A 1.0 mg sample of SWNT [(6,5) or (7,6) chirality] was added to 2.00 mg of pyrC_{60} dissolved in 15 mL of dry DMF and the reaction mixture was stirred for 48 hrs at room temperature. The resulting mixture was sonicated (Fisher Scientific, 60 Hz, 40 W) for 6 hrs at 20°C followed by centrifugation (Fisher Scientific, 50/60 CY) for 2 hrs. The excess of C_{60} pyrene was removed by separating the centrifugate from the black precipitate. Further purification is carried out by dissolving the black mixture in 5 mL of fresh DMF, sonicating for 30 min at 20 °C, followed by centrifugation for 1 hr, and removal of unadsorbed C_{60} pyrene by separating from the black centrifugate. This process was repeated (at least twice) until the solution in the centrifuge tube turned colorless. At the end, 10 mL of fresh solvent was added to the resulting deposit and was sonicated for 15 min at 20 °C. This homogenous black dispersion was used for mentioned studies.

The TEM images recorded for the dry SWNT(*n*,*m*)/pyrC_{60} samples (Fig. 6.13) revealed that the SWNT bundles ravel upon treatment of pyrC_{60} suggesting appreciable $\pi-\pi$ interaction between the adsorbed pyrene moiety and the surface of SWNTs.[172] Each SWNT becomes thick with blur, probably by the adsorption of pyrC_{60} molecules on the SWNT surface with some spaces.

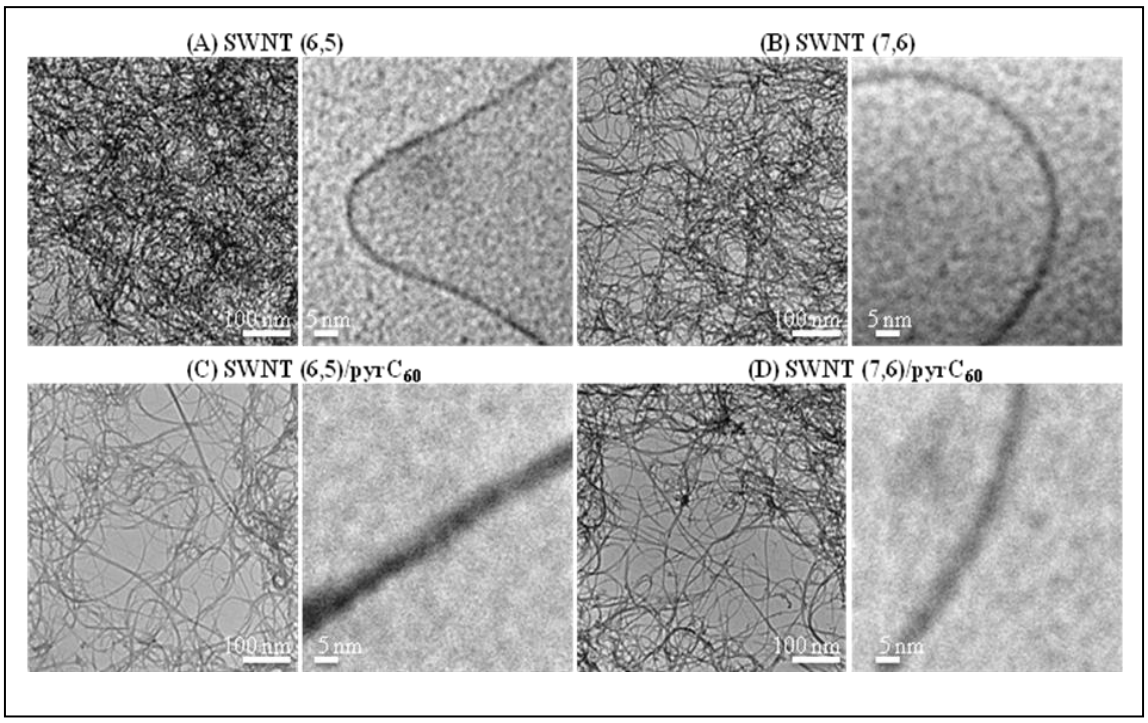

Figure 6.14: TEM images of (A) SWNT (6,5), (B) SWNT (7,6), (C) SWNT(6,5)/pyrC_{60}, and (D) SWNT(7,6)/pyrC_{60} nanohybrids.

The Raman spectra of the dry SWNT(*n*,*m*)/pyrC_{60} samples (Figure 6.13) show the characteristic RBM bands at 300 cm^{-1} for SWNT(6,5)/pyrC_{60} and at 200 cm^{-1} for SWNT(7,6)/pyrC_{60}, in addition to D-mode (1320-1340 cm^{-1}) and G-bands (1500-1600 cm^{-1}),[160] showing a small shift from the pristine SWNTs, which supports that the electronic structure of the SWNTs is intact upon adsorption with pyrC_{60}.

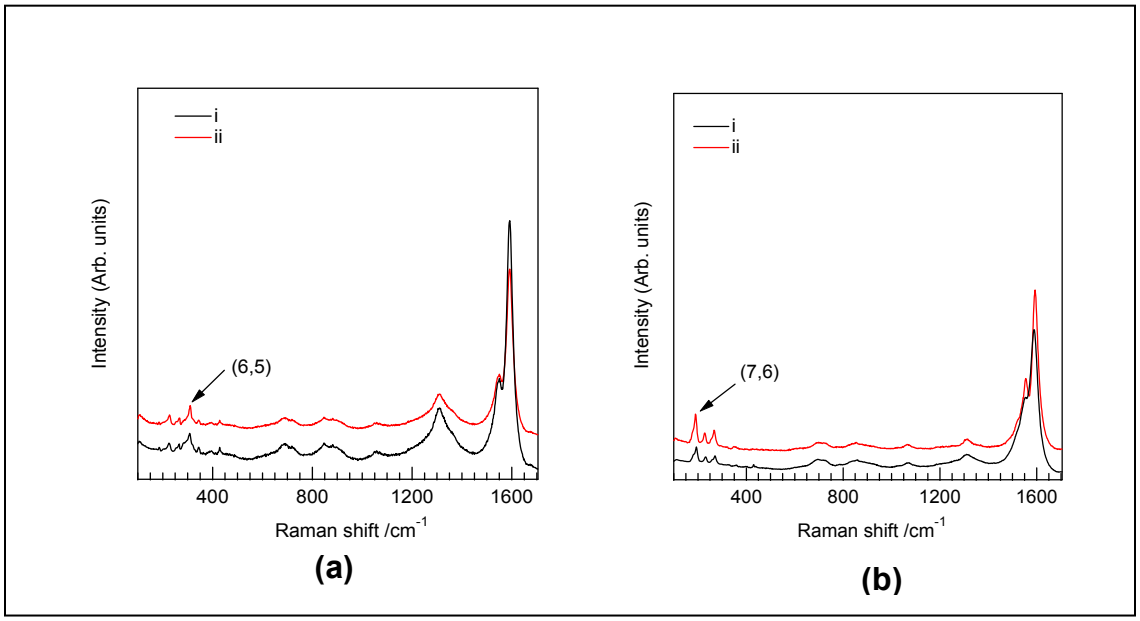

Figure 6.15: Raman spectra of (a) (i) SWNT(6,5)/pyC_{60}, and (ii) SWNT(6, 5), and (b) (i) SWNT(7,6)/pyC_{60}, and (ii) SWNT(7, 6) at the laser excitation wavelength of 632.8 nm.

The optical absorption spectra shown in Figure 6.15 of the nanohybrids revealed bands corresponding to fullerene (the bands shorter than 700 nm increasing to the UV region with 430 nm sharp peak as a shoulder) and the SWNTs covering the visible and near-IR region,[182] although the pyrene absorptions are overlapped in the lower wavelength (< 350 nm) region. In addition, considerable red-shifts of the SWNT peaks were observed due to π-stacking of the SWNTs with pyrene units. From the absorption peaks at the longest wavelength, an estimation of band gaps of the nanaohybrids was performed. Such calculations revealed decreased band gaps, viz., from 1.26 eV of SWNT(6,5) to 1.23 eV for SWNT(6,5)/pyrC_{60}, and from 1.20 eV of SWNT(7,6)

to 1.05 eV for SWNT(7,6)/pyrC_{60} suggesting stronger interaction of pyrC_{60} with thick SWNT(7,6) than that with thin SWNT(6,5).

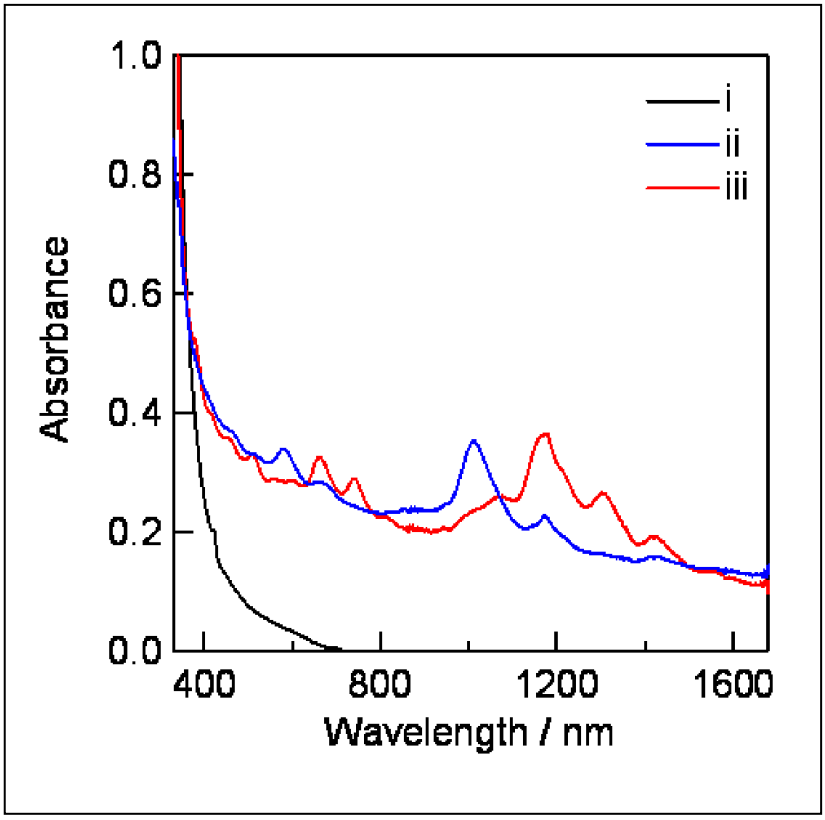

Figure 6.16: Absorption spectrum of (i) pyrC_{60}, (ii) SWNT(6,5)/pyrC_{60}, and (iii) SWNT(7,6)/pyrC_{60} nanohybrids in DMF.

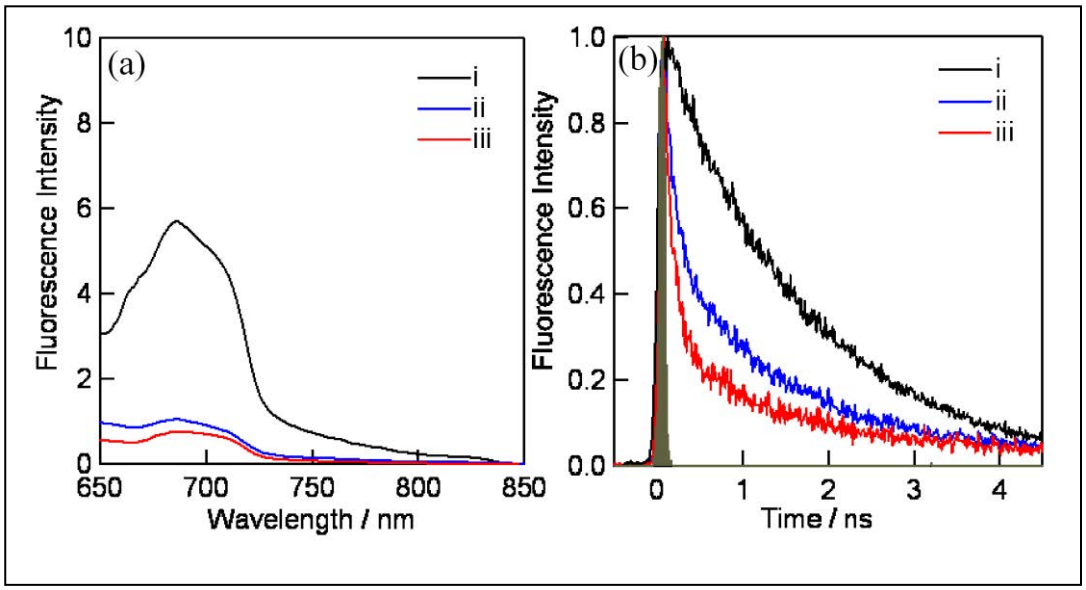

Figure 6.17: (a) Steady-state fluorescence spectra and (b) time-resolved fluorescence emission decays of (i) pyrC_{60}, (ii) SWNT(6,5)/ pyrC_{60}, and (iii) SWNT(7,6)/pyrC_{60} hybrids in the 675-725 nm region in DMF. λ_{ex} = 408 nm.

The steady-state fluorescence spectra of SWNT(*n,m*)/pyrC_{60} (Figure 6.16a) revealed that the pyrC_{60}-fluorescence peak appears around 690 nm and that the fluorescence intensities are quenched in more than 80% upon formation of the nanohybrids. Since the excitation light is also absorbed by SWNT(*n,m*), it was difficult to quantify the extent of fluorescence quenching from the fluorescence intensities alone. In order to confirm such excited state processes more quantitatively, the time-resolved fluorescence studies were performed as shown in Figure 6.16b. The fluorescence decays of pyrC_{60} in both

SWNT(6,5)/pyrC_{60} and SWNT(7,6)/pyrC_{60} hybrids were found to be substantially rapid compared with that of pyrC_{60} decaying slowly with a monoexponential function giving fluorescence lifetime of 1400 ps. The lifetimes of the rapid fluorescence decay time profiles of SWNT(*n,m*)/pyrC_{60} were evaluated by curve-fitting with a biexponential function, giving 180 ps (75%) and 1400 ps (25%) for SWNT(6,5)/pyrC_{60} and 150 ps (80%) and 1500 ps (20%) for SWNT(7,6)/pyrC_{60}. The minor slow decaying components suggest the presence of loosely bound or free pyrC_{60} in DMF.

To understand the mechanism of the observed fluorescence quenching, the energy levels of the radical ion pairs (RIPs) were calculated to be 1.01 eV for SWNT(6,5)$^{\bullet+}$/pyr$C_{60}^{\bullet-}$ and 0.87 eV for SWNT(7,6)$^{\bullet+}$/pyr$C_{60}^{\bullet-}$ by employing oxidation potentials (vs. Ag/AgCl) of 0.64 V for SWNT(6,5) and 0.50 V for SWNT(7,6) reported by Nakashima and coworkers[175] as the highest energy level of the valence bands of SWNT(*n,m*) and the reduction potential of pyrC_{60} (-0.37 V vs. Ag/AgCl) on the basis of Rehm-Weller approach.[111] Thus, the free-energy changes for the charge-separation (CS) process (ΔG_{CS}) via pyr-$^1C_{60}$* (1.80 eV) are both negative (ΔG_{CS}= -0.79 eV for SWNT(6,5)/pyrC_{60} and ΔG_{CS}= -0.93 eV for SWNT(7,6)/pyrC_{60}), predicting exothermic CS process. Then, the fast fluorescence decay component can be due to CS process via pyr-$^1C_{60}$*, which is further confirmed in the next sections. The CS rates (k_{CS}) are calculated by the difference of the fluorescence lifetimes[11] to be 4.75 × 10^9 s^{-1} for SWNT(6,5)/

pyrC_{60} and 6.09 × 10^9 s^{-1} for SWNT(7,6)/pyrC_{60}. The trend in the k_{CS} values is along the exothermicity of the CS process via pyr-$^1C_{60}$*.

Further, nanosecond transient absorption studies were performed to characterize the CS products and to evaluate the charge recombination (CR) process. Figure 6.17a shows transient spectral data for SWNT(7,6)/pyrC_{60}; similar spectra were obtained for SWNT(6,5)/pyrC_{60} hybrids (see Figures 6.18 (a) and (b)).

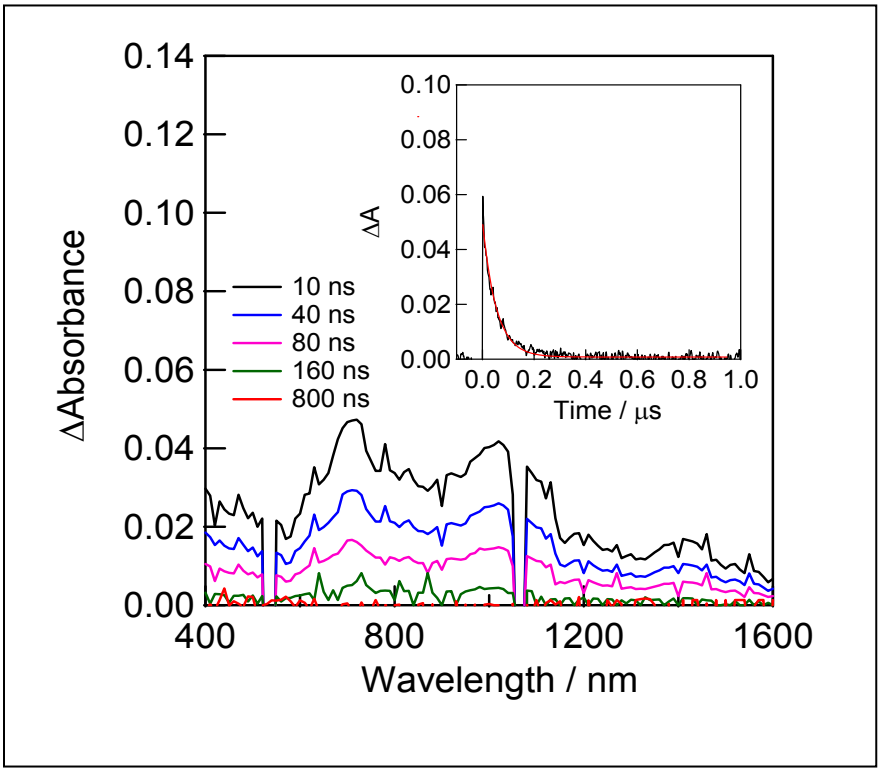

Figure 6.18: (a) Nanosecond transient absorption spectra of SWNT(7,6)/pyrC_{60} hybrids in DMF. Inset: time-profile at 1020 nm; λ_{ex} = 532 nm (ca. 3 mJ/pulse).

Absorption bands around 1020 nm corresponding to $pyrC_{60}^{\bullet-}$ are clearly seen,[4b] in addition to weak peaks in the 1200-1600 nm region possibly due to the one-electron oxidized SWNTs, suggesting the formation of $SWNT(7,6)^{\bullet+}/pyrC_{60}^{\bullet-}$, although the appearance of the 740 nm corresponding to $pyr\text{-}^3C_{60}$* indicates the loosely bound or free $pyrC_{60}$. The CR rate (k_{CR}) evaluated by the first-order curve-fitting of the $pyrC_{60}^{\bullet-}$ decay (Figure 6.17b) was 1.80×10^7 s^{-1} for $SWNT(7,6)/pyrC_{60}$; similarly, k_{CR} was evaluated as 1.21×10^7 s^{-1} for $SWNT(6,5)/pyrC_{60}$ (Figure 6.18b). The ratios of k_{CS}/k_{CR}, are found to be ~360, suggesting feasibility of these nanohybrids for the construction of photovoltaic cell and other devices using the CS states.

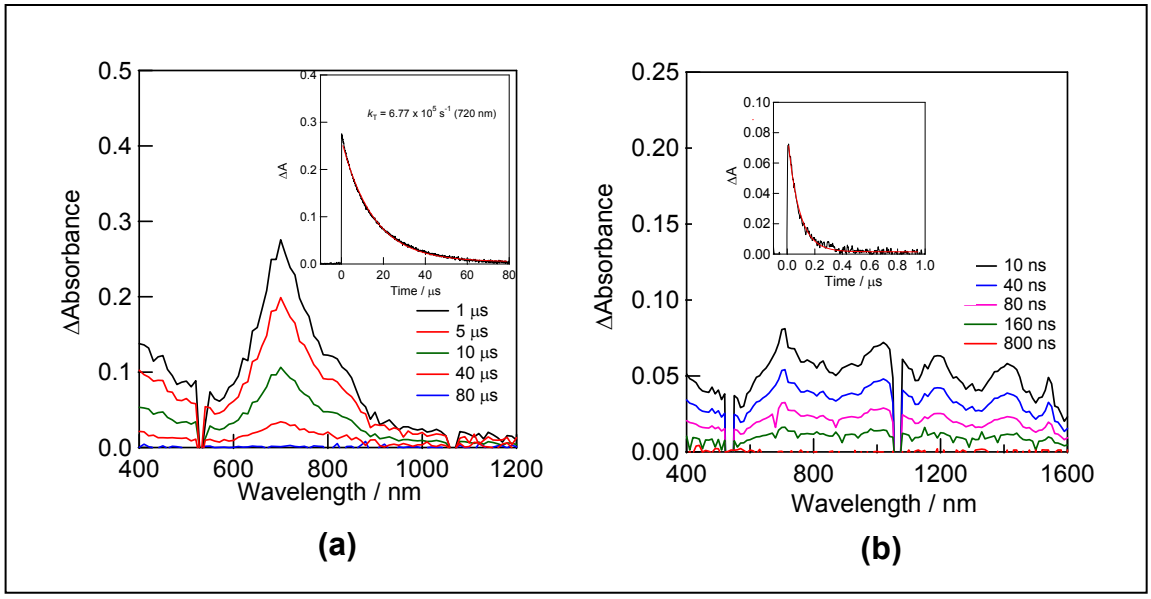

Figure 6.19: (a) Nanosecond transient absorption spectra of C_{60}pyr observed by 532 nm (ca. 3 mJ/ pulse) laser irradiation in Ar-saturated DMF. Inset: Absorption-time profile. (b) Nanosecond transient absorption spectra of $SWNT(6,5)/pyrC_{60}$ hybrids in DMF. λ_{ex} = 532 nm (ca. 3 mJ/pulse).

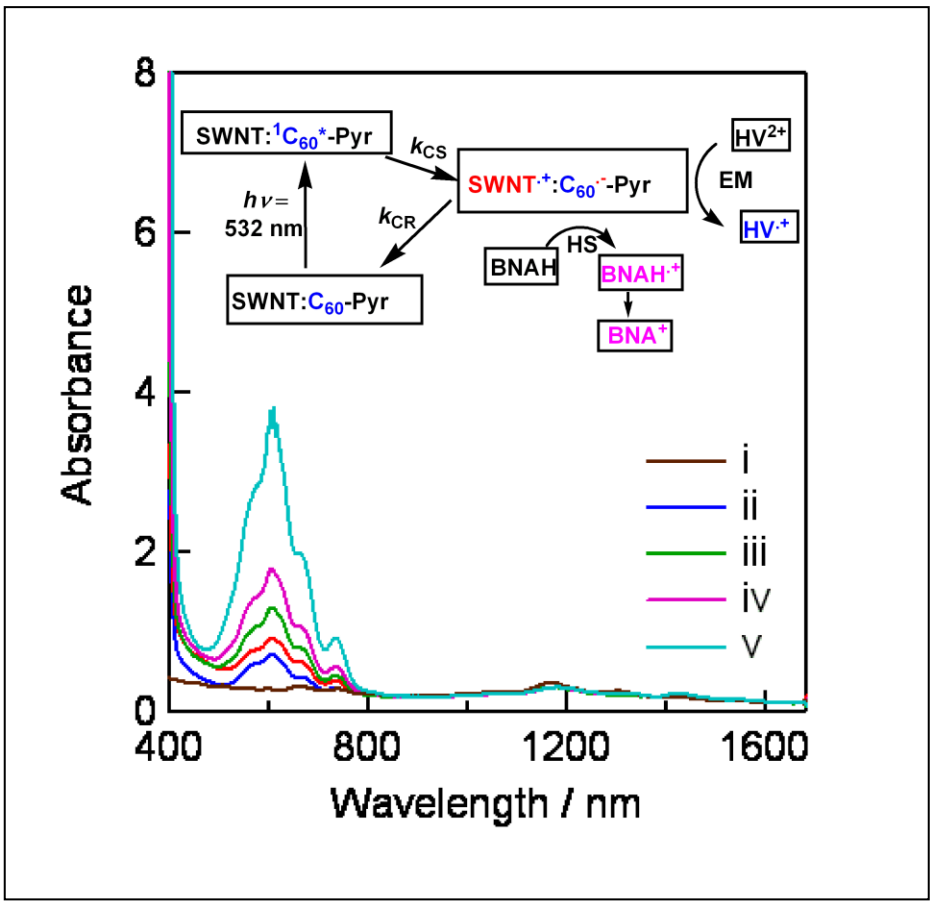

Figure 6.20: Steady-state absorption spectra of SWNT(7,6)/pyrC_{60} measured after five laser-shots at 532-nm in the presence of HV^{2+} (0.5 mM) and BNAH 0-5 mM with 1 mM step in Ar-saturated DMF. Inset: Electron transfer mechanism (EM = electron migration, HS = hole shift).

Electron mediation experiments were performed by the addition of hexyl viologen dication (HV^{2+}) and a sacrificial electron donor, 1-benzyl-1,4-dihydronicotinamide (BNAH) to the SWNT(*n,m*)/pyrC_{60} nanohybrid solution to

obtain additional proof for the photoinduced electron-transfer processes.[177] By the absorption spectral measurements after the repeated laser light irradiation (532 nm) of SWNT(7,6)/pyrC_{60}, the accumulation of $HV^{\bullet+}$ was observed at 620 nm as shown in Figure 6.19, in which the $HV^{\bullet+}$ increased with the BNAH concentration, supporting the role of BNAH as a sacrificial hole shifting reagent by changing to 1-benzyl-nicotinamide cation (BNA^{+}).

These observations support that the 532-nm light irradiation induced the CS process within SWNT(*n,m*)/pyrC_{60}, generating SWNT(*n,m*)$^{\bullet+}$/pyr$C_{60}^{\bullet-}$, from which the electron mediates to HV^{2+} and the hole shifts to BNAH as shown in Scheme (in Figure 6.19). The overall maximal absorbance of $HV^{\bullet+}$ was observed in the presence of 0.5 mM of HV^{2+} and 4.0 mM of BNAH; thus, the maximal concentration of $HV^{\bullet+}$ was evaluated to be 0.35 mM, which amounts to 70% conversion of added HV^{2+} for SWNT(7,6)/pyrC_{60}, which are higher than those for SWNT(6,5)/ pyrC_{60} ([$HV^{\bullet+}$] = 0.23 mM, conversion = 46%).

Photoelectrochemical measurements were performed for SWNTs/pyrC_{60} on the optical transparent electrode (OTE/SnO_2) prepared by drop-cast method.[101,183] The photocurrent action spectra of OTE/SnO_2/SWNTs/pyrC_{60} were measured by the wavelength dependence of the incident photon to current conversion efficiency (IPCE).[178] As shown in Figure 6.20, the increasing

tendency of the IPCE from 600 nm to the maxima at 450-480 nm is similar to the absorption increase of $pyrC_{60}$, whereas the decrease from the maxima to 400 nm may be due to the absorption of SWNT(*n,m*) interrupting the $pyrC_{60}$-excitation. The IPCE of OTE/SnO_2/-SWNT(7,6)/$pyrC_{60}$ reaches 1% as a maximal value at 460 nm, which is about 3 times larger than that of OTE/SnO_2/SWNT(6,5)/$pyrC_{60}$ (0.35% at 480 nm). This order in the maximal IPCE values is the same to the $HV^{\bullet+}$–accumulation conversions.

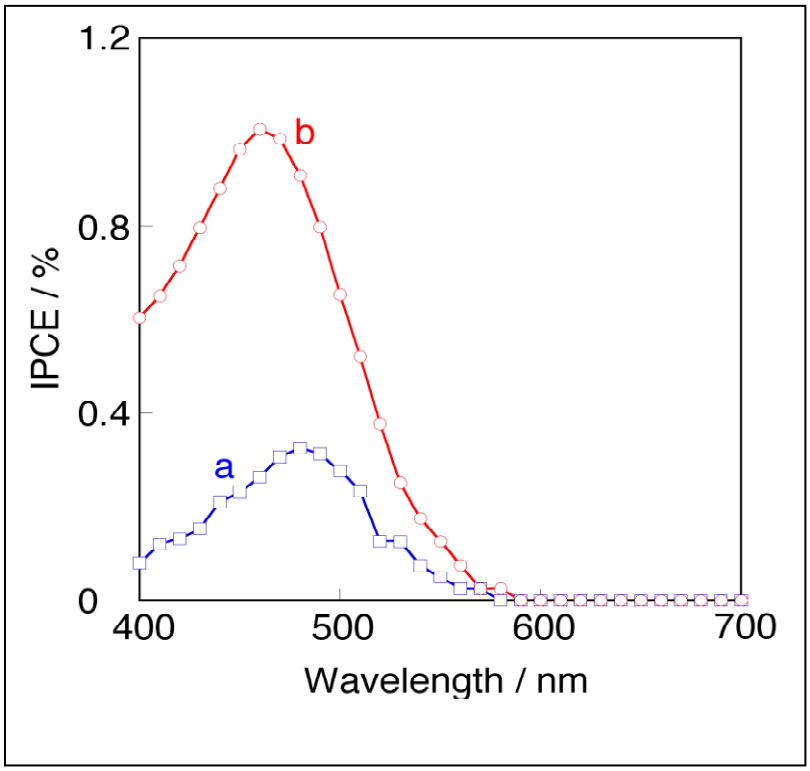

Figure 6.21: Photocurrent action spectra of IPCE; (a) OTE/ SnO_2/SWNT(6,5)/$pyrC_{60}$ and (b) OTE/SnO_2/SWNT(7,6)/ $pyrC_{60}$. Electrolyte: LiI 0.5 M, I_2 0.01 M in acetonitrile.

6.4 Summary

Electron-donor ability of semiconducting SWNTs toward the photoexcited fullerene was conclusively proven by constructing supramolecular nanohybrids with the help of pyrene functionalized fullerene as electron acceptor. The electron-donor ability depends on the energy level of the conduction band of semiconducting SWNTs; i.e., SWNT(7,6) > SWNT(6,5). Further, the experimentally determined kinetic parameters of the charge separation and the subsequent charge separation processes were helpful in rationally explaining the higher efficiencies of the electron pooling and electrochemical photocurrent for SWNT(7,6)/pyrC_{60} nanohybrids with narrow band gap than the SWNT(6,5)/pyrC_{60} nanohybrids with wide band gap.

CHAPTER 7

Conclusion

The work presented in this thesis has made an attempt to mimic the primary events of natural photosynthesis by constructing nanostructured based donor-acceptor systems that can undergo photoinduced energy and electron transfer processes. In order to build these systems, different kinds of covalent and non-covalent binding approaches have been utilized to investigate and photinduced events, viz., electronic energy transfer, electron transfer and electronic energy tarsnfer followed by electron transfer are investigated.

As demonstrated in chapter 3, photosynthetic antenna chromophore mimicry was attempted by contructing self-assembled donor-acceptor conjugates using imidazole appended (at different positions of one of the *meso*-phenyl entities) free-base tertraphenylporphyrin and Zn phthalocyanine or Zn naphthalocyanine via one of the biomimitic methodologies, *i.e.,* axial coordination. The binding constants of the newly formed supramolecular dyads measured from optical absorption spectral data were found to be in the range of 10^4-10^5 M^{-1} for the 1:1 dyads, suggesting fairly stable complex formation. Interestingly, the position of imidazole substitution on phenyl ring of porphyrin governed the affinity of supramolecular complex. Ortho substitution had least binding constant value compared to other two (para and meta) due the steric constrains. Electrochemical and computational studies suggested that photoinduced electron transfer is a thermodynamically unfavorable process when free-base porphyrin is excited in these dyads.

Selective excitation of the donor free-base porphyrin entity was possible in both types of dyads formed by either of the ZnPc or ZnNc energy acceptors. Ultrafast singlet-singlet energy transfer was observed in these dyads, and the position of imidazole linkage on the free-base porphyrin entity, although flexible, seems to have some control over the overall efficiency of excited energy transfer process. Hence, these model systems visualize that the defined distance and orientation play an important role for making efficient, ultrafast energy transfer.

Kinetics of energy transfer was monitored by performing transient absorption measurements using both up-conversion and pump-probe techniques. Such studies revealed ultrafast singlet-singlet energy transfer in the studied dyads to mimic antenna functionality with time constants on the order of 2-25 ps depending upon the type of the dyad.

In order to mimic reaction center functionlaity, ultrafast electron transfer was demonstrated with covalently linked pacman-type face-to-face Zn porphyrin-fullerene dyads in chapter 4. Owing to the close proximity of the donor and acceptor entities, strong π–π intramolecular interactions between the porphyrin and fullerene entities resulted in modulating the spectral and electrochemical properties of the dyads. New absorption and emission bands that correspond to the charge transfer interactions were observed in the near-IR region.

Time-resolved transient absorption spectra of pacman dyads in femtosecond laser flash photolysis in deaerated PhCN displayed the monofunctionalized

fullerene radical anion at 1000 nm and the ZnP π radical cation at 675 nm. These spectral data revealed efficient photoinduced electron transfer from the singlet excited porphyrin to the fullerene entity. The rate constants for photoinduced electron transfer are analyzed in terms of the Marcus theory of electron transfer, which afforded a large electron coupling matrix element (V=140 cm^{-1}) for the face-to-face dyads. These ultrafast rates (~10^{11} – 10^{12} s^{-1}) are found to be one or two orders of magnitude higher than those reported for a number of porphyrin–fullerene dyads in the literature. As a consequence of the large charge-recombination driving force in the Marcus inverted region, a relatively long lifetime of the charge-separated state in nonpolar solvents has been achieved. There is a possibility to modulate the energy states that ultimately result in CS in a nonpolar solvent due to the close proximity and the strong charge-transfer-type interactions between the donor and acceptor entities in the Pacman porphyrin–fullerene dyads.

To improve ultrafast electron transfer with higher charge stabilization, mimicking a "special pair" of two bacteriochlorophylls, a primary electron donor in the reaction center is an interesting approach to the development of artificial supramolecular systems capable of performing specific functions. Next we constructed a cofacial Zn tetra crown phthalocyanine dimer, self-assembled with an alkyl ammonium cation bearing pyridine fulleropyyrolidine. Here, utilization of "two-point' binding methodology involving crown ether-cation complexation and either axial coordination or π–π type interactions yielded highly stable, self-

assembled zinc phthalocyanine dimer-fullerene conjugates. These ~~–t~~wo-point" bound rigid dyads allowed us to perform the spectral and photochemical studies in a polar solvent such as benzonitrile and, thereby, control the intramolecular interactions between the donor and acceptor entities. Unlike the previously reported porphyrin analog, the present phthalocyanine macrocycle based model system exhibited superior electron-transfer properties including formation of a long-lived charge separated state, a key step of the photosynthetic light energy conversion process. On the basis of detailed analysis of the kinetic data from the time-resolved emission and transient absorption spectroscopy of different time scales, it was found that the charge separation occurs from the triplet excited state of the ZnPc moiety to the C_{60} moiety rather than the singlet excited state to afford the long-lived CS state of the supramolecular complex. These supramolecular donor–acceptor pairs showed superior electron-transfer properties, including the formation of a long-lived charge-separated state with 6.7 μs for the phthalocyanine dimer-C_{60} supramolecular complex, $K_4[ZnTCPc]_2$:$(pyC_{60}NH_3^+)_2$ and 4.8 μs the monomer complex, ZnTCPc:$pyC_{60}NH_3^+$, despite the smaller driving force of back electron transfer because of smaller reorganization energy of the phthalocyanine dimer, clearly delineating the role of the cofacial phthalocyanine dimer in stabilizing the CS state in donor-acceptor systems. The importance of the cofacial dimer in stabilizing the charge-separated state is borne out in the present all-supramolecular ~~–r~~eaction center" donor-acceptor mimic.

Our synthetic and supramolecular methodologies are applied for contructing photosynthetic architectures to mimic antenna functionality and reaction center functionality separately. In chapter 5, we futher extended our suparmolecular donor-acceptor hybrids to mimic combined antenna and reaction center functionalities by incorporation of covalent and non-covalent linkages which appear to be more promising in the field of artificial photosynthesis. The antenna mimic, a boron dipyrrin entity, was covalently linked to the reaction center electron donor mimic, a zinc porphyrin possessing a 18-crown-6 entity, as the opposite side of the macrocycle. Next, an alkyl ammonium functionalized fullerene was used to self-assemble the crown ether entity via non-covalent, ion-dipole interactions.

The newly formed supramolecular triad was fully characterized by spectroscopic, computational, and electrochemical methods. Selective excitation of the boron dipyrrin moiety in the dyad resulted in energy transfer over 97% efficiency creating singlet excited zinc porphyrin. The rate of energy transfer from the decay measurements of time-correlated singlet photon counting (TCSPC) and up-conversion techniques agreed well with that obtained by the pump-probe technique and revealed efficient photoinduced energy transfer in the dyad (time constant in the order of 10-60 ps depending upon the conformer). Upon forming the supramolecular triad by self-assembling fullerene, the excited zinc porphyrin resulted in electron transfer to the coordinated fullerene yielding a charge-separated state, thus mimicking the antenna-reaction center functionalities of

photosynthesis. Nanosecond transient absorption studies yielded a lifetime of the charge-separated state to be 23 μs indicating charge stabilization in the supramolecular triad. The present supramolecular system represents a successful model to mimic the rather complex –combined antenna-reaction center" events of photosynthesis.

In order to see the effect of energy transfer by increasing number of antenna units, novel supramolecular triads are developed to mimic the ‗antenna-reaction center' functionality of photosynthetic reaction center. These triads comprised of zinc porphyrin covalently linked to one, two or four numbers of boron dipyrrin (BDP) entities. Both steady-state and time-resolved emission as well as transient absorption studies revealed occurrence of efficient singlet–singlet energy transfer from BDP to zinc porphyrin with the time scale ranging between 28 and 48 ps. A decrease in time constants for energy transfer with increasing the number of BDP units is observed revealing better antenna effect of dyads bearing higher number of boron dipyrrin entities. Further, supramolecular triads to mimic the ‗antenna-reaction center' functionality of photosynthetic reaction center have been successfully constructed by coordinating fulleropyrrolidine appended with an imidazole ligand to the zinc porphyrin. The structural integrity of the supramolecular triads was arrived by optical, computational and electrochemical studies. Free energy calculations revealed possibility of photoinduced electron transfer from singlet excited zinc porphyrin to fullerene, and the preliminary transient absorption studies involving

pump–probe technique are supportive of occurrence of electron transfer from ^{1}ZnP* to fullerene in the supramolecular triads.

One of the most important aspects of photo-induced electron transfer is to reduce the probability of back electron transfer in donor-acceptor systems. In this regard, all carbon nanotubes and relavent nanostructures have received considerable attention due to their electrical, electronic and mechanical properties. To derive meaningful and conclusive nanotube structure-reactivity relationship, we constructed donor-acceptor nanohybrids with semiconducting nanotubes, viz., (6,5) and (7,6), having different band gaps. As demonstrated in chapter 6, the zinc porphyrin, along with four pendant pyrene entities (ZnP(pyr)$_4$), stacked on the SWNT surface due to π–π interactions, resulting in exfoliation of the semiconducting nanotubes. The nanohybrids thus formed were isolated and characterized by TEM, UV-visible-near-IR, and Raman spectroscopy. Free-energy calculations suggested the possibility of electron transfer in both the (7,6)- and (6,5)-possessing ZnP(pyr)$_4$/SWNT nanohybrids. Accordingly, fluorescence studies revealed efficient quenching of the singlet excited state of ZnP in the nanohybrids, originating from the charge separation, as confirmed by observation of a ZnP π-cation radical in transient absorption spectra. The rates of charge separation were found to be slightly higher for (7,6)-SWNT-derived hybrids compared to the (6,5)-SWNT-derived hybrids. Charge recombination revealed an opposite effect, indicating that the (7,6)-SWNTs are slightly better for charge stabilization compared to the (6,5)-SWNTs. The present nanohybrids were

further utilized to photochemically reduce the hexyl viologen dication in the presence of a sacrificial electron donor in an electron-pooling experiment, offering additional proof for the occurrence of photoinduced charge separation and potential utilization of these materials in light-energyharvesting applications. Finally, solar cells constructed using the ZnP/SWNT hybrids revealed higher efficiency for the ZnP(pyr)$_4$/(7,6)-SWNT hybrid with narrower nanotube band gap compared with the ZnP(pyr)$_4$/(6,5)-SWNT having a relatively wider band gap.

In the majority of these studies, the single-wall carbon nanotubes (SWNTs) acted as electron acceptors in artificial photosynthetic model systems. We investigated the electron donor ability of SWNTs by constructing hybrids using well-known electron acceptor such as a fullerene. These nanohybrids were generated by self-assembling the SWNT/pyrene NH_3^+ to a benzo-18-crown-6 functionalized fullerene via ion-dipole interactions.

The electron-donor ability depends on the energy level of the conduction band of semiconducting SWNTs; i.e., SWNT(7,6) > SWNT(6,5). Further, the experimentally determined kinetic parameters of the charge separation and the subsequent charge separation processes were helpful in rationally explaining the higher efficiencies of the electron pooling and electrochemical photocurrent for SWNT(7,6)/pyrC_{60} nanohybrids with narrow band gap than the SWNT(6,5)/pyrC_{60} nanohybrids with wide band gap.

The nanotubes of different band gaps (tube-diameter-governed) to build donor-acceptor hybrids were employed. Further it has been demonstrated diameter dependent photochemical properties for fundamental studies involving photoinduced ET originating from these supramolecular donor-acceptor conjugates of carbon nanotubes of different band gaps. Those complexes might serve as good examples to expedite research in the areas of photovoltaic, sensing, photocatalysis including hydrogen production, and building supercapacitors for energy storage. Intersetingly, the photoelectrochmeical behavior of the nanohybrids, although less efficient, points out that by choosing nanotubes of appropriate diameter, it is possible to improve the light-harvesting conversion efficiency.

REFERENCES

References

(1) (a) Kamat, P. V. *J. Phys. Chem. C.* **2007,** *111,* 2834-2860 (b) Dresselhaus, M. S.; Thomas, I. L. Alternative energy technologies. *Nature.* **2001**, *414*, 332-337

(2) (a) Barber, J.; Anderson, B. *Nature.* **1994**, *370*, 31. (b) El-Kobbani, O.; Chang, C. H.; Tiede, D.; Norris, J.; Schiffer, M. *Biochemistry.* **1991**, *30*, 5361. (c) Fromme, P. *Curr. Opin. Struct. Biol*. **1996**, *6*, 473. (d) Krauss, N.; Schubert, W. D.; Klukas, O.; Fromme, P.; Witt, H. T.; Saenger, W. *Nat. Struct. Biol*. **1996**, *3*, 965. (e) Nugent, J. H. A. *Eur. J. Biochem.* **1996**, *237*, 519. (f) *The Photosynthetic Reaction Center*; Deisenhofer, J., Norris, J. R., Eds.; Academic Press: San Diego, 1993. (g) Deisenhofer, J.; Epp, O.; Miki, K.; Huber, R.; Michel, H. *J. Mol. Biol.* **1984**, *180*, 385.

(3) (a) Gust, D.; Moore, T. A. *Science.* **1989**, *244*, 35-41 (b) Gust, D.; Moore, A. T.; Moore, A. L. *Acc. Chem. Res*. **2001**, *34*, 40-48 (c) Wasielewski, M. R. *Chem. Rev.* **1992**, *92*, 435-461 (d) Closs, G. L.; Miller, J. R. *Science*, **1998**, *240*, 440-447 (e) Sutin, N. *Acc. Chem. Res*. **1982**, *15*, 275. (f) Gust, D.; Moore, T. A.; Moore, A. L. *Acc. Chem. Res*. **1993**, *26*, 198. (g) Paddon-Row, M. N. *Acc. Chem. Res*. **1994**, *27,* 18. (h) Hayashi, T.; Ogoshi, H. *Chem. Soc. Re*v. **1997**, *26*, 355. (i) Piotrowiak, P. *Chem. Soc. Re*v. **1999**, *28*, 143. (j) Guldi, D. M. *Chem. Soc. Re*v. **2002**, *31*, 22.

(4) Wasielewski, M. R. *Photochem. Photobiol.* **1991**, 53, 119

(5) Connolly, J. S.; Boltan, J. R. In *Photoinduced electron transfer* Part A,; Fox, M. A., Channon, M., Eds.; Elsevier, **1988**, 161

(6) Gust, D. *Nature.* **1997**, 386, 21

(7) Wasielewski, M. R., In *Photoinduced electron transfer* Part D,; Fox, M. A., Channon, M., Eds.; Elsevier, **1988**, 303

(8) Seesler, J. S.; Wang, B.; Springs, S. L.; Brown, C. T., In *Comprehensive Supramolecular Chemistry*, Eds. Atwood, J. L.; Davies, J. E. D.; MacNicol, D. D.; Vogtle, F. Chapter 9, Pergamon, **1996**

(9) *Principles of Fluorescence Spectroscopy*; 3rd ed.; Lakowicz, J. R., Ed.; Springer: Singapore, 2006.

(10) *Principles of Molecular Photochemistry An Introduction;* 1st ed.; Turro, N. J.; Ramamurthy, V.; Scaiano, J. C., Ed.; University Science Books: 2009

(11) a) Marcus, R. A.; Sutin, N. *Biochim. Biophys. Acta*. **1985**, *811*, 265 b) Marcus, R. A. *Angew. Chem*. **1993**, *105*, 1161; *Angew. Chem. Int. Ed. Engl*. **1993**, *32*, 1111

(12) (a) Balzani, V. *Electron Transfer in Chemistry*, Vol I-V, ed., Wiley-VCH, Weinheim, **2001**, (b) Gust, D.; Moore, A. T.; Moore, A. L**.** IUPAC, *Pure & Applied Chemistry,* **1998,** *70* 2189-2200

(13) El-Khouly, M. E.; Ito, O.; Smith, P. M.; D'Souza, F. *J. Photochem. Photobiol., C*. **2004**, *5*, 79.

(14) D'Souza, F.; Ito, O. *Coordination Chem. Rev*. **2005**, 249, 1410

(15) Martı´nez-Dı´az, Guldi, D. M.; Torres, T. *J. Am. Chem. Soc*. **2006**, 128, 4112- 4118

(16) Torre, G. de la.; Va´zquez, P.; Agullo´-Lo´pez, F.; Torres, T. *Chem. Rev.* **2004,** *104,* 3723-3750

(17) De la Escosura, A.; Martı´nez-Dı´az, M. V.; Thordarson, P.; Rowan, A. E.; Nolte, R. J. M.; Torres, T. *J. Am. Chem. Soc.* **2003**, 125, 12300-12308

(18) Coskun, A.; Akkaya, E. U. *J. Am. Chem. Soc.* **2005**, 127, 10464-10465

(19) Li, F.; Yang, S.; Ciringh, Y.; Seth, J.; Martin, C. H.; Singh, D. L.; Kim, D.; Birge, R. R.; Bocian, D. F.; Holten, D.; Lindsey, J. S. *J. Am. Chem. Soc.* **1998**, *120,* 10001-10017

(20) Hsiao, J-S.; Krueger, B. P.; Wagner, R. W.; Johnson, T. E.; Delaney, J. K.; Mauzerall, D. C.; Fleming, G. R.; Lindsey, J. S.; Bocian, D. F.; Donohoe, R. J. *J. Am. Chem. Soc.* **1996**, *118,* 11181-11193

(21) Holten, D.; Bocian, D. F.; Lindsey, J. S. *Acc. Chem. Res*. **2002,** *35*, 57-69

(22) Wagner, R. W.; Lindsey, J. S. *J. Am. Chem. Soc.* **1994**, *116,* 9759-9760

(23) Wagner, R. W.; Lindsey, J. S.; Seth, J.; Palaniappan, V.; Bocian, D. F. *J. Am. Chem. Soc.* **1996,** *118,* 3996-3997

(24) Prathapan, S.; Johnson, T. E.; Lindsey, J. S. *J. Am. Chem. Soc.* **1993***,115,* 7519-7520

(25) (a) Lam, H.; Marcuccio, S. M.; Svirskaya, P. I.; Greenberg, S.; Lever, A. B. P.; Leznoff, C. C.; Cerny, R. L. *Can. J. Chem*. **1989**, *67*, 1087-1097. (b) Leznoff, C. C.; Svirskaya, P. I.; Khouw, B.; Cerny, R. L.; Seymour, P.; Lever, A. B. P*. J. Org. Chem*. **1991**, *56*, 82-90. (c) Vigh, S.; Lam, H.; Janda, P.; Lever, A. B. P.; Leznoff, C. C.; Cerny, R. L. *Can. J. Chem*. **1991**, *69*, 1457-1461. (d) Bryant, G. C.; Cook, M. J.; Ryan, T. G.; Thorne, A. J. *Tetrahedron.* **1996**, *52*, 809-824. (e) Maya, E. M.; Va´zquez, P.; Torres, T. *Chem. Commun*. **1997**, 1175-1176. (f) Gonza´ lez, A.; Va´zquez, P.; Torres, T. *Tetrahedron Lett.* **1999**, *40*, 3263-3266. (g) Maya, E. M.; Va´zquez, P.; Torres, T. *Chem. Eur. J*. **1999**, *5*, 2004-2013.

(26) Gaspard, S.; Giannotti, C.; Maillard, P.; Schaeffer, C.; Tran-Thi, T.-H. *J. Chem. Soc., Chem. Commun.* **1986**, 1239-1241.

(27) (a) Li, L.; Shen, S.; Yu, Q.; Zhou, Q.; Xu, H. *J. Chem. Soc., Chem. Commun.* **1991**, 619-620. (b) Li, X.; Zhou, Q.; Tian, H.; Xu, H. *Chin. J. Chem.* **1998**, *16*, 97-108.

(28) (a) Kobayashi, N.; Nishiyama, Y.; Ohya, T.; Sato, M. *J. Chem.Soc., Chem. Commun.* **1987**, 390-392. (b) Kobayashi, N.; Ohya, T.; Sato, M.; Nakajima, S. *Inorg. Chem.* **1993**, *32*, 1803-1808.

(29) Li, J.; Diers, J. R.; Seth, J.; Yang, S. I.; Bocian, D. F.; Holten, D.; Lindsey, J. S. *J. Org. Chem*. **1999**, *64*, 9090-9100

(30) Guldi, D. M. Chem. Soc. Rev. 2002, 31, 22-36

(31) (a) Otsuki, J.; Kanazawa, Y.; Kaito, A.; Islam, D-M. S.; Araki, Y.; Ito, O. Chem. Eur. J. 2008, 14, 3776 – 3784 (b) Otsuki, J.; Iwasaki, K.; Nakano, Y.; Itou, M.; Araki, Y.; Ito, O. *Chem. Eur. J*. **2004**, 10, 3461 – 3466

(32) (a) Springs, S. L.; Gosztola, D.; Wasielewski, M. R.; Kra´l, V.; Andrievsky, A.; Sessler, J. S. *J. Am. Chem. Soc*. **1999**, 121, 2281-2289. (b) Kra´l, V.; Springs, S. L.; Sessler, J. S. *J. Am. Chem. Soc.* **1995**, 117, 8881-8882

(33) Yatskou, M. M.; Koehorst, R. B. M.; Donker, H.; Schaafsma, T. J. *J. Phys. Chem. A.* **2001**, *105,* 11425-11431

(34) Kelley, R. F.; Goldsmith, R. H.; Wasielewski, M. R. *J. Am. Chem. Soc*. **2007**, *129*, 6384-6385

(35) Imahori, H. *Org. Biomol. Chem*. **2004**, *2*, 1425-1433

(36) D'Souza, F.; Maligaspe, E.; Karr, P. A.; Schumacher, A. L.; Ojaimi, M. E.; Gros, C. P.; Barbe, J-M.; Okubo, K.; Fukuzumi, S. *Chem. Eur. J.* **2008**, 14, 674

(37) Guldi, D. M.; Hirsch, A.; Scheloske, M.; Dietel, E.; Troisi, A.; Zerbetto, F.; Prato, M. *Chem. Eur. J*. **2003**, *9*, 4968 – 4979

(38) Schuter, D. I.; Cheng, P.; Jarowski, P. D.; Guldi, D. M.; Luo, C.; Echegoyen, L.; Pyo Soomi.; Holzwarth, A. R.; Braslavsky, S. E.; Williams, R. M.; Klihm, G. *J. Am. Chem. Soc*. **2004**, *126*, 7257-7270

(39) Gouloumis, A.; Liu, S-G.; Sastre, A.; Vazquez, P.; Echegoyen, L.; Torres, T. *Chem. Euro. J*, **2000**, *6*, 3600-3607

(40) Isosomppi, M.; Tkachenko, N. V.; Efimov, A.; Vahasalo, H.; Jukola, J.; Vainiotalo, P.; Lemmetyinen, H. *Chem. Phys. Lett.* **2006**, 430, 36-40

(41) (a) Luo, C.; Guldi, D. M.; Imahori, H.; Tamaki, K.; Sakata, Y, *J. Am.Chem. Soc.* 2000, **122**, 6535. (b) Imahori, H.; El-Khouly, M. E.; Fujitsuka, M.; Ito, O.; Sakata, Y.; Fukuzumi, S. *J. Phys. Chem. A*, 2001, **105**, 325. (c) Fukuzumi, S.; Imahori, H.; Yamada, H.; El-Khouly, M-E.; Fujitsuka, M.; Ito, O.; Guldi, D. M. *J. Am. Chem. Soc.* 2001, **123**, 2571.

(42) (a) Fukuzumi, S.; Ohkubo, K.; Imahori, H.; Shao, J.; Ou, Z.; Zheng, G.; Chen, Y.; Pandey, R. K.; Fujitsuka, M.; Ito, O.; Kadish, K. M. *J. Am. Chem. Soc.*, **2001***, 123*, 10676 (b) Ohkubo, K.; Imahori, H.; Shao, J.; Ou, Z.; Kadish, K. M.; Chen, Y.; Zheng, G.; Pandey, R. K.; Fujitsuka, M.; Ito, O.; Fukuzumi, S. *J. Phys. Chem. A*. **2002***, 106*, 10991.

(43) Quintiliani, M.; Kahnt, A.; Wolfle, T.; Hieringer, W.; Vazquez, P.; Gorling, A.; Guldi, D. M.; Torres, T. *Chem. Eur. J*. **2008**, *14*, 3765-3775

(44) Liddell, P. A.; Kuciauskas, D.; Sumida, J. P.; Nash, B.;Nguyen, D.; Moore, A. L.; Moore, T. A.; Gust, D. *J. Am. Chem. Soc.* **1997**, *119,* 1400-1405

(45) Kuciauskas, D.; Liddell, P. A.; Lin, S.; Stone, S.G.; Moore, A. L.; Moore, T. A.; Gust, D. *J. Phys. Chem. B.* **2000**, *104,* 4307-4321

(46) Carbonera, D.; Valentin, M. D.; Corvaja, C.; Agostini, G.; Giacometti, G.; Liddell, P.A.; Kuciauskas, D.; Moore, A. L.; Moore, T. A.; Gust, D. *J. Am. Chem. Soc.* **1998**, *120,* 4398-4405

(47) Imahori, H.; Tamaki, K.; Guldi, D. M.; Luo, C.; Fujitsuka, M.; Ito, O.; Sakata, Y.; Fukuzumi, S. *J. Am. Chem. Soc.* **2001**, *123,* 2607-2617

(48) Bottari, G.; de la Torre, G.; Guldi, D. M.;Torres, T. *Chem. Rev*. **2010**, ASAP

(49) Sessler, J. L.; Jayawickramarajah, J.; Gouloumis, A.; Torres, T.; Guldi, D. M.; Maldonado, S.; Stevenson, K. J. *Chem. Commun*. **2005**, 1892-1894

(50) Sanchez, L.; Martin, N.; Guldi, D. M. *Angew. Chem., Int. Ed.* **2005**, *44*, 5374 – 5382

(51) Torres, T.; Gouloumis, A.; Sanchez-Garcia, D.; Jayawickramarajah, J.; Seitz, W.; Guldi, D. M.; Sessler, J. L. *Chem. Commun*. **2007**, 292–294

(52) Sanchez, L.; Sierra, M.; Martin, N.; Myles, A. J.; Dale, T. J.; Rebek, J.; Seitz, W.; Guldi, D. M. *Angew. Chem. Int. Ed.* **2006**, *45*, 4637 –4641

(53) Balbinot, D.; Atalick, S.; Guldi, D. M.; Hatzimarinaki, M.; Hirsch, A.; Jux, N. *J. Phys. Chem. B.* **2003,** *107,* 13273-13279

(54) Zilbermann, I.; Lin, A.; Hatzimarinaki, M.; Hirsch, A.; Guldi, D. M. *Chem.Commun*. **2004**, 96-97.

(55) Tashiro, K.; Aida, T.; Zheng,J-Y.; Kinbara, K.; Saigo, K.; Sakamoto, S.; Yamaguchi, K. *J. Am. Chem. Soc.* **1999,** *121,* 9477-9478

(56) Scheidt, W. R.; Reed, C. A. *Chem. Rev*. **1981**, *81*, 543-555

(57) D'Souza, F.; Deviprasad, G. R.; Zandler, M. E.; Hoang, V. T.; Arkady, K.; Van Stipdonk, M.; Perera, A.; El-Khouly, M. E.; Fujitsuka, M.; Ito, O. *J. Phys. Chem. A*. **2002**, *106*, 3243-3252

(58) (a) Pedersen, C. J. *J. Am. Chem. Soc.* **1967**, *89*, 7017 (b) Saha, A.; Nayak, S. K.; Chottopadhyay, S.; Mukherjee, A. K., *J. Phys. Chem. B.* **2003**, *107,* 11889-11892 (c) Mazik, M.; Kuschel, M.; Sicking, W., *Org. Lett*. **2006**, *8*, 855-858

(59) Solladié, N.; Walther, M. E.; Gross, M.; Duarte, T. M. F.; Bourgogne, C.; Nierengarten, J-F. *Chem. Commun*. **2003**, 2412-2413

(60) Guldi, D. M., Ramey, J., Martínez-Díaz, M. .; De la Escosura, Torres, T.; Da Ros, T.; Prato, M. *Chem. Comm*. **2002**, 2774-2775

(61) D'Souza, F.; Chitta, R.; Gadde, S.; Rogers, L. M.; Karr, P. A.; Zandler, M. E.; Sandanayaka, A. S. D.; Araki, Y.; Ito, O. *Chem.*A, *Eur. J.* **2007**, *13*, 916–922.

(62) Luo, C.; Guldi, D. M.; Imahori, H.; Tamaki, K.; Sakata, Y., *J. Am. Chem. Soc.* **2000**, *122,* 6535-6551

(63) Imahori, H.; Guldi, D. M.; Tamaki, K.; Yoshida, Y.; Luo, C.; Sakata, Y.; Fukuzumi, S., *J. Am. Chem. Soc.* **2001**, *123,* 6617-6628

(64) Imahori, H.; Tamaki, K.; Araki, Y.; Sekiguchi, Y.; Ito, O.; Sakata, Y.; Fukuzumi, S., *J. Am. Chem. Soc.*, **2002**, *124*, 5165.

(65) Imahori, H.; Sekiguchi, Y.; Kashiwagi, Y.; Sato, T.; Araki, Y.; Ito, O.; Yamada, H.; Fukuzumi, S., *Chem. Eur. J.* **2004**, *10*, 3184 – 3196

(66) D'Souza, F.; Smith, P. M.; Zandler, M. E.; McCarty, A. L.; Itou, M.; Araki, Y.; Ito, O. *J. Am. Chem. Soc.* **2004**, *126*, 7898.

(67) Terazono, Y.; Kodis, G.; Liddell, P. A.; Garg, V.; Moore, T. A.; Moore, A. L.; Gust, D. *J. Phys. Chem. B.* **2009**, *113,* 7147–7155

(68) (a) Kratschmer, K.; Lamb, L. D.; Fostiropoulos, K.; Huffman, R. D. *Nature.* **1990**, *347*, 354. (b) *Introduction to Nanotechnology*; Poole, C. P., Owens, F. J. Eds.; Wiley-Interscience: Weinheim, Germany, 2003; (c) *Nanophysics and Nanotechnology: An Introduction to Modern Concepts in Nanoscience*; Wolf, E. L., Ed.; John Wiley and Sons: New York, **2004**.

(69) (a) *Carbon Nanotubes: Synthesis, Structure, Properties, and Applications*; Dresselhaus, M. S., Dresselhaus, G., Avouris, P., Eds.; Springer: Berlin, Germany, **2001** (b) Reich, S.; Thomsen, C.; Maultzsch, J. *Carbon Nanotubes: Basic Concepts and Physical Propertie*s; VCH: Weinheim, Germany, 2004. (c) *Special issue on Carbon Nanotubes*. *Acc. Chem. Res.* **2002**, *35*, 997-1113.

(70) Dai, H. *Acc. Chem. Res*. **2002,** *35*, 1035-1044

(71) Liang, W.; Bockrath, M.; Bozovic, D.; Hafner, J.; Tinkham, M.; *Nature.* **2001**, *411*, 665-669.

(72) Kong, J.; Yenilmez, E.; Tombler, T. W.; Kim, W.; Liu, L. *Phys. Rev. Lett.* **2001**, *87*, 106801.

(73) Dai, H. Nanotube Growth and Characterization. Carbon Nanotubes; Springer: Berlin, **2001**, 29-53.

(74) (a) Li, J.; Zhang, Y.; Zhang, M. *Chem. Phys. Lett*. **2002**, 364, 328. (b) Yoshida, M.; Aihara, J. I. *Phys. Chem. Chem. Phys*. **1999**, 1, 227. (c) Aihara, J-I.; Kanno, H. *Chem. Phys. Lett.*, **2004**, *398*, 440.

(75) Guldi, D. M.; Aminur Rahman, G. M; Sgobba, V.; Ehli, C. *Chem. Soc. Rev.* **2006**, *35*, 471–487.

(76) Tasis, D.; Tagmatarchis, N.; Bianco, A.; Prato, M. *Chem. Rev*. **2006**, 106, 1105-1136.

(77) Liu, J.; Rinzler, A.G.; Dai, H.; Hafner, J. H.; Bradley, R. K.; Boul, P. J.; Lu, A.; Iverson, T.; Shelimov, K.; Huffman, C.; Rodriguez-Macias, F.; Shon, Y.-S.; Lee, T. R.; Colbert, D. T.; Smalley, R. E. *Science*. **1998**, *280*, 1253.

(78) (a) Niyogi, S.; Hamon, M. A.; Hu, A.; Zhao, B.; Browmik, P.; Sen, R.; Itkis, M. E.; Haddon, R.C. *Acc. Chem. Res*. **2002**, 35, 1105. (b) Chen, J.; Hamon, M. A.; Hu, H.; Chen, Rao, A. M.; Eklund, P. C.; Haddon, R. C. *Science*. **1998**, 282, 95. (c) Hamon, M. A.; Chen, J.; Hu, H.; Chen, Y.; Rao, A. M.; Eklund, P.C.; Haddon, R. C. *Adv. Mater*. **1999**, 11, 834. (d) Chen, J.; Rao, A. M.; Lyuksyutov, S.; Itkis, M. E.; Hamon, M. A.; Hu, H.; Cohn, R. W.; Eklund, P. C.; Colbert, D. T.; Smalley. R. E.; Haddon, R. E. *J. Phys. Chem. B*. **2001**, 105, 2525.

(79) Li, H.; Martin, R. B.; Harruff, B. A.; Carino, R. A.; Allard, L. F.; Sun, Y. P. *Adv. Mater*. **2004**, 16, 896.

(80) Baskaran, D.; Ways, J. W.; Zhang, X. P.; Bratcher, M. S. *J. Am. Chem. Soc.* **2005**, 127, 6916.

(81) (a) Georgakilas, V.; Kordatos, K.; Prato, M.; Guldi, D. M.; Holzinger, M.; Hirsch, A. *J. Am. Chem. Soc.* **2002**, *124*, 760. (b) Georgakilas, V.; Tagmatarchis, N.; Pantarotto, D.; Bianco, A.; Briand, J.-P.; Prato, M. *Chem. Commun.* **2002**, 3050. (c) Kordatos, K.; Da Ros, T.; Bosi, S.; Va´zquez, E.; Bergamin, M.; Cusan, C.; Pellarini, F.; Tomberli, V.; Baiti,

B.; Pantarotto, D.; Georgakilas, V.; Spalluto, G.; Prato, M. *J. Org. Chem.* **2001**, *66*, 4915-4920.

(82) Campidelli, S.; Sooambar, C.; Diz, E. L.; Ehli, C.; Guldi, D. M.; Parto, M.; *J. Am. Chem. Soc*. **2006**, 128, 12544.

(83) Ballesteros, B.; Torre, G de la.; Ehli, C.; Rahman, G. M. A.; Agullo´-Rueda, F.; Guldi, D. M.; Torres, T*. J. Am. Chem. Soc.* **2007**, *129*, 5061-5068

(84) Rahman, G. M. A.; Guldi, D. M.; Campidelli, S.; Prato, M. *J. Mater. Chem*. **2006**, *10*, 62.

(85) Saito, K.; Troiani, V.; Qiu, H.; Solladie, N.; Sakata, T.; Mori, H.; Ohama, M.; Fukuzumi, S. *J. Phys. Chem. C.* **2007**, *111*, 1194.

(86) Guldi, D. M.; Rahman, G. M. A.; Jux, N.; Balbinot, D.; Tagmatarchis, N.; Prato, M. *Chem. Commun*. **2005**, 2038. (b) Guldi, D. M.; Prato, M. *Chem. Commun*. **2004**, 2517. (c) Guldi, D. M..; Rahman, G. M. A.; Jux, N.; Balbinot, D.; Hartnagel, U.; Tagmatarchis, N.; Prato, M. *J. Am. Chem. Soc.* **2005**, *127*, 9830.

(87) Guldi, D. M.; Rahman, G. M. A.; Sgobba, V.; Campidelli, S.; Prato, M.; Kotov, N. A. *J. Am. Chem. Soc*. **2006,** *128*, 2315.

(88) Chitta, R.; Sandanayaka, A. S. D.; Schumacher, A. L.; D'Souza, L.; Araki, Y.; Ito, O.; D'Souza, F. *J. Phys. Chem. C*. **2007**, *111*, 6947.

(89) D'Souza, F.; Chitta, R.; Sandanayaka, A. S. D.; Subbaiyan, N. K.; D'Souza, L.; Araki, Y.; Ito, O. *Chem.Eur. J*. **2007**, *13*, 8277.

(90) D'Souza, F.; Chitta, R.; Sandanayaka, A. S. D.; Subbaiyan, N. K.; D'Souza, L.; Araki, Y.; Ito, O. *J. Am. Chem. Soc*. **2007**, *129*, 15865.

(91) (a) Connolly, J. S., Ed. *Photochemical Conversion and Storage of Solar Energy*; Academic: New York, **1981**. (b) *Molecular Level Artificial Photosynthetic Materials*; Meyer, G. J., Ed.; Wiley: New York, **1997**. (c) Wasielewski, M. R. *Chem. Rev.* **1992**, *92*, 435. (d) Verhoeven, J. W.

Adv. Chem. Phys. **1999**, *106*, 603. (e) Osuka, A.; Mataga, N.; Okada, T. *Pure Appl. Chem.* **1997**, *69*, 797. (f) Flamigni, L.; Barigelletti, F.; Armaroli, N.; Collin, J.-P.; Dixon, I. M.; Sauvage, J.-P.; Williams, J. A. G. *Coord. Chem. Rev.* **1999**, *190-192*, 671. (g) Diederich, F.; Gomez-Lopez, M. *Chem. Rev. Soc.* **1999**, *28*, 263.

(92) (a) Blanco, M.-J.; Consuelo Jimenez, M.; Chambron, J.-C.; Heitz, V.; Linke, M.; Sauvage, J.-P. *Chem. Rev. Soc.* **1999**, *28*, 293. (b) Balzani, V.; Ceroni, P.; Juris, A.; Venturi, M.; Campagna, S.; Puntoriero, F.; Serroni, S. *Coord. Chem. Re*v. **2001**, *219*, 545. (c) Balzani, V.; Credi, A.; Venturi, M. *ChemSusChem.* **2008**, *1*, 26.

(93) Benesi, H. A.; Hildebrand, J. H. *J. Am. Chem. Soc.* **1949**, *71*, 2703.

(94) Frisch, M. J.; Trucks, G. W.; Schlegel, H. B.; Scuseria, G. E.; Robb, M. A.; Cheeseman, J. R.; Zakrzewski, V. G.; Montgomery, J. A.; Stratmann, R. E.; Burant, J. C.; Dapprich, S.; Millam, J. M.; Daniels, A. D.; Kudin, K. N.; Strain, M. C.; Farkas, O.; Tomasi, J.; Barone, V.; Cossi, M.; Cammi, R.; Mennucci, B.; Pomelli, C.; Adamo, C.; Clifford, S.; Ochterski, J.; Petersson, G. A.; Ayala, P. Y.; Cui, Q.; Morokuma, K.; Malick, D. K.; Rabuck, A. D.; Raghavachari, K.; Foresman, J. B.; Cioslowski, J.; Ortiz, J. V.; Stefanov, B. B.; Liu, G.; Liashenko, A.; Piskorz, P.; Komaromi, I.; Gomperts, R.; Martin, R. L.; Fox, D. J.; Keith, T.; Al-Laham, M. A.; Peng,C. Y.; Nanayakkara, A.; Gonzalez, C.; Challacombe, M.; Gill, P. M. W.; Johnson, B. G.; Chen, W.; Wong, M. W.; Andres, J. L.; Head-Gordon, M.; Replogle, E. S.; Pople, J. A. Gaussian 03, Gaussian, Inc., Pittsburgh PA, **2003**.

(95) Zandler, M. E.; D'Souza, F. *C. R. Chemie.* **2006**, *9*, 960.

(96) (a) Weller, A. Z. *Phys. Chem.* **1982**, *132*, 93. (b) Cozzi, P.; Carganico, G.; Fusar, D.; Grossoni, M.; Menichincher, M.; Pinciroli, V.; Tonani, R.; Vaghi, F.; Salvatig, P. *J. Med. Chem.* **1993**, *36*, 2964.

(97) Jordan, K. D.; Paddon-Row, M. N. *Chem. Rev*. **1992**, *92*, 395.

(98) D. Gust, T. A. Moore, The *Porphyrin Handbook*, Vol. 8 (Eds.: K. M. Kadish, K. M. Smith, R. Guilard), Academic Press, San Diego, CA, **2000**,153 –190.

(100) a) Fukuzumi, S. *Org. Biomol. Chem*. **2003**, *1,* 609; b) Fukuzumi, S. *Bull. Chem. Soc. Jpn.* **2006**, *79*, 177.

(101) Hasobe, T.; Imahori, H.; Kamat, P. V.; Ahn, T. K.; Kim, D.; Hanada, T.; Hirakawa, T.; Fukuzumi, S. *J. Am. Chem. Soc*. **2005**, *127*, 1216.

(102) a) D'Souza, F.; Gadde, S.; Shafiqul, D-M. I.; Pang, S-C.; Schumacher, A. L.; Zandler, M. E.; Horie, R.; Araki, Y.; Ito, O. *Chem. Commun*. **2007**, 480. b) D'Souza, F.; Chitta, R.; Gadde, S.; Islam, D-M. S.; Schumacher, A. L.; Zandler, M. E.; Araki, Y.; Ito, O. *J. Phys. Chem. B*, **2006**, *110*, 25240.

(103) a) Liddell, P. A.; Sumida, J. P.; Macpherson, A. N.; Noss, L.; Seely, G. R.; Clark, K. N.; Moore, A. L.; Moore, T. A.; Gust, D. *Photochem. Photobiol.* **1994**, *60*, 537. b) D'Souza, F.; Gadde, S.; Zandler, M. E.; Arkady, K.; El-Khouly, M. E.; Fujitsuka, M., Ito, O. *J. Phys. Chem. A.* **2002**, *106*, 12393. c) Fukuzumi, S.; Okamoto, K.; Gros, C. P.; Guilard, R.; *J. Am. Chem. Soc*. **2004**, *126*, 10441. d) Fukuzumi, S.; Okamoto, K.; Tokuda, Y.; Gros, C. P.; Guilard, R. *J. Am. Chem. Soc*. **2004**, *126*, 17059.

(104) a) Deng Y.; Chang, C. J.; Nocera, D. G. *J. Am. Chem. Soc*. **2000,** 122, 410. b) Chang, C. J.; Deng, Y.; Shi, C.; Chang, C. K.; Anson, F. C.; Nocera, D. G. *Chem. Commun*. **2000**, 1355.

(105) Fletcher, J. T.; Therien, M. J. *J. Am. Chem. Soc*. **2002**, *124*, 4298.

(106) Kadish, K. M.; Shao, J.; Ou, Z.; Fremond, L.; Zhan, R.; Burdet, F.; Barbe,J-M.; Gros, C. P.; Guilard, R. *Inorg. Chem*. **2005**, *44*, 6744.

(107) a) Tanaka, M.; Ohkubo, K.; Gros, C. P.; Guilard, R.; Fukuzumi, S. J. Am. Chem. Soc. 2006, 128, 14625 b) Gros, C. P.; Brisach, F.; Theristoudi, A.; Espinosa, E.; Guilard, R.; Harvey, P. D. *Inorg. Chem*. **2007**, *46*, 125 c) Harvey, P. D.; Stern, C.; Gros, C. P.; Guilard, R. *Coord. Chem. Rev*. 2007, 251, 481.

(108) Maggini, M.; Scorrono, G.; Prato, M. *J. Am. Chem. Soc.* **1993**, *115*, 9798.

(109) a) Imahori, H.; Tkachenko, N.V.; Vehmanen, V.; Tamaki, K.; Lemmetyinen,H.; Sakata, Y.; Fukuzumi, S. *J. Phys. Chem. A 2001*, **105**, 1750. b) Tkachenko, N. V.; Lemmetyinen, H.; Sonoda, J.; Ohkubo, K.; Sato, T.; Imahori, H.; Fukuzumi, S. *J. Phys. Chem. A*. **2003**, *107*, 8834.

(110) a) Boyd, P. D. W.; Reed, C. A. *Acc. Chem. Res.* **2005**, *38*, 235; b) Balch, A. L.; Olmstead, M. M. *Coord. Chem. Rev*. **1999**, *601*, 185–186.

(111) Rehm, D.; Weller, A. *Isr. J. Chem.* **1970**, *8*, 259.

(112) Ohkubo, K.; Kotani, H.; Shao, J.; Ou, Z.; Kadish, K. M.; Chen, Y.; Zheng, G.; Pandey, P. K.; Fujitsuka, M.; Ito, O.; Imahori, H.; Fukuzumi, S. *Angew. Chem*. **2004**, *116*, 871; *Angew. Chem. Int. Ed*. **2004**, *43*, 853.

(113) At 1000 ps, the singlet absorption at 1200 nm mostly disappears (Figure 4.10), whereas the absorption at 1000 nm due to the C_{60} radical anion still remains. This indicates that the C_{60} radical anion is formed via the porphyrin singlet excited state.

(114) Galili, T.; Regev, A.; Levanon, H.; Schuster, D. I.; Guldi, D. M. *J. Phys. Chem. A*. **2004**, *108*, 10632.

(115) For the Pacman effect on the excited-state dynamics of pillard cofacial bisporphyrins, see: Chang, C. J.; Loh, Z-H.; Deng, Y.; Nocera, D. G. *Inorg. Chem.* **2003**, *42*, 8262.

(116) (a) Deisenhofer, J.; Michel, H. *Science.* **1989**, *245*, 1463–1473. (b) Allen, P.; Feher, G.; Yeates, T. O.; Rees, D. C.; Deisenhofer, J.; Michel, H.; Huber, R. *Proc. Natl. Acad. Sci. U.S.A.* **1986**, *83*, 8589–8593. (c) Deisenhofer, J.; Epp, O.; Sinning, I.; Michel, H. *J. Mol. Biol.* **1995**, *246*, 429–457. (d) Jordan, P.; Fromme, P.; Witt, H.-T; Klukas, O.; Saenger, W.; Krauss, N. *Nature,* **2001**, *411*, 909–917.

(117) Kurreck, H.; Huber, M. *Angew. Chem., Int. Ed. Engl.* **1995**, *34*, 849–866

(118) Imahori, H.; Fukuzumi, S. *Adv. Funct. Mater.* **2004**, *14*, 525–536.

(119) (a) Fukuzumi, S. *Phys. Chem. Chem. Phys.* **2008**, *10*, 2283–2297. (b) Chitta, R.; D'Souza, F. *J. Mater. Chem.* **2008**, *18*, 1440–1471. (c) Fukuzumi, S.; Kojima, T. *J. Mater. Chem.* **2008**, *18*, 1427–1439. (d) Fukuzumi, S. *Eur. J. Inorg. Chem.* **2008**, 1351–1362.

(120) (a) Sessler, J. L.; Johnson, M. R.; Lin, T.-Y.; Creager, S. E. *J. Am. Chem. Soc.* **1988**, *110*, 3659–3661. (b) Rodriguez, J.; Kirmaier, C.; Johnson, J. R.; Friesner, R. A.; Holten, D.; Sessler, J. L. *J. Am. Chem.Soc.* **1991**, *113*, 1652–1659. (c) Osuka, A.; Nakajima, S.; Maruyama, K.; Mataga, K.; Asahi, T.; Yamazaki, I.; Nishimura, Y.; Ohno, T.; Nozaki, K. *J. Am. Chem. Soc.* **1993**, *115*, 4577–4589. (d) Nakashima, S.; Taniguchi, S.; Okada, T.;

Osuka, A.; Mizutani, Y.; Kitagawa, T. *J. Phys. Chem. A* **1999**, *103*, 9184–9189.

(121) (a) Ozeki, H.; Nomoto, A.; Ogawa, K.; Kobuke, Y.; Murakami, M.; Hosoda, K.; Ohtani, M.; Nakashima, S.; Miyasaka, H.; Okada, T. *Chem.sEur. J.* **2004**, *10*, 6393–6401. (b) Isosomppi, M.; Tkachenko, N. V.; Efimov, A.; Lemmetyinen, H. *J. Phys. Chem. A.* **2005**, *109*, 4881–4890.

(122) (a) Sessler, J. L.; Wang, B.; Springs, S. L.; Brown, C. T. In *Comprehensive Supramolecular Chemistry*; Atwood, J. L., Davies, J. E. D., MacNicol, D. D., Vo¨gtle, F., Eds.; Pergamon: New York, 1996; Chapter 9. (b) Hayashi, T.; Ogoshi, H. *Chem. Soc. Rev.* **1997**, *26*, 355–364. (c) Ward, M. W. *Chem. Soc. Rev.* **1997**, *26*, 365–375.

(123) (a) BalzaniV.; Scandola, F. *Supramolecular Chemistry*; Ellis Horwood: New York, 1991. (b) Schlicke, B.; De Cola, L.; Belser, P.; Balzani, V. *Coord. Chem. Re*v. **2000**, *208*, 267–275. (c) De Silva, A. P.; Gunaratne, H. Q. N.; Gunnlaugsson, T.; Huxley, A. J. M.; Mccoy, C. P.; Rademacher, J. T.; Rice, T. E. *Adv. Supramol. Chem.* **1997**, *4*, 1–53. (d) Ashton, P. R.; Ballardini, R.; Balzani, V.; Credi, A.; Dress, K. R.; Ishow, E.; Kleverlaan, C. J.; Kocian, O.; Preece, J. A.; Spencer, N.; Stoddart, J. F.; Venturi, M.; Wenger, S. *Chem.-Eur. J.* **2000**, *6*, 3558–3574.

(124) (a) *Supramolecular Chemistry*; Atwood, J. L., Davies, J. E. D., MacNicol, D. D., Vo¨gtle, F., Reinhoudt, D. N., Eds.; Pergamon: Oxford, **1996**; Vol. 10, 171-185. (b) Bell, T. W.; Hext, N. M. *Chem. Soc. Rev.* **2004**, *33*, 589–598. (c) Sun, S.-S.; Lees, A. J. *Coord.Chem. Rev.* **2002**, *230*, 171–192. (d) de Silva, A. P.; Gunaratne, H. Q. N.; Gunnlaugsson, T.; Huxley, A. J. M.; McCoy, C. P.; Rademacher, J. T.; Rice, T. E. *Chem. Re*v. **1997**, *97*, 1515–1566. (e) Lehn, J. M. *Front. Supramol. Org. Chem. Photochem.* **1991**, *1*, 28. (f) Verhoeven, J. W. *J. Photochem. Photobiol. C.* **2006**, *7*, 40–60.

(125) (a) *Phthalocyanine Materials: Structure, Synthesis and Function*, McKeown, N. B., Ed.; Cambridge University Press: Cambridge, 1998. (b) *Phthalocyanine: Properties and Applications*; Leznoff, C. C., Lever, A. B. P., Eds.; VCH: New York, 1993. (c) de la Torre, G.; Claessens, C. G.; Torres, T. *Chem. Commun.* **2007**, 2000–2015. (d) Kobayashi, N. *Coord. Chem. Rev.* **2002**, *227*, 129–152. (e) Claessens, C. G.; Gonza´lez-Rodrı´guez, D.; Torres, T. *Chem. Rev.* **2002**, *102*, 835. (f) de la Torre, G.; Va´zquez, P.; Agullo´-Lo´pez, F.; Torres, T. *J. Mater. Chem.* **1988**, *8*, 1671.

(126) (a) Linssen, T. G.; Durr, K.; Hanack, M.; Hirsch, A. *J. Chem. Soc.,Chem. Commun.* **1995**, *103*, 104. (b) Sastre, A.; Gouloumis, A.; Va´zquez, P.;

Torres, T.; Doan, V.; Schwartz, B. J.; Wudl, F.; Echegoyen, L.; Rivera, J. *Org. Lett.* **1999**, *1*, 1807–1810. (c) Martı`nez-Dı`az, M. V.; Fender, N. S.; Rodrı`guez-Morgade, M. S.; Go`mez-Lo´pez, M.; Diederich, F.; Echegoyen, L.; Stoddart, J. F.; Torres, T. *J. Mater. Chem.* **2002**, *12*, 2095–2099. (d) Guldi, D. M.; Gouloumis, A.; Va´zquez, P.; Torres, T. *Chem. Commun.* **2002**, 2056–2057. (e) Loi, M. A.; Neugebauer, H.; Denk, P.; Brabec, C. J.; Sariciftci, N. S.; Gouloumis, A.; Va´zquez, P.; Torres, T. *J. Mater.Chem.* **2003**, *13*, 700–704. (f) Guldi, D. M.; Zilbermann, I.; Gouloumis, A.; Va´zquez, P.; Torres, T. *J. Phys. Chem. B* **2004**, *108*, 18485–18489.

(127) (a) Kobayashi, N.; Lever, A. B. P. *J. Am. Chem. Soc.* **1987**, *109*, 7433–7341. (b) Kobayashi, N.; Togashi, M.; Osa, T.; Ishii, K.; Yamauchi, S.; Hino, H. *J. Am. Chem. Soc.* **1996**, *118*, 1073–1085. (c) Sielcken, O. E.; van Tilborg, M. V.; Roks, M. F. M.; Hendriks, R.; Drenth, W.; Nolte, J. M. *J. Am. Chem. Soc.* **1987**, *109*, 4261–6265. (d) Sielcken, O. E.; Schram, J.; Nolte, R. J. M.; Schoonman, J.; Drenth, W. *J. Chem.Soc.,Chem. Commun.* **1988**, 108–109. (e) Nikolaitchik, A. V.; Korth, O.; Rodgers, M. A. *J. Phys. Chem. A.* **1999**, *103*, 7587–7596. (f) Nikolaitchik, A. V.; Rodgers, M. A. J. *J. Phys. Chem. A.* **1999**, *103*, 7597–7605.

(128) For cation induced dimerization of crown ether appended porphyrin analogs, see: (a) Thanabal, V.; Krishnan, V. *J. Am. Chem. Soc.* **1982**, *104*, 3643–3650. (b) Thanabal, V.; Krishnan, V. *Inorg. Chem.* **1982**, *21*, 3606–3613. (c) van Willigen, H.; Chandrashekar, T. K. *J. Am. Chem. Soc.* **1986**, *108*, 709–713. (d) Chandrashekar, T. K.; van Willigen, H.; Ebersole, M. *J. Phys. Chem.* **1985**, *89*, 3453–3459. (e) Chitta, R.; Rogers, L. M.; Wanklyn, A.; Karr, P. A.; Kahol, P. K.; Zandler, M. E.; D'Souza, F. *Inorg. Chem.* **2004**, *43*, 6969–6978.

(129) (a) D'Souza, F.; Chitta, R.; Gadde, S.; Zandler, M. E.; Sandanayaka, A. S. D.; Araki, Y.; Ito, O. *Chem. Commun.* **2005**, 1279–1281. (b) D'Souza, F.; Chitta, R.; Gadde, S.; Zandler, M. E.; McCarty, A. L.; Sandanayaka, A. S. D.; Araki, Y.; Ito, O. *Chem.*A.*Eur. J.* **2005**, *11*, 4416–4428.

(130) (a) Kasha, M. *Radiat. Res.* **1963**, *20*, 55–70. (b) Gouterman, M.; Holten, D.; Lieberman, E. *Chem. Phys.* **1977**, *25*, 139–153. (c) Hunter, C. A.; Sanders, J. K. M.; Stone, A. J. *Chem. Phys.* **1989**, *133*, 395–404. (d) Tran-Thi, T. H.; Lipskier, J. F.; Maillard, P.; Momenteau, M.; Lopez-Castillo, J.-M.; Jay-Gerin, J.-P. *J. Phys. Chem.* **1992**, *96*, 1073–1082. (e) Tran-Thi, T.-H. *Coord. Chem. Rev.* **1997**, *160*, 53–91. (f) Toupance, T.; Ahsen, V.; Simon, J. *J. Am. Chem. Soc.* **1994**, *116*, 5352–5361. (g) Toupance, T.; Benoit, H.; Sarazin, D.; Simon, J. *J. Am. Chem. Soc.* **1997**, *119*, 9191–9197.

(131) A small deviation from the straight line segment around 1 equiv of K+ is observed in Figure 6b, suggesting 2 equiv of K^+ essentially starts forming

the ZnTCPc dimer. Steady-state fluorescence emission data analysis in Figure 6 inset also revealed such a trend.

(132) (a) El-Khouly, M. E.; Rogers, L. M.; Zandler, M. E.; Gadde, S.; Fujitsuka, M.; Ito, O.; D'Souza, F. *ChemPhysChem* **2003**, *4*, 474–481. (b) El-Khouly, M. E.; Araki, Y.; Ito, O.; Gadde, S.; Zandler, M. E.; D'Souza, F. *J. Porphyrins Phthalocyanines* **2006**, *10*, 1156–1164.

(133) *Gaussian 03*; Frisch, M. J., et al. Gaussian, Inc.: Pittsburgh, PA, **2003**.

(134) For applications of DFT on tetrapyrrole-fullerene systems, see: Zandler, M. E.; D'Souza, F. In *DFT Calculations on Fullerenes and Carbon Nanotubes*; Basiuk, V. A., Irle, S., Eds.; Research Signpost: Kerala, India, **2008**; pp 81-126.

(135) Mataga, N.; Miyasaka, H. In *Electron Transfer*; Jortner, J., Bixon, M., Eds.; John Wiley & Sons: New York, **1999**; Part 2, pp 431-496.

(136) (a) Pekkarinen, L.; Linschitz, H. *J. Am. Chem. Soc.* **1960**, *82*, 2407–2411. (b) Gratz, H.; Penzkofer, A. *Chem. Phys.* **2000**, *254*, 363–374.

(137) For the favorable effects of π-expansion of porhyrins on electron transfer reactions, see: (a) Fukuzumi, S.; Ohkubo, K.; E, W.; Ou, Z.; Shao, J.; Kadish, K. M.; Hutchison, J. A.; Ghiggino, K. P.; Sintic, P. J.; Crossley, M. J. *J. Am. Chem. Soc.* **2003**, *125*, 14984–14985. (b) Ohkubo, K.; Sintic, P. J.; Tkachenko, N. V.; Lemmetyinen, H.; Ou, Z.; Shao, J.; Kadish, K. M.; Crossley, M. J.; Fukuzumi, S. *Chem. Phys.* **2006**, *326*, 3–14. (c) Kadish, K. M.; Wenbo, E.; Sintic, P. J.; Ou, Z.; Shao, J.; Ohkubo, K.; Fukuzumi, S.; Govenlock, L. J.; McDonald, J. A.; Try, A. C.; Cai, Z.-L.; Reimers, J. R.; Crossley, M. J. *J. Phys. Chem. B* **2007**, *111*, 8762–8774. (d) Fukuzumi, S.; Ohkubo, K.; Zhu, W.; Sintic, M.; Khoury, T.; Sintic, P. J.; Wenbo, E.; Ou, Z.; Crossley, M. J.; Kadish, K. M. *J. Am. Chem. Soc.* **2008**, *130*, 9451–9458.

(138) The photoexcitation of the supramolecular complex with λ = 430 nm also results in formation of $^1C_{60}$*. However, the contribution of $^1C_{60}$* is negligible because no $^3C_{60}$* is detected, as shown in Figure 4.18c.

(139) Tanaka, M.; Ohkubo, K.; Gros, C. P.; Guilard, R.; Fukuzumi, S. *J. Am. Chem. Soc.* **2006**, *128*, 14625–14633.

(140) Vincett, P. S.; Voigt, E. M.; Rieckoff, K. E. *J. Chem. Phys.* **1971**, *55*, 4131–4140.

(141) (a) *Introduction of Molecular Electronics*, Petty, M. C., Bryce, M. R., Bloor, D., Eds.; Oxford University Press: New York, 1995. (b) *Molecular Electronics: Science and Technology*; Aviram, A., Ratner, M., Eds.; New York Academy of Science: New York, 1998; p 852. (c) *Molecular Switches*, Feringa, B. L., Ed.; Wiley-VCH GmbH: Weinheim, Germany, 2001. (d) Gust, D.; Moore, T. A.; Moore, A. L. *Chem. Commun.* **2006**, 1169–1178. (e) Balzani, V.; Credi, A.; Venturi, M. In *Organic Nanostructures*; ed. Atwood, J. L., Steed, J. W., Eds.; Wiley-VCH: Weinheim, Germany, 2008.

(142) (a) Bixon, M.; Fajer, J.; Feher, G.; Freed, J. H.; Gamliel, D.; Hoff, A. J.; Levanon, H.; Mo¨bius, K.; Nechushtai, R.; Norris, J. R.; Scherz, A.; Sessler, J. L.; Stehlik, D. *Isr. J. Chem.* **1992**, *32*, 449. (b) Lewis, F. D.; Letsinger, R. L.; Wasielewski, M. R. *Acc. Chem. Res.* **2001**, *34*, 159.

(143) Imahori, H.; Sekiguchi, Y.; Yukiyasu, S.; Tohru, A.; Araki, Y.; Ito, O.; Yamada, H.; Fukuzumi, S. *Chem.-Eur. J.* **2004**, *10*, 3184. (e) Fukuzumi,S.; Kotani, H.; Ohkubo, K.; Ogo, S.; Tkachenko, J. V.; Lemmetyinen, H. *J. Am. Chem. Soc.* **2004**, *126*, 1600.

(144) Fukuzumi, S.; Kotani, H.; Ohkubo, K.; Ogo, S.; Tkachenko, J. V.; Lemmetyinen, H. *J. Am. Chem. Soc.* **2004**, *126*, 1600.

(145) (a) Seth, J.; Palaniappna, V.; Wagner, R. W.; Johnson, T. E.; Lindsey, J. S.; Holten, D.; Bocian, D. F. *J. Am. Chem. Soc.* **1996**, *118*, 11194. (b) Seth, J.; Palaniappan, V.; Johnson, T. E.; Prathapan, S.; Lindsey, J. S.; Bocian, D. F. *J. Am. Chem. Soc.* **1994**, *116*, 10578.

(146) (a) Kuciauskas, D.; Liddell, P. A.; Lin, S.; Johnson, T. E.;Weghorn, S. J.; Lindsey, J. S.; Moore, A. L.; Moore, T. A.; Gust, D. *J. Am. Chem.Soc.* **1999**, *121*, 8604. (b) Kodis, G.; Liddell, P. A.; de la Garza, L.; Clausen, C.; Lindsey, J. S.; Moore, A. L.; Moore, T. A.; Gust, D. *J. Phys. Chem. A* **2002**, *106*, 2036. (c) Tamaki, K.; Imahori, H.; Nishimura, Y.; Yamazaki, I.; Sakata, Y. *Chem. Commun.* **1999**, 625. (d) Imahori, H.; Norieda, H.; Yamada, H.; Nishimura, Y.; Yamazaki, I.; Sakata, Y.; Fukuzumi, S. *J. Am.Chem. Soc.* **2001**, *123*, 100. (e) Liddell, P. A.; Kodis, G.; de la Garza, L.; Moore, A. L.; Moore, T. A.; Gust, D. *J. Phys. Chem. B* **2004**, *108*, 10256. (f) Kodis, G.; Terazono, Y.; Liddell, P. A.; Andreasson, J.; Garg, V.; Hambourger, M.; Moore, A. L.; Moore, T. A.; Gust, D. *J. Am. Chem. Soc.* **2006**, *128*, 1818. (g) Terazono, Y.; Kodis, G.; Liddell, P. A.; Garg, V.; Moore, T. A.; Moore, A. L.; Gust, D. *J. Phys. Chem. B* **2009**, *113*, 7147.

(147) (a) Loudet, A.; Burgess, K. *Chem. Re*V. **2007**, *107*, 4891. (b) Li, F.; Yang, S. I.; Ciringh, T.; Seth, J.; Martin, C. H., III.; Singh, D. L.; Kim, D.; Birge,

R. R.; Bocian, D. F.; Holten, D.; Lindsey, J. S. *J. Am. Chem.Soc.* **1998**, *120*, 10001.

(148) Nierengarten, J.-F.; Hahn, U.; Duarte, M. F.; Cardinali, F.; Solladie, N.; Walther, M. E.; Dorsselaer, A. V.; Herschbach, H.; Leize, E.; Gary, A.; Trabolsi, A.; Elhabiri, M. C. R. *C. R. Chim.* **2006**, *9*, 1022.

(149) Lee, C. H.; Lindsey, J. S. *Tetrahedron,* **1994**, *50*, 39–11427.

(150) D'Souza, F.; Chitta, R.; Gadde, S.; Zandler, M. E.; McCarty, A. L.; Sandanayaka, A. S. D.; Araki, Y.; Ito, O. *J. Phys. Chem. A.* **2006**, *110*, 4338.

(151) (a) Kim, K. S.; Tarakeshwar, P.; Lee, J. Y. *Chem. Rev.* **2000**, *100*, 4145. (b) Jensen, K. P.; Ryde, U. *J. Phys. Chem. A.* **2003**, *107*, 7539.

(152) *Electrochemical Methods: Fundamentals and Applications*, 2nd ed; Bard, A. J., Faulkner, L. R., Eds.; John Wiley: New York, **2001**.

(153) Smith, K. M. *Porphyrins and Metalloporphyrins*; Elsevier: New York, **1977**.

(154) (a) *Photosynthetic Protein Complexes*; *A Structural Approach*, ed. P. Frome, Wiley-VCH Verlag GmbH & Co., Germany, **2008**; (b) *Phtosynthetic Light Harvesting*, ed. R. Cogdell and C. Mullineaux, Springer, Dordrecht, Netherlands, **2008**; (c) Handbook of Photosynthesis, ed. M. Pessarakli, CRC Press LLC, Boca Raton, FL, 2nd edn, **2005**; (d) *Light-Harvsting Antennas in Photosynthesis*, ed. B. R. Green and W. W. Parson, Kluwer, Dordrecht, Netherlands, **2003**; (e) R. E. Blankenship, *Molecular Machanisms of Photosynthesis*, Blackwell Sciences, Oxford, **2002**.

(155) (a) Karrasch, S.; Bullough, P. A.; Ghosh, R, *EMBO J.* **1995**, *14*, 631; (b) Roszak, A. W.; Howard, T. D.; Southall, J.; Gardiner, A. T.; Law, C. L.; Isaacs, N. W.; Cogdell, R. J. *Science*. **2003**, *302*, 1969; (c) McDermott, G.; Prince, S. M.; Freer, A. A.; Hawthornthwaite- Lawless, A. M.; Papiz, M. Z.; Cogdell, R. J.; Isaacs, N. W.; *Nature.* **1995**, *374*, 517; (d) Bahatyrova, S.; Frese, R. N.; Siebert, C. A.; Olsen, J. D.; van der Werf, K.O.; van Grondelle, R.; Niederman, R. A.; Bullough, P. A.; Otto, C.; Hunter, C. N. *Nature*. **2004**, *430*, 1058; (e) Scheuring, S; Sturgis, J. N.; Prima, V.; Bernadac, A.; Levy, D.; Rigaud, J.-L. *Proc. Natl. Acad. Sci. USA*. **2004**, *101*, 11293; (f) Scheuring, S.; Sturgis, J. N. *Science*. **2005**, *309*, 484.

(156) (a) Sakata, Y.; Imahori, H.; Tsue, H.; Higashida, S.; Akiyama, T.; Yoshizawa, E.; Aoki, M.; Yamada, K.; Hagiwara, K.; Taniguchi, S.; Okada, T. *Pure Appl. Chem.* **1997**, *69*, 1951; (b) Imahori, H.; Sakata, Y. *Eur. J. Org. Chem*. **1999**, 2445; (c) Umeyama, T.; Imahori, H. *Energy Environ. Sci.* **2008**, *1*, 120. (d) Guldi, D. M. *Chem. Commun*. **2000**, 321.

(157) (a) Ulrich, G.; Ziessel R.; Harriman, A. *Angew. Chem., Int. Ed*. **2008**, *47*, 1184; (b) Benniston, A. C.; Copley, G. *Phys. Chem. Chem. Phys*. **2009**, *11*, 4124

(158) (a) Lammi, R. K.; Wagner, R. W.; Ambroise, A.; Diers, J. R.; Bocian, D. F.; Holten, D.; Lindsey, J. S. *J. Phys. Chem. B.* **2001**, *105*, 5341; (b) Wagner, R. W.; Lindsey, J. S. Pure *Appl. Chem*. **1996**, *68*, 1373; (c) Kee, H. L.; Kirmaier, C.; Yu, L.; Thamyongkit, P.; Youngblood, W. J.; Calder, J. E.; Ramos, L.; Noll, B. C.; Bocian, D. F.; Scheidt, W. R.; Birge, R. R.; Lindsey, J. S.; Holten, D. *J. Phys. Chem. B*. **2005**, *109*, 20433. (d) Maligaspe, E.; Tkachenko, N. V.; Subbaiyan, N. K.; Chitta, R.; Zandler, M. E.; Lemmetyinen, H.; D'Souza, F. *J. Phys. Chem. A*. **2009**, *113*, 8478; (e) Harriman, A.; Mallon, L. J.; Elliot, K. J.; Haefele, A.; Ulrich, G.; Ziessel, R. *J. Am. Chem. Soc.* **2009**, *131*, 13375; (f) Harriman, A.; Mallon, L. J.; Goeb, S.; Ulrich, G.; Ziessel, R. *Chem. A. Eur. J.* **2009**, *15*, 4553; (g) Diring, S.; Putoriero, F.; Nastasi, F.; Campagna, S.; Ziessel, R. *J. Am. Chem. Soc.* **2009**, *131*, 6108; (h) Liu, J.-Y.; Ermilov, E. A.; Roder, B.; Ng, D. K. P. *Chem. Commun*. **2009**, 1517; (i) Liu, J.-Y.; Yeung, H.-S.; Xu, W.; Li, X.; Ng, D. K. P. *Org. Lett*. **2008**, *10*, 5421; (j) Zhang, X.; Xiao, Y.; Zian, X. *Org. Lett*. **2008**, *10*, 29; (k) Ziessel, R.; Allen, B. D.; Rewinska, D. B.; Harriman, A. *Chem.–Eur.J*. **2009**, *15*, 7382; (l) Kumaresan, D.; Datta, A.; Ravikanth, M. *Chem. Phys. Lett*. **2004**, *395*, 87; (m) Harriman, A.; Cesqario, J. P.; Ulrich, G.; Ziessel, R. *J. Phys. Chem. A*. **2006**, *110*, 7994.

(159) (a) Iijima, S. *Nature.* **1991**, *354*, 56. (b) Iijima, S.; Ichihashi, T. *Nature.* **1993**, *364*, 737.

(160) (a) Harris, P. J. F. *Carbon Nanotubes and Related Structures: New Materials for the Twenty-First Century*; Cambridge University Press: Cambridge, UK, **2001**. (b) *Carbon Nanotubes: Synthesis, Structure and Applications*; Dresselhaus, M. S., Dresselhaus, G., Avouris, Ph., Eds.; Springer Publishing: New York, **2001**. (c) Special issue on Carbon Nanotubes. *Acc. Chem. Res.* **2002**, *35*, 997.

(161) (a) Reich, S.; Thomsen, C.; Maultzsch, J. *Carbon Nanotubes: Basic Concepts and Physical Properties*; Wiley-VCH: Weinheim, **2004**; (b) Roth, S.; Carroll, D. *One-Dimensional Metals: Conjugated Polymers,Organic Crystals, Carbon Nanotubes*; Wiley-VCH: Weinheim, Germany, **2004**. (c)

Meyyappan, M. *Carbon Nanotubes, Science and Application*; Wiley-VCH: Weinheim, Germany, **2006**.

(162) (a) *Introduction to Nanotechnology*; Poole, C. P., Owens, F. J., Eds.; Wiley-Interscience: Weinheim, **2003**. (b) *Nanophysics and Nanotechnology: An Introduction to Modern Concepts in Nanoscience*; Wolf, E. L., Ed.; John Wiley & Sons: New York, **2004**.

(163) (a) Mamada, N.; Sawada, S.; Oshiyama, A. *Phys. Rev. Lett.* **1992**, *68*, 1579. (b) Saito, R.; Dresselhaus, G.; Dresselhaus, M. S. *Physical Properties of Carbon Nanotubes*; Imperial College Press: London, **1998**.

(164) (a) O'Connell, M. J.; Bachilo, S. M.; Huffman, C. B.; Moore, V. C.; Strano, M. S.; Haroz, E. H.; Rialon, K. L.; Boul, P. J.; Noon, W. H.; Kittrell, C.; Ma, J. P.; Hauge, R. H.; Weisman, R. B.; Smalley, R. E. *Science.* **2002**, *297*, 593. (b) Zheng, M.; Jagotwa, A.; Strano, M. S.; Santos, A. P.; Barone, P.; Chou, S. G.; Diner, B. A.; Dresselhaus, M. S.; McLean, R. S.; Onoa, G. B.; Samsonidze, G. G.; Semke, E. D.; Usrey, M.; Walls, D. J. *Science.* **2003**, *302*, 1545. (c) Strano, M. S.; Dyke, C. A.; Usrey, M. L.; Barone, P. W.; Allen, M. J.; Shan, H. W.; Kittrell, C.; Hauge, R. H.; Tour, J. M.; Smalley, R. E. *Science.* **2003**, *301*, 151.

(165) (a) Bachilo, S. M.; Balzano, L.; Herrera, J. E.; Pompeo, F.; Resasco, D. E.; Weisman, R. B. *J. Am. Chem. Soc.* **2003**, *125*, 11186. (b) Chattopadhyay, D.; Galeska, L.; Papadimitrakopoulos, F. *J. Am. Chem. Soc.* **2003**, *125*, 3370. (c) Arnold, M. S.; Stupp, S. I.; Hersam, M. C. *Nano Lett.* **2005**, *5*, 713. (d) An, K. H.; Park, J. S.; Yang, C. M.; Jeong, S. Y.; Lim, S. C.; Kang, C.; Son, J. H.; Jeong, M. S.; Lee, Y. H. *J. Am. Chem. Soc.* **2005**, *127*, 5196. (e) Maeda, Y.; et al. *J. Am. Chem. Soc.* **2005**, *127*, 10287–10290.

(166) (a) Menard-Moyon, C.; Izard, N.; Doris, E.; Mioskowski, C. *J. Am.Chem. Soc.* **2006**, *128*, 6552. (b) Arnold, M. S.; Green, A. A.; Hulvat, J. F.; Stupp, S. I.; Hersam, M. C. *Nat. Nanotechnol.* **2006**, *1*, 60. (c) Hersam, M. C. *Nat. Nanotechnol.* **2008**, *3*, 387. (d) Hwang, J. Y.; Nish, A.; Doig, J.; Douven, S.; Chen, C. W.; Chen, L. C.; Nicholas, R. J. *J. Am. Chem. Soc.* **2008**, *130*, 3543.

(167) (a) Collins, P. C.; Arnold, M. S.; Avouris, P. *Science* **2001**, *292*, 706. (b) Krupke, R.; Hennrich, F.; von Lohneysen, H.; Kappes, M. M. *Science.* **2003**, *301*, 344. (c) Zhang, G. Y.; Qi, P. F.; Wang, X. R.; Lu, Y. R.; Li, X. L.; Tu, R.; Bangsaruntip, S.; Mann, D.; Zhang, L.; Dai, H. J. *Science.* **2006**, *314*, 974. (d) Song, J. W.; Seo, H. W.; Park, J. K.; Kim, J. E.; Cho, D. G.; Han, C. S. *Curr. Appl. Phys.* **2008**, *8*, 725. (e) Qui, H.; Maeda, Y.; Akasaka, T. *J. Am. Chem. Soc.* **2009**, *131*, 16529.

(168) (a) Sgobba, V.; Rahman, G. M. A.; Guldi, D. M. In *Carbon Nanotubes in Electron Donor-Acceptor Nanocomposites, Chemistry of Carbon Nanotubes*; Basiuk, V. A., Ed.; American Scientific Publishers: Stevenson Ranch, CA, 2006. (b) Sgobba, V.; Rahman, G. M. A.; Ehli, C.; Guldi, D. M. Covalent and Non-covalent Approaches Toward Multifunctional Carbon Nanotubes Materials In *Fullerenes-Principles and Applications*; Langa, F., Nierengarten, J. F., Eds.; Royal Society of Chemistry: Cambridge, UK, 2007. (c) Sgobba, V.; Guldi, D. M. *Chem. Soc. Rev.* **2009**, *38*, 165.

(169) (a) Kataura, H.; Maniwa, Y.; Suzuki, S.; Achiba, Y. *Jpn. J. Appl. Phys.* **2001**, *40*, L1229. (b) Georgakilas, V.; Kordatos, K.; Prato, M.; Guldi, D. M.; Holzinger, M.; Hirsch, A. *J. Am. Chem. Soc.* **2002**, *124*, 760. (c) Cao, L.; Chen, H.; Wang, M.; Sun, J.; Zhang, X.; Kong, F. *J. Phys. Chem. B.* **2002**, *106*, 8971. (d) Star, A.; Steuerman, D. W.; Heath, J. R.; Stoddart, J. F. *Angew. Chem., Int. Ed.* **2002**, *41*, 2508. (e) Dyke, C. A.; Tour, J. M. *J. Am. Chem. Soc.* **2003**, *125*, 1156. (f) Freitag, M.; Martin, Y.; Misewich, J. A.; Martel, R.; Avouris, P. *Nano Lett.* **2003**, *3*, 1067.

(170) (a) Holzinger, M.; Abraham, J.; Whelan, P.; Graupner, R.; Ley, L.; Hennrich, F.; Kappes, M.; Hirsch, A. *J. Am. Chem. Soc.* **2003**, *125*, 8566. (b) Murakami, H.; Nomura, T.; Nakashima, N. *Chem. Phys. Lett.* **2003**, *378*, 481. (c) Guldi, D. M.; Marcaccio, M.; Paolucci, D.; Paolucci, F.; Tagmatarchis, N.; Tasis, D.; Vazquez, E.; Prato, M. *Angew. Chem., Int. Ed.* **2003**, *42*, 4206. (d) Fukushima, T.; Kosaka, A.; Ishimura, Y.; Yamamoto, T.; Takigawa, T.; Ishii, N.; Aida, T. *Science* **2003**, *300*, 2072. (e) Sun, J.; Gao, L.; Iwasa, M. *Chem. Commun.* **2004**, 832.

(171) (a) Robel, I.; Bunker, B. A.; Kamat, P. V. *Adv. Mater.* **2004**, *17*, 2458. (b) Campidelli, S.; Sooambar, C.; Lozano, Diz, E.; Ehli, C.; Guldi, D. M.; Prato, M. *J. Am. Chem. Soc.* **2006**, *128*, 12544. (c) Herranz, M. A.; Martin, N.; Campidelli, S.; Prato, M.; Brehm, G.; Guldi, D. M. *Angew. Chem., Int. Ed.* **2006**, *45*, 4478. (d) Zheng, M.; Rostovtsev, V. V. *J. Am. Chem. Soc.* **2006**, *128*, 7702.

(172) (a) Chen, R. J.; Zhang, Y.; Wang, D.; Dai, H. *J. Am. Chem. Soc.* **2001**, *123*, 3838. (b) Simmons, T. J.; Bult, J.; Hashim, D. P.; Linhardt, R. J.; Ajayan, P. M. *ACS Nano.* **2009**, *3*, 865.

(173) Dresselhaus, M. S.; Dresselhaus, G.; Jorio, A.; Souza Filho, A. G.; Saito, R. *Carbon.* **2002**, *40*, 2043.

(174) (a) Herrera, J. E.; Resasco, D. E. *Chem. Phys. Lett.* **2003**, *376*, 302. (b) Herrera, J. E.; Pompeo, B. F.; Resasco, D. E. *J. Nanosci. Nanotechnol.* **2003**, *3*, 1. (c) Jorio, A.; Santos, A. P.; Ribeiro, H. B.; Fantini, C.; Souza, M.; Vieira, J. P. M.; Furtado, C. A.; Jiang, J.; Saito, R.; Balzano, L.; Resasco, D. E.; Pimenta, M. A. *Phys. Rev. B.* **2005**, *72*, 075207. (d)

Hennrich, F.; Krupke, R.; Lebedkin, S.; Arnold, K.; Fischer, R.; Resasco, D. E.; Kappes, M. M. *J. Phys. Chem. B.* **2005**, *109*, 10567.

(175) Tanaka, Y.; Hirana, Y.; Niidome, Y.; Kato, K.; Saito, S.; Nakashima, N. *Angew. Chem., Int. Ed.* **2009**, *48*, 1.

(176) The 532-nm laser light excites the shorter wavelength side of the Q-band of ZnP. Since the most of the broad absorption of SWNTs in the visible region is usually attributed to background, only small absorption of the SWNTs can be absorbed by the 532-nm laser light. It is difficult to evaluate the excited molecules quantitatively, because it depends on the abstraction of the background absorption and on the absorption coefficients, which are not possible to evaluate with reasonable accuracy for both the SWNT and absorbed ZnP in the hybrids.

(177) (a) Fukuzumi, S.; Suenobu, T.; Patz, M.; Hirasaka, T.; Itoh, S.; Fujitsuka, M.; Ito, O. *J. Am. Chem. Soc.* **1998**, *120*, 8060. (b) Pagona, G.; Sandanayaka, A. S. D.; Araki, Y.; Fan, J.; Tagmatarchis, N.; Yudasaka, M.; Iijima, S.; Ito, O. *J. Phys. Chem. B.* **2006**, *110*, 20729.

(178) IPCE(%) = 100 × 1240 × $I_{SC}/(W_{in}\ \lambda)$, where I_{SC} is the short circuit photocurrent (A/cm^2), W_{in} is the incident light intensity (W/cm^2), and λ is the wavelength in nm.

(179) D'Souza, F.; Ito, O. in *Handbook of Porphyrin Science* Eds. Kadish, K. M.; Guilard, R.; Smith K. M. World Science Publishers, **2010**, Vol. 1, Chapter 4, pp 307-437.

(180) Maligaspe, E.; Sandanayaka, A. S. D.; Hasobe, T.; Ito, O.; D'Souza, F. *J. Am. Chem. Soc.* **2010**, *132*, 8158–8164.

(181) (a) Paolucci, D.; Franco, M. M.; Iurlo, M.; Marcaccio, M.; Prato, M.; Zerbetto, F.; Penicaud, A.; Paolucci, F. *J. Am. Chem. Soc*. **2008**, *130*, 7393. (b) Ehli, C.; Oelsner, C.; Guldi, D. M.; Mateo-Alonso, A.; Prato, M.; Schmidt, C.; Backes, C.; Hauke, F.; Hirsch, A. *Nat. Chem*. **2009**, *1*, 243.

(182) Bachilo, S. M.; Strano, M. S.; Kittrell, C.; Hauge, R. H.; Smally, R. E.; Weisman, R. B.; *Science.* **2002,** *298*, 2361.

(183) Hasobe, T. *Phys. Chem. Chem. Phys.* **2010**, *12*, 44.

APPENDIX

APPENDIX

Publications during my PhD program

1. **Maligaspe, E**.; Sandanayaka, A.; Hasobe, T.; Ito, O.; D'Souza, F. Sensitive Efficiency of Photovoltaic Cell to Band Gaps of Semi-Conductive SWNTs with Supramolecularly Attached Zinc Porphyrin bearing Pyrene Glues. *J. Am. Chem. Soc*. **2010**, *132*, 8158–8164

2. **Maligaspe, E**.; Kumpulainen , T.; Subbaiyan, N. K.; Zandler, M. E.; Lemmetyinen, H.; Tkachenko, N. V.; D'Souza, F. Electronic Energy Harvesting Multi BODIPY Zinc Porphyrin Dyads Accommodating Fullerene as Photosynthetic Composite of Antenna-Reaction Center. *Phys. Chem. Chem. Phys.* **2010**, *12,* 7434-7444

3. Pietrzyk, A.; Suriyanarayanan, S.; Kutner, W.; **Maligaspe, E**.; Zandler, M.; and D'Souza, F. Molecularly Imprinted Poly[bis(2,2'-bithienyl)methane] Film with Built-in Molecular Recognition Sites for a Piezoelectric Microgravimetry Chemosensor for Selective Determination of Dopamine. *Bioelectrochemistry*. **2010**, *In press*

4. **Maligaspe, E**.; and D'Souza, F. NOR and AND Logic Gates Based on Supramolecular Porphyrin-Fullerene Conjugates. *Org. Lett*. **2010**, 12, 3, 624-627

5. **Maligaspe, E**.; Kumpulainen, T.; Tkachenko, N.; Subbaiyan, N.; Zandler, M.; Lemmetyinen, H.; D'Souza, F. Ultrafast Singlet-Singlet Energy Transfer in Self-Assembled via Metal-Ligand Axial Coordination Free-Base Porphyrin-Zinc Phthalocyanine and Free-base Porphyrin-Zinc Naphthalocyanine Dyads *J. Phys. Chem. A.* **2010,** *114,* 268–277

6. D'Souza, F.; **Maligaspe, E.**; Ohkubo, K.; Zandler, Melvin.; Subbaiyan, N.; Fukuzumi, S. Photosynthetic Reaction Center Mimicry: Low-Reorganization Energy Driven Charge Stabilization in Self-Assembled Co-facial Zinc Phthalocyanine Dimer – Fullerene Conjugates. *J. Am. Chem. Soc.*, **2009**, *131*, 8787–8797

7. **Maligaspe, E.**; Tkachenko, N.; Subbaiyan, N.; Chitta, R.; Zandler, M.; Lemmetyinen, H.; D'Souza, F. Photosynthetic Antenna-Reaction Center Mimicry: Sequential Energy- and Electron Transfer in a Self-assembled Supramolecular Triad Composed of Boron Dipyrrin, Zinc Porphyrin and Fullerene. *J. Phys. Chem. A* **2009,** *113,* 8478–8489

8. D'Souza, F.; **Maligaspe, E**.; Zandler, M. E.; Subbaiyan, N. K.; Ohkubo, K.; Fukuzumi, S. Metal Quinolinolate–Fullerene(s) Donor-Acceptor Complexes: Evidence for Organic LED Molecules Acting as Electron Donors in Photoinduced Electron-Transfer Reactions. *J. Am. Chem. Soc.*, **2008**, *130*, 16959–16967.

9. D'Souza, F.; **Maligaspe, E.**; Karr, P. A.; Schumacher, A. L.; Ojaimi, M. E.; Gros, C.P.; Barbe, J.-M. Ohkubo, K.; Fukuzumi, S. Face-to-Face Held Pacman Type Porphyrin-Fullerene Dyads: Design, Synthesis, Charge Transfer Interactions and Photophysical Studies. *Chem. Euro. Journal,* **2008**, *14*, 674-681.

10. D'Souza, F.; **Maligaspe, E**.; Sandanayaka, A.; Subbaiyan, N.; Karr, P.; Hasobe, T.; Ito, O. Photochemical Charge Stabilization in Supramolecular Phthalocyanine-Multifullerene Conjugates Assembled by Crown Ether-Alkyl Ammonium Cation Interactions. *J. Phys. Chem. A*., **2010***. 114*, 10951-10959.

11. Sandanayaka, A. S. D.; **Maligaspe, E**.; Hasobe, T.; Ito, O.; D'Souza, F. Band Gap Dependent Electron Transfer in Supramolecular Nanohybrids of (6,5)- or (7,6)-Enriched Semiconducting SWNT as Donors and Fullerene as Acceptor. *Chem. Commun.* **2010**, *46*, 8749-8751.

12. Stranius, K.; Jacobs, R.; **Maligaspe, E**.; Lemmetyinen, H.; Tkachenko, N.; Zandler, M.; D'Souza, F. Excitation Transfer in Metal-Ligand Coordinated Free-Base Porphyrin-Magnesium Phthalocyanine and Free-Base Porphyrin-Magnesium Naphthalocyanine Dyads. *Journal of Porphyrins and Phthalocyanines*, **2010**, *14*, 948-961.

13. Free-base porphyrin and Fe porphyrin based Supramolecular Solar cells. *Manuscript in preparation.*